MAGNETIC AND FERROELECTRIC PROPERTIES OF SOME ADVANCED FUNCTIONAL OXIDES AND RELATED PHENOMENA

By

SUDIPTA MAHANA

(PHYS07201204005)

INSTITUTE OF PHYSICS, BHUBANESWAR

A thesis submitted to the

Board of studies in Physical Sciences

In partial fulfillment of the requirements

For the Degree of

DOCTOR OF PHILOSOPHY
of
HOMI BHABHA NATIONAL INSTITUTE

July, 2018

HOMI BHABHA NATIONAL INSTITUTE

Recommendations of the Viva Voce Board

As members of the Viva Voce Board, we certify that we have read the dissertation prepared by Miss Sudipta Mahana entitled "**Magnetic and ferroelectric properties of some advanced functional oxides and related phenomena**" and recommend that it may be accepted as fulfilling the dissertation requirement for the Degree of Doctor of Philosophy.

Date: 25-07-2018

Chairman- Prof. Arun M Jayannavar

Date: 25-07-2018

Guide / Convener- Dr. Dinesh Topwal

Debraj Choudhury

Date: 25-07-2018

Thesis Examiner- Dr. Debraj Choudhury

Date: 25-07-2018

Member- Prof. Biju Raja Sekhar

Saptarshi Mandal

Date: 25-07-2018

Member- Dr. Saptarshi Mandal

S

Final approval and acceptance of this dissertation is contingent upon the candidate's submission of the final copies of the dissertation to HBNI.

I hereby certify that I have read this dissertation prepared under my direction and recommend that it may be accepted as fulfilling the dissertation requirement.

Date: 25-07-2018

Place: IOP, Bhubaneswar, India

Dr. Dinesh Topwal
(Thesis Supervisor)

Statement by author

This dissertation has been submitted in partial fulfillment of requirements for an advanced degree at Homi Bhabha National Institute (HBNI) and is deposited in the Library to be made available to borrowers under rules of the HBNI.

Brief quotations from this dissertation are allowable without special permission, provided that accurate acknowledgement of source is made. Requests for permission for extended quotation from or reproduction of this manuscript in whole or in part may be granted by the Competent Authority of HBNI when in his or her judgment the proposed use of the material is in the interests of scholarship. In all other instances, however, permission must be obtained from the author.

Sudipta Mahana

Sudipta Mahana

Declaration

I, Sudipta Mahana, hereby declare that the investigation presented in the thesis has been carried out by me. The work is original and has not been submitted earlier as a whole or in part for a degree / diploma at this or any other University / Institution.

Sudipta Mahana

Sudipta Mahana

List of Publications:

1. “Giant magnetocaloric effect in Gd_2NiMnO_6 and Gd_2CoMnO_6”, J K Murthy, K D Chandrasekhar, **Sudipta Mahana**, D Topwal and A Venimadhav, *J. Phys. D.: Appl. Phys.*, **2015**, *48*, 355001-1-6.
2. “Resonance Raman spectroscopic study for radial vibrational modes in ultra-thin walled TiO_2 nanotubes”, R. P. Antony, A. Dasgupta, **Sudipta Mahana**, D. Topwal, Tom Mathews and Sandip Dhara., *J. Raman Spec.*, **2015**, *46*, 231-235.
3. “Structural and electronic phase evolution of Tin dioxide”, **Sudipta Mahana**, Pitambar Sapkota, Saptarshi Ghosh, U. Manju and D. Topwal, *arxiv*, **2016**, *1606:08137*, 1-6.
4. * “Giant magnetocaloric effect in $GdAlO_3$ and a comparative study with $GdMnO_3$”, **Sudipta Mahana,** U Manju and D Topwal, *J. Phys. D: Appl. Phys*., **2017**, *50*, 035002-1-8.
5. * “Complex spin glass behavior in $Ga_{2-x}Fe_xO_3$”, **Sudipta Mahana** and D Topwal, *Appl. Phys. Lett.*, **2017**, *110*, 102907-1-5.
6. * “Local inversion symmetry breaking and spin-phonon coupling in perovskite $GdCrO_3$”, **Sudipta Mahana**, Bipul Rakshit, Raktima Basu, Sandip Dhara, Boby Joseph, U. Manju, Subhendra D. Mahanti and D. Topwal, *Phys. Rev. B*, **2017**, *96*, 104106-1-9.
7. * “Defect induced polarization and dielectric relaxation in $Ga_{2-x}Fe_xO_3$”, **Sudipta Mahana**, C. Dhanasekhar, A. Venimadhav and D. Topwal, *Appl. Phys. Lett.*, **2017,** *111*, 132902-1-4.
8. Synthesis and characterization of layered metal sulfates containing $M^{II}_3(\mu_3\text{-OH/F})_2$(M = Mg, Co) diamond chains, Subba R. Marri, **Sudipta Mahana**, Dinesh Topwal and J. N. Behera, *Dalton Trans.*, **2017**,*46*, 1105-1111.
9. * “Role of local structural distortion in driving ferroelectricity in $GdCrO_3$”, **Sudipta Mahana**, U. Manju, Pronoy Nandi, Edmund Welter, K. R. Priolkar and D. Topwal, *Phys. Rev. B*, **2018**, *97*, 224107-1-6.
10. * “$GdCrO_3$: a potential candidate for low temperature magnetic refrigeration”, **Sudipta Mahana**, U. Manju, and D. Topwal, *J. Phys. D.: Appl. Phys*., **2018**, *51*, 305002-1-6.

Conference Proceedings:

1. * "Complex magnetic behavior in $GdCrO_3$", **Sudipta Mahana,** U. Manju, and D. Topwal, *AIP Conference Proceedings*, **2017**, *1832*, 130046-1-3.
2. "Thermoelectric properties of ternary half-heuslar LuPdBi", A. Mukhopadhyay, **Sudipta Mahana**, S. Chowki, D. Topwal and N. Mohapatra, *AIP Conference Proceedings*, **2017**, 1832, 110024-1-3.
3. "Optical and low temperature magnetic properties study on sol-gel derived misfit calcium cobaltite, A. Mishra, **Sudipta Mahana,** Dinesh Topwal, U Manju, Sarama Bhattacharjee, *AIP Conference Proceedings*, **2017**, *1832*, 030019-1-3.

Communicated manuscripts:

1. * "Site dilution in Cr-doped $GdMnO_3$: effects on structural, electronic and magnetic properties", Sudipta Mahana, Bipul Rakshit, Pronoy Nandi, Raktima Basu, Sandip Dhara, U. Manju, Subhendra D. Mahanti and D. Topwal.

Conference Presentations:

1. * Indo-Japan Workshop on Magnetism at Nanoscale (IJWMN) during 9th - 12th January, 2015, at NISER, Bhubaneswar, India (Poster presentation: Magnetic behavior in $GdMO_3$, M = Mn, Cr and Al).
2. * Frontiers in Advanced Materials (FAM) during 15th - 18th June, 2015 at IISC, Bangalore, India (Poster presentation: Complex spin glass behavior in $Ga_{2-x}Fe_xO_3$).
3. * Emerging Trends in Advanced Functional Materials (ETAFM) during 18th - 21st January, 2016 at IOP, Bhubaneswar, India (Poster presentation: Complex spin glass behavior in $Ga_{2-x}Fe_xO_3$)
4. * 61st DAE Solid State Physics Symposium (DAE SSPS) during 26th - 30th December 2016, KIIT University, Bhubaneswar, India (Poster presentation: Complex magnetic behavior in $GdCrO_3$)

5. * 9th International Conference on Materials for Advanced Technologies (ICMAT) during 18th – 23rd June 2017 at Suntec, Singapore (Oral presentation: Giant magnetocaloric effect in $GdAlO_3$ and a comparative study with $GdMnO_3$ and Poster presentation: Complex spin glass behavior in $Ga_{2-x}Fe_xO_3$)

* Indicates the papers on which this thesis is based.

Sudipta Mahana

Sudipta Mahana

DEDICATED TO MY PARENTS & GRANDPARENTS

Acknowledgments

The journey at IOP Bhubaneswar during my doctoral research period has been fantastic. It has been a period of intense learning for me, not only in the scientific arena, but also on a personal level. I would like to express my sincere gratitude towards them who have support me and led to fruition of this thesis.

Firstly, I thank my supervisor Dr. Dinesh Topwal for his guidance, advice, support and constant encouragement throughout my Ph.D. research period. His guidance helped me in all the time of research and writing this thesis. He has given me full freedom to carry out research works in my own interest, which I have enjoyed a lot and I must extend my great depth of gratitude and indebtedness to him for that. I also thank him for standing beside me with constant support through thick and thin. I do hope more supports in the future.

I am honestly obliged to Prof. S. D. Mahanti (Michigan State University, USA) for his useful suggestions, discussions and concealed help during the course of theoretical calculations. I thank Dr. Bipul Rakshit (UNIST, South Korea) for doing all the theoretical calculations. I would like to thank Prof. P. V. Satyam (IOP, Bhubaneswar) for providing computational facilities. I am gratified to Dr. Manju Unnikrishnan (IMMT, Bhubaneswar) for providing me samples during the early days of my research as well as for her kind cooperation in my research work. I would like to acknowledge Prof. A. Venimadhav (IIT, Kharagpur) and his student C. Dhanasekhar for carrying out several dielectric and pyroelectric measurements for me. I thank Dr. S. Dhara (IGCAR, Kalpakkam) and his student Raktima Basu for doing Raman experiments. My good wishes to C. Dhanasekhar and R. Basu for their research works. I thank Prof. K. Priolkar (Goa University) for helping me to learn EXAFS data analysis.

I got the opportunity to perform experiments at circular polarization (CIPO) beamline at ELLETRA synchrotron centre, Italy and P65 beam line at Petra III, DESY, Germany. I gratefully acknowledge the people of these beamlines for their support during the beam times. I thank Department of Science and Technology, Govt. of India for the financial support provided for participating in beam time.

I take this opportunity to thank my review commite members; Prof. Arun M Jayanavar, Prof. Biju Raja Sekhar and Dr. Saptarshi Mandal for their encouraging words and attention.

My earnest appreciation to all the Directors at IOP for their support and kindness over these years. I thank the administrative and support staff of IOP for their direct or indirect help in many cases. I would to like to acknowledge the excellent library and computer facilities provided by the IOP and all the members of IOP.

I convey my gratefulness to all my former and present labmates; P. Nandi, Dr. R. Bommali, Dr. C. Giri, Dr. A. Ghosh, Dr. R. Das for their immense help and support. They have provided a friendly, concerted and an excellent research environment. A very special appreciation goes to Pronoy, for his company during the beam times and other visits. I cannot thank enough to him for his care when I feel sick during journey and for being a listening ear and bearing my idiosyncrasy during my bad days. I wish him the best of luck for his research journey.

Thanks to my friends, batch mates, seniors, juniors and others for making enjoyable and memorable experience during my whole stay here. A special thanks to Pramita di and Rubina for their friendly and caring attitude which made my stay homely at IOP.

I would be amiss if I do not mention my best friend Shubhajyoti Mohapatra from IIT Kanpur for his support during the time of Ph.D. interview and being with me during this tough journey. My best wishes for his research endeavors and success.

Last but not the least, I would like to express my deepest gratitude to my family members, especially my *Maa* and *Baba*, for always being there for me and without their support this thesis would not have been possible.

Thank you very much, everyone !!!

Contents

Synopsis

Strongly correlated electron systems are very active research area of condensed matter physics owing to their underlying rich fundamental physics and possibilities of amazing technological applications. Electronic correlations can cause striking many-body effects that cannot be described in the independent particle picture. The subtle coupling and competition between electron, lattice, spin, charge and orbital degrees of freedom are the essence of these systems, which leads to the emergence of exciting novel properties such as magnetism [1], ferroelectricity [2], multiferroicity [3], piezoelectricity [4], charge ordering [5], metal-insulator transition [6], colossal magnetoresistance [7], spin-state transitions [8], superconductivity [9] and many more. The interplay of the internal degrees of freedom also make them extremely sensitive to small external perturbations such as temperature, pressure or substitution [10]. Strong correlation effects are observed in transition metal compounds, mainly oxides [11], rare earth-based materials [12], organic metals [13] etc. Among these materials, oxides have always been a topic of intense discussion among the researchers as these are the basis of smart and functional materials. Some of these functional oxides are investigated in this thesis, both in terms of their fundamental understanding as well as from the application point of view.

$GaFeO_3$ is a unique system, where the properties are heavily influenced by disorder at the atomic level [14] and hence can be tuned. It adopts non-centrosymmetric crystal structure with space group $Pc2_1n$ and remain in a highly disorder state i.e. Fe is often found in the Ga site and *vice versa* due to similar ionic radii of Ga and Fe. The significant inherent cationic disorder and noncentrosymmetric crystal structure leads to ferrimagnetism, piezoelectricity, ferroelectricity and pronounced magnetoelectric effects in the system, making it one of the few chemical systems to possess multiferroic ordering near room temperature [14-16]. Eventhough ferroelectricity with unusually high coercive field and remnant polarization was obtained in thin film [16], the presence of ferroelectricity in bulk $GaFeO_3$ is rather inconclusive due to leaky behavior of the sample [17]. Furthermore, there are contradictory claims about the existence of spin-glass-like behavior in $GaFeO_3$ [8]. Therefore, we have systematically studied magnetic and ferroelectric properties in bulk $GaFeO_3$ and its various compositions with varying proportions of Ga and Fe i.e. $Ga_{2-x}Fe_xO_3$.

Functional perovskite oxide (ABO_3) is an expanding interdisciplinary paradigm which encompasses diverse fields of science and engineering. A particular aspect of perovskites is their ability to incorporate most of the element of the periodic table into their structure due to their capacity to accommodate various structural distortions [19]. The external parameters like temperature, pressure and chemical compositions, can also drive such distortions, which leads to an extraordinary richness of physical properties within the family of perovskites. Structural distortions in perovskites is mainly associated with three main features with respect to their ideal cubic structure [19,20]: (i) rotation (tilt) of BO_6 octahedra, (ii) polar cation displacements, which often lead to ferroelectricity, and (iii) distortions of the octahedra, such as the Jahn-Teller (JT) distortion. A particular resurgence of intense activity in investigating the properties of these systems followed by colossal magnetoresistence in the manganites [7], simultaneous ferroelectric and complex magnetic ordering in the manganites [3], multiferroicity and metal-insulator transition in nickelates [21] and considerable high temperature ferroelectric ordering in chromites [22]. The rare-earth manganites ($RMnO_3$) possess JT character of Mn^{3+} ions ($t_{2g}^3 e_g^1$) and exhibit orbital ordering along with highly anisotropic Mn-O bond lengths. Such a complex interplay among the spin, orbit and lattice degrees of freedom have led to a plenty of intriguing physical properties in $RMnO_3$. On the other hand, Cr^{3+} is JT inactive due to its completely empty e_g orbitals, hence octahedra are more regular. Inspite of this, the most of RCrO$_3$ systems are high temperature ferroelectrics [22]. Additionally, they exhibit complex magnetic properties such as spin-reorientation (SR), spin-flipping (SF) and temperature induced magnetization reversal (TMR) etc [23]. Eventhough immense research activities have been pursued in these areas, the underlying phenomena is not fully understood yet. Therefore, we have carried out a detailed study of the structural, magnetic and electronic properties of GdMnO$_3$ and GdCrO$_3$ and their evolutions with substitutions, viz. GdMn$_{1-x}$Cr$_x$O$_3$. Furthermore, existence and/or origin of ferroelectricity in GdCrO$_3$ system is still debated [24]. In order to obtain detailed understanding of origin of ferroelectricity in GdCrO$_3$, we have performed temperature-dependent synchrotron powder x-ray diffraction studies along with first-principles density-functional-theory-based calculations.

Detailed investigations on some of the Gd-based oxides, GdMO$_3$ (M = Al, Mn and Cr) have been done for possible usage in magnetic refrigeration (MR) applications, as they exhibit field-induced metamagnetic transition from antiferromagnetic (AFM) to to ferromagnetic (FM) state near the Gd-ordering temperature. MR technology has attended great attention in recent years due to its high energy efficiency and eco-friendly characteristics over conventional gas compression/expansion cooling technology [25]. The working principle of MR is based on isothermal magnetic entropy change (ΔS_M) or the adiabatic temperature change (ΔT_{ad}) caused by change in the magnetic field, which is, in a way, similar to the process that occurs in a gas in response to the change in pressure [25]. During the isothermal magnetization process, magnetic entropy is decreased significantly near the magnetic transition temperature (FM to paramagnetic (PM) transition and field-induced AFM to FM state) due to a reduction of disorder in the spin system. Hence, such materials are suitable candidates for magnetic refrigeration in the vicinity of the transition temperature. Materials having a room temperature cooling capacity can be used for domestic and industrial refrigeration purposes, whereas materials with low working temperatures are useful for helium liquefaction (4 K) and hydrogen liquefaction (20 K).

The thesis organized in to seven chapters. **Chapter 1** is a brief introduction and motivation to various concepts discussed in this thesis followed by the experimental and the theoretical techniques used in the present study in **Chapter 2**. This includes sample synthesis technique: solid state reaction, characterization tools: powder x-ray diffraction (XRD), dc and ac magnetization, dielectric, pyroelectric, heat capacity, Raman spectroscopy, x-ray absorption spectroscopy (XAS) and extended x-ray absorption fine structure (EXAFS) studies and density functional theory (DFT) calculations to study the structural, electronic and magnetic properties and density functional perturbation theory (DFPT) approach for phonon calculations.

Chapter 3 is divided into two parts. In the first part, we discuss the detailed magnetic properties of solid solutions of $Ga_{2-x}Fe_xO_3$ ($x = 0.75$, 1.0, and 1.25). Magnetic behaviour in this series of compounds could broadly be explained by the molecular-field-approximation of a three-sublattice ferrimagnetic model considering three inequivalent octahedral sites. $x = 0.75$ composition exhibits a transition from the cluster-glass-like phase to the spin-glass-like phase with decreasing temperature. Mentioned glassy behaviour is found to gradually evolve with the composition (x) from the Ising type character to Heisenberg type behaviour to unconventional glassy behaviour for the $x = 1.25$ composition. The complex spin glass behaviour in these systems is due to the inherent site disorder driven magnetic inhomogeneity, competing FM and AFM interactions along with spin frustration and their modifications with compositions (x). In the second part, we discuss detailed dielectric and pyroelectric studies in $Ga_{2-x}Fe_xO_3$. These systems exhibit multiple dielectric relaxations associated with high frequency Debye type relaxation in grains and low frequency Maxwell-wagner type relaxation at grain boundaries. Further, pyroelectric study confirmed that the emergence of polarization in these systems can be understood in terms of thermally stimulated depolarization current (TSDC) effect caused by the freezing of defect dipoles possibly associated with charged oxygen vacancies rather than the intrinsic ferroelectric behaviour.

Chapter 4 also consists of two parts**.** In first part we discuss detailed studies on the possible non-centrosymmetric structure of $GdCrO_3$ using XRD measurements and first principle calculations. We also discuss the possible polar phonon mode instability in its cubic structure to understand the origin of ferroelectricity at considerable high temperature. The actual lattice symmetry is found to be noncentrosymmetric orthorhombic $Pna2_1$ structure, supporting the polar nature of the system. Polar distortion is associated with the Gd displacements with respect to the oxygen cage. An intimate analogy between $GdCrO_3$ and $YCrO_3$ systems is revealed, even though a distinctive difference exists that Gd is less displacive compared to Y, which results in an orthorhombic $Pna2_1$ structure in $GdCrO_3$ in contrast to monoclinic structure in $YCrO_3$ and consequently, decreases its polar property. It is found that magnetic coupling between Gd-4*f* and Cr-3*d* plays an important role in ferroelectric distortion. Temperature dependent EXAFS study also infers Gd-O bond polarization might play significant role for the emergence of ferroelectricity. Detailed magnetic properties and spin-phonon coupling studies in $GdCrO_3$ are discussed in the second part. Magnetic interactions in this system is quite complex and hence exhibit various exotic magnetic phenomena like temperature induced magnetization reversal, spin flipping and spin reorientation etc. These behaviors can be successfully explained by symmetric (Si**.**Sj) and antisymmetric (Si×Sj) exchange interactions within and between Cr and Gd-sublattices. Detailed temperature dependent Raman study reveals a strong magneto-electric coupling in the system, which provides a complementary tool for the ferroelectric modulation.

Evolution of structural, electronic and magnetic properties of Cr-doped $GdMnO_3$ for Cr doping levels $0 \leq x \leq 1$ is discussed in **Chapter 5**. In the solid solutions, the JT-distortion associated with Mn^{3+} ions gives rise to major changes in the *bc*-plane sub-lattice and also the effective orbital ordering in the *ab*-plane, which persist up to the compositions $x \sim 0.35$. These distinct features in the lattice and orbital degrees of freedom are also correlated with the *bc*-plane anisotropy in the local Gd environment. A gradual evolution of electronic states with compositions is also clearly seen in O *K*-edge x-ray absorption spectra. Evidence of magnetization reversal in field-cooled-cooling mode for $x \geq 0.35$ compositions coinciding with JT-crossover, suggests a close correlation between magnetic interactions and structural distortions. These observations indicate a strong entanglement between lattice, spin, electronic and orbital degrees of freedom. The nonmonotonic variation of remnant magnetization can be explained by doping induced modification of magnetic interactions. Density functional theory calculations are consistent with a layer-by-layer type doping with ferromagnetic (antiferomagnetic) coupling between Mn (Cr) ions for intermediate compound ($x = 0.5$), which is distinct from that observed for the end members $GMnO_3$ (*A*-type) and $GdCrO_3$ (*G*-type).

Magnetocaloric effect (MCE) of polycrystalline $GdMO_3$ (M = Al, Mn and Cr) near the Gd-ordering temperature are discussed in **Chapter 6**. A giant magnetic entropy change (ΔS_m) occurs under moderate magnetic field change in $GdAlO_3$, where as $GdMnO_3$ exhibits comparably less ΔS_m at same magnetic field changes, due to the Gd-Mn negative exchange interaction. Even though $GdMnO_3$ has quite less ΔS_m compared to $GdAlO_3$, both the compounds have comparable cooling power. However, absence of magnetic and thermal hysteresis in $GdAlO_3$ make it a more efficient and reversible magnetic refrigerant than $GdMnO_3$. $GdCrO_3$ exhibits exceptionally large ΔS_m, adiabatic temperature change (ΔT_{ad}) and relative cooling power (RCP) at moderate magnetic field change. Such exceptionally large MCE possibly arises from the suppression of the spin entropy associated with the suppression of spin reorientation transition, in addition to the Gd-ordering, which makes it the best candidate for magnetic refrigeration among all the potential low temperature magnetic refrigerants known so far.

Summary and outlook of the present thesis work are given in **Chapter 7.**

References:

[1] P. Coleman, *Handbook of Magnetism and Advanced Magnetic Materials* (Wiley, New York), 2007.

[2] R. E. Cohen, Nature (London) **358**, 136 (1992); M. Mahesh Kumar, V. R. Palkar, K. Srinivas and S. V. Suryanarayana, Appl. Phys. Lett. **76**, 2764 (2000).

[3] S-W Cheong and M. Mostovoy, Nat. Mater. **6**, 13 (2007).

[4] S. Shao, J. Zhang, Z. Zhang, P. Zheng, M. Zhao, J. Li and C. Wang, J. Phys. D: Appl. Phys. **41**, 125408 (2008).

[5] R. Kajimoto, K. Ishizaka, H. Yoshizawa and Y. Tokura, Phys Rev B **67**, 014511 (2003).

[6] M. Imada, A. Fujimori and Y. Tokura, Rev. Mod. Phys. **70**, 1039 (1998).

[7] R. von Helmolt, J. Wecker, B. Holzapfel, L. Schultz, and K. Samwer, Phys. Rev. Lett. **71**, 2331 (1993); Y. Tokura and N. Nagaosa, Science **288**, 462 (2000).

[8] H. Gretarsson, S. R. Saha, T. Drye, J. Paglione, Jungho Kim, D. Casa, T. Gog, W. Wu, S. R. Julian, and Young-June Kim, Phys. Rev. Lett. **110**, 047003 (2013

[9] A. Schilling, M. Cantoni, J. D. Guo and H. R. Ott, Nature **363**, 56 (1993); C. Wang, L. Li, S. Chi, Z. Zhu, Z. Ren, Y. Li, Y. Wang, X. Lin, Y. Luo, S. Jiang, X. Xu, G. Cao and Z. Xu, Europhys. Lett. **83,** 67006 (2008).

[10] S. Cao, H. Zhao, B. Kang, J. Zhang and W. Ren, Sci. Rep. **4**, 5960 (2014); V. Pardo and W. E. Pickett, Phys. Rev. B 85, 045111 (2012); N. Sakiyama, I. A.

Zaliznyak, S. H. Lee, Y. Mitsui and H. Yoshizawa, Phys. Rev. B **78**, 180406(R) (2008).

[11] Y. Tokura, Physics Today **56**, 7, 50 (2003).

[12] S. K. Dhar, R. Kulkarni, P. Manfrinetti, M. Pani, Y. Yonezawa and Y. Aoki, Phys. Rev. B **76**, 054411 (2007); L. Jiao , S. Robler, D.J. Kim, L.H. Tjeng, Z. Fisk, F. Steglich and S. Wirth, Nat. Comm. **7**, 13762 (2016).

[13] J. Merino and R. H. McKenzie, Phys. Rev. B **62**, 16442 (2000); M. Filibian, P. Carretta, M. C. Mozzati, P. Ghigna, G. Zoppellaro, and M. Ruben, Phys. Rev. Lett. **100**, 117601 (2008).

[14] T. Arima, D. Higashiyama, Y. Kaneko, J. He, T. Goto, S. Miyasaka, T. Kimura, K. Oikawa, T. Kamiyama, R. Kumai *et al.*, Phys. Rev. B 70, 064426 (2004).

[15] J. P. Remeika, J Appl Phys **31**, S263 (1960).

[16] S. Song, H. M. Jang, N. S. Lee, J. Y. Son, R. Gupta, A. Garg, J. Ratanapreechachai, and J. F. Scott, NPG Asia Materials 8, e242 (2016).

[17] V. Naik and R. Mahendiran, J. Appl. Phys. 106, 123910 (2009); R. Saha, A. Shireen, S. N. Shirodkar, U. V. Waghmare, A. Sundaresan, and C. Rao, Solid State Comm. 152, 1964 (2012).

[18] S. Mukherjee, A. Garg, and R. Gupta, Appl. Phys. Lett. 100, 112904, (2012); N. Wang, F. Wen, L. Li, Y. Lu, S. Liu, Y. Lu, Z. Liu, B. Xu, J. He, D. Yu and Y. Tian, J. Magn. Magn. Mater. 322, 3595 (2010); K. Sharma, V. R. Reddy, A. Gupta, A. Banerjee, and A. Awasthi, J. Phys.: Condens. Matter 25, 076002 (2013).

[19] R. H. Mitchell, Perovskites: Modern and Ancient (Almaz Press, Ontario, 2002)

[20] A. M. Glazer, Acta Crystallogr. Sect. A 31, 756 (1975)

[21] G. Giovannetti, S. Kumar, D. Khomskii, S. Picozzi, and J. van den Brink, Phys. Rev. Lett. **103**, 156401 (2009); J. A. Alonso, M. J. Martínez-Lope, M. T. Casais, J.

L. GarcíaMunoz, and M. T. Fernández-Díaz, Phys. Rev. B 61, 1756 (2000).

[22] B. Rajeswaran, D. I. Khomskii, A. K. Zvezdin, C. N. R. Rao and A. Sundaresan, Phys. Rev. B **86**, 214409 (2012).

[23] A. H. Cooke, D. M. Martin and M. R. Wells, J. Phys. C: Solid State Phys. **7**, 3133 (1974); Y. Cao, S. Cao, W. Ren, Z. Feng, S. Yuan, B. Kang, B. Lu and J. Zhang, Appl. Phys. Lett. **104**, 232405 (2014).

[24] C. R. Serrao, A. K. Kundu, S. B. Krupanidhi, U. V. Waghmare, and C. N. R. Rao, Phys. Rev. B **72**, 220101 (2005); V. S. Bhadram, B. Rajeswaran, A. Sundaresan, and C. Narayana, Europhys. Lett. **101**, 17008 (2013); A. Ghosh, K. Dey, M. Chakraborty, S. Majumdar and S. Giri, Europhys. Lett. **107**, 47012 (2014).

[25] K. A. Gschneidner Jr, V. K. Pecharsky and A. O. Tsokol, Rep. Prog. Phys. **68,** 1479 (2005)

List of Figures

List of Tables

Chapter 1

Introduction

1.1 General background

Strongly correlated electron systems has attracted enormous research interest over several decades due to their underlying rich fundamental physics and amazing technological applications. The strong electron-electron interactions causes striking many-body effects that cannot be described in the independent particle picture. The subtle coupling and competition between electron, lattice, spin, charge and orbital degrees of freedom leads to the emergence of wide spectrum of exotic properties like magnetism [1], ferroelectricity [2,3], multiferroicity [4], piezoelectricity [5], charge ordering [6], metal-insulator transition [7], colossal magnetoresistance [8,9], spin-state transitions [10], superconductivity [11,12] and many more. Further the complex interplay among all internal degrees of freedom also make them extremely sensitive to small external perturbations such as temperature, pressure or substitution [13–15].

Strong correlation effects are observed in various transition metal compounds, mainly oxides [16], rare earth-based materials [17,18], organic metals [19,20] etc. Among these materials, oxides have always been a topic of intense discussion among the researchers as these are the basis of smart and functional materials. For example high-dielectric oxide materials are used in mobile telecommunication as resonators, capacitors, and frequency filters [21]. High temperature oxide superconductors are used in high-field magnets [22], while layered oxide materials are used as read/write heads in computer hard drives [23]. Piezoelectric oxide materials have applications in actuators and transducers where as ionic conductors are used in fuel cells [24]. Another aspect of oxides is that they can posses cations with mixed valence state and anions with vacancies [25], thus providing an opportunity to tune physical properties and giving rise to the possibilities of wide range of device applications. Such unique characteristic makes oxides one of the most important class of materials, with properties covering almost all areas of physics and materials science such as magnetism, superconductivity, ferroelectricity and many more fields.

1.2 Scope of the thesis

Some of the advanced functional oxides such as gallium ferrites and its different compositions ($Ga_{2-x}Fe_xO_3$) and various perovskite oxides (ABO_3) are investigated in this thesis. The general motivation behind the research is to study the magnetic and ferroelectric properties and related phenomena, in terms of fundamental understanding as well as from the application point of view. Although several multiferroic materials are known, there are still many aspects of the mechanisms giving rise to ferroelectricity that are not well understood. Furthermore, in the search for novel systems, the role of disorder, defects, oxygen vacancy, nature of magnetic and ferroelectric behavior, etc. need to be carefully investigated.

1.2.1 Gallium ferrrite

Gallium ferrrite ($GaFeO_3$) is one of the few chemical systems to possess multiple ferroic ordering like ferrimagnetism [26, 27], ferroelectricity [28–30] and pizeoelectricity [31] near the room temperature and is thus suitable for practical applications. It crystallizes in to orthorhombic structure with a non-centrosymmetric space group $Pc2_1n$ and retains the same crystal structure with stoichiometries ranging between $x = 0.7$ and $x = 1.4$ in $Ga_{2-x}Fe_xO_3$ [26, 27, 31]. The crystallographic unit cell have four different cation sites labeled as Ga1, Ga2 (mainly occupied by gallium) and Fe1, Fe2 (mainly occupied by iron), as shown in Figure 1.1. The environment of Ga1 is almost a regular tetrahedron,

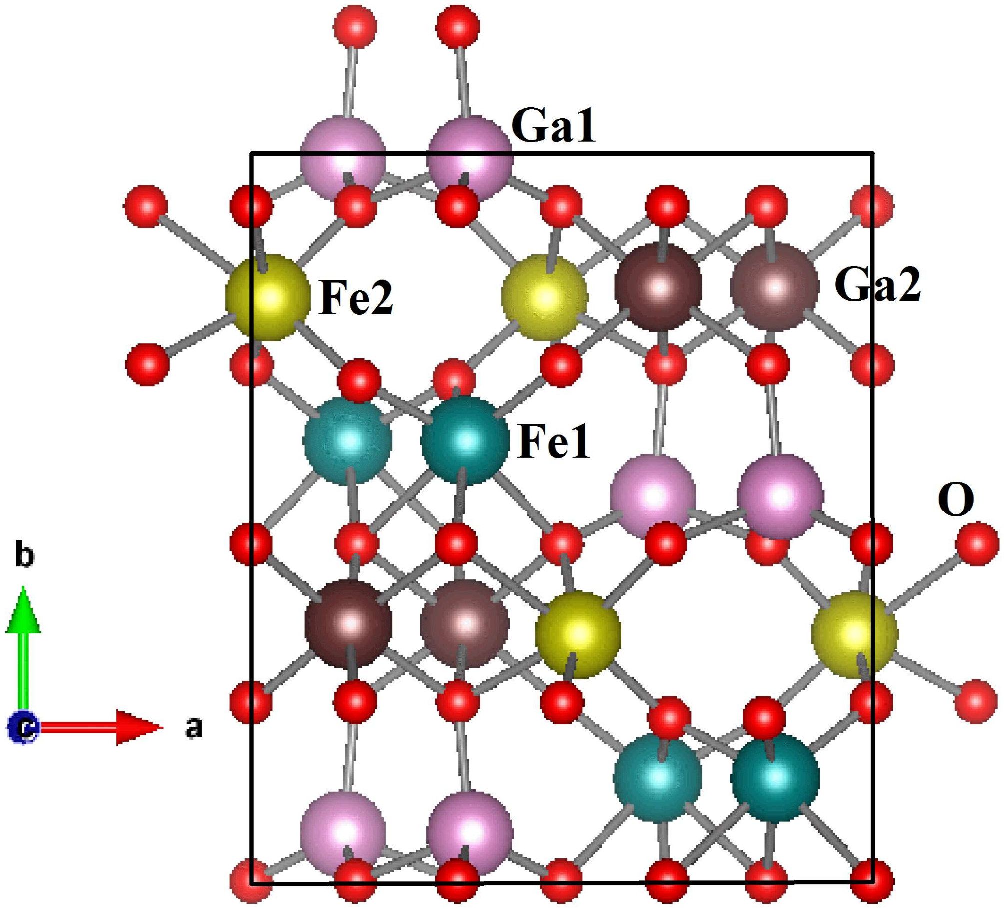

Figure 1.1: Crystal structure of $GaFeO_3$.

where as Ga2, Fe1 and Fe2 are in octahedral co-ordinations. Practically, this system always remain in disorder state as Fe is often found in the Ga site and vice versa due to the similar ionic radii of Ga and Fe [26]. This inherent cationic site disorder leads to multiple exchange paths between Fe at different sites: antiferromagnetic coupling between Fe ions at Fe1 and Fe2 sites, antiferromagnetic coupling between Fe at Ga2 and Fe1 sites and ferromagnetic coupling between Fe at Ga2 and Fe2 sites, resulting in overall ferrimagnetic behavior in $GaFeO_3$ [26, 32]. Magnetic property of $GaFeO_3$ can be tuned either by various synthesis techniques or by varying stochiometric compositions in turn by varying the cation distribution among the different sites. Flux grown single crystal shows magnetic transition temperature of about 300 K while sample obtained either by float zone method [26] or solid state reaction [27] show a transition temperature of around 200 K. For quenched and slowly cooled samples prepared by the solid state reaction, the magnetic transition temperature are 210 K and 260 K, respectively [33]. The Curie temperature can also be varried from 50 K to 370 K by changing the compositions from $x = 0.7$ to $x = 1.4$ in $Ga_{2-x}Fe_xO_3$ system prepared in solid state method [26, 27] . This anti-site disorder is also origin of the ferroelectricity in this compound and room temperature ferroelectricity has been reported in the thin-films of the material [28–30, 34]. Song *et al.* [30] achieved unusually large value of coercive field (E_c) and remnant polarization (P_r) in the thin film grown on hexagonal strontium titanate or cubic yttrium-stabilized zirconia substrate, by applying a very high bias electric field.

1.2.2 Perovskite oxides (ABO_3)

The family of perovskite oxides (ABO_3) have proven to be a fertile research area in condensed matter physics due to the fascinating array of physical properties they exhibit such as from conductor to insulator and superconductor, from (anti)ferromagnetic to spin glass and more complex magnetic ordered state, high k dielectric to ferroelectric and multiferroic, from antiferro-distorted to orbital ordered etc. A particular aspect of perovskites is their ability to incorporate most of the element of the periodic table in A and B sites due to their capacity to accommodate various structural distortions [35]. Besides, the external parameters such as temperature, pressure and chemical compositions can also tune such distortions, which results in wide range of physical properties. Structural distortion in perovskites is governed by Goldschimdts tolerance factor (t_G) rule defined as [35]

$$t_G = \frac{r_A + r_O}{\sqrt{2}(r_B + r_O)} \tag{1.1}$$

were, r_A, r_B and r_O represent the average ionic radii of respective elements. The perovskite will be cubic if $0.9 < t_G < 1.0$ and orthorhombic if $0.75 < t_G < 0.9$. Whereas for $t_G < 0.75$, the compound adopts hexagonal structure. Structural distortions in perovskites are mainly associated with three main features with respect to parent cubic structure: [35–37] (i) polar cation displacements, which generally give rise ferroelectricity, (ii) octahedral rotation (tilting) of BO_6 octahedra,which corresponds to the non-polar antiferro-distorted phase transition and (iii) octahedral distortions, like the Jahn-Teller distortions.

Octahedral tilting

Glazer′s notation is commonly used to describe the octahedral tilting in perovskites [36]. It describes the rotation of oxygen octahedra around the three orthogonal axes of the ideal cubic structure. The tilt about a particular axis is denoted by a^+ for in-phase rotation, a^- for out-of-phase rotation and a^0 for no rotation at all. One symbol for each tetrad axis is sufficient to fully determine the structure. The tilting leads to decrease in the distances between octahedral centres perpendicular to the tilt axis, thus results in modification of unit-cell lengths. If α, β and ϕ are the tilting angles about the pseudocubic [100], [010]

Table 1.1: Possible perovskites structures obtained from various octahedral tilting of ideal cubic structure.

Type	Tilt system	Space Group	Relative Pseudocubic subcell parameters
No Tilt	$a^0a^0a^0$	$Pm\bar{3}m$	$a_p = b_p = c_p$
One Tilt	$a^0a^0c^+$	$P4/mbm$	$a_p = b_p < c_p$
	$a^0a^0c^-$	$I4/mcm$	$a_p = b_p < c_p$
Two Tilts	$a^0b^+b^+$	$I4/mmm$	$a_p < b_p = c_p$
	$a^0b^+c^-$	$Cmcm$	$a_p < b_p \neq c_p$
	$a^0b^-c^-$	$C2/m$	$a_p < b_p \neq c_p$, $\alpha \neq 90°$
	$a^0b^-b^-$	$Imma$	$a_p < b_p = c_p$, $\alpha \neq 90°$
Three Tilts	$a^+b^+c^+$	$Immm$	$a_p \neq b_p \neq c_p$
	$a^+a^+a^+$	$Im\bar{3}$	$a_p = b_p = c_p$
	$a^+a^+c^-$	$P4_2/nmc$	$a_p = b_p \neq c_p$
	$a^+b^-c^-$	$P2_1/m$	$a_p \neq b_p \neq c_p$, $\alpha \neq 90°$
	$a^-a^-c^+$	$Pbnm$	$a_p = b_p \neq c_p$, $\gamma \neq 90°$
	$a^-b^-c^-$	$P\bar{1}$	$a_p \neq b_p \neq c_p$, $\alpha \neq \beta \neq \gamma \neq 90°$
	$a^-b^-b^-$	$C2/c$	$a_p \neq b_p = c_p$, $\alpha \neq \beta \neq \gamma \neq 90°$
	$a^-a^-a^-$	$R\bar{3}c$	$a_p = b_p = c_p$, $\alpha = \beta = \gamma \neq 90°$

and [001] directions, then the new axial lengths can be expressed as

$$a_p = a_0 cos\beta cos\phi \tag{1.2}$$

$$b_p = a_0 cos\alpha cos\phi \tag{1.3}$$

$$c_p = a_0 cos\alpha cos\beta \tag{1.4}$$

where a_0 the cell edge length of the aristotype and a_p, b_p, and c_p, are the pseudocubic subcell lengths. Within the framework of group theory undertaken by Howard and Stokes [38], there are 15 possible structures obtained from various octahedral tilting of ideal cubic structure, which are given in Table 1.1.

Jahn-Teller distortion

Jahn-Teller effect states that if in a nonlinear molecule the degenerate orbitals are asymmetrically occupied, a geometrical distortion will occur to lift the degeneracy. In octahedral complexes, the JahnTeller effect is most pronounced when the e_g orbitals are occupied by odd number of electrons since they are directed towards the ligands and the energy gain is considerably more. The effect also occurs when there is uneven electrons in the t_{2g} orbitals. In such cases, however, the effect is very weak, because the t_{2g} orbitals do not point directly at the ligands and therefore the energy gain is much less. Because of same reason, the tetrahedral complexes also do not exhibit Jahn-Teller distortion.

The Jahn-Teller distortion for high spin d^4 system is shown in Figure 1.2. The degeneracy of e_g state is removed, resulting in elongation of octahedron along Z-axis.

The rare-earth manganites (RMnO$_3$) have been subject of intensive studies owing to the Jahn-Teller character of Mn^{3+} ions, exhibiting orbital ordering along with highly anisotropic Mn-O bond lengths [39]. These class of materials show wide variety of magnetic and electric properties as a function of ionic radius of the R^{3+} ion. Due to the co-operative Jahn-Teller orbital ordering, next-nearest-neighbor antiferromagnetic (NNN-AFM) coupling plays a significant role in addition to nearest-neighbor ferromagnetic (NN-FM) coupling in ab-plane and the subtle coupling competition between the NN and NNN interaction results in various complex magnetic ground state such as cycloidal, A-type,

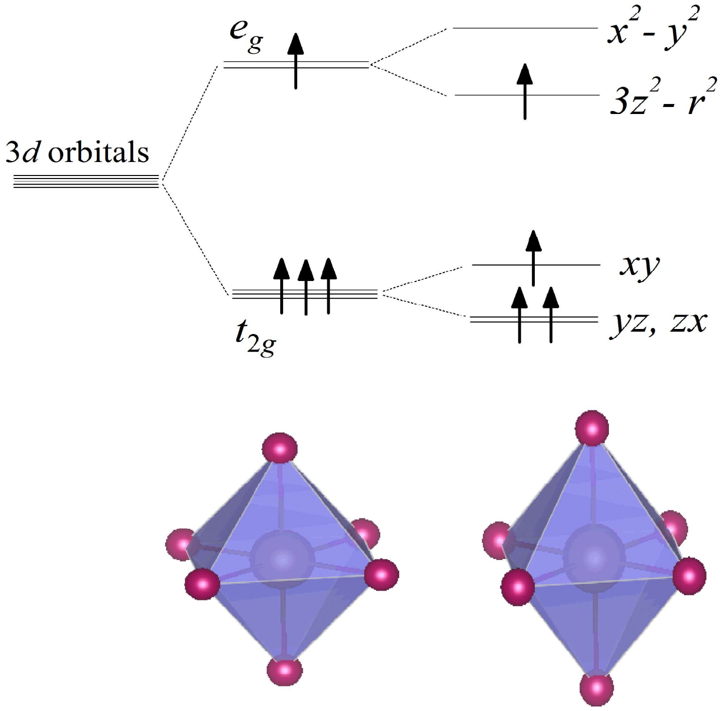

Figure 1.2: Jahn-Teller distortion observed in high spin d^4 system.

E-type etc [40]. Manganites are also of great interest as they exhibit multiferroelectric behavior with strong magneto-electric coupling, originating from magnetic interactions, through lattice modulations [40, 41] .

The family of rare-earth chromites (RCrO$_3$) have invoked great interest as they exhibit complex magnetic properties such as spin-reorientation (SR), spin-flipping (SF), temperature induced magnetization reversal (TMR) and many more caused by symmetric ($S_i.S_j$) and antisymmetric ($S_i \times S_j$) exchange interactions within and between Cr and R-sublattices. Besides most of the members have been reported to be multiferroics at considerable high temperature [42–44].

In this thesis we have studied some Gd-based perovskites (Gd$M_xM'_{1-x}$O$_3$, M, M' = Cr, Mn, Al and $0 \leq$ x ≤ 1). All the compounds posses orthorhombically distorted perovskite structure as shown Figure 1.3.

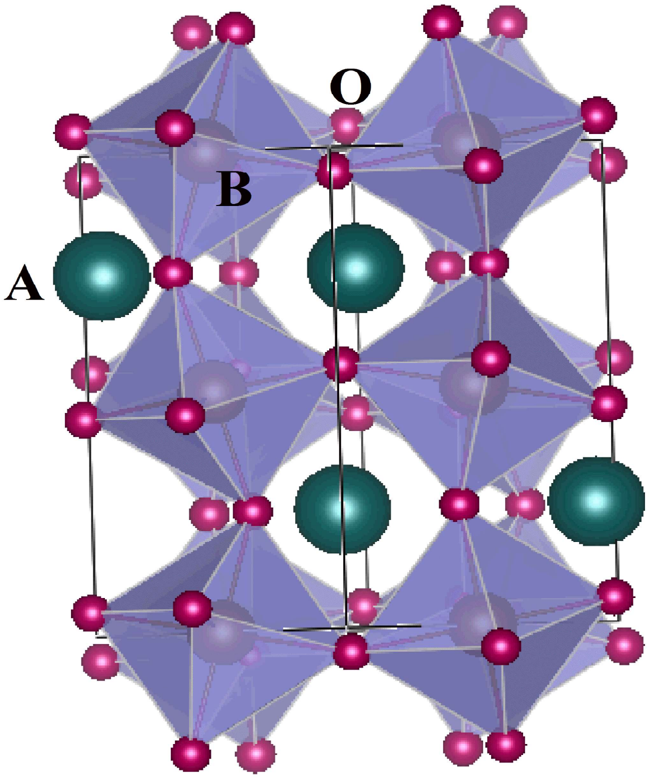

Figure 1.3: The orthorhombic perovskite structure (ABO_3).

1.3 Magnetism

Magnetism is associated with the spin and orbital degrees of freedom, which arises from the partially filled d or f orbitals of transition metal or rare-earth ions. Generally, the magnetic interaction is caused by overlapping of partially filled outer electronic orbitals of neighboring atoms, which leads to correlated electronic behavior. The magnetic interaction is described by a quantum mechanical mechanism, expressed by the Heisenberg spin Hamiltonian,

$$H = -\sum_{i}\sum_{i\neq j} J_{ij} S_i . S_j \tag{1.5}$$

where, J_{ij} is the exchange integral (coupling constant), which indicates the strength of the coupling between the spins and S_i, S_j are i^{th} and j^{th} site spin magnetic moments, respectively. The positive sign of J_{ij} indicates that the interaction between the magnetic moments of neighboring atoms is ferromagnetic type, while the negative sign of J_{ij} corresponds to antiferromagnetic type interaction. The exchange interaction is mediated by different mechanisms depending on the material system under consideration. Various mechanisms which are relevant to this thesis are described below.

1.3.1 Superexchange interaction

This is an indirect exchange interaction between two magnetic cations mediated by a non-magnetic anion lying between the two. Figure 1.4 illustrates the principle with two Mn^{3+} ions separated by an oxygen ion. The nature of the superexchange interactions are usually explained by Goodenough-Kanamori-Anderson (GKA) rules, which is based on various orbital arrangements in d shell as described by ligand field theory [45].The rules say, if two magnetic ions are connected through legand with a bond angle of 180° i.e. 180° superexchange, the interaction will be strongly antiferromagnetic, while if the bond angle is 90° i.e. 90° superexchange, the interaction will be ferromagnetic and will be much weaker. The general GKA rules are based on the symmetry relations and the electron occupancy of atomic orbitals overlapped are described below: [45]

(A) when the lobes of orbitals of two magnetic ions are pointing towards each other in such a way that overlap integral is large, the exchange will be antiferromagnetic. There are following subcases.

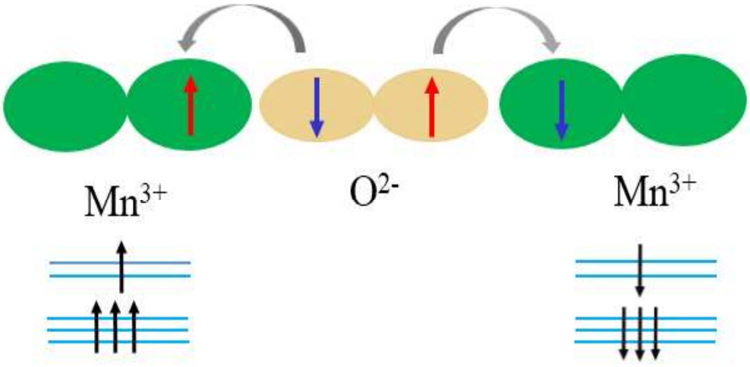

Figure 1.4: A schematic representation of superexchange interaction showing the virtual transfer of electrons between two neighboring Mn^{3+} ions *via* oxygen ion (legand). The antiferromagnetic coupling is favored according to Pauli exclusion principle.

(a) When $d_{3z^2-r^2}$ orbitals are in the 180° position to each other (generally in octahedral case) so that the lobes of orbitals point directly towards the ligand and each other, it results in to strong antiferromagnetic superexchange interaction.
(b) When d_{xy} orbitals are in the 180° position to each other, in which interaction occurs *via* $p\pi$ orbitals of the ligand, one can obtain moderate exchange.
(e) When one magnetic ion has $d_{3z^2-r^2}$ occupied and the other has d_{xy} with 90° ligand situation, then interaction occurs *via* $p\pi$ for one and $p\sigma$ for the other, which provide a strong overlap and antiferromagnetic exchange.
(B) When $d_{3z^2-r^2}$ and d_{xy} are in 180° position, the overlap integral is zero by symmetry, the rule gives ferromagnetic interaction.

1.3.2 RKKY interaction

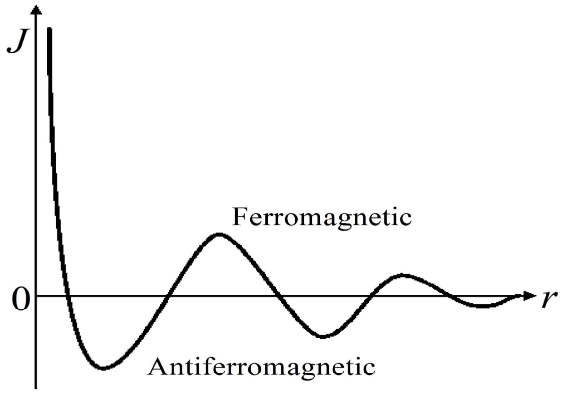

Figure 1.5: Variation of the indirect exchange coupling constant (J) with the distance between the magnetic ions.

The indirect exchange or RKKY (Ruderman-Kittel-Kasuya-Yosida) interaction is an indirect interaction between two magnetic ions having localized orbitals which is mediated by the polarization of the conduction electrons [46]. The exchange coupling J shows damped oscillatory behavior which changes its sign as a function of distance between the magnetic ions (Figure 1.5). Therefore, depending upon the separation between the ions their magnetic coupling can be ferromagnetic or antiferromagnetic. The coupling of $4f$ electrons in rare-earth materials occurs via RKKY interaction as they have localized orbitals .

1.3.3 Dzyaloshinskii-Moriya interaction

There is also an anisotropic interaction which is mediated by spin-orbit coupling [47, 48]. Dzyaloshinskii-Moriya interaction is very weak as it is just a relativistic correction. Nevertheless this interaction favors canting of spins by small amounts (non-collinear spin ordering) leads to weak ferromagnetic behavior. The Hamiltonian is written as

$$H_{DM} = D_{ij}.(S_i \times S_j) \tag{1.6}$$

where vector D_{ij} vanishes if the crystal field has an inversion symmetry at the mid point of the vector joining the two spins, r_{ij} (Figure 1.6). It is proportional to $x \times r_{ij}$, where x is the perpendicular displacement of the ligand ion from the line [49].

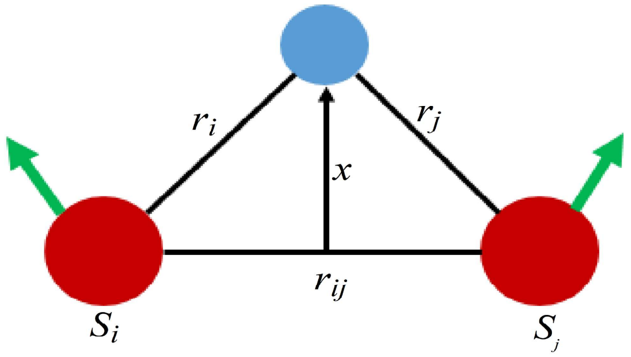

Figure 1.6: Schematic illustration of Dzyaloshinskii-Moriya interaction resulting in spin canting in an antiferromagnet.

1.4 Spin glass

The spin glass is a complex state of magnetism, distinctly different from long range ordered ferromagnetic and antiferromagnetic phases [50]. No apparent order phase forms in the system rather metastable frozen states appear below the transition temperature.

Necessary ingredients for spin glass behavior are frustration of spins, disorder in magnetic interactions, and competing ferromagnetic and antiferromagnetic interactions [50]. Magnetic frustration means that all the interactions can not be satisfied simultaneously, this results in to a wide range of relaxation times. The time averaged value of spin S_i is non-zero. Spin-spin correlation function $<S_iS_j>$ does not show long-range order due to the absence of periodically ordered spin structure. Therefore, a spin glass transition results in a cusp at the spin glass freezing temperature (T_f) in the real part of ac susceptibility (χ'). Such system has many metastable ground states covering a broad range of relaxation time scales (Figure 1.7), from atomic timescales (10^{-12} s) to experimental time scales (seconds) at low temperatures and finally, diverges at the glass transition temperature (T_g) to remain infinite at lower temperatures [50]. Thus, with cooling, the spins in the system form locally correlated units, denoted as domains, clusters or droplets. When $T \rightarrow T_g$, the fluctuations in the clusters are slowed down progressively, resulting in growth of clusters and glassy correlations between the spins become large and each spin

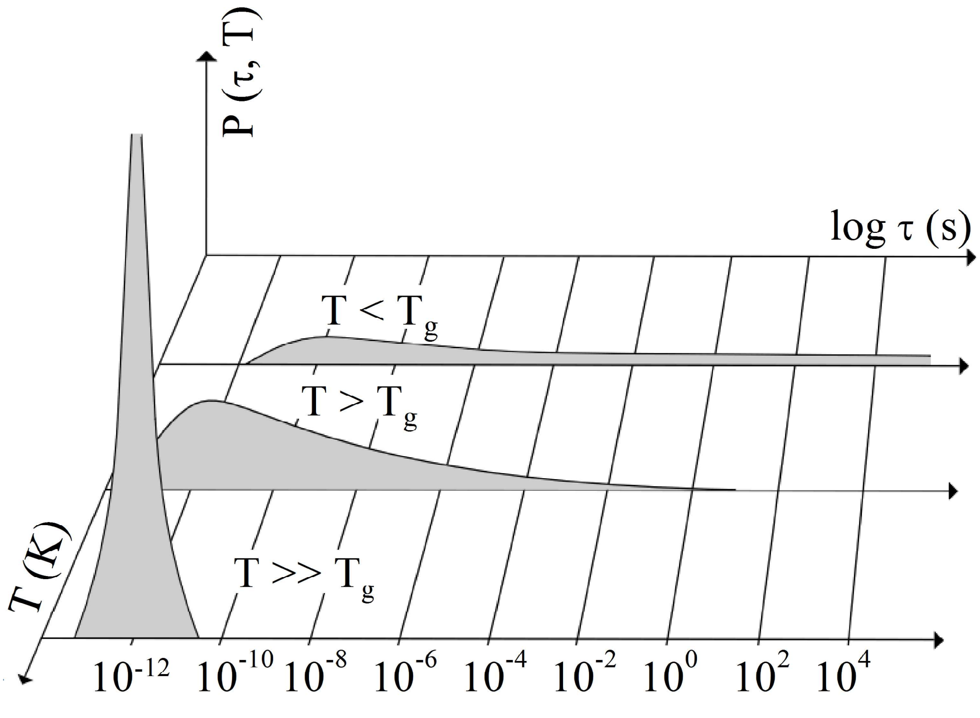

Figure 1.7: Schematic representation of distribution of spin relaxation times (τ) with temperature.

starts interacting with the neighboring spins. Consequently, at T_g the system is expected to freeze into a random albeit well-defined frozen ground state. Depending on the cooling rate, the system can trapped in a metastable state and at temperatures higher than T_g, called as freezing temperature (T_f). Between T_f and T_g the system shows slow relaxation, which tends to achieve the glassy ground state only asymptotically when approaching T_g [51]. Peculiarly, the spin glass ground state is chaotic by nature [52] such that at different temperatures below T_g the system have different spin configurations, which can, again, be reached only asymptotically slowly. Therefore, it shows memory effect upon aging, which is the signature of glassy behavior.

1.5 Magneto caloric effect (MCE)

MCE is the process of heating or cooling (i.e., the temperature change) of a magnetic material when exposed to adiabatic magnetization and demagnetization [53]. The working principle of MCE is based on isothermal magnetic entropy change (ΔS_M) or the adiabatic temperature change (ΔT_{ad}) caused by change in the magnetic field, which is, in a way, similar to the process that occurs in a gas in response to the change in pressure [53]. During the isothermal magnetization process, magnetic entropy is decreased significantly near the magnetic transition temperature (ferromagnetic (FM) to paramagnetic (PM) transition and field-induced metamagnetic transition from antiferromagnetic (AFM) to ferromagnetic (FM) state) due to a reduction of disorder in the spin system. Therefore, magnetic materials can be used for refrigeration purpose in the vicinity of the transition temperature.

MCE was discovered by E. Warburg in 1881 from pure Iron [54] and subsequently by P. Weiss and A. Piccard in 1917 [55]. Debye [56] and Giauque [57] independently explained origin of the MCE: the adiabatic demagnetization. First breakthrough application (working magnetic refrigerators) was achieved Giauque and MacDougall in 1933, cooling below about 0.3 K using $Gd_2(SO_4)_3.8H_2O$ as the magnetic refrigerant [58]. In 1976, Brown [59] constructed a magnetic heat pump operating at room temperature using the rare-earth metal Gd and demonstrated magnetic refrigeration can be realized in room temperature region. In 1997, Pecharsky and Gschneidner discovered the room temperature giant MCE effect in $Gd_5Si_2Ge_2$. After that many researchers concede that it has good potential for refrigeration from room temperature to low temperature.

1.5.1 Working principle

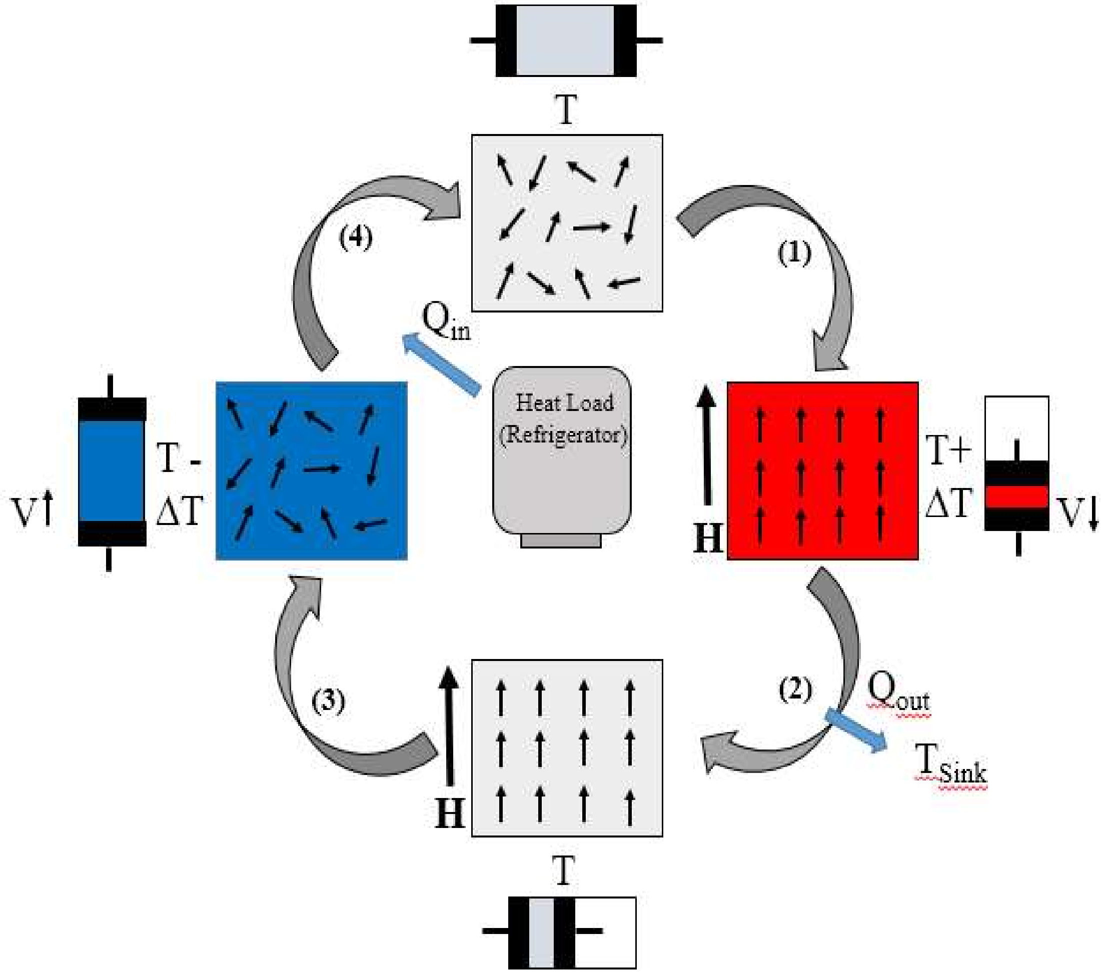

Figure 1.8: Pictorial representation of various thermodynamic processes in magnetic refrigeration cycle in comparision with the gas refrigeration cycle. When the magnetic field is applied or removed under isothermal condition, leads to an entropy change and the adiabatic process, yields a variation in temperature.

Analogous to the conventional vapor-compression cycle, the basic thermodynamic cycle of the magnetic refrigerator operates between following two adiabatic and two isothermal conditions which is pictorially shown in Figure 1.8 and schematic of closed Carnot cycle (ABCDA) is shown in Figure 1.9.

1- Adiabatic magnetization: When a magnetic material is magnetized under adiabatic condition (Q = 0,) this results in alignment of the magnetic dipoles along the field direction and magnetic entropy decreases. Since total energy is constant during the process, it results in an increase in temperature (T + $\triangle T$) of the refrigerant by increasing lattice and electron entropy to compensate reduced magnetic entropy.

2- Isothermal heat extraction: After that heat is removed by a heat sink under the isothermal condition without changing applied magnetic field. This leads to a decrease in entropy ($\triangle S$). Once completely cooled, the magnetocaloric substance and the heat sink are separated.

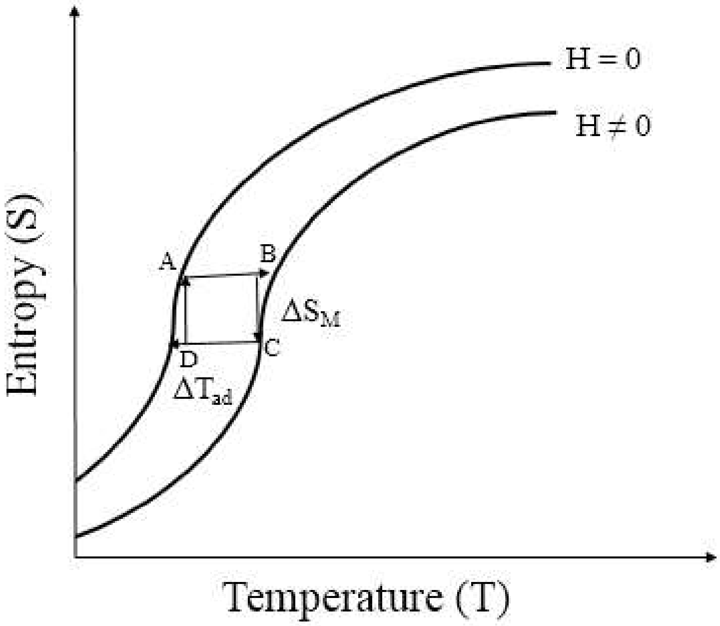

Figure 1.9: Schematic representation of Carnot cycle (ABCDA) in the magnetic refrigeration process.

3- Adiabatic demagnetization: In this step magnetic field is removed adiabatically (Q = 0), which results in disorder in magnetic dipoles and consequently, increase of magnetic entropy. This results into an decrease in temperature (T - $\triangle T$) caused by lowering lattice and electron entropy to compensate the increased magnetic entropy.

4- Isothermal heat absorption: Finally, the material is placed in thermal contact with the environment being refrigerated, which is at higher temperature than the refrigerant material (by design). Thus heat energy (+Q) migrates into the refrigerant material from the refigerated environment.

Note that both isothermal magnetic entropy change (ΔS_M) and the adiabatic temperature change (ΔT_{ad}) are crucial for the achievement of magnetic refrigeration.

1.5.2 Fundamental aspects

The entropy (S) of a magnetic substance at constant pressure (P) depends on both external magnetic field and temperature. The change in magnetic entropy (S_m) is correlated with the magnetization (M), magnetic field strength (H) and the absolute temperature (T) by the Maxwell′s relations as given by,

$$\left(\frac{\partial S_m(T,H)}{\partial H}\right)_T = \left(\frac{\partial M(T,H)}{\partial T}\right)_H \tag{1.7}$$

Integrating above equation under Isothermal (T = constant) and isobaric (P = constant) conditions, one can obtain

$$\Delta S_m(T,\Delta H) = \int_0^H \left(\frac{\partial M(T,H)}{\partial T}\right)_H dH \tag{1.8}$$

Above equation indicates that magnetic entropy change,$\Delta S_M(T,\ \Delta H)$ is proportional to both derivative of magnetization with respect to temperature at constant magnetic field and to the magnetic field variation.

According to second law of thermodynamics, heat capacity (C) at constant H can be represented as,

$$C(T,H) = T\left(\frac{\partial S}{\partial T}\right)_H \tag{1.9}$$

Thus, total entropy (S) can also be calculated from specific heat data by using following equation,

$$S(T,H) = \int_0^T \frac{C(T,H)}{T} dT \tag{1.10}$$

The isothermal magnetic entropy change (ΔS_M) at different field variations can also be calculated from specific heat data acquired at various magnetic fields, using the following thermodynamic relations,

$$\Delta S_m(T,H) = \Big(S(T,H) - S(T,0)\Big)_T = \int_0^T \frac{C(T,H)}{T}dT - \int_0^T \frac{C(T,0)}{T}dT \tag{1.11}$$

It can be written following thermodynamic relations,

$$\left(\frac{\partial T}{\partial H}\right)_S = -\left(\frac{\partial S}{\partial H}\right)_T \left(\frac{\partial T}{\partial S}\right)_H \tag{1.12}$$

Using Eq. 1.8, 1.9 and 1.12, the infinitesimal adiabatic temperature change can be expressed as follows,

$$dT_{ad} = -\left(\frac{T}{C(T,H)}\right)_H \left(\frac{\partial M(T,H)}{\partial T}\right)_H dH \tag{1.13}$$

Integrating above equation, one can obtain adiabatic temperature change (ΔT_{ad}) as follows,

$$\Delta T_{ad}(T,\Delta H) = -\int_0^H \left(\frac{T}{C(T,H)}\right)_H \left(\frac{\partial M(T,H)}{\partial T}\right)_H dH \tag{1.14}$$

Above equations provide an understanding of the behavior of the MCE and serve as a guide for the search of potential magnetocaloric materials. First, for paramagnets and simple ferromagnets, magnetization decreases with increasing temperature at constant applied field [i.e. $\partial M/\partial T)_H < 0$], this implies $\Delta S_M(T,\Delta H)$ is negative (Eq. 1.14), while $\Delta T_{ad}(T,\ \Delta H)$ is positive (Eq. 1.8). Second, in ferromagnets $|(\partial M/\partial T)_H|$ is the largest at the T_C and therefore, $\Delta S_M(T,\Delta H)$ will be maximum at T_C and will be gradually reduced both below and above the T_C (Eq. 1.8). Third, for the same $|(\partial M/\partial T)_H|$, the $\Delta T_{ad}(T,\ \Delta H)$ will be larger at a higher absolute temperature, and also when the total heat capacity is lower (Eq. 1.14).

1.6 Multiferroics and mechanism of ferroelectricity

Multiferroics refer to the class of materials in which two or more ferroic states such as ferroelectric, ferromagnetic, ferroelastic or ferrotoroidic coexist. The ferroic states are generally characterized by a stable and switchable order parameter under the application of external stimuli, e.g. magnetic field, electric field, pressure, temperature and strain. More specifically, the current research on multiferroics focuses on the materials exhibiting ferroelectric order and long-range magnetic order that also includes antiferromagnetic and more complex spin order such as spiral/cycloidal. In spite of their huge potentials, multiferroic materials are rare because of contradictory requirements of magnetism and ferroelectricity as former one requires an odd number of d electrons, whilst later one generally occurs only in materials without d electrons [60]. This has led to an intense research activities in this area aimed at identifying alternative mechanisms by which both the degrees of freedom can coexist and couple strongly.

Electric polarization can be induced by several mechanisms; based on the origin of electric polarization, ferroelectrics are classified into two categories: proper ferroelectrics and improper ferroelectrics. In proper ferroelectrics, polarization is a primary effect directly associated with the structural instability arising out of the hybridization and change in the chemical bonding. One example of proper ferroelectrics is $BaTiO_3$ [2,61], in which ferroelectricity originates from the off-centering of the Ti with respect to the oxygen octahedral cage due to the virtual hopping of electrons between empty Ti-d and occupied O-p states. Ferroelectric polarization in improper ferroelectrics on the other hand develops as a byproduct of other spin, lattice or charge ordering. Different mechanisms inducing ferroelectricity are described below.

1.6.1 Lone pair driven ferroelectricity

In $BiFeO_3$ [62], $BiMnO_3$ [63] and $PbVO_3$, the A-site cation (Bi^{3+}, Pb^{2+}) has two outer $6s$ electrons that do not participate in chemical bonds, called lone-pairs, or sometimes dangling bonds, which causes the Bi $6p$ (empty) orbital to come closer in energy to the O $2p$ orbitals and hybridize resulting in the displacement of A-site ion from centrosymmetric positions with respect to the surrounding oxygen ions and drives ferroelectricity. Such ferroelectrics are also classified as proper ferroelectrics.

1.6.2 Geometric ferroelectricity

The improper ferroelectrics in which spontaneous electric polarization is induced by some geometric effects such as non-centrosymmetric atomic arrangements of the crystal rather than chemical bonding are termed as Geometric ferroelectrics. Hexagonal rare-earth manganites (h-RMnO$_3$, R = Ho-Lu, Y) are the improper geometric ferroelectrics in which polarization arises from the tilting of MnO$_5$ polyhedra accompanied by displacement of the R ions [4, 64].

1.6.3 Charge ordering induced ferroelectricity

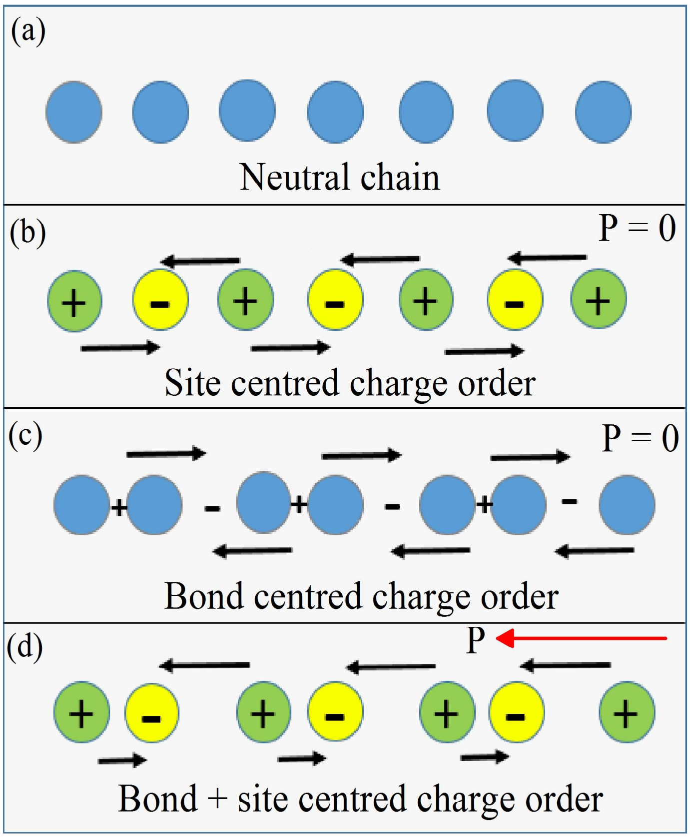

Figure 1.10: Schematic representation of neutral one-dimensional chain (a) showing site-centered charge ordering (b), bond-centered charge ordering (c), and linear combination of both site-centered and bond-centered charge orderings (d), which exhibits non-zero ferroelectric polarization [65].

Another mechanism that can lead to ferroelectricity is charge ordering, in which compound contains transition metal ions with mixed valence. A specific periodic pattern (like alternative ordering or checkerboard type ordering) of transition metal ions with different valence states is generally referred as site-centered charge ordering. The second type of charge ordered pattern develops due to the lattice dimerization as observed in the case of Peierls distortion. In this charge order pattern, each lattice site is occupied by equivalent charges but the bond strengths between the sites are unequal which result in charge disproportion on alternating strong and weak bonds between ions. This type of charge ordering is called bond-centered charge ordering. In both the type of charge order pattern (Figure 1.10), the net polarization turns out to be zero. However, the simultaneous presence of site centered and bond centered charge ordering in a system breaks inversion symmetry and results in ferroelectricity [65]. Charge ordered compounds such as $LuFe_2O_4$ [66], RNiO$_3$ [67], $Pr_{1-x}Ca_xMnO_3$ [68] etc show ferroelectric ordering.

1.6.4 Magnetically driven ferroelectricity

Magnetically driven ferroelectrics are the interesting class of multiferroics, which trigger a lot of research activities owing to their large magnetoelectric coupling. In these materials, spontaneous polarization appears due to spatial inversion symmetry breaking by magnetic ordering which involves various microscopic mechanism as described below.

(a) Inverse Dzyloshinskii-Moriya interaction

In orthorhombic rare-earth manganites (RMnO$_3$, $R =$ Gd, Tb, Dy) [4,41,69] and $MnWO_4$ [70], ferroelectricity arises due to the breaking of inversion symmetry from the helicoidal/spiral spin order, which is connected with the spin-orbit interaction. Underlying mechanisms for the generation of electric polarization in this class of compounds is the inverse Dzyloshinskii-Moriya interaction, where the spin configuration displaces oxygen (ligand) ions through the electron-lattice interaction and breaks the inversion symmetry [71].

(b) Exchange striction mechanism

Besides the non-collinear magnetic structure, the ferroelectricity can also be induced in the collinear magnetic structure caused by the lattice distortions associated with the competing magnetic interactions so-called exchange striction mechanism. Best known

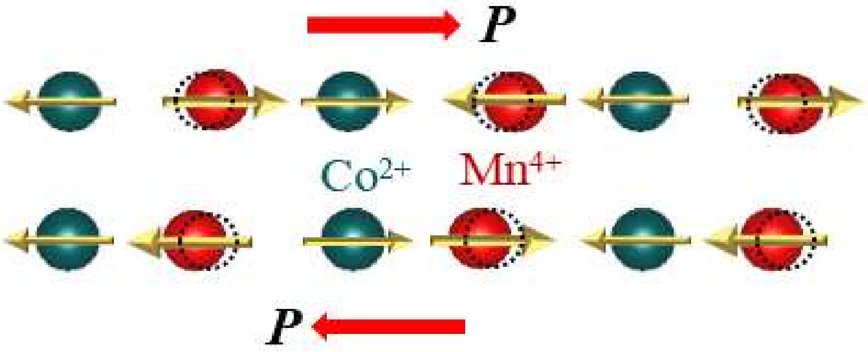

Figure 1.11: Alternating ionic order and up-up-down-down (↑↑↓↓) spin structure in Ca_3CoMnO_6, where ferroelectricity arises from exchange striction mechanism. Dashed circles represent the undistorted positions of the atoms [72].

such type of ferroelectric is one-dimensional Ising spin chain system, Ca_3CoMnO_6 [72]. In this type chain system, there exist nearest-neighbor ferromagnetic exchange interactions (J_F) and next-nearest-neighbor antiferromagnetic exchange interactions (J_{AF}) such that J_{AF} $/J_F$>1/2, which results in up-up-down-down (↑↑↓↓) type spin structure, as shown in Figure 1.11. The exchange striction associated with this unequal strength of exchange interactions shortens the bonds between the parallel spins and elongates the bonds connecting the antiparallel spins and breaks the inversion symmetry which leads to ferroelectric polarization.

(c) Metal-ligand orbital hybridization mechanism

The microscopic theory which describes the induced polarization by the metal-ligand orbital hybridization was first introduced by Katsura, Nagaosa and Balatsky (KNB) taking into account the transition metal orbital states and crystal field effects [71]. According to this model, the dipolar polarization develops along the direction of M-O-M (M = transition metal) cluster (as shown in Figure 1.12) which require a noncollinear magnetic structure with non-zero spin-orbit coupling. If we consider two transition metals with spin moments m_r and m_l located at positions r and $r+l$ and connected via a ligand (oxygen) at the center $r+l/2$, the dipole moment of this cluster (spin dimer) at the center of the ligand site can be expressed as

$$P_{r+l/2} = P^{ms} q(m_r.m_{r+l/2}) + P^{sp} q \times (m_r \times m_{r+l/2}) + P^{orb}[(q.m_r)m_r - (q.m_{r+l})m_{r+l}]$$

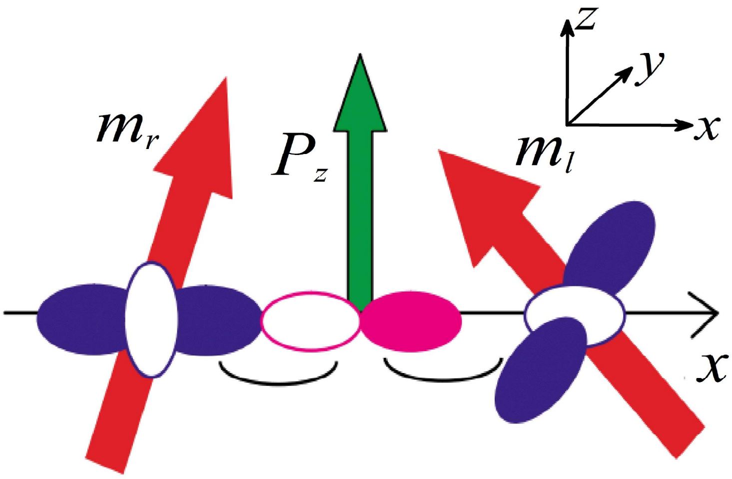

Figure 1.12: The M-O-M cluster model with the $d_{3x^2-r^2}$ /$d_{3y^2-r^2}$ staggered orbital order under a noncollinear spin configuration m_l and m_r with the associated electric polarization P_z [73].

where P^{ms} , P^{sp} and P^{orb} are the magnetostriction, spin current and orbital terms, respectively. The third term arises due to the asymmetry in metal-ligand (p-d) hybridization. It may be noted that the asymmetry in p-d hybridization depends on the local environment of the transition metal and ligand i.e. on the spin orbit coupling and the specific lattice structure. Example of such systems are Cu(Fe,Al)O_2 [74] and $Ba_2CoGe_2O_7$ [75].

1.6.5 Other ferroelectrics

Apart from the above mentioned feroelectrics, $CdTiO_3$ is a unique system, in which ferroelectricity is driven by a phase transition from the centrosymmetric orthorhombic structure ($Pbnm$) to a non-centrosymmetric structure ($Pna2_1$) via displacement of Ti and O ions, even though overall orthorhombic symmetry is maintained [76, 77].The Concept of "local non-centrosymmetry" has been suggested to understand the weak ferroelectric behavior of $YCrO_3$ [78]. Yet another novel mechanism has been proposed where the rotation of oxygen octahedra coupled with lattice distortion can lead to a ferroelectric phase [79–81].

1.7 TSDC effect and dielectric relaxation

Defect engineering have generated considerable attention in recent years as it opens up novel opportunities to drive and control various physical properties, gives rise to increase in functionality of the materials. Oxides are very prone to lattice defects, mainly atomic vacancies, which drive a wide range of extra properties that the host materials do not exhibit intrinsically, including photoconductivity [82], conductivity [83], unusual dielectric behavior [84], magnetization [85], polarization [86] and many more.

The emergence of polarization from the defect dipole reorientation is termed as thermally stimulated depolarization current (TSDC) effect. When a material is poled by the application of electric field at relatively high temperatures, barely mobile charge carriers of defects get distributed so as to screen the electric field and with cooling, these charge carriers get trapped. Since at low temperatures the relaxation time is infinitely long, an internal electric field by the frozen-in dipoles persists even when external electric field is switched-off. Further, during heating cycle this trapped carriers get released giving rise to pyrocurrent/polarization.

Theory of TSDC

The theoretical basis for the TSDC phenomena was established by Bucci, Fieschi and Guidi in 1966 [87]. The time and temperature dependence of the dipolar polarization is determined by the competition between the orienting action of the field and the randomizing action of thermal motions. The time-dependent polarization at a constant temperature, T can be expressed as,

$$P(t) = P_0[1 - exp(-t/\tau)] \tag{1.15}$$

where τ is the dipolar relaxation time and P_0 is the equilibrium or steady-state polarization which can be described by the Langevin function:

$$P_0 = \frac{sN_d P_\mu^2 E_p}{k_B T_p} \tag{1.16}$$

where s is a geometrical factor depending on the possible dipolar orientations, N_d is the concentration of defect dipoles, E_p is the polarizing field, T_p is the poling temperature, P_μ is the dipolemoment and k_B is Boltzmann constant.

The decay of polarization after removal of the field at $t = \infty$ is given by,

$$P(t) = P_0 exp(-t/\tau) \tag{1.17}$$

Assuming the time taken to polarize defect dipoles at a given temperature is same as the time taken for those dipoles to depolarize at the same temperature and adopting the decay process as a thermal activated process of Arrhenius type, $\tau(T) = \tau_0 \exp(E_a/k_B T)$, where τ_0 is the characteristic relaxation time for a vacancy jump from one lattice site to another for reorientation of defect dipole and is independent of temperature and E_a is the activation energy, the Eq. 1.17 can be rewritten as,

$$P(t) = P_0 exp\bigg(-\int_0^t \frac{dt}{\tau(T)}\bigg) = P_0 exp\bigg(-\int_0^t \frac{exp(-E_a/k_B T)}{\tau_0} dt\bigg) \tag{1.18}$$

The depolarization current is given by, $I(t) =$ -$dP(t)/dt$. For linear heating process, $T = T_0 + bt$, where $b = dT/dt$ heating rate, the depolarization current can be expressed as,

$$I(T) = -\frac{P_0}{\tau_0} exp(-E_a/k_B T) exp\bigg[-\frac{1}{b\tau_0}\int_{T_0}^{T} exp(-E_a/k_B T')dT'\bigg] \tag{1.19}$$

The first exponential, which dominates in the low temperature range, leads to initial increase of the current with temperature, while the second exponential dominates at high temperature range which is accompanied by decrease of current. Thus the temperature dependence depolarization current represents an asymmetrical glow curve, where the amplitude is a linear function of the poling field.

1.8 Organization of thesis

The various chapters of the thesis are briefly described below.

In **Chapter 2** we discuss the various experimental and the theoretical techniques used in this thesis work. This includes sample synthesis technique: solid state reaction and various characterization tools such as powder x-ray diffraction (XRD), dc and ac magnetization, dielectric, pyroelectric, heat capacity, Raman spectroscopy, x-ray absorption spectroscopy (XAS) and extended x-ray absorption fine structure (EXAFS) studies and density functional theory (DFT) calculations to study the structural, electronic and magnetic properties and density functional perturbation theory (DFPT) approach for phonon calculations.

Chapter 3 is divided into two parts. In the first part, we discuss the detailed magnetic properties of solid solutions of $Ga_{2-x}Fe_xO_3$ (x = 0.75, 1.0, and 1.25). Magnetic behavior throughout the series could be well explained by the molecular-field-approximation of three-sublattice ferrimagnetic model. The series of compounds exhibit complex spin glass behavior which gradually evolve with the compositions (x) from the Ising type character to Heisenberg type behavior to unconventional glassy behavior for Fe-rich compositions. Hence, $Ga_{2-x}Fe_xO_3$ can serve as an ideal system for modeling complex spin glasses. The glassy behavior these systems is due to the inherent site-disorder driven magnetic inhomogeneity and random distribution of ferromagnetic and antiferromagnetic interactions and their modifications with compositions (x). In the second part, we discuss detailed dielectric and pyroelectric studies throughout the series. These systems exhibit multiple dielectric relaxations associated with dominating low frequency Maxwell-Wagner type relaxation through the interfaces, i.e., grain boundaries and high frequency Debye type relaxation through the bulk (grains). Further, emergence of polarization in these systems is a thermally stimulated process caused by the freezing of defect dipoles possibly associated with charged oxygen vacancy instead of intrinsic ferroelectric behavior.

Chapter 4 also consists of two parts. In first part we discuss our detailed investigations on structural studies by temperature dependence synchrotron x-ray diffraction and theoretical calculations to understand the microscopic origin and underlying physics of ferroelectricity in $GdCrO_3$ at relatively high temperature. The preferred symmetry is found to be non-centrosymmetric orthorhombic $Pna2_1$ structure, favoring the polar nature of the system. The weak polarization arises from the small ferroelectric instability associated with the Gd displacements with respect to the oxygen cage. Furthermore, magnetic coupling between Gd-4f and Cr-3d also plays an important role in ferroelectric distortion. Second part of the chapter contains detail magnetic and spin-phonon coupling studies in $GdCrO_3$. It shows various interesting magnetic features like temperature induced magnetization reversal (TMR), spin flipping (SF), spin reorientation, nonlinear coercivity etc, which arise due to the symmetric (S_i . S_j) and antisymmetric Dzyaloshinsky-Moriya interaction ($S_i \times S_i$) interactions within and between Cr and Gd-sublattices. The system also exhibits strong spin-phonon coupling, which provides a complementary tool for the enhancement of ferroelectric polarization.

In **Chapter 5** we discuss detailed structural, electronic and magnetic properties of $GdMn_{1-x}Cr_xO_3$. In the solid solutions, the Jahn-Teller distortion associated with Mn^{3+} ions gives rise to major changes in the bc-plane sublattice and also the effective orbital ordering in the ab-plane, which persist up to the compositions $x \sim 0.35$. These distinct features in the lattice and orbital degrees of freedom are also correlated with the bc-plane anisotropy in the local Gd environment. Evidence of magnetization reversal in field-cooled-cooling mode for x $\sim$ 0.35 coinciding the Jahn-Teller crossover, suggests a close correlation between magnetic interaction and structural distortion. These observations indicate a strong entanglement between lattice, spin, electronic and orbital degrees of freedom. Density functional theory calculations find that the intermediate compound ($x = 0.5$) consists of alternate ferromagnetic Mn layers and antiferromagnetic Cr layers, which is distinct from that observed for the end members $GMnO_3$ (A-type) and $GdCrO_3$ (G-type).

In **Chapter 6** we discuss magnetocaloric effect (MCE) of polycrystalline GdMO3 (M = Al, Mn and Cr) assess their potential usage as magnetic refrigerants at cryogenic temperatures. $GdAlO_3$ exhibits a giant magnetic entropy change (δS_M), while the moderate effect is observed in $GdMnO_3$. This is possibly due to the presence of Gd-Mn negative exchange interaction in $GdMnO_3$. The relative cooling power (RCP) and adiabatic temperature change (δT_{ad}) of both the materials are similar. However, absence of magnetic and thermal hysteresis in $GdAlO_3$ make it a more efficient and reversible magnetic refrigerant than $GdMnO_3$. $GdCrO_3$ possesses exceptionally large magnetocaloric parameters (δS_M, δT_{ad} and RCP), which arises from the suppression of spin entropy associated with the suppression of spin reorientation transition, in addition to the Gd-ordering. The giant MCE parameters along with high insulating nature of the sample and weak magnetic hysteresis, make it one of the best candidates for low temperature magnetic refrigeration among all known potential low temperature magnetic refrigerants known so far.

Summary and outlook of the present thesis work are given in **Chapter 7**.

Chapter 2

Experimental and theoretical techniques

This chapter presents a brief overview of the experimental methods used for synthesizing bulk (powder) samples and characterization of their properties. We synthesized polycrystalline samples of various functional oxides by the solid-state route. Powder x-ray diffraction (XRD) technique was used to confirm phase purity and determine the crystal structure. Thereafter, samples were characterized using dc and ac susceptibility measurements, heat capacity measurement, Raman spectroscopy, x-ray absorption spectroscopy (XAS), extended x-ray absorption fine structure (EXAFS) study and dielectric measurement and pyroelectric measurement, etc. In addition, we also performed first-principles density functional theory based calculations to study the structural, electronic and magnetic properties of various systems.

2.1 Sample synthesis

The synthesis techniques used for the preparation of polycrystalline oxide samples in this thesis works is solid-state reaction route. The solid-state synthesis reaction techenique is the most conventional and widely used synthesis method for the preparation of bulk oxides. Basically, thermodynamic and kinetic factors are important in solid state reactions; thermodynamic considerations show whether a particular reaction should occur or not by considering the changes in free energy that are involved; kinetic factors determine the rate at which the reaction occurs. The rate of reaction between the starting materials are controlled by three important parameters: (i) the contact area between the reacting solids and hence there surface areas (surface area depends on particle size, therefore precursors are needed to crush into fine powder), (ii) the nucleation rate of product phase (it is facilitated if there is a structural similarity between the product and one or both of the reactants because this reduces the amount of structural reorganization) and (iii) the diffusion rate of ions through the various phases and especially through the product phase. The diffusion length ($\sqrt{2Dt}$) should be greater than the particle size (L) of raw materials which is expressed as $\sqrt{2Dt} \geq L$, where, D is the diffusion constant (depends on the reaction temperature and the material) and t is the time of reaction. As the ionic diffusion is a slow process, it requires a high temperature (typically 1000-1500 ^{0}C) and a longer heating duration. In this method, stoichiometric ratios of powder binary oxides and carbonates of metals of interest are finely ground in an agate mortar for homogenization. The first heating of the mixture is carried out at 700-900 ^{0}C for calcination. Subsequently, the powder is pressed in to pellets by using hydraulic pellet-making press under an external pressure ($\sim$ 600-800 MPa) and sintered at high temperatures. The sintering temperature is chosen based on the relevant phase diagram (information available from literature). Multiple heating and grinding of the precursor is required to achieve single-phase desired materials. Some compounds need to be annealed in restricted environment like any inert/reactive gas medium e.g Ar, N_2, O_2 to maintain stoichiometry. If the raw materials have variable oxidation states or a certain oxidation state is desired in the product phase, then depending on the requirement control of either temperature or atmosphere may be needed. In addition, a suitable container material for annealing is taken having high melting point and which is chemically inert to the reactants under the heating conditions. The alumina and platinum crucibles/boats are usually used. Compounds investigated for this thesis work, were synthesized by this route while the detail synthesis conditions such as annealing temperature and duration are described in the respective chapters.

2.2 X-ray diffraction and Rietveld refinement

The crystal structure, phase purity and site-specific order/disorder of the polycrystalline samples were determined using powder x-ray diffraction (XRD) technique. XRD is an ideal characterization tool to extract the structural information due to the fact that wave length of x-ray radiation is comparable to the interatomic distances. Von Laue first introduced this technique in 1912 [88]. In a laboratory system, x-rays are generated when high energetic electrons collide with a metal target within a sealed tube that is under vacuum. The source of electrons is a tungsten filament that is connected to a high voltage transformer. The wavelength of x-rays produced is a characteristic of the metal target. The x-rays are collimated and directed towards the powder sample, which consists of various lattice planes in every possible orientation. The incident ray gets scattered elastically from different atoms arranged periodically in lattice planes. The constructive interference is favored when the path difference of scattered x-rays is an integral multiple of the phase difference and it is expressed by the Bragg condition [89] given by

$$2dsin\theta = n\lambda \tag{2.1}$$

where d denotes inter-planer distance, θ denotes the diffraction angle and λ, the wavelength of the x-rays. The schematic representation of x-ray diffraction process is shown in Figure 2.1.

The intensity distribution of the scattered wave or distribution pattern is the fingerprint of the crystalline solid. Lattice parameters (a, b, c) of a unit cell are related to the inter-planer distance *via* miller indices (h, k, l) as given by,

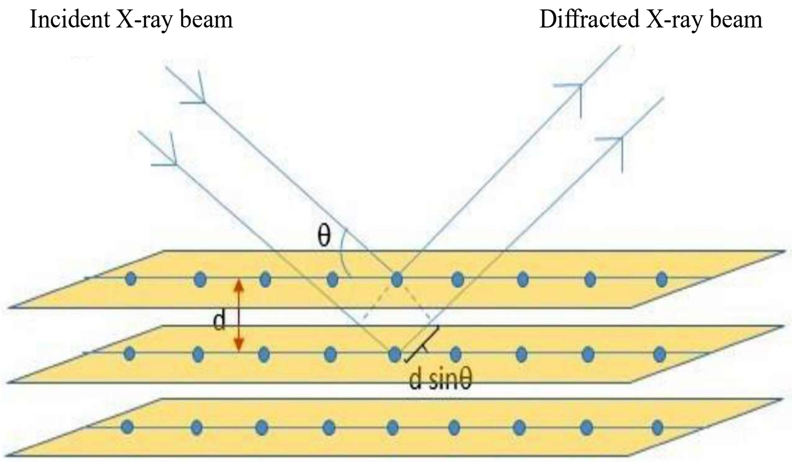

Figure 2.1: Schematic representation of x-ray diffraction from the parallel planes of the periodic crystal lattice.

$$\frac{1}{d^2} = \frac{h^2}{a^2} + \frac{k^2}{b^2} + \frac{l^2}{c^2} \tag{2.2}$$

In principle, the intensity of diffracted beam depends on the structure factor (F_{hkl}) of the specimen. F_{hkl} varies with the atomic form factor of the atoms present in the unit cell, their population and thermal motion as given by following expression,

$$F_{hkl} = \sum_{n=1}^{N} g^n t^n(s) e^{2\pi i(hu_n + kv_n + lw_n)} \tag{2.3}$$

where, g^n is the population factor of nth atom, $t^n(s)$ is the temperature factor, f^n is the atomic scattering factor and (u, v, w) are the fractional coordinates of nth atom in the unit cell. The integrated intensity of a diffracted peak in the XRD pattern is proportional to the amplitude of the structure factor, as expressed below,

$$I_{hkl} = \mid F_{hkl} \mid^2 \tag{2.4}$$

In addition, some external factors may also affect the position, intensity and width of the diffracted peak, such as lattice strain, orientation/disprientation of grains, particle size and instrument parameters.

In this work, the XRD measurements were carried out using Bruker D8 diffractometer (Figure 2.2) in Bragg-Brentano geometry with Cu K_α radiation available in our lab. Diffracted x-rays are collected by the detector, which is a sodium iodide (NaI) scintillation detector. While performing the measurements, a Ni filter was used to eliminate Cu K_β lines. X-ray diffraction pattern of corundum (standard sample) collected in our lab is shown in Figure 2.3.

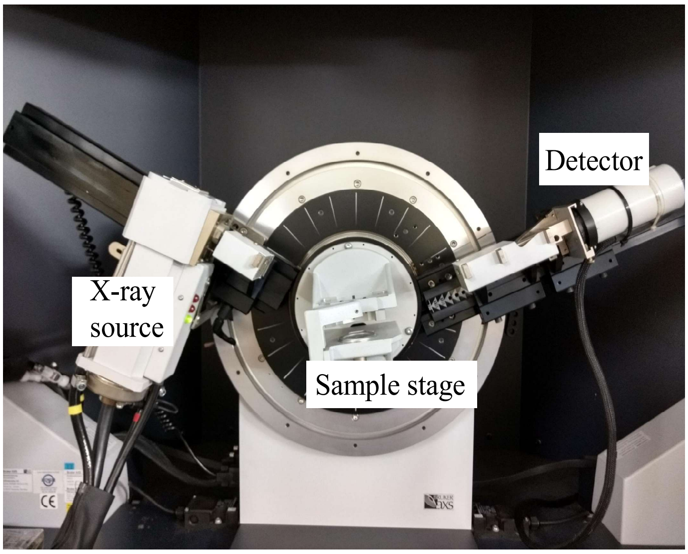

Figure 2.2: X-ray diffraction set up (Bruker D8 Advance) in our lab.

Temperature dependent XRD measurements were carried out at the XRD1 beamline at ELETTRA synchrotron radiation facility using photons of wavelength 0.85507 $\mathring{A}$.

Rietveld refinement

We analyzed the measured XRD data by Rietveld refinement method using Fullprof software package. In this refinement method, the theoretical diffraction pattern is generated by considering the given initial structural parameters such as Wyckoff positions, lattice constants, anisotropic parameters, peak shape parameters, asymmetry parameters and

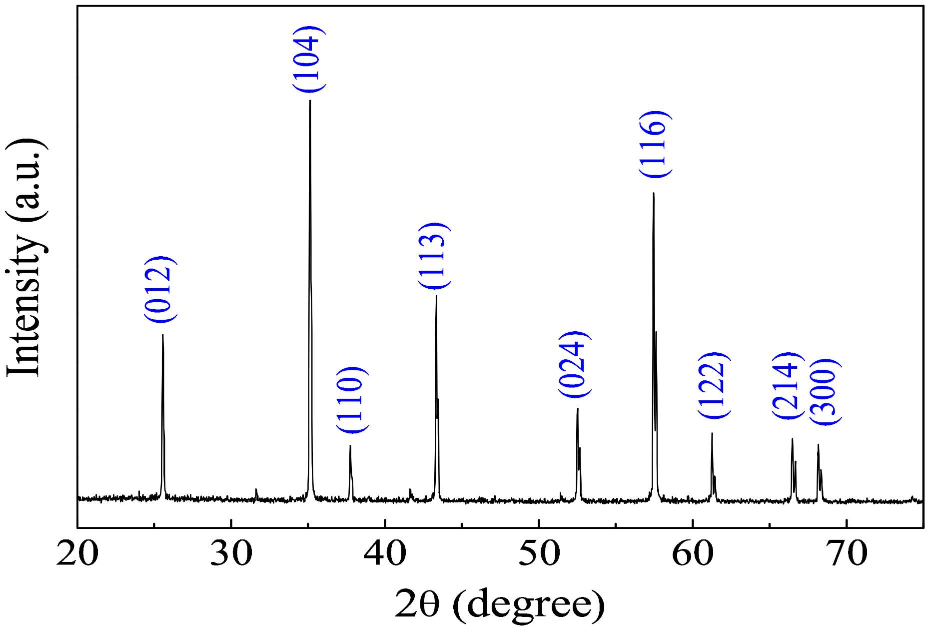

Figure 2.3: X-ray diffraction pattern of corundum (standard sample) collected in our lab. Peak indices are also marked.

instrument parameters such as peak shape and background. Refinement is based on least square fitting of the data and minimization of the difference between the experimental pattern and theoretical pattern. During the refinement, Pseudo-Voigt (PV) function is used to describe the peak shape. The initial parameters are then optimized to improve the reliability of the fit, which are expressed in terms of R-factors such as profile factor (R_p), weighted profile factor (R_{wp}), expected weighted profile factor (R_{exp}) and goodness of fit indicator (χ^2).

$$R_p = \frac{\sum_{i=1}^{n} \mid y_i - y_{c,i} \mid}{\sum_{i=1}^{n} y_i} \tag{2.5}$$

$$R_{wp} = \sqrt{\frac{\sum_{i=1}^{n} w_i \mid y_i - y_{c,i} \mid^2}{\sum_{i=1}^{n} y_i^2}} \tag{2.6}$$

$$R_{exp} = \sqrt{\frac{n-p}{\sum_{i=1}^{n} w_i y_i^2}} \tag{2.7}$$

$$\chi^2 = \frac{R_{wp}}{R_{exp}} \tag{2.8}$$

where, y_i is the profile intensity, $y_{c,i}$ is the calculated intensity, w_i=$1/\sigma_i^2$ (σ_i^2 is the standard deviation) is the weighing factor for the ith data point and n-p is the number of degrees of freedom. R_p provides the information of the difference between the observed and calculated intensity points, R_{wp} contains weighted profile which gives more accurate difference between the observed and calculated intensity peaks rather than considering the background intensity. R_{exp} is calculated based on the number data points (n) in the profile and number of variable parameters (p) used in the refinement procedure. It should be noted that n should be always greater than p. The lower values of χ^2 and R-factors suggest a good profile fit to the data.

2.3 Physical Property Measurement System - PPMS Evercool-II

The PPMS EverCool-II is an integrated cryocooler-based design to condense liquid helium directly within the dewar. Under normal operation, the system recovers all the helium gas generated by static boil-off and temperature control functions. It consists of liquid-helium bath called as dewar. The dewar has reflective super-insulation to help minimize helium consumption. The probe is immersed inside the dewar. The probe contains the basic temperature-control hardware, gas lines, the superconducting magnet, sample puck connectors and various electrical connections. Its outer layer isolates sample chamber from liquid-helium bath. Two concentric tubes separated by a sealed. evacuated region, prevent heat exchange between the sample chamber and helium bath. Major components are the sample chamber, impedance assembly, magnet, baffle rods and probe head. The sample chamber is inside the two vacuum tubes. The region between sample chamber and the inner vacuum tube is called as the cooling annulus. Helium is pulled through the impedance tube into the cooling annulus so that it can warm and cool the sample chamber evenly. The impedance assembly enables and disables the flow of helium into the cooling annulus from the dewar and accordingly maintains the desired temperature

Figure 2.4: PPMS Evercool-II set up in our lab.

of the sample chamber. PPMS contains a magnet which is a superconducting solenoid composed of a niobium-titanium alloy embedded in copper, which is immersed in liquid helium, outside the the probe. The cryocooler unit consists of the cold head and the compressor. The cold head is a closed-cycle, Gifford-McMahon style cryo-refrigerator that uses high-pressure helium as the working gas and an indoor control unit and an outdoor compressor and heat exchanger are there to supply high-pressure and oil-free helium gas to cold head. PPMS Evercool-II system installed in our lab is shown in Figure 2.4. It has been designed to measure various physical properties such as specific heat, resistivity, thermal conductivity, Seebeck coefficient, hall measurement, ac magnetic susceptibility, etc. in a wide range of temperature (1.9 - 400 K) and magnetic field ($\pm$9 T). For the present thesis work, we extensively used heat capacity and ACMS options.

2.3.1 Heat capacity

The heat capacity measurement is of special interest in the study of magnetic and dielectric materials since it essentially determines the thermodynamic behavior of the sample and provides a signature of phase transitions, which may be structural, magnetic or electric. All the specific heat results reported in this thesis were obtained by using the heat capacity option of PPMS. A specially designed sample holder (the puck) is used for specific heat measurement in the PPMS, as shown in Figure 2.5. The sample is mounted on a platform of typical size 3×3 mm^2 square, which is suspended in the middle of the puck by thin wires. For better accuracy, thin sample with large surface area (less than 3×3 mm^2) should be used so that thermal gradient can be avoided. The platform is made up of sapphire while heater and thermometer are connected at the bottom of the puck platform. Apiezon N-grease (addenda) is generally used to stick the sample on the puck platform, which ensures a good thermal contact between sample and platform.

The measurements of heat capacity is performed using ac relaxation technique. During the measurement (at constant temperature), a known amount of heat energy is supplied to the sample for a fixed duration at the constant power which is then followed by a cooling cycle. The thermal response of the measured sample with time is then fitted with a single or pair of exponential functions. Generally, we used the latter one which corresponds to two tau model.

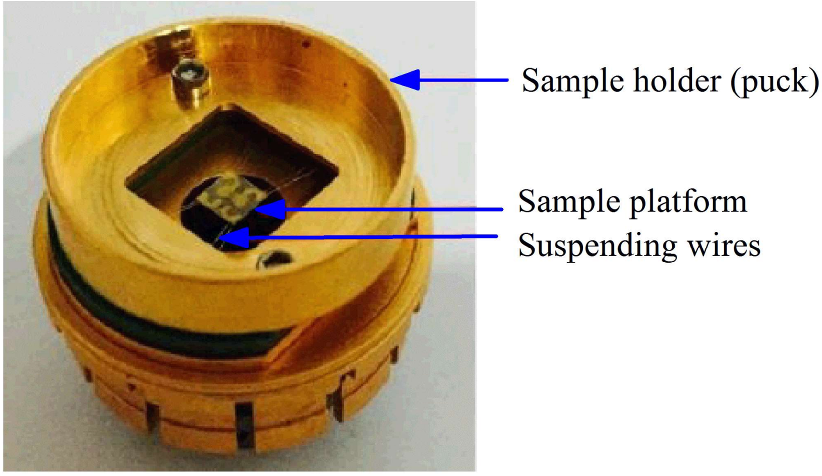

Figure 2.5: The sample holder used for heat capacity measurements in PPMS.

$$C_{platform}\frac{dT_p}{dt} = P(t) - K_w(T_p(t) - T_b) - K_g(T_s(t) - T_p(t)) \tag{2.9}$$

$$C_{sample}\frac{dT_s}{dt} = -K_g(T_s(t) - T_p(t)) \tag{2.10}$$

Where, $C_{platform}$ is the heat capacity of sample platform, C_{sample} is the heat capacity of sample, $P(t)$ heat power, K_w thermal conductivity of supporting wires, K_g is the thermal conductance of grease, T_p is the platform temperature, T_s is the sample temperature and T_b is the temperature of thermal bath. The room temperature specific heat measurement takes more time as compared to that of low temperature measurements, since the relaxation time at lower temperatures is very less (few secs) than that at higher temperature (few minutes). In order to find the heat capacity of sample alone the addenda heat capacity (contribution from the sample stage and grease) must be subtracted from the total measured value.

In general, the low temperature (preferably below 20 K) heat capacity contains information related to the ground state lattice, magnetic and electronic properties of the solid crystalline material. The total heat capacity of a magnetic material can be expressed as follows

$$C = \gamma T + \delta T^n + \beta T^3 + \beta_5 T^5 + \beta_7 T^7 + ... \tag{2.11}$$

where the first term on the right-hand side represents heat capacity from electronic contribution, second term represents magnetic contribution (n = 2 for ferromagnets and n = 3 for antiferromagnets) and third and higher order terms represent lattice contribution of heat capacity.

In present thesis work, we performed temperature dependence of heat capacity measurements on various samples at various magnetic fields ranging from 0 T to 9 T.

2.3.2 Ac magnetic susceptibility - ACMS

The ACMS mainly consists of an ac-drive coil set and a detection coil set.The former one gives an alternating excitation field and later one responds to the combined sample moment and excitation field inductively, as shown in Figure 2.6. The copper drive and detection coils are situated within the ACMS insert, concentric with the superconducting dc magnet of the PPMS.

The drive coil is wound longitudinally around the detection coil set, which generates ac fields up to ±10 Oe with a frequency range 10 Hz to 10 kHz. To isolate the sample′s signal from the uniform background the detection coils are configured in the form of first-order gradiometer, which consists of two sets of counterwound copper coils connected in series along with a separation of several centimeters. During the measurement, the sample is placed at the center of each detection coil and ac field is applied to the measurement region. The detection coils indicate how the applied field is altered by the sample. Ac susceptibility measurements do not directly measure a sample′s magnetic moment. A small alternating field, dH, is applied, while a large constant field can still be applied by the superconducting magnet. The amplitude and phase of the sample′s response is received by the detection coils and compared with the drive signal. The change in the samples moment, dM, is found from this. The ac susceptibility is then calculated by:

$$\chi_{ac} = dM/dH \tag{2.12}$$

This is the local slope of the sample′s magnetization curve. The ideal sample response signal is 90° out of phase with the drive signal in accordance with Faraday′s law, but other factors lead to deviations. Therefore, the ac susceptibility can also be described by a real component, $\chi\prime$, that is in phase with the ideal response and an imaginary component, $\chi\prime\prime$, that is 90° out of phase with the ideal response. These values are indicative of the

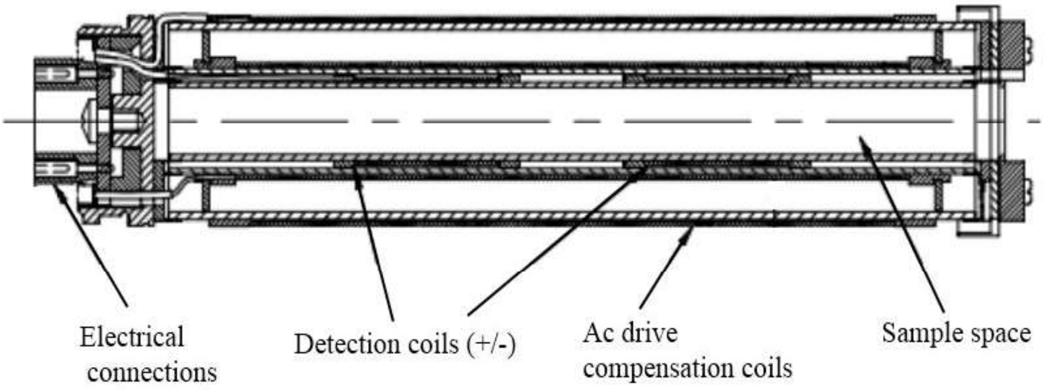

Figure 2.6: Schematic diagram for ACMS coil setup.

stiffness of the spins, or their resistance to flipping with the changing field.

In present thesis work, we performed temperature dependence ac susceptibility measurements of some systems over a wide range of frequencies (17 - 9997 Hz) and also at several applied dc magnetic fields (0 - 10^4 Oe).

2.4 Dc Magnetic measurement system - SQUID VSM

Dc magnetization measurements were carried out using the SQUID-VSM (superconducting quantum interference devices -vibrating sample magnetometer),which is a combination of high sensitivity of the SQUID along with high speed measurement of conventional VSM, as shown in Figure 2.7. It consists of primarily VSM linear motor transport (VSM head) to oscillate the sample and sample oscillates across a superconducting detection coils, which are arranged in a second-order gradiometer configuration. When the sample moves up and down in the presence of the applied magnetic field, it produces an alternating magnetic flux in the detection coils, consequently, current is produced in response to magnetic flux. Current in detection coils is inductively coupled to the SQUID, which serves as an extremely sensitive current-to-voltage converter. The SQUID consists of two superconductors separated by thin insulating layers to form two parallel Josephson junctions, which is very sensitive to measure extremly small magnetic fields.

The SQUID signal (V) generate in the form of a flux profile as a function of time (t) is given by,

$$V(t) = AB^2 sin^2(\omega t) \tag{2.13}$$

where ω is the frequency of oscillation by which sample is vibrating about the center of detection coils, A is a scaling factor relating to the sample magnetic moment and B is the amplitude of sample vibration. Finally, the magnetization of the sample is deduced by fitting the measured flux profile to that expected for a point dipole.

In present thesis work, we performed temperature dependence of magnetization (M vs T) and isothermal magnetization (M vs H) and magnetic relaxation (M vs t) measurements on various samples using SQUID-VSM, to understand the magnetic properties of the

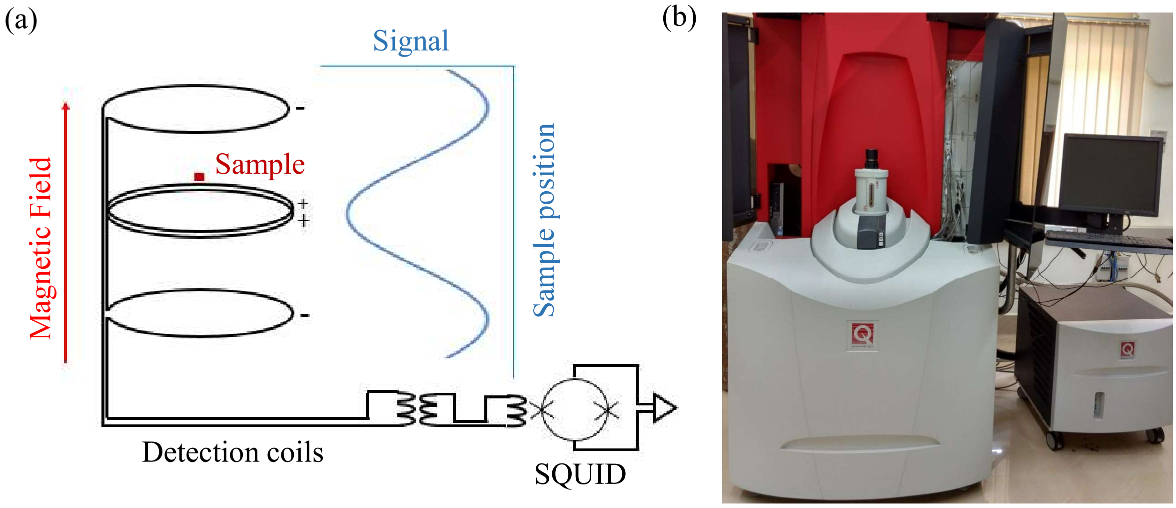

Figure 2.7: (a) Schematic of SQUID magnetometer. (b) SQUID-VSM setup at IOP, Bhubaneswar.

materials.

2.5 Dielectric measurement

Dielectric measurements were performed using impedance analyzer is used. Silver paste is applied on both sides of the dielectric sample to make parallel plate capacitor geometry and the measurements were carried out using two-point configurations as shown in Figure 2.8. Two Teflon coated coaxial cables are connected to the BNC connectors attached to the aluminum flange of the sample probe. Another side of these two cables is connected to Impedance Analyzer. The outer shielding wires on these coaxial cables are connected to the instrument guard to maintain the equipotential surface on the designed probe, while the inner core parts of the BNC connectors are connected to the top and bottom electrodes. The area of the sample holder where samples are mounted is covered with A thin layer of mica sheet to prevent the electrical short-circuit and to maintain good thermal contact with Cu-based material. To investigate the temperature dependent dielectric measurements, it has been inserted into a closed cycle cryogenic system. In parallel plate

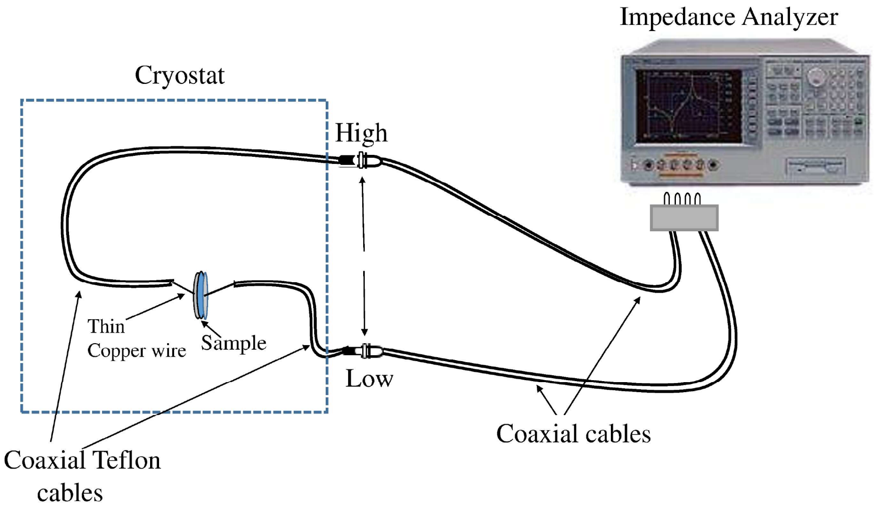

Figure 2.8: Schematic diagram for dielectric measurements setup.

capacitor geometry, the capacitance of a dielectric medium is defined as the ratio of charge (Q) induced on capacitor to the applied voltage (V), as given by

$$C = \frac{dQ}{dV} = \varepsilon\frac{\varepsilon_0 A}{d}, \qquad \text{where } \varepsilon = \varepsilon_0\varepsilon_r \tag{2.14}$$

Here, ε_0 represents dielectric the permittivity of the free space (8.854×10^{-12} F/m) and ε_r relative permittivity of the dielectric medium which is a complex parameter and can be given by,

$$\varepsilon^* = \varepsilon_r' - \varepsilon_r'' \quad \text{and} \quad tan\delta = \frac{\varepsilon_r''}{\varepsilon_r'} \tag{2.15}$$

Here, tanδ indicates the loss tangent and its physical significance is the ratio of energy dissipated per radian to the total energy stored in the dielectric medium at the maximum value of polarization.

In the present thesis work, we investigated temperature dependent dielectric relaxation behavior of some systems using impedance analyzer 4291A in the frequency range of 1 kHz -1 MHz, under dc bias voltage of 1 V.

2.6 Pyroelectric measurement

To measure electric polarization, commonly used method is thermally stimulated pyroelectric current measurement. In these measurements parallel plate capacitor-type samples are used with silver contacts on both sides of the samples. The pyroelectric current is recorded with respect to temperature in quasistatic method. An electrometer is used in the current mode to measure the current through a circuit between the electrodes. This method typically involves poling of the sample during cooling mode under an electric field through the ferroelectric phase transition temperature. Applied electric field is then set to zero and both the electrodes of the samples are shorted for sufficiently long-time to remove thermally induced extrinsic surface charges. Thereafter, in the heating mode, the current generated in the sample due to constant temperature ramping rate is measured. The spontaneous polarization (P) for a given poling field can be estimated from the pyrocurrent as follows,

$$I_p = Ap(T)\frac{dT}{dt} \tag{2.16}$$

Where, A is an electrode area, p(T)= dP/dT is the pyroelectric coefficient and dT/dt is the rate of temperature change.The temperature dependent polarization can be estimated by integrating this current with respect to time as,

$$P(T) = \frac{1}{A}\int I(T)dt \tag{2.17}$$

In the present thesis work, we investigated the pyroelectric current measurements in some systems using Keithley 6517A electrometr, under the poling field , E_p = ± 1.1 kV/cm along with different poling temperature.

2.7 Raman spectroscopy

Raman spectroscopy is a powerful tool to observe vibrational, rotational and other low-frequency modes in a system. The basic principle is based on Raman effect, which was discovered by sir C. V. Raman and K. S. Krishnan [90]. It is an inelastic scattering process of the light with the vibrations of the molecules. Especially, in magnetic systems, the coupling between the softening of phonon modes and various magnetic excitations can be investigated using this optical technique. In Raman spectra, the incidence of photon is scattered elastically (i.e. Raleigh scattering) and inelastically as shown schematically in Figure 2.9. In inelastic scattering process, the energy of the scattered light is weakly modified by the characteristic vibrational mode of the molecule. When energy is lost the Raman scattering is designated as **Stokes**, when energy is gained it is called as **anti-Stokes**. Generally, Stokes Raman light is used in measurement as it has more intensity than the anti-Stokes, however both give same vibrational informations of the compound.

The spectral modes can only be observed in the case of change in polarizability (α) of the molecule during the scattering process. Intensity of inelastic scattered light is,

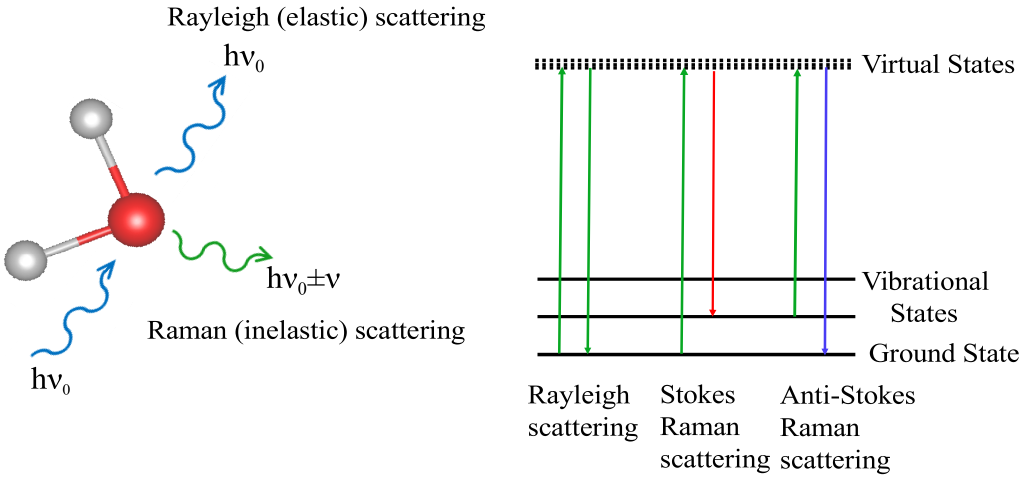

Figure 2.9: Mechanism of Raman scattering effect when molecule exposed to LASER light.

$$I_S = I_0 L(\frac{d\alpha}{dq})^2(\frac{1}{\lambda})^4 \tag{2.18}$$

Here, λ is wavelength of the monochromatic source, $\frac{d\alpha}{dq}$ is change in polarizability, I_0 and L are the intensities of incident light and sample optical path respectively. For lattice vibrations in a crystalline solid, the typical Raman shift is of the order 100-1000 cm^{-1}, and the lifetime of a scattering is $\tau < 10^{-14}$ sec.

In the present thesis, the vibrational properties were measured using a micro-Raman spectrometer (inVia, Renishaw, United Kingdom) with 514.5 nm excitation of an Ar^{+} laser. Spectra were collected in the back scattering configuration using a thermoelectrically cooled CCD camera as the detector. A long working distance 50× objective with numerical aperture of 0.45 was used for the spectral acquisition. For the temperature dependent Raman spectroscopic measurements, the sample was kept in a Linkam (THMS600) stage, driven by an auto-controlled thermoelectric heating and cooling func-

Figure 2.10: Raman spectrometers at IGCAR, Kalpakkam (upper one) and IOP, Bhubaneswar (lower one).

tion within a temperature range of 80 to 300 K. Preliminary analysis of Raman spectra were done using ISA JobinYovn U1000 Raman spectrometer available in IOP (Figure 2.10).

2.8 X-ray Absorption Spectroscopy (XAS) and Extended X-ray Absorption Fine Structure (EXAFS)

X-ray absorption spectroscopy is useful in probing the local environment of the elements present in the systems as well as for studying the conduction band via the electron excitations. This techenique is sensitive to the local structure around the absorbing central atom. Here, one electron is excited to one of the unoccupied state using a tunable photon source. This absorption of photons as a function of the photon energy is the essential process for XAS. The extent of photon absorption can be monitored directly measuring the incident and the transmitted photons; this method is often employed for very high energy photons in several keV range. For low energy x-ray absorption measurements with typically less than1 keV photon energy, it is often more advantageous to monitor the number of photons absorbed or alternately the number of core electrons excited in an indirect manner. The process of de-excitation of the highly excited state gives rise to emission of electrons and photons is proportional to the number of core holes created. If the emitted photons are detected to extract the information, it is known as the total fluorescence yield (TFY) mode. On the other hand, if the emitted electrons are detected to obtain information about the unoccupied part, the technique is known as the total electron yield (TEY) process. Since the absorption process involves the transition of electron from a core level to the unoccupied part, the various features in the spectrum can be characterized by appropriate selection rules (Δl = ± 1, Δs = 0). Thus, this technique provides information about the site and momentum projected spectral functions. In the present thesis work, we recorded XAS spectra of some systems to probe the unoccupied state at CIPO beamline, ELETRA synchrotron centre, Italy.

Extended X-ray Absorption Fine Structure (EXAFS)

The oscillatory variation of the x-ray absorption as a function of photon energy beyond the absorption edge is called as Extended X-ray Absorption Fine Structure (EXAFS). The absorption, normally expressed in terms of absorption coefficient (μ), can be determined from a measurement of the attenuation of x-rays when it passes through through a material. When the x-ray photon energy (E) is same as that of the binding energy of some core level of an atom in the material, an abrupt increase in the absorption coefficient occurs, known as the absorption edge. Beyond the edge the absorption coefficient decreases monotonically as a function of energy. For atoms either in a molecule or embedded in a condensed phase, the variation of absorption coefficient at energies above the absorption edge displays a fine structure called as EXAFS. Such fine structures have a range up to 1000 eV above the absorption edge and have an amplitude of up to a few tenths (normally 1-20 %) of the edge jump.

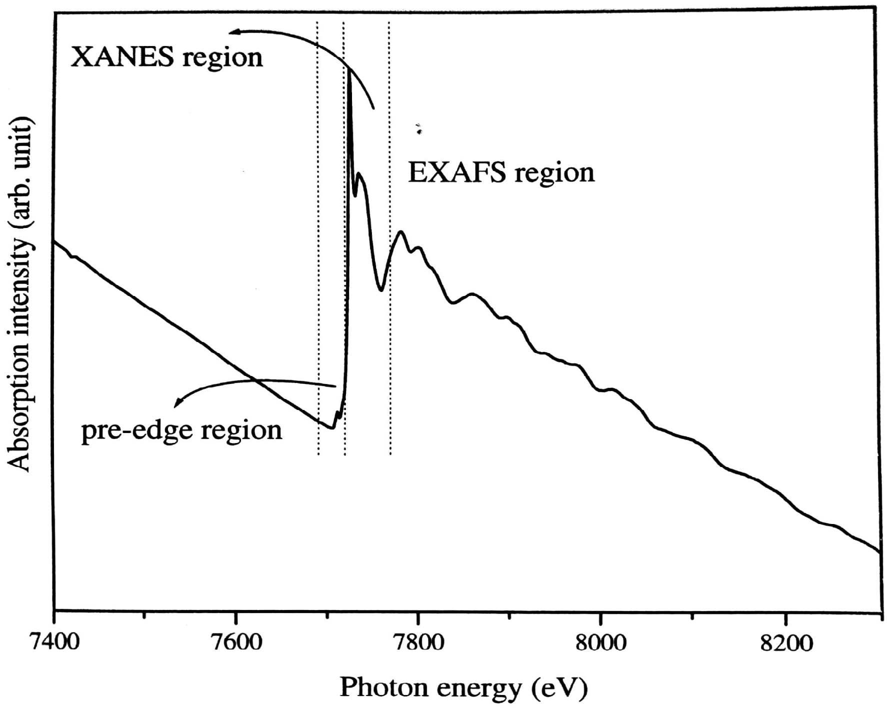

Figure 2.11: XAFS spectrum showing the pre-edge, XANES and EXAFS regions.

EXAFS spectroscopy represents the variation of the x-ray absorption coefficient (μ)

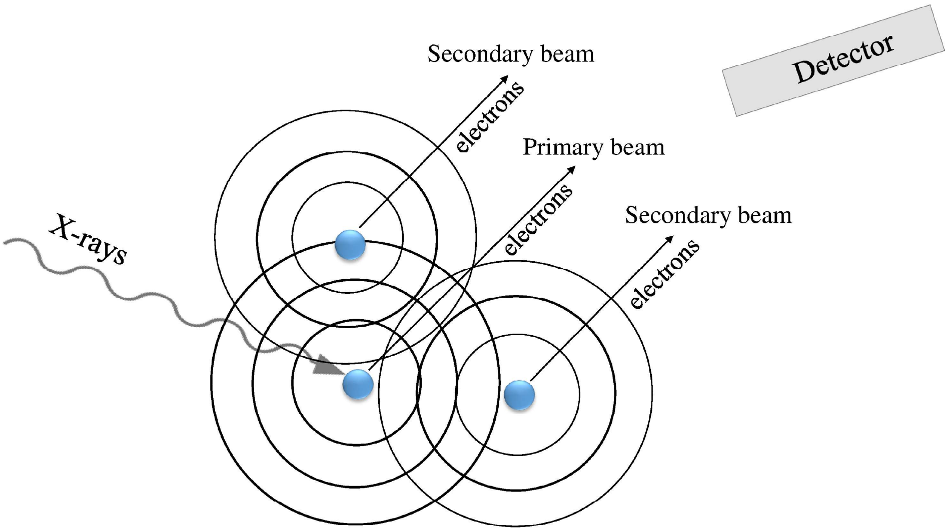

Figure 2.12: A schematic representation of EXAFS process.

as a function of photon energy (E) above the threshold of an absorption edge as shown in Figure 2.11. The region between 50 to 1000 eV above the absorption edge represents the EXAFS spectrum. The absorption peaks appear near or below the edge, due to excitation of core electrons to some bound states. The excitation of electrons from $1s$ state to nd, $(n{+}1)s$, or $(n{+}1)p$ orbitals are represent as K-edge , and from $2s$ state is denoted as L_I edge, from $2p$ state is denoted as L_{II}, L_{III} edges to the same set of vacant orbitals. This pre-edge region gives the information about the electronic configuration, the energetics of virtual orbitals, and the site symmetry. The position of edge also contains information about the charge on the absorber. The region between the pre-edge and the EXAFS is called as x-ray absorption near edge structure (XANES). It generally arises from various complex effects such as many-body interactions, multiple scatterings, band structures, distortion of the excited state wavefunction by the Coulomb field and many more.

EXAFS is the final state interface effect involving scattering of the outgoing photoelectron from neighboring atoms. The probability that an x-ray photon will be absorbed by a core electron depends both on the initial and final state of the electron. The initial state is the localized core level corresponding to the absorption edge. The final state is that of the ejected photo electron which can be represented as outgoing spherical wave originating from the x-ray absorbing atom. The presence of neighboring atoms incoming electron waves are produced. Thus, final state is the resultant of outgoing and all the incoming waves. This interference between the outgoing and the incoming waves results in to the sinusoidal variation of μ vs E known as EXAFS.

For a monoatomic gas with no neighboring atoms, a photoelectron ejected by absorption of an x-ray photon will travel as a spherical wave with a wavelength $\lambda = 2\pi/k$, where

$$k = \sqrt{\frac{2m}{\hbar^2}(E - E_0)} \tag{2.19}$$

where E and E_0 represent the incident photon energy and the threshold energy of that particular absorption edge. If neighboring atoms are present, the backscattering of outgoing photoelectron occur from the neighboring atoms, thereby producing an incoming wave which can interfere either constructively or destructively with the outgoing wave near the origin, resulting in the oscillatory behavior of the absorption rate. The amplitude of the sinusoidal modulation of μ vs E depends on the bonding and type of the neighboring atoms and frequency on their distances away from the absorber. A short-range single-electron single-scattering theory has been developed to visualize this simple picture of EXAFS. For reasonably high energy ($\geq$ 60 eV) and moderate thermal or static disorders, the modulation of the absorption rate normalized to the background absorption (μ_0) can be expressed as,

$$\chi(E) = \frac{\mu(E) - \mu_0(E)}{\mu_0(E)} \tag{2.20}$$

Above equation can be expressed as function of the photoelectron wavevector k as following,

$$\chi(k) = \sum_j N_j S_i(k) F_j(K) e^{-2\sigma_j^2 k^2} e^{-2r_j/\lambda_j(k)} \frac{sin(2kr_j + \phi_{ij}(k))}{kr_j^2} \tag{2.21}$$

where $F_j(k)$ is the back scattering amplitude from each of the neighboring atoms of the jth type, N_j. σ_j and r_j denote Debye-Waller factor and distance between neighboring atoms.

This accounts thermal vibration (assuming harmonic vibration) and static disorder. $\phi_{ij}(k)$ is the total phase shift experienced by the photoelectron. e^{-2r_j/λ_j} represent the inelastic losses in the scattering process (due to neighboring atoms and the medium in between) with electron mean free path,λ_j. $S_i(k)$ is the amplitude reduction factor due to many-body effects such as shake up/down processes at the central atom denoted by j. Hence each EXAFS wave is determined by the backscattering amplitude $N_jF_j(k)$, modified by the reduction factors $S_i(k)$, $e^{-2\sigma_j^2k^2}$ and e^{-2r_j/λ_j} and the $1/kr_j^2$ distance dependence, and the sinusoidal oscillation is a function of interatomic distance ($2kr_j$) and the phase shift $\phi_{ij}(k)$. While the amplitude function depends only on the type of the backscatters, the phase function contains contributions from both the absorber and the backscatter.

The Debye-Waller factor (σ) provides structural and chemical information, thus is an important parameter in EXAFS spectroscopy. It consists of two components, σ_{stat} and σ_{th} due to static disorder and thermal vibrations, respectively.

In the present thesis work, we performed the temperature dependent EXAFS study using P65 beam line at Petra III, Deutsches Elektronen-Synchrotron (DESY), Germany.

2.9 Theoretical approach

Density Functional Theory (DFT) has emerged as one of the widely used methods to describe the properties of various systems. The basic problem in condensed matter physics is dealing with the interactions among large number of particles. The full Hamiltonian for a many body problem in the non-relativistic case consists of two species, electrons and nuclei, with Coulomb interaction within and between themselves. To make situation simple, the Born-Oppenheimer approximation [91] is considered which assumes that the nuclei are fixed and generate constant external potential in which the electrons move. Schrodinger equation for a system containing N electrons can be expressed as,

$$\Big[-\frac{\hbar^2}{2m}\sum_{i=1}^{N}\nabla_i^2+\sum_{i=1}^{N}V_{ext}(r_i)+\frac{1}{2}\sum_{j\neq i=1}^{N}\frac{e^2}{\mid r_i-r_j\mid}\Big]\Psi(x_1,x_2.....,x_N)=E\Psi(x_1,x_2.....,x_N)$$

where, $x_i = r_i$, σ_i. r and σ are the electron space and spin coordinates, respectively. The first term represents the kinetic energy T, the second term denotes the external potential

V_{ext} and the third term describes the electron-electron interaction U. The electrostatic potential, V_{ext} generated by the nuclei can be given by,

$$\sum_{i=1}^{N} V_{ext}(r_i) = \sum_{i,k} \frac{Z_k e^2}{\mid r_i - R_k \mid}$$

where, Z_k is the atomic number of nucleus k at R_k.
The quantum mechanical approach to solve this many body problem involves specification of external potential, calculation of wave function and observables by taking the expectation value of operators with this wave function. The early attempts to solve the many body problem started with the free electron model, which could explain metals satisfactorily. Thereafter, Hartree and Hartree-Fock approaches came and finally, the Thomas-Fermi model was developed, which is assumed as a very early form of DFT since it uses the electron charge density as the basic variable instead of the wave function.

In 1964, Hohenberg and Kohn [92] proposed the density functional theory (HK-DFT), which is based on the two theorems. The first theorem demonstrates that the ground state properties of a many electron system are uniquely determined by an electron density that depends on three spatial coordinates, through the use of the functionals of electron density. The second theorem defines an energy functional, which is minimum at the correct ground state. The HK-DFT lacked in accuracy due to the absence of exchange and correlation (XC) terms. In 1965, Kohn and Sham [93] formulated the DFT theory (KS-DFT) including the XC terms. In the KS-DFT approximation, the many-body problem of interacting electrons in a static external potential is treated as a system of non-interacting electrons moving in an effective potential. The effective potential includes the external potential and the effects of the Coulomb interactions between the electrons, like the XC interactions. However, as XC term is in general unknown, its correct modeling are difficult within the framework of KS-DFT. The most widely accepted approximations are the local density approximation (LDA) and generalized gradient approximation (GGA) to incorporate the XC interactions. Under LDA, it is assumed that charge density $n(r)$ varies smoothly with respect to r. However, in strongly correlated systems, the LDA based results markedly deviates from the experimental findings. For these cases GGA has emerged as promising attempt, in which exchange functional not only depends on the electron density, like LDA but also on the gradient $\mid \nabla_n \mid$ of the electron density. Valence wavefunctions tend to have rapid oscillations near ion cores due to the requirement that they be orthogonal to core states. The oscillatory behavior in the core regions, requires a very large set of plane waves, or equivalently a very fine grid, to be described correctly. One way of solving this problem is the use of pseudopotentials such as ultrasoft [94] and projector argumented wave (PAW) [95], in which the collective system of nuclei and core electrons are described by an effective, much smoother potential. Generally, the PAW potentials are more accurate than the ultrasoft pseudopotentials. This is due to the smaller radial cutoffs (core radii) for PAW than the radii used for the ultrasoft pseudopotentials, and it reconstructs the exact valence wavefunction with all nodes in the core region. Due the smaller core radii of the PAW potentials, the required energy cutoffs and basis sets are also somewhat larger. GGA of Perdew-Burke-Ernzerhof (PBE) [96] parameterization for the XC potential is the most widely used functional in the first-principles DFT calculations. But, it overestimates lattice parameters. PBEsol [97] functional has been proposed by a restoration of the density-gradient expansion in PBE. This functional is intended to provide accurate values of equilibrium properties for solids and their surfaces. Also, it provides better values of lattice constant in the densely packed solids and in solids under pressure.

Many physical properties depend upon a system response to some form of perturbation such as polarisabilities, phonons, Raman intensities etc. Density functional perturbation theory (DFPT) is a technique that allows calculation of such properties within the density functional framework, thereby facilitating an understanding of the microscopic quantum mechanical mechanisms behind such processes. The DFPT formalism is, in many ways, very similar to the DFT itself. DFT states that the total energy is the functional of the electron density; thus one can solve the DFT equations by minimizing the total energy. Similarly, the DFPT problem can be solved by minimizing the second order perturbation in the total energy, which gives the first order changes in density, wavefunctions and potential [98, 99].

Theoretical calculations of the structural, electronic and magnetic properties of this thesis work is based on DFT, using GGA with PBEsol parameterization for the XC potential along with the PAW method as implemented in the Vienna ab-initio simulation package (VASP) [100]. Phonon calculations has been done using DFPT implemented in the VASP package.

Chapter 3

Investigating complex spin glass ad probable ferroelectric nature of $\mathbf{Ga_{2-x}Fe_xO_3}$

This chapter consists of two sections, in the first section we discuss detailed magnetic properties of $Ga_{2-x}Fe_xO_3$ *(x = 0.75, 1.0 and 1.25). Magnetic behavior in this series of compounds could be well explained by the molecular-field-approximation of three-sublattice ferrimagnetic model considering three inequivalent octahedral sites Ga2, Fe1 and Fe2, suggesting weak magnetic exchange coupling related to Fe present at tetrahedral Ga1 site. Analysis of frequency dispersion of ac susceptibility reveals a transition from cluster-glass-like phase to spin-glass-like phase with decreasing temperature for x = 0.75 composition. Mentioned glassy behavior is found to gradually evolve with composition (x) from Ising type character to Heisenberg type behavior to unconventional glassy behavior for x = 1.25 composition.* $Ga_{2-x}Fe_xO_3$ *can hence serve as an ideal system for modeling complex spin glasses. In the second section we deal with dielectric and pyroelectric studies. The emergence of polarization in these systems is a thermal stimulated process caused by freezing of defect dipoles associated with charged oxygen vacancies rather than the intrinsic ferroelectric behavior.*

3.1 Ferrimagnetism and complex spin glass behavior

3.1.1 Introduction

Over the past several decades spin glass systems have drawn a considerable attention of the scientific community as a prototype of complex systems which demands various physical models for understanding. Spin glass concepts, ideas, and mathematical tools provide a way to analyze some interesting real-world problems in computer science [101], biological applications [102], memory applications, neural networks [103] etc. Necessary ingredients for spin glass behavior are frustration of spins, disorder in magnetic interactions and competing ferromagnetic (FM) and antiferromagnetic (AFM) interactions which destroys the long range magnetic ordering in the system [50, 104–106].

Of late Gallium ferrite ($GaFeO_3$) is found to exhibit spin glass behaviour [107], apart from several promising characteristics such as room temperature piezoelectricity [31], ferrimagnetism [26, 27] and electric polarization with significant magnetoelectric coupling [26]. It adopts non-centrosymmetric crystal structure with space group $Pc2_1n$ and remain in a highly disorder state i.e. Fe is often found in the Ga site and vice versa due to similar ionic radii of Ga and Fe [26, 27]. This inter-site disorder also provides an novel opportunity to tune its various physical properties by various synthesis methods or by varying stoichiometric compositions in turns by varying the cation distribution among the different sites. There are contradictory claims about existence of spin-glass-like behavior in $GaFeO_3$. Flux grown single crystal of $GaFeO_3$ exhibits spin glass behavior at temperatures much below the ferrimagnetic transition temperature in [107, 108]. However, Sharma *et al.* [109] and Wang *et.al.* [27] contradicted this claim on samples grown by sol-gel method and solid state synthesis, respectively. However, the lack of observation of spin-glass like phase in the sol-gel processed samples is possibly due to the presence of grain boundaries in the polycrystalline samples which can amplify the magnetic anisotropy over spin glass like behavior or any deleterious effects of sol-gel processing and in solid state synthesized sample ac susceptibility measurements were done in a narrow high frequency range. This warrants a detailed investigations of glassy behavior in polycrystalline sample.

In this work, we have tuned the extent of disorder by preparing a series of polycrystalline compounds of the type $Ga_{2-x}Fe_xO_3$ and systematically analyzed the magnetic glassy behavior using dc and ac magnetization and magnetic relaxation measurements. Our results suggest double spin glass behavior for x=0.75 composition and a gradual evolution to complex glassy behavior with increasing Fe concentration (x).

3.1.2 Experimental details

The polycrystalline samples of $Ga_{2-x}Fe_xO_3$ (x = 0.75, 1.0 and 1.25) were prepared by solid state synthesis technique. Stoichiometric proportions of Ga_2O_3 and Fe_2O_3 were mixed thoroughly and heated in air at 1400 °C for 24 h with several intermediate heating and grinding. The crystalline structure and phase purity of the samples were confirmed by x-ray diffraction (XRD) measurements using Bruker D8 Advance x-ray diffractometer. Rietveld refinements were performed using the FULLPROF program to determine site occupancies. The dc magnetization and ac susceptibility measurements were performed using SQUID-VSM and Physical Property Measurement System (PPMS), respectively from Quantum Design, US.

3.1.3 Results and discussion

3.1.3.1 Structural studies

X-ray diffraction patterns of $Ga_{2-x}Fe_xO_3$ (x = 0.75, 1.0 and 1.25) acquired at room temperature along with the corresponding refined patterns are shown in Figure 3.1. Refinement was performed considering $Pc2_1n$ space group for all the samples. It is found that the site specific disorder between Ga and Fe results in partial occupation of Fe at Ga sites and vice-versa. All the crystallographic parameters, mixed occupancies at different Ga and Fe sites obtained from refinements and reliability parameters of refinements for all compositions are tabulated in Table 3.1. The lattice constants a, b and c show a monotonic increase with the Fe content (x) consistent with those reported previously [26, 110].

3.1.3.2 Magnetic studies

Zero-field-cooled (ZFC) and field-cooled (FC) magnetization data of $Ga_{2-x}Fe_xO_3$, x = 0.75, 1.0 and 1.25 acquired at 100 Oe are shown in Figure 3.2. ZFC curves show negative magnetization at low temperatures for $x = 0.75$ and 1.0 compositions. To confirm whether

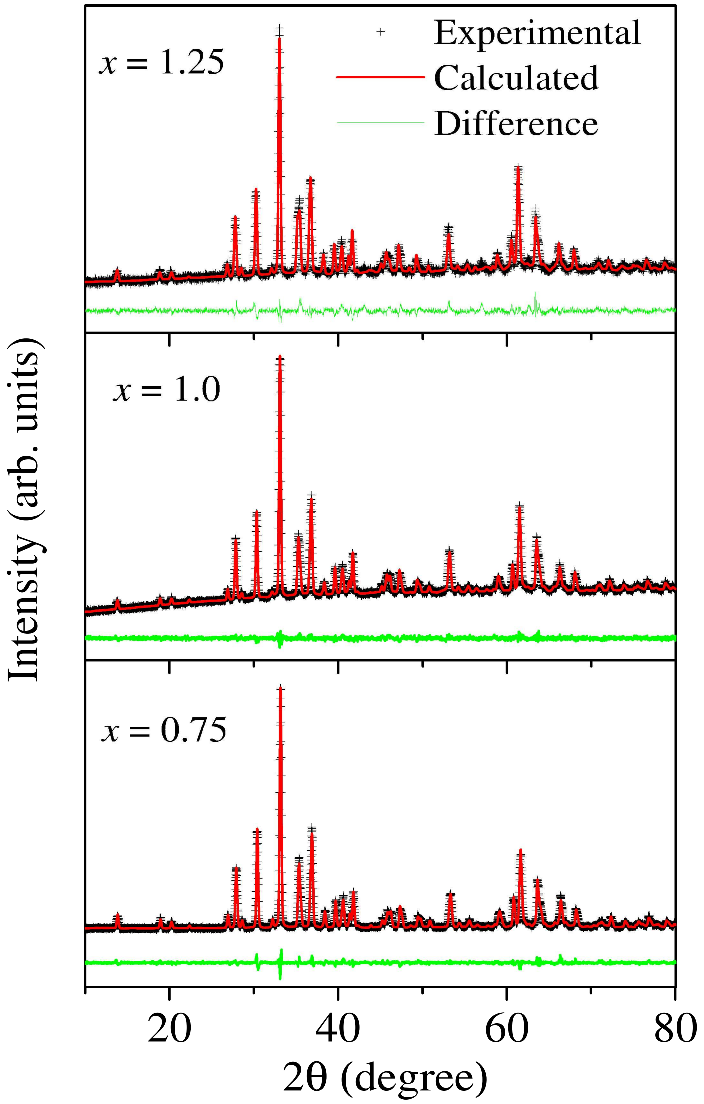

Figure 3.1: X-ray powder diffraction patterns of $Ga_{2-x}Fe_xO_3$ (x = 0.75, 1.0 and 1.25) at room temperature. Experimental data is presented with symbol while the fitted curves from the Rietveld analysis are represented as solid line. Difference spectra (difference between experimental data and fitting) is also plotted.

it is a genuine effect or an experimental artefact, we have done magnetization measurements at various magnetic fields. It is observed that ZFC curves still remain negative at low temperatures up to a 750 Oe for x = 0.75 and up to 500 Oe applied field for x = 1.0 compound. The negative magnetization at this considerable large field can not be an artefact due to the negative trap field and therefore believe that this is a genuine effect.

Table 3.1: Lattice constants, atomic positions, sites occupancies and reliability parameters obtained from Rietveld analysis for $Ga_{2-x}Fe_xO_3$ ($x = 0.75$, 1.0 and 1.25).

x	0.75	1.0	1.25
Lattice constants	$a(\text{Å}) = 8.7219$	$a(\text{Å}) = 8.7406$	$a(\text{Å}) = 8.7556$
	$b(\text{Å}) = 9.3655$	$b(\text{Å}) = 9.3842$	$b(\text{Å}) = 9.4083$
	$c(\text{Å}) = 5.0719$	$c(\text{Å}) = 5.0789$	$c(\text{Å}) = 5.0851$
Atomic positions	(x, y, z)	(x, y, z)	(x, y, z)
Ga1(4a)	(0.1522, 0, 0.1775)	(0.1474, 0, 0.1702)	(0.1529, 0, 0.1767)
Ga2(4a)	(0.1580, 0.3188, 0.8146)	(0.1563, 0.3109, 0.8072)	(0.1615, 0.2952, 0.8150)
Fe1(4a)	(0.1467, 0.5910, 0.1935)	(0.1552, 0.5829, 0.1924)	(0.1487, 0.5907, 0.1839)
Fe2(4a)	(0.0287, 0.7931, 0.6783)	(0.0271, 0.7953, 0.6747)	(0.0285, 0.7939, 0.6602)
O1(4a)	(0.3228, 0.4385, 0.9637)	(0.3298, 0.4302, 0.9811)	(0.3524, 0.4304, 0.9591)
O2(4a)	(0.4956, 0.4536, 0.5261)	(0.5003, 0.4301, 0.4976)	(0.4204, 0.4494, 0.4440)
O3(4a)	(0.9869, 0.2163, 0.6454)	(0.9992, 0.1944, 0.6459)	(0.9961, 0.1971, 0.6301)
O4(4a)	(0.1594, 0.2074, 0.1597)	(0.1674, 0.1959, 0.1578)	(0.1546, 0.2081, 0.1503)
O5(4a)	(0.1487, 0.6772, 0.8337)	(0.1738, 0.6715, 0.8359)	(0.1684, 0.6884, 0.8588)
O6(4a)	(0.1712, 0.9512, 0.4967)	(0.1681, 0.9303, 0.5219)	(0.2118, 0.9222, 0.4968)
Sites Occ.	Ga/Fe	Ga/Fe	Ga/Fe
Ga1	0.47/0.03	0.44/0.06	0.37/0.13
Ga2	0.435/0.065	0.32/0.18	0.25/0.25
Fe1	0.155/0.345	0.115/0.385	0.06/0.44
Fe2	0.19/0.31	0.125/0.375	0.07/0.43
R-factors			
R_{exp}	4.67	3.65	2.45
R_{wp}	8.14	8.03	7.44
R_p	7.77	7.01	6.63

Such negative magnetization is not an uncommon feature in ferrimagnetic materials, as the total magnetization is the sum of two sublattice magnetizations. $Ga_{2-x}Fe_xO_3$ consists of four types of cation sites: octahedral Fe1, Fe2, Ga2 sites and tetrahedral Ga1 sites and magnetization at these sites might have different temperature dependence of magnetic transition temperature, coercive field etc. and the total magnetization is the vector sum of magnetizations of all four sub-lattices, resulting in negative value at low temperatures. Note that there is increase of ferrimagnetic transition temperature (T_c) with increase of Fe concentration in the sample (i.e. for large value of x). This is due to the increase in Fe occupancy at Ga2 site which is strongly antiferromagnetically coupled with Fe at Fe1 site [26]. Further, these are not simple two-sublattice classical ferrimagnetic systems as Fe ions are distributed at all four inequivalent cationic sites as noted in Table

3.1. For $x = 0.75$ and 1.0 compounds Fe occupancy at tetrahedral Ga1 site is negligibly small. Therefore these systems could be explained by molecular-field-approximation using the three-sublattice ferrimagnetic model [111], where magnetism is contributed only by Fe present in Fe1, Fe2 and Ga2 sites. The paramagnetic susceptibility can hence be expressed as,

$$\frac{1}{\chi} = \frac{T + \theta_p}{C} - \frac{\sigma T + m}{T^2 - \theta T + p} \tag{3.1}$$

where C is the Curie constant and θ_p, θ, σ, m and p are intersublattice and intrasublattice

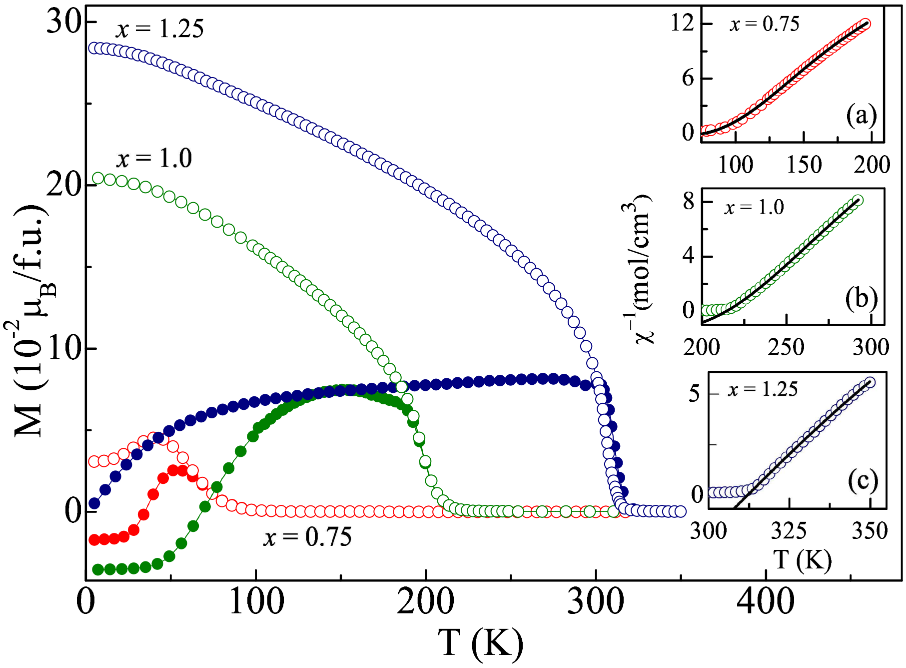

Figure 3.2: ZFC (closed circle) and FC (open circle) dc magnetization plots of $Ga_{2-x}Fe_xO_3$, with $x = 0.75$, 1.0 and 1.25 compositions as a function of temperature acquired at 100 Oe. (a), (b) and (c) are the respective fitting of inverse susceptibility plot to Eq. 3.1 in the paramagnetic region.

molecular-field coefficients. The fitting of inverse susceptibility for $x = 0.75$ compound is shown in Figure 3.2 (a) (inset) and the deduced parameters are presented in Table 3.2. The effective magnetic moment can be calculated from Curie constant (C) using the relation, $\mu_{eff}^2 = 3Ck_B/N$, k_B = Boltzmann Constant and N = Avogadro′s constant. The calculated magnetic moment values for $x = 0.75$ compounds are very close to those

Table 3.2: The magnetic parameters extracted from fitting the paramagnetic region of inverse susceptibility data using three-sublattice ferrimagnetic model (Eq. 3.1) for $Ga_{2-x}Fe_xO_3$ ($x = 0.75$, 1.0 and 1.25). The fitting parameters are C ($cm^3.mol^{-1}$), θ_p (K), θ (K), σ (K. mol. cm^3), m (K^2 .mol. cm^3), p (K^2), calculated effective moments, μ_{eff}^{cal} (μ_B) and theoretical effective moments μ_{eff} (μ_B).

x	0.75	1.0	1.25
C	40.8 ± 0.1	54.6 ± 0.18	68.21 ± 0.5
θ_p	495 ± 30	618 ± 35	699 ± 40
θ	182± 2	433 ± 4	505 ± 7
σ	-488 ± 6	-1050 ± 9	-1220 ± 16
p	20118 ± 140	56952 ± 110	81216 ± 218
m	206562 ± 1470	371071 ± 2520	697025 ± 2850
μ_{eff}^{cal}	5.1 ± 0.05	5.89 ± 0.1	6.58 ± 0.3
μ_{eff}	5.11	5.91	6.61

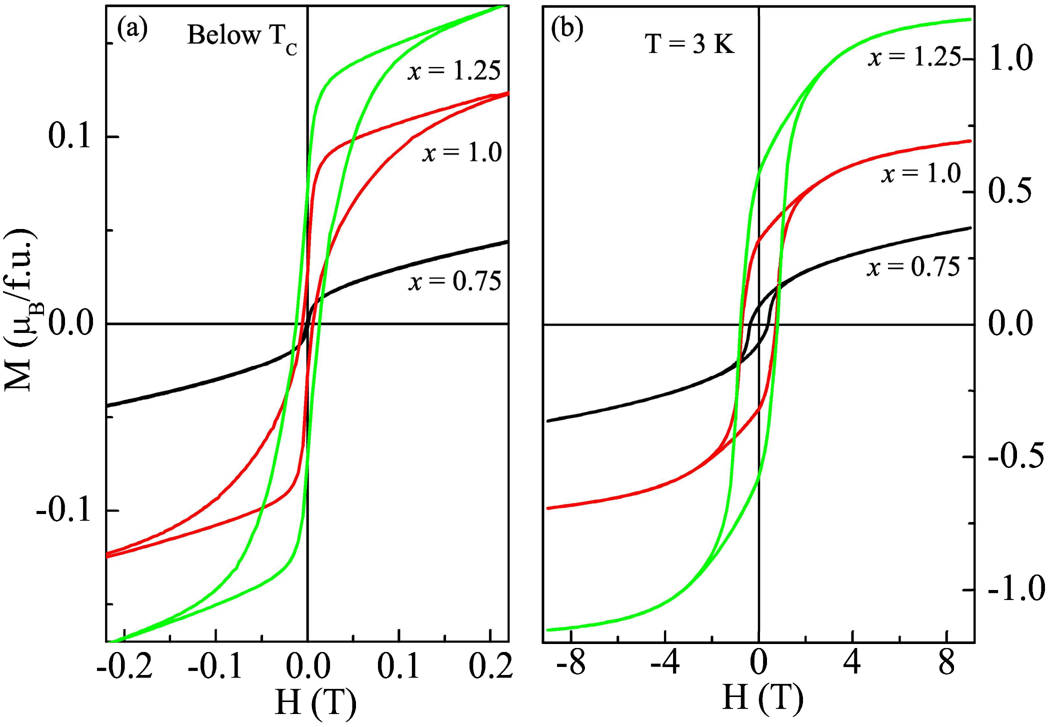

Figure 3.3: M-H loop immediate below T_c (magnified) (a) and at 3 K (b) of $Ga_{2-x}Fe_xO_3$, with $x = 0.75$, 1.0 and 1.25 compositions.

estimated from the free-ion moments suggesting good quality of the fit and correctness of the model used. Similar fitting was also performed for $x = 1.0$ and 1.25 systems (Figure 3.2 (b) and (c)), where there is significant amount of Fe present at Ga1 site. Three-sublattice ferrimagnetic model hence may not suffice in these case. However, the goodness of the fit for these systems suggests that magnetic exchange coupling related to Fe present at tetrahedral Ga1 site is very weak [26,27] compared to Fe present at other three tetrahedral sites.

Figure 3.3 (a) and (b) represents magnetization as a function of applied field. The pinched like shape of M-H loop mainly for $x = 1.0$ and 1.25 compounds is an evidence of two phase systems consisting of hard and soft magnetic phases, indicating occupation of significant amount of Fe at Ga2 sites, which is magnetically softer relative to Fe1 and Fe2 sites [26, 112]. A careful inspection of M-H loop at 3 K also finds that there is no saturation of magnetization up to 9 T field and the observed value of magnetization is much lower than the expected spin only value, evidencing disorder and/or ferrimagnetic behavior in the system.

Observation of strong divergent behavior of ZFC and FC curves below T_c (Figure 3.2) is indicative of magnetic freezing such as spin glass, cluster glass, superparamagnet etc. Comprehensive investigation to distinguish the collective glassy behavior was performed using ac susceptibility measurements over a wide range of frequencies from 17-9997 Hz. Figure 3.4 (a) and (b) show real (χ') and imaginary (χ'') part of ac susceptibility for $x = 0.75$ sample, where a main peak at T_{f1} and a small shoulder at slightly lower temperature (T_{f2}) are observed. Maxima of both the peaks shift towards higher temperatures with increasing frequency. Such frequency dispersions of susceptibility have been observed in various oxides and dilute magnetic systems [72, 104–106, 113] and is an indicative of spin glass behavior or short range spin interactions.. For detailed understanding, frequency dependence of freezing temperature (T_f) was analyzed using the concepts of dynamic scaling theory which predicts critical power law of the form [50]

$$\tau = \tau_0(\frac{T_f - T_s}{T_s})^{-z\nu} \tag{3.2}$$

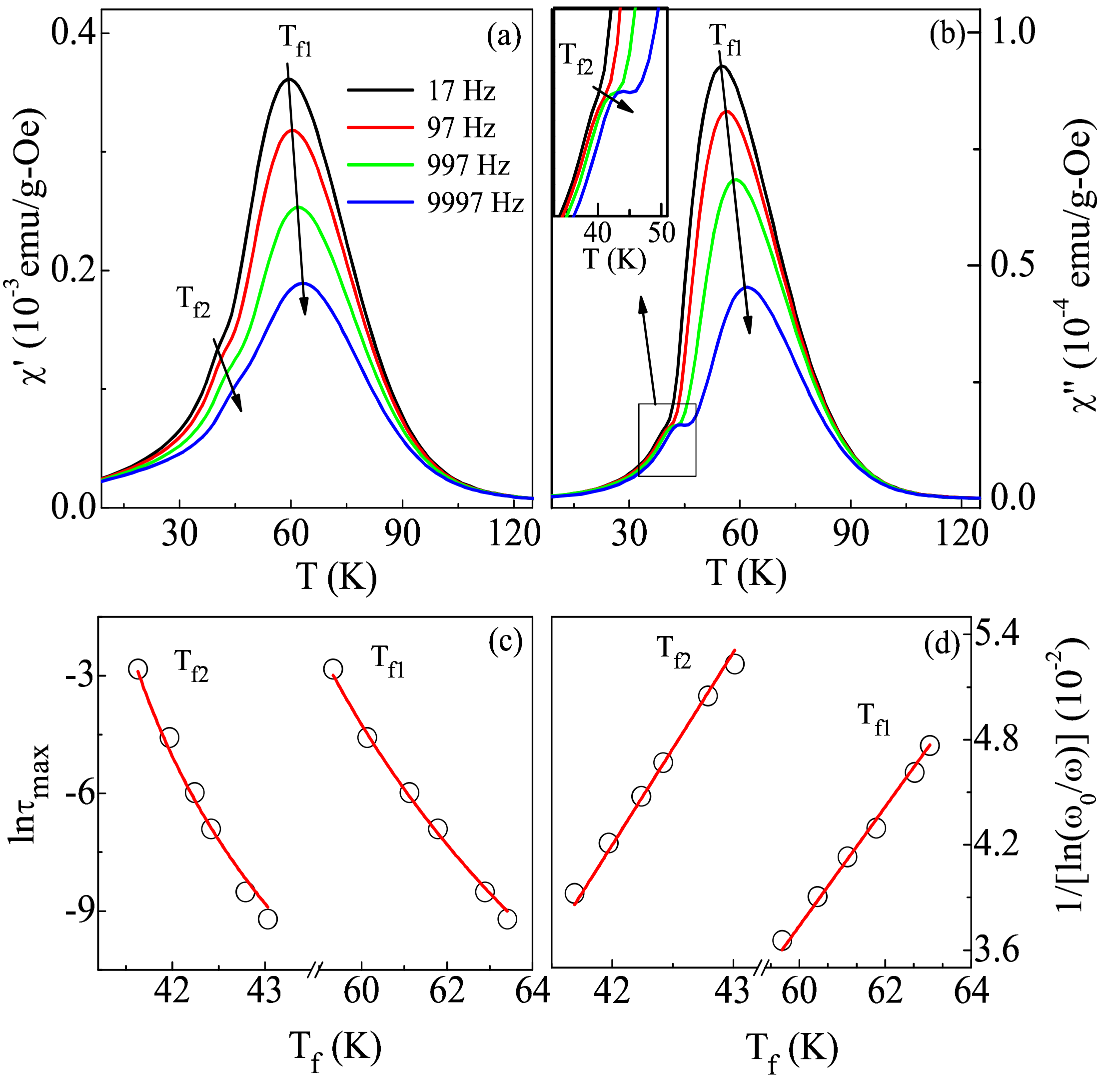

Figure 3.4: (a) Real (χ') and (b) imaginary (χ'') part of ac susceptibility measured at different frequencies with an applied ac magnetic field of magnitude 10 Oe for $Ga_{1.25}Fe_{0.75}O_3$. Inset in (b) displays magnified view of low temperature peak in χ'' plot. Plot of ln$_{max}$ (c) and $1/\ln(\omega_0/\omega)$ (d) with dynamic spin freezing temperature where solid lines represents the best fit with Eq. 3.2 and Eq. 3.3, respectively.

where $z\nu$ is the critical exponent of the correlation length, τ_0 is the shortest relaxation time and T_s is the spin glass transition temperature determined by the interactions in the system. Fitting of frequency dependent variations of T_{f1} and T_{f2} using the critical slowing down model is shown in Figure 3.4 (c). The best fitting yields $T_s = 54$ K, $z\nu = 9.1 \pm 0.7$, $\tau_0 \sim 10^{-12}$ s for T_{f1} and $T_s = 39$ K, $z\nu = 6.8 \pm 0.5$, $\tau_0 \sim 10^{-13}$ s for T_{f2}. These values are well with in the range of typical spin glass system, eg. for $z\nu \sim 5$ -10 and $\tau_0 \sim 10^{-10}$ -

10^{-13}s [105–107,113,114], confirming the spin glass nature for $x = 0.75$ composition. These parameters are, however, not sufficient to differentiate between different types of spin-glass freezing *viz* canonical spin glass, where a true equilibrium phase transition occurs at a fixed temperature and cluster glass, in which magnetic (ferro/antiferro) inhomogeneous clusters exists with non-equilibrium freezing [115]. For such differentiation Vogel-Fulcher (V-F) law [50] can be used which presumes correlations between spin clusters as follows,

$$\omega = \omega_0 exp[\frac{-E_a}{k_B(T_f - T_0)}] \tag{3.3}$$

Here the activation energy E_a separating different metastable states are related to the characteristic frequency ω_0 while T_0 is the Vogel-Fulcher temperature, measuring inter-particle or intercluster interaction strength. Using relaxation time as calculated from critical power law, the Vogel-Fulcher law is fitted with the experimental data. Figure 3.4 (d) shows a linear fit between $1/\ln(\omega_0/\omega)$ and freezing temperatures $T_{f1}(T_{f2})$ plots and best fit yields $T_0 = 50$ K and $E_a \sim 5.5k_BT_s$ for T_{f1} and $T_0 = 39$ K and $E_a \sim 2.3k_BT_s$ for T_{f2}. E_a/k_BT_s is less than 3 for spin-glass-like systems and for cluster-glass-like systems it is quite large [106, 107, 116]. Our analysis hence suggests the existence of cluster-glass-like state below T_{f1} and a transition from cluster-glass-like state to spin-glass-like state below T_{f2}. This is also confirmed by Mydosh parameter, $K = \frac{\triangle T_f}{T_f \triangle(\log_{10}\omega)}$ [50], where the calculated value of K for T_{f1} and T_{f2} are 0.027 and 0.009, respectively. This lies within the expected range of 0.02 - 0.06 for cluster glass [50, 117] and between 0.005 - 0.01 for canonical spin glass systems [50, 116, 117].

This is a case similar to nano manganite $La_{0.7}Ca_{0.3}MnO_3$ [113] which exhibits cluster-glass-like state below Curie temperature (T_c) followed by a spin-glass-like behavior at low temperature ($<$ 40 K) where interruption of long range ferromagnetic double exchange interaction due to the reduction of grain size results in a ferromagnetic cluster-glass-like state below T_c. However, in $Ga_{1.25}Fe_{0.75}O_3$, Ga breaks long range magnetic correlation caused by inherent site disorder and results in cluster glass like state below T_{f1} [106] and this site disorder also introduces random ferromagnetic and antiferromagnetic interactions leading to additional freezing of individual spin below T_{f2}. [105, 106, 114, 118].

To further understand the nature of spin-glass-like behavior we performed ac susceptibil-

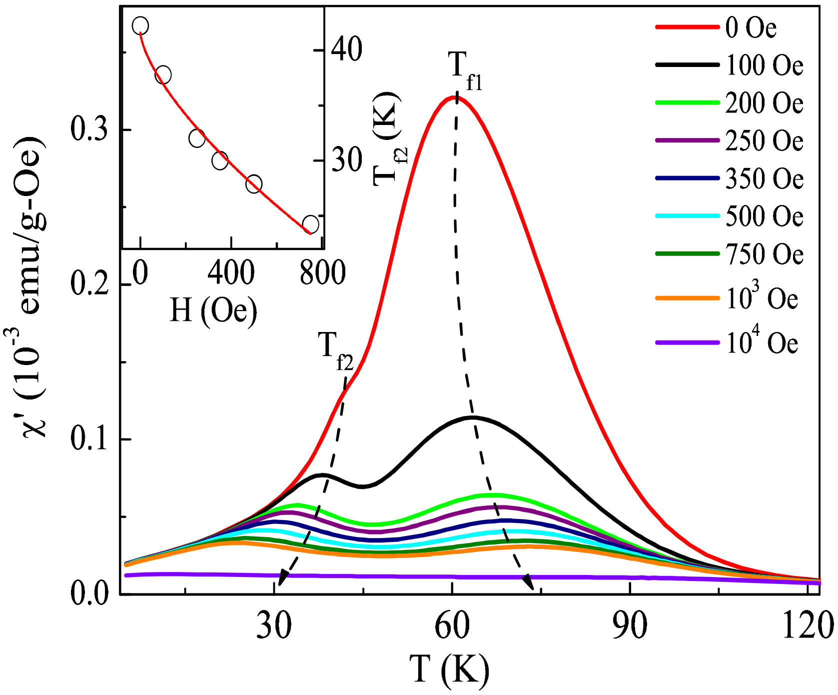

Figure 3.5: Temperature dependent ac susceptibility (χ') plotted at several applied dc fields with an ac magnetic field of magnitude 10 Oe and a driving frequency of 97 Hz for $x = 0.75$ composition. Inset shows field dependence of T_{f2} with solid line representing the best fit to the Eq. 3.4.

ity measurements with superimposed dc magnetic fields (H) as shown in Figure 3.5. With increasing dc field, T_{f1} was found to shift towards higher temperature whereas T_{f2} shifted towards lower temperature, corroborating cluster-glass-like behavior below T_{f1} and classical spin-glass-like behavior. [104] Field-dependent variation of T_{f2} can be qualitatively described by the following expression

$$T_f(H) = T(0)[1 - (\frac{H}{H_0})^n] \tag{3.4}$$

where the exponent n defines the nature of spin glass system. For $n = \frac{2}{3}$, Eq. 3.4 represents the well known de Almeida-Thouless (AT) line corresponding to anisotropic Ising spin glass system, [105] while for $n = 2$, Eq. 3.4 is known as Gabay-Thouless (GT) line representing typical Heisenberg spin glass system having weak magnetic anisotropy. [105] As depicted in inset of Figure 3.5, T_{f2}(H) fits well with the above equation with the best fitting parameters being T(0) = 40 K, H_0 = 2810 Oe and n = 0.67, suggesting Ising nature of the spin glass below T_{f2}.

Apart from x = 0.75 sample, detailed investigations were also carried out on other members of the Ga$_{2-x}$Fe$_x$O$_3$ series *viz* x = 1 and 1.25. Figure 3.6 (a) and (b) represent

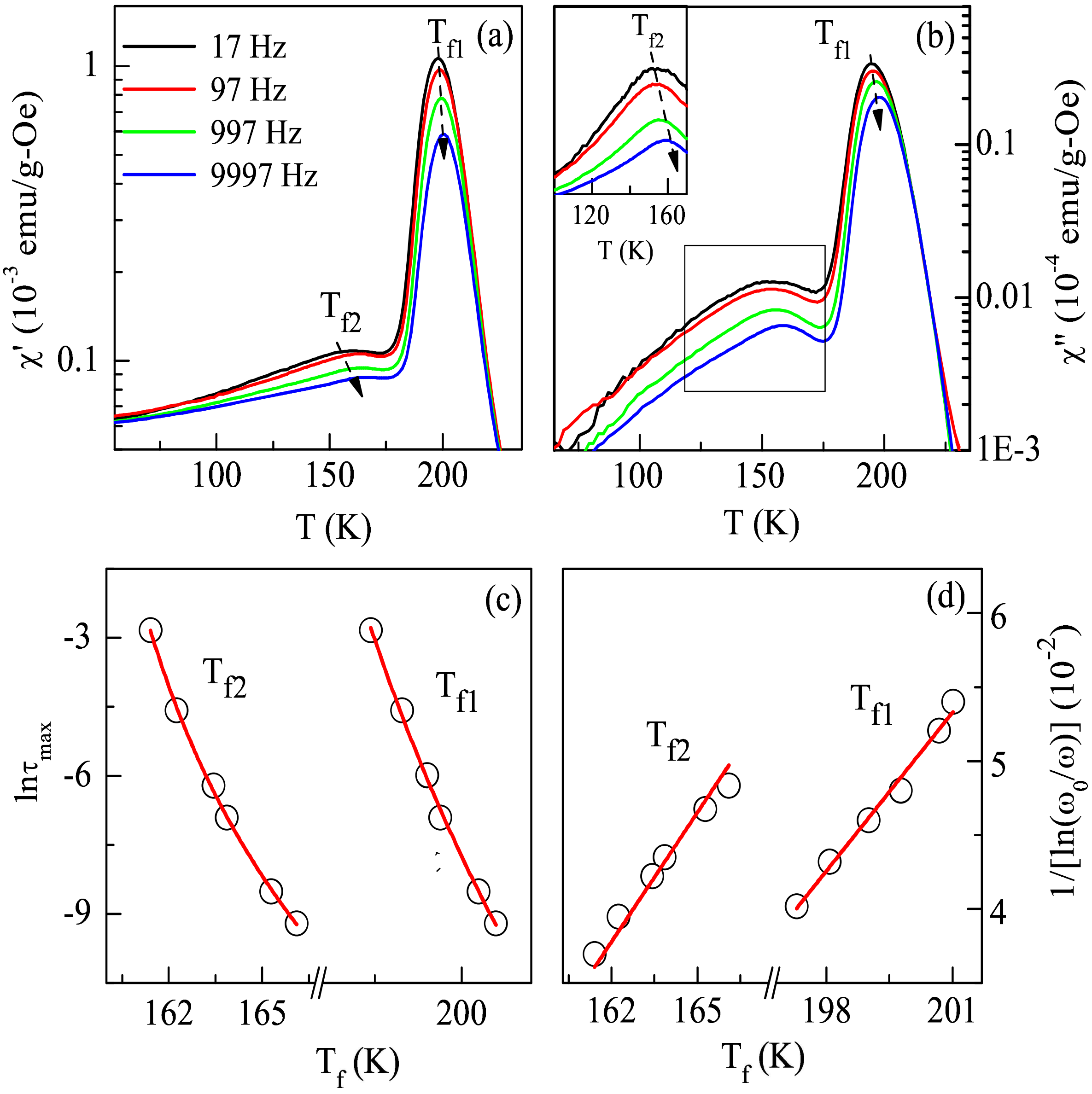

Figure 3.6: (a) Real (χ') and (b) imaginary (χ'') part of ac susceptibility measured at different frequencies with an applied ac magnetic field of magnitude 10 Oe for Ga$_{1.25}$Fe$_{0.75}$O$_3$. Inset in (b) displays magnified view of low temperature peak in χ'' plot. Plot of ln$_{max}$ (c) and $1/\ln(\omega_0/\omega)$ (d) with dynamic spin freezing temperature where solid lines represents the best fit with Eq. 3.2 and Eq. 3.3, respectively.

frequency dependent real (χ') and imaginary (χ'') part of ac susceptibility plots for $x = 1$ sample, respectively. Similar to the $x = 0.75$ case, here too, two frequency dependent peaks were observed but at different temperatures, $T_{f1} \sim 200$ K and $T_{f2} \sim 160$ K. Parameters obtained by fitting the frequency dependence with critical slowing down model ($z\nu = 5.4 \pm 1$ and $\tau_0 \sim 10^{-13}$ s, fitting shown in Figure 3.6 (c), V-F law ($E_a \sim 1.67$ $k_B T_s$, fitting shown in Figure 3.6 (d) and Mydosh parameter ($K = 0.006$) supports the idea of classical spin-glass-like behavior below T_{f2} as in the case of $x = 0.75$ sample and as suggested by Mukherjee *et. al.* [107]. However, unlike previous studies where no frequency or field dependence was observed for T_{f1}, due to coarser data points [107] or not

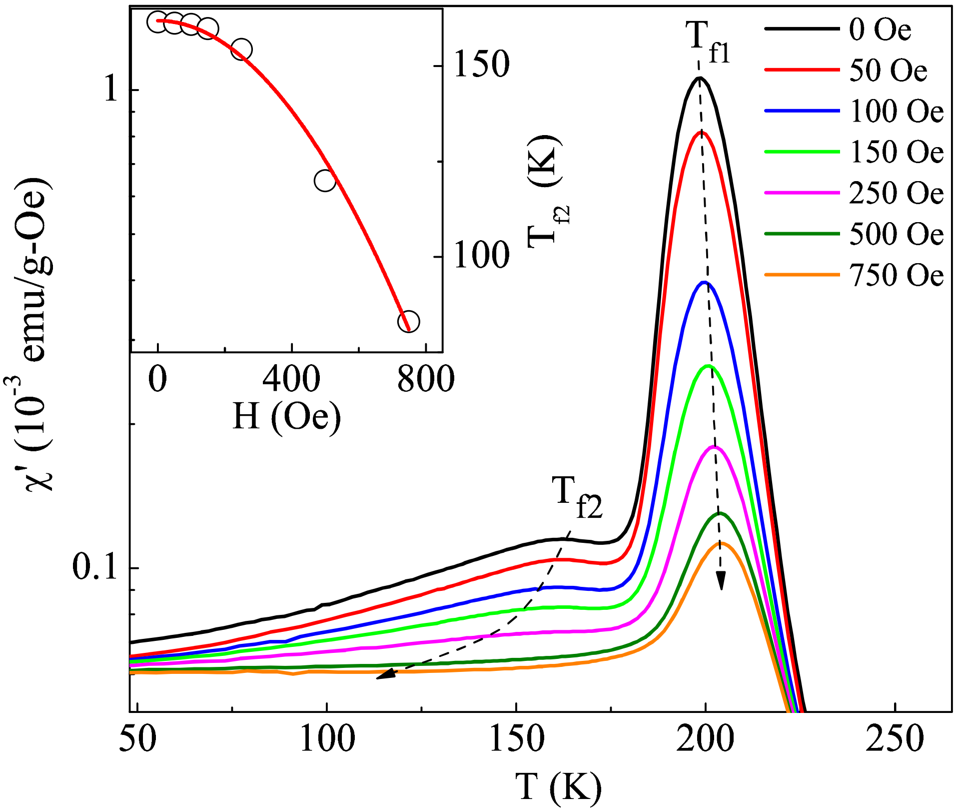

Figure 3.7: Temperature dependent ac susceptibility (χ') plotted at several applied dc fields with an ac magnetic field of magnitude 10 Oe and a driving frequency of 97 Hz for $x = 1.0$ composition. Inset shows field dependence of T_{f2} with solid line representing the best fit to the Eq. 3.4.

spanning larger frequency range [27], we clearly observe frequency dependent behavior for

T_{f1} peak. Extracted parameters after fitting the frequency dependence of T_{f1} with V-F law (Figure 3.6 (d)) and Mydosh law yields $E_a \sim 3.17\ k_BT_s$ and $K = 0.01$, respectively, which suggests a behavior that is at the boundary of spin-glass-like and cluster-glass-like states. However, fitting the data points with critical slowing down model (as shown in Figure 3.6 (c)), yields an unrealistic spin relaxation time $\tau_0 \sim 10^{-23}$ s, suggesting unconventional glassy phase below T_{f1} like in $Ca_3Co_{1.04}Mn_{0.96}O_6$ [72] and in perovskite manganite $Pr_{0.7}Ca_{0.3}MnO_3$ [119]. This arises possibly due to the progressive reduction of short range magnetic effects with increasing Fe concentration (x), resulting in increased magnetic homogeneity and long range ordering.

Furthermore, to understand the nature of spin-glass-like behavior below T_{f2} ac susceptibility measurements were performed by varying dc field (Figure 3.7). With increasing field T_{f2} peak was found to shift towards lower temperature (shown in inset of Figure 3.7) and its fitting with Eq. 3.4 gave best results for exponent $n = 1.9$, very close to $n = 2$, which corresponds to GT line, suggesting Heisenberg type spin glass state below T_{f2} in contrast to Ising type behavior obtained for $x = 0.75$ sample (as discussed above) and flux-grown $GaFeO_3$ single crystal [107]. This difference could arise due to the presence of considerable amount of magnetic anisotropy present in $x = 0.75$ and flux-grown $GaFeO_3$ single crystal samples [26, 27] where Fe ions are distributed mostly among octahedral Fe1, Fe2 and Ga2 sites having strong magnetic anisotropy and negligible amount of Fe is present in Ga1 site which are less anisotropic [26, 120]. Such decrease in magnetic anisotropy is also favored by decrease of coercivity with increasing of Fe content (x) in $Ga_{2-x}Fe_xO_3$ [26].

For x=1.25 sample we observe lack of frequency dependence in ac susceptibility for T_{f1} (as shown in Figure 3.8) in addition to a broad peak around $T_{f2} \sim 220$ K. T_{f2} shows inverse trend of peak shifting with frequency (shifting to low temperature with increasing frequency), which is unusual for conventional spin glass systems. Similar behavior has also been observed $Pr_{0.9}Ca_{0.1}MnO_3$ thin film , which has been ascribed to the presence of large distribution of ferromagnetic clusters within spin glass matrix [121]. Such unusual behavior has also been observed in $SrRuO_3$, rendering glassy behavior caused by possible existence of spin canting or antiferromagnetically coupled spins embedded in the ferromagnetic matrix [122] and in layered $NaNiO_2$ antiferromagnet, it has been explained by multi-relaxation rates due to the coalescence of magnetic clusters [123].

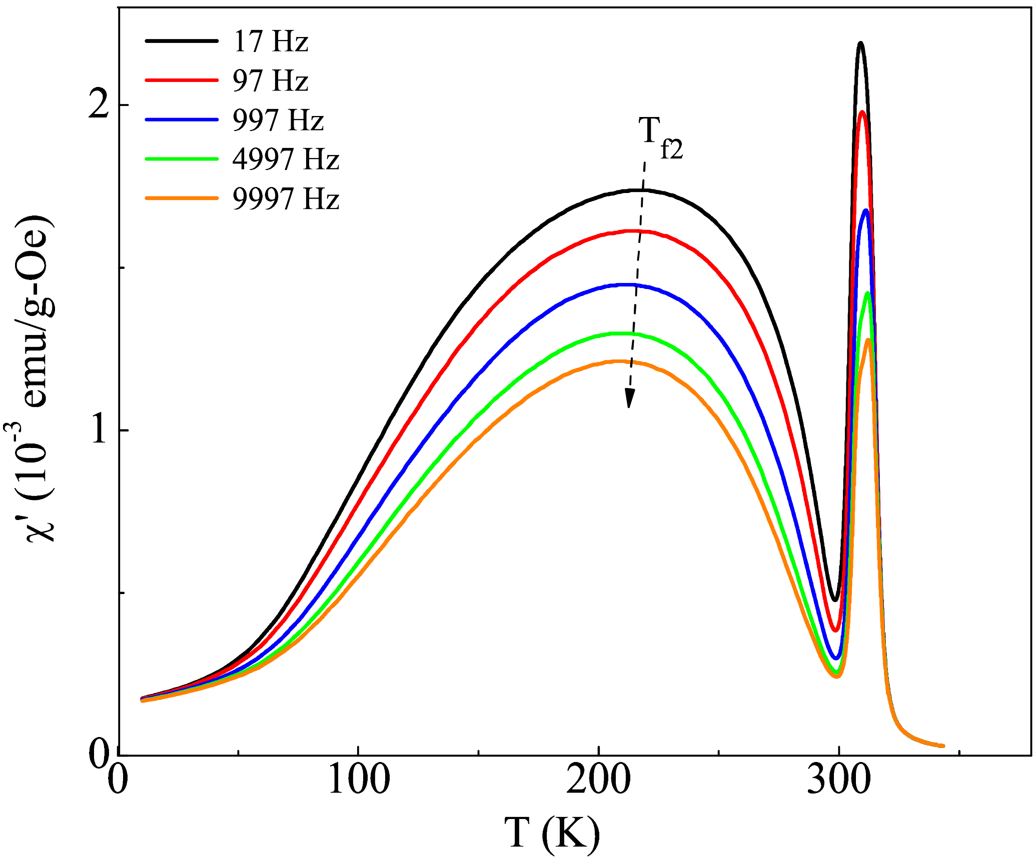

Figure 3.8: $\chi'(T)$ measured at several frequencies with an applied ac magnetic field of magnitude 10 Oe for $x = 1.25$ composition.

To have clear understanding we have carried out magnetic relaxation measurement at 50 K and also studied the influence of a temperature cycling on the relaxation behavior as shown in Figure 3.9. The experiments were done as follows, the sample was cooled down to 50 K in a constant magnetic field of 20 Oe. Then magnetization was recorded as a function of time immediately after removing the field. After a period of time t_1, the sample was quenched to 46 K (54 K for the temporary heating experiment) and magnetization was recorded for a period of time $t_2 = 3600$ s. Finally, the temperature was brought back to 50 K and magnetization was recorded for another interval of time t_3. It was observed that in case of negative temperature cycle, the starting value of the magnetization at t_3, was almost the same value observed at the end of the stage t_1. The

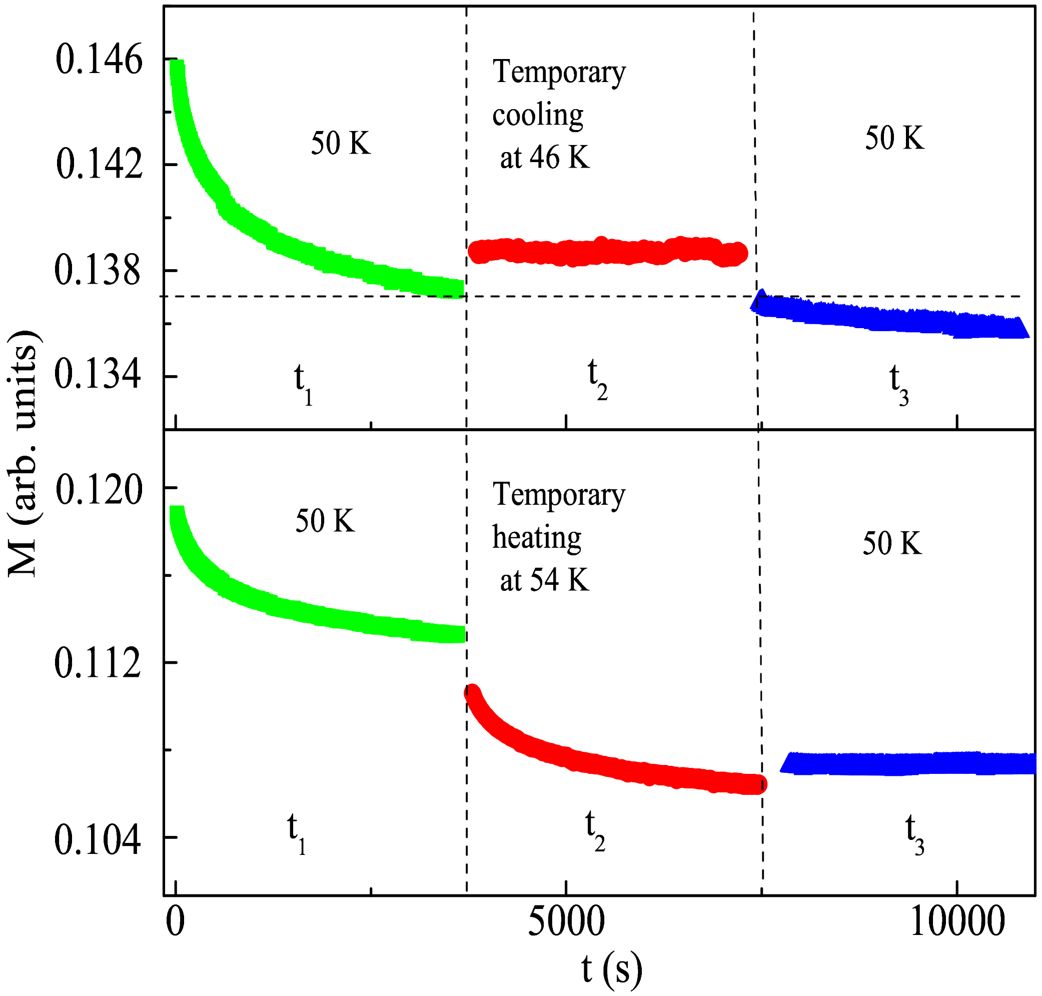

Figure 3.9: Magnetic relaxation data at 50 K obtained after FC (20 Oe) process, showing the effects of (b) temporary cooling the sample at 46 K for a time t_2= 3600 s, and (c) temporary heating at 54 K for a time, t_2=3600 s, without any magnetic field change during t_2.

observation of this memory effect is a clear signature of glass-like state in the system. However, in case of temporary heating cycle, the memory from previous aging was lost and at t_3, the relaxation started with an entirely different value from that of t_1 and t_2. Such an asymmetric response with respect to positive and negative temperature cycles can be explained by the hierarchical model where there exists multiple metastable states at a given temperature [124]. Similar behavior has been observed in $La_{0.7}Ca_{0.3}MnO_3$ nanomanganite, having two kinds of glassy regions, one ferromagnetic-like and the other spin-glass-like. [113] Here also we could say that the magnetic dynamics in $Ga_{0.75}Fe_{1.25}O_3$

is controlled by a ferrimagnetic part and a glassy magnetic part. This kind of scenario was proposed by Jonason *et al.* [113, 125] by fractural cluster glass model, which leads to the coexistence of many different time scales in the system and many length scales too. The presence of different time and length scales might be responsible for the broadening of the peak around T_{f2} and reverse trend of shifting of ac susceptibility peak with frequency.

To get further information, we have also performed long-time FC relaxation measurement

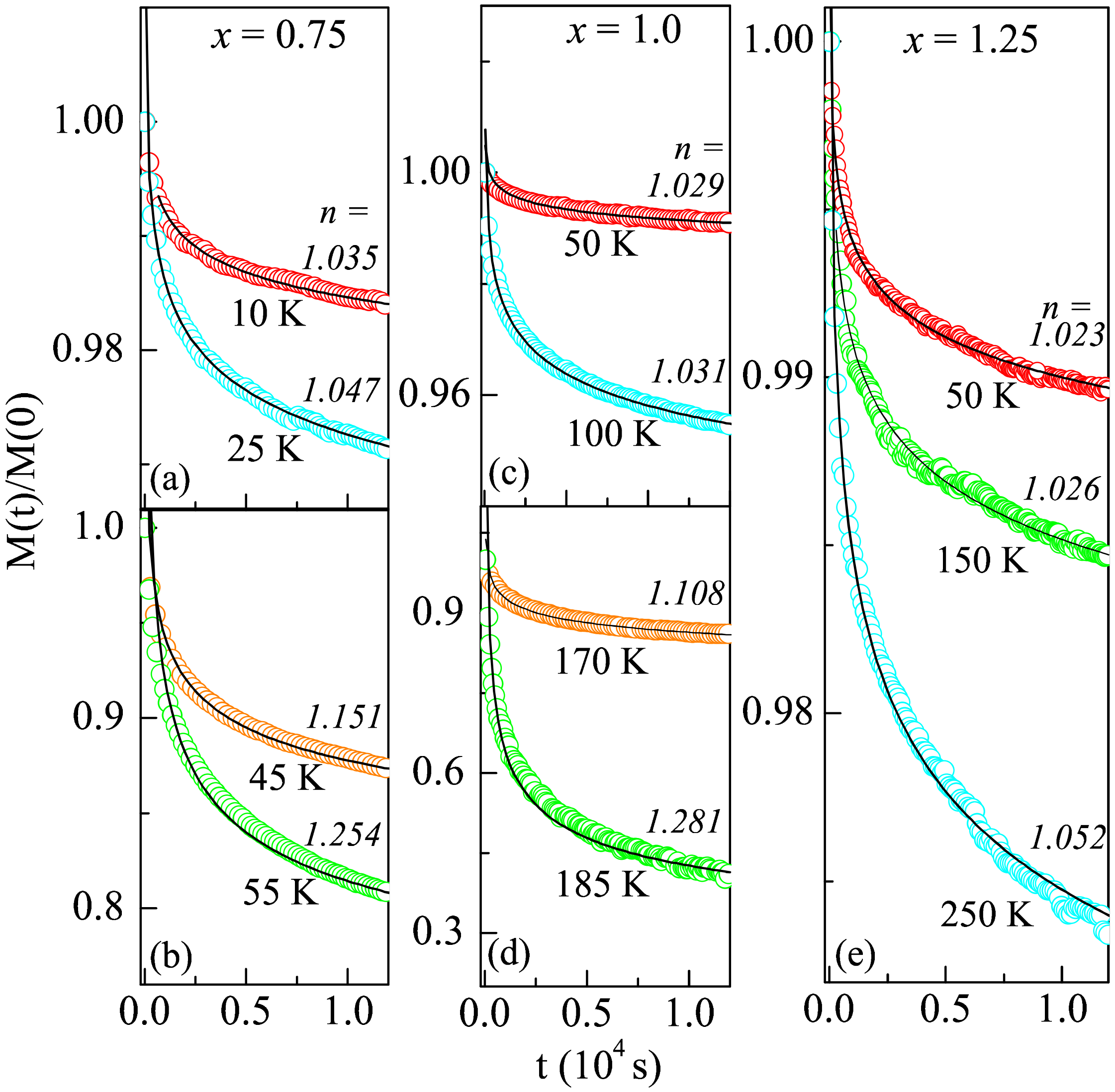

Figure 3.10: Normalized magnetic relaxation data ($M(t)/M(0)$) obtained after FC (50 Oe) process of $Ga_{2-x}Fe_xO_3$, for x = 0.75 (a) and (b), 1.0 (c) and (d) and 1.25 (e). The solid curves represent the fitted curves using Eq. 3.5.

at various temperatures for all compositions (Figure 3.10, where M is plotted in normalized form as $M(t)/M(0)$). The sample was cooled from well above T_c to the measurement temperature in a constant magnetic field of 50 Oe. Then magnetization was recorded as a function of time immediately after removing the field. Ulrich *et al.* [126] proposed a model for interacting magnetic particles and demonstrated that above some crossover time t_0, the relaxation rate, $W(t) = d[lnM(t)]/dt$, decays by a power law, $W(t) = At^n$, where exponent n depends on the concentration and hence on the strength of magnetic interaction and A is a temperature dependent prefactor. For $n > 1$ (high density), the magnetization can be written as [113, 126]

$$\frac{M(t)}{M(t_0)} = e^{-C_n}[1 + C_n(\frac{t}{t_0})^{1-n}], \tag{3.5}$$

with $C_n = A{t_0}^{1-n}/|1-n|$. The best fitting of relaxation curves with Eq. 3.5 (solid line), suggest spin glass effects in a dense cooperative systems. It is observed that the compounds with $x = 0.75$ and 1 ,show an increase of n with increase of temperature below T_{f1}, corroborating cluster-glass-like behavior as inter-cluster interaction gradually increases with increase of temperature [127]. In contrast, n is found to be independent of temperature below T_{f1}, favoring spin-glass-like state as discussed earlier [127]. The system with $x = 1.25$ also show relaxation behavior not only below T_{f1}, but also above T_{f1}, evidencing existence of glassy matrix beyond T_{f1} like in $La_{0.7}Ca_{0.3}MnO_3$ nanomanganite [113].

3.1.4 Conclusion

Systematic investigation of $Ga_{2-x}Fe_xO_3$ suggests a gradual evolution of glassy behavior with composition. By varying the Fe content (x), we could tune magnetism by controlling the number of antiferromagnetic and ferromagnetic bonds and their relative abundance which also results into gradual evolution from cluster-glass-like state just below T_c for x=0.75 to strongly interacting magnetic domains for x=1.0 composition and with no sign of spin glass behavior. Furthermore, spin-glass-like state is observed for all the compositions at lower temperatures and there is an evolution of spin dynamics from anisotropic Ising type character (for $x = 0.75$) to isotropic Heisenberg type behavior for higher Fe compositions, hence can hence serve as an ideal system for modeling spin glasses wherein by just tuning the Fe content in turns the inherent site disorder driven magnetic inhomogeneity, competing ferromagnetic and AFM interactions along with spin frustration can be tuned to give rise to transition from one glassy state to other.

3.2 Defect induced polarization and dielectric relaxation

3.2.1 Introduction

Mutiferroics have gained considerable attention because of their scientific interest and potential for technological applications in magnetic sensors, multi-state memories and many more [128]. Most of the multiferroics have ferroelectric transition either at very low temperature or very high temperature. However, for practical applications, it is of prime importance to establish such properties in the vicinity of room temperature.

$GaFeO_3$ is expected to be room temperature ferroelectric because of the non-centrosymmetric $Pc2_1n$ crystal symmetry up to very high temperature (1368 K) [129] and is believed to have very large polarization caused by the inherent site disorder as calculated theoretically [34, 130]. Several groups have studied polarization vs electric field (P-E) response in $GaFeO_3$, mostly using thin-films and found very small coercieve field (E_c) and remnant polarization (P_r), inconsistent with the theoretical calculations [29, 112, 131]. Mukherji *et al.* argued the presence of room temperature nanoscale ferroelectricity from their observation of a 180^0 phase shift in the piezoresponse [28]. However, this phase shift does not necessarily indicate ferroelectric (FE) behavior. On the contrary, Song *et al.* [30] achieved very large E_c and P_r in the thin film grown on hexagonal strontium titanate (STO) or cubic yttrium-stabilized zirconia (YSZ) substrate and applying very high bias electric field , which is in good agreement with ab-initio calculations [34, 130] . However, presence of ferroelectricity in bulk $GaFeO_3$ is rather inconclusive due to leaky behavior of the sample [132]. Saha *et al.* [133] studied FE property in bulk $GaFeO_3$ by pyroelectric measurements and showed the emergence of polarization below magnetic transition. They claimed from symmetry analysis that non-centrosymmetric magnetic ordering coupled with inherent site-disorder below T_C drives ferroelectricity in $GaFeO_3$. Note, pyroelectric measurements showing spontaneous polarization does not necessarily indicate intrinsic FE behavior, pyrocurrent (polarization) can also arise from dipole reorientation and release of charges from localized states as observed in $Y_3Fe_5O_{12}$ [86], $YFe_{0.8}Mn_{0.2}O_3$ [134] and various manganites [135–137] etc. Therefore, it is essential to explore the differences of pyroelectric currents related to FE phase transition and that induced by dipole reorientation or the release of charges from localized states i.e. thermally stimulated depolarization current (TSDC) effect.

In this study, we discuss in detail pyroelectric measurements in solid solutions of $Ga_{2-x}Fe_xO_3$ (x = 0.75, 1.0 and 1.25) to elucidate the origin of ferroelectric polarization. Our results indicate that induced polarization is associated with TSDC effect rather than the true FE behavior. We have also discussed dielectric relaxations behavior of these systems and their correlations with TSDC effect.

3.2.2 Experimental details

Temperature dependent dielectric measurements were performed using an impedance analyser 4291A in the frequency range of 1 kHz-1 MHz, under a dc bias voltage of 1 V. The pyroelectric current (I) was measured using a Keithley 6517A electrometer and was recorded during the heating process after the sample was cooled down under a poling field (E_p = ± 61.1 kV/cm) from high temperature and was shortcircuited for long time to remove any residual charges. Spontaneous electric polarization was obtained by integrating the current with respect to time.

3.2.3 Results and discussion

3.2.3.1 Dielectric studies

Figure 3.11 (a-c) and (d-f) depict temperature dependence of the dielectric permitivity ($\varepsilon'(T)$) and corresponding loss (D) of $Ga_{2-x}Fe_xO_3$ (x = 0.75, 1.0 and 1.25) at different frequencies ranging from 1 kHz to 1 MHz, respectively. $\varepsilon'(T)$ shows frequency dependent dielectric relaxations for all the compounds. A large variation in ε' with respect to frequency near room temperature and very high value of D (> 1) indicate the extrinsic

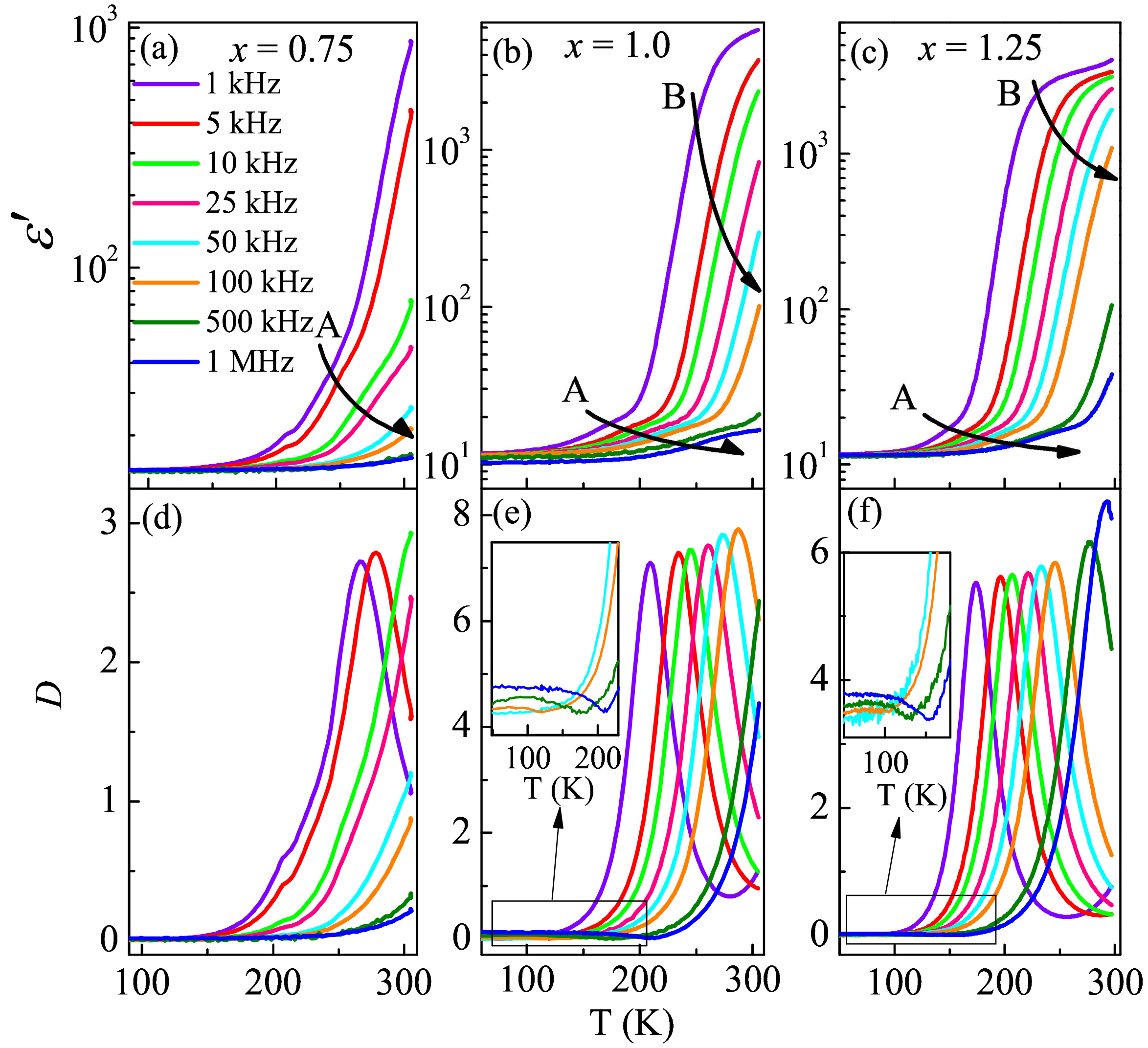

Figure 3.11: (a), (b) and (c) Temperature dependent dielectric permitivity ($\epsilon'(T)$) measured at several frequencies of $Ga_{2-x}Fe_xO_3$, for $x = 0.75$ (a), 1.0 (b) and 1.25 (c). Corresponding dielectric loss (D = tanδ) are shown in (c), (d) and (f), respectively. Insets in (e) and (f) represent enlarged view of D at low temperature region for x = 1.0 and 1.25 compositions, respectively.

source of dielectric relaxations, known as Maxwell-Wagner type relaxation. Generally, it originates from the presence of accumulated charge carriers between regions in the sample that have different conductivities such as near the grain boundaries. Furthermore, two dielectric relaxations, A and B, are clearly visible in $\varepsilon'(T)$, for $x = 1.0$ and 1.25 compositions, where as a single peak is observed for x = 0.75 compound in the limited measurement window. Such an observation suggests a combined relaxation mechanism associated with dominating low frequency Maxwell-Wagner type relaxation through the interfaces i.e. grain boundaries, as described above and low frequency Debye type relaxation through the bulk (grains) arising from polaron hopping process originating from the asymmetric hopping of charge carriers in the presence of an electric field. Such type of combined relaxation observed in various systems such as $YFe_{0.8}Mn_{0.2}O_3$ [134], La_2NiMnO_6 [138] $BiFeO_3$ [139], $LaCoO_3$ [140] and $Nd_{0.22}Sr_{1.78}MnO_4$ [141]. Recently, Singh *et. al.* [142] also

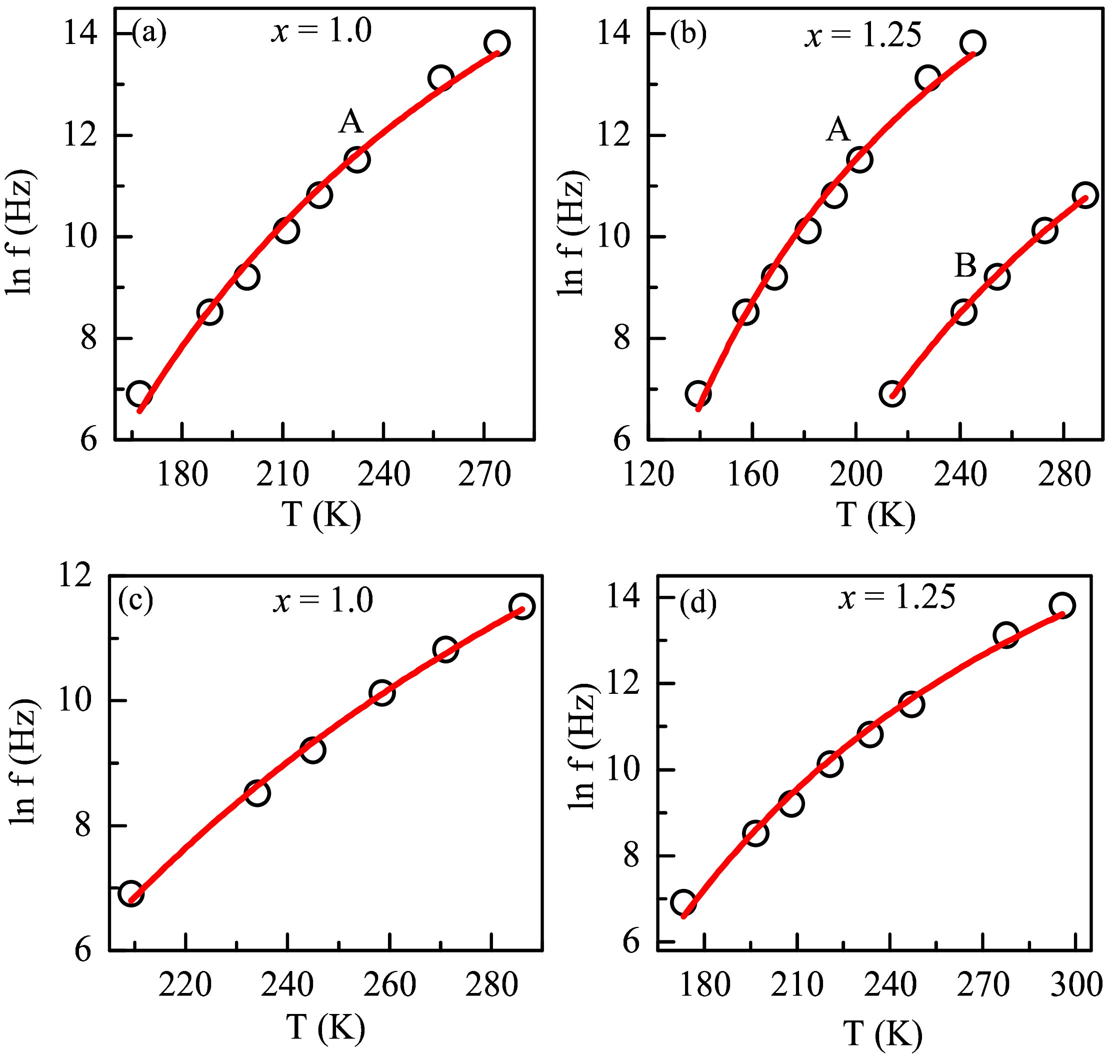

Figure 3.12: Plot of ln f vs. peak temperature (T) obtained from the relaxations A and B from $\varepsilon'(T)$, with solid line representing the best fit with the Arrhenius law of $Ga_{2-x}Fe_xO_3$, for (a) $x = 1.0$ and (b) $x = 1.25$. (c) and (d) represent the same obtained from the peak of D for $x = 1.0$ and 1.25 compositions, respectively.

Table 3.3: Various physical parameters obtained from the fitting of frequency dependence of peak temperature of $\varepsilon'(T)$ and $D(T)$ with the Arrhenius law for $Ga_{2-x}Fe_xO_3$ ($x = 1.0$ and 1.25).

	Compositions (x)		1.0	1.25
Dielectric permitivity (ε')	Relaxation A	E_a (eV)	0.24±0.006	0.20±0.007
		τ_0 (s)	7.8×10^{-11}	6.6×10^{-11}
	Relaxation B	E_a (eV)		0.28±0.006
		τ_0 (s)		2.7×10^{-10}
Dielectric loss (D)		E_a (eV)	0.31±0.01	0.25±0.009
		τ_0 (s)	3.1×10^{-11}	1.1×10^{-10}

observed two dielectric relaxations behavior in polycrystalline $GaFeO_3$ at high temperatures, consistent with our results. As the dielectric relaxations are thermally activated process, can be analyzed using Arrhenius law, as given by,

$$f = f_0 exp[\frac{-E_a}{k_B T_m}], \tag{3.6}$$

where f_0 is the characteristic frequency, T_m is the peak temperature of dielectric loss curve, k_B is the Boltzmann constant and E_a is the activation energy of relaxation. The peak positions are extracted by differentiating the $\varepsilon'(T)$. Both the relaxations A and B are fitted well with the Arrhenius behavior. We could fit only relaxation A for $x = 1.0$ composition due to the limitation of the measured temperature range and both relaxations A and B for $x = 1.25$ composition, as shown in Figure 3.12 (a) and (b), respectively. The best fitted parameters obtained from the fitting with the Arrhenius law are listed in Table 3.3 and are comparable with the recent report in polycrystalline $GaFeO_3$ [142]. The presence of a strong and broad dielectric relaxation peak in the corresponding dielectric loss ($D = \tan\delta$) (Figure 3.11 (d-f)) suggests joint effect of relaxations of grains and grain boundaries as like observed in $DyMnO_3$ [143]. The fitting of loss data with the Arrhenius law (solid line) for $x = 1.0$ and 1.25 compounds are shown in Figure 3.12 (c) and (d), respectively. The best fitted parameters are listed in Table 3.3 and are comparable with the parameters that obtained from $\varepsilon'(T)$. The activation energy obtained signifies electron transfer or hopping between Fe^{2+} and Fe^{3+} ion [66, 86, 139, 144], another possibility could be the relaxation due to the short range movement of charged oxygen vacancies, which are generally formed during high temperature synthesis process as seen in various systems [145, 146] as per Kroger-Vink notation, [147] given by the following reactions:

$$O_o \rightarrow V_o^{\times} + \tfrac{1}{2}O_2\uparrow$$

$$V_o^{\times} \rightarrow V_o^{\bullet} + e'$$

$$V_o^{\bullet} \rightarrow V_o^{\bullet\bullet} + e'$$

In addition, there exists a weak high frequency relaxation at low temperature as clearly seen in x =1.0 and 1.25 compositions (insets of Figure 3.11 (e) and (f)) is likely to be related to the bulk relaxation. Such multilple relaxations has been observed in various systems such as Pb-doped $LaFeO_3$ [148], $BiFeO_3$ [139], $LaCoO_3$ [140] and $Nd_{0.22}Sr_{1.78}MnO_4$ [141]. Observation of double bulk relaxations in present systems is possibly due to the presence of intragrain electric inhomoginities similar to that of Pb-doped $LaFeO_3$ [148].

3.2.3.2 Pyroelectric studies

We discuss polarization properties of $Ga_{2-x}Fe_xO_3$ in this section. Pyroelectric current measurements were performed at various poling temperatures (T_p) and also with different heating rates keeping fixed poling field (E_p) and T_p. Due to the high leakage current pyroelectric measurement on x =1.25 composition could not be performed. Figure 3.13 (a) depicts temperature dependence of pyroelectric current and polarization measurements for $GaFeO_3$ under a E_p of 1.1 kV/cm and T_p of 90 K, in which polarization starts to emerge below 120 K and it is switchable under reversed E_p. Our results are in agreement with earlier study reported by Saha *et al.* [133]. They argued from symmetry analysis that polarization induced is not switchable if it is caused by the inversion symmetry breaking due to anti-site disorder only. Moreover, polarization obtained from structural distortions associated with non-centrosymmetric magnetic ordering coupled with inherent site-disorder can be switchable in this system. We also present results for $x = 0.75$ compound in Figure

3.13 (b) for a T_p of 150 K. It has to be noted that for $x = 0.75$ composition, polarization emerges well above T_c, suggesting that it can not be driven by magnetic ordering as proposed by Saha *et al.* for $GaFeO_3$ [133]. However, it is needed to confirm whether it is true ferroelectric or not. The observed phenomena could be a thermally stimulated process, which mainly originates from the thermal release of trapped-charges and gives rise to current peak upon heating [149]. The correlation between TSDC and polarization is clearly seen in Figure 3.13 (c) and (d), which show an increase of transition temperature and polarization with increase of poling temperature.

Further analysis was performed to understand the TSDC effect. The TSDC measurement is a major probe to study the dielectric relaxation dynamics and is used to obtain the relaxation parameters. In the Bucci-Fieschi-Guidi framework, which assumes that a system has a single relaxation time ($\tau(T)$) and the decay rate of Polarization (P) that means pyroelectric current (I) is proportional to P, as described by following equation,

$$\frac{dP}{dt} = \frac{-P}{\tau(T)}, \tag{3.7}$$

Adopting it as a thermally activated process governed by Arrhenius law, which leads to a correlation between pyroelectric current, polarization, relaxation time and activation energy described by the following relation, [86]

$$ln\frac{P(T)}{I(T)} = \frac{E}{k_BT} + ln\tau_0, \tag{3.8}$$

where T is the temperature, E is the activation energy and τ_0 is the shortest relaxation time. Plot of $\log(P/I)$ vs the inverse temperature ($1/T$) along with its fitting with Eq. 3.8 for $x = 1.0$ and 0.75 compositions are shown in Figure 3.14 (a) and (b), respectively. The best fitting parameter obtained are $E = 0.08 \pm 0.0002$ eV and $\tau_0 = 7.01 \times 10^{-5}$ s for $x = 1.0$ compound and those for $x = 0.75$ composition these parameters are 0.11 ± 0.0002 eV and 6.11×10^{-6} s, respectively.

The dependency of pyroelectric peak temperature (T_m) on heating rate ($b = dT/dt$) for

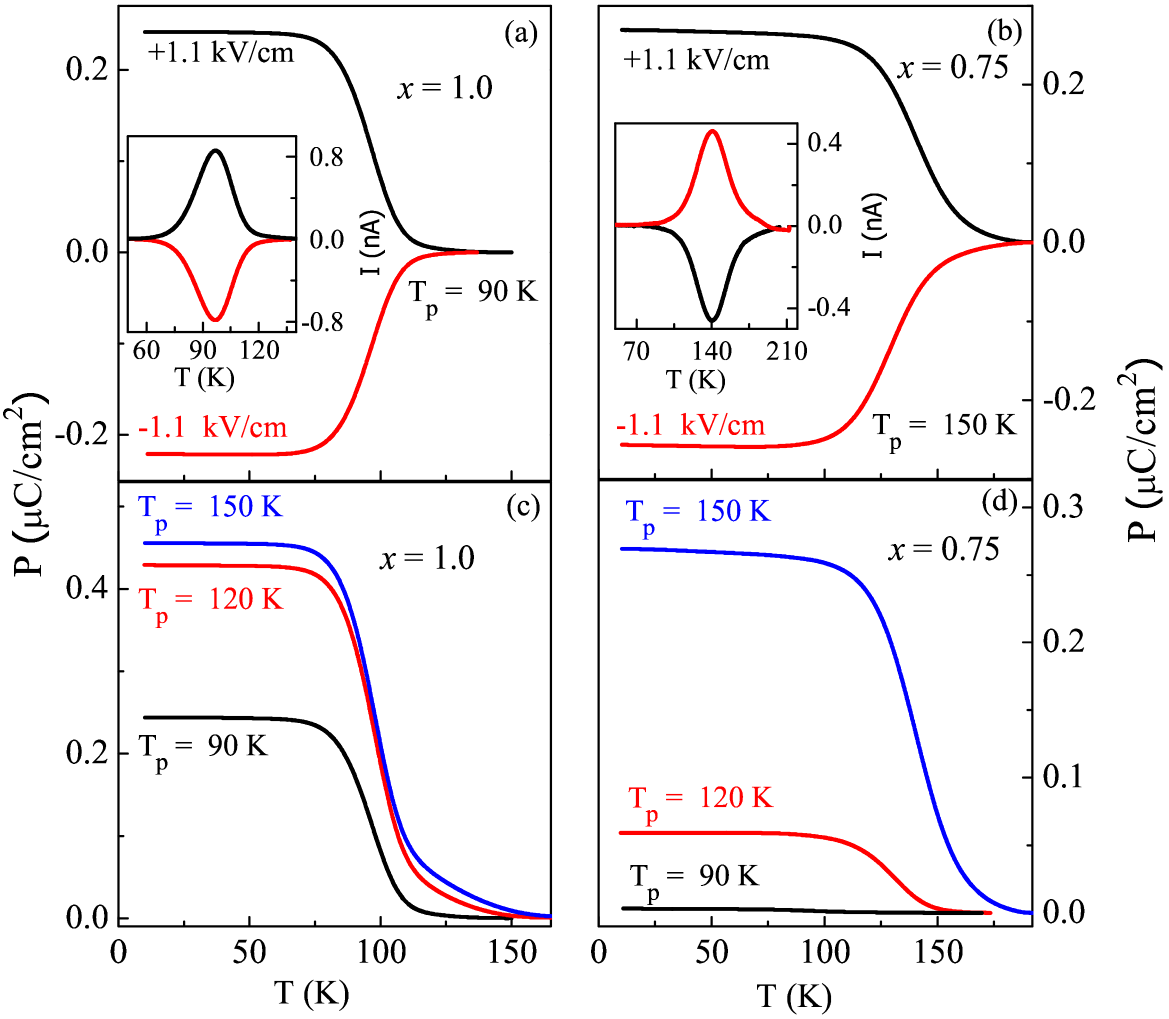

Figure 3.13: Temperature dependent polarization of $Ga_{2-x}Fe_xO_3$, for $x = 1.0$ (a) and 0.75 (b). Corresponding pyroelectric current peaks are shown in the insets. Temperature dependent polarization at different poling temperatures of $Ga_{2-x}Fe_xO_3$, for $x = 1.0$ (c) and 0.75 (d).

TSDC process is governed by the following equation, [86]

$$ln\frac{T_m^2}{b} = \frac{E}{k_B T_m} + ln\frac{\tau_0 E}{k_B} \tag{3.9}$$

It is expected that T_m shifts to high temperature with increasing heating rates as per Eq. 3.9 and it is also observed for the present systems as shown in Figure 3.14 (c) and (d). This confirms TSDC nature of the pyroelectric current instead of intrinsic FE behavior

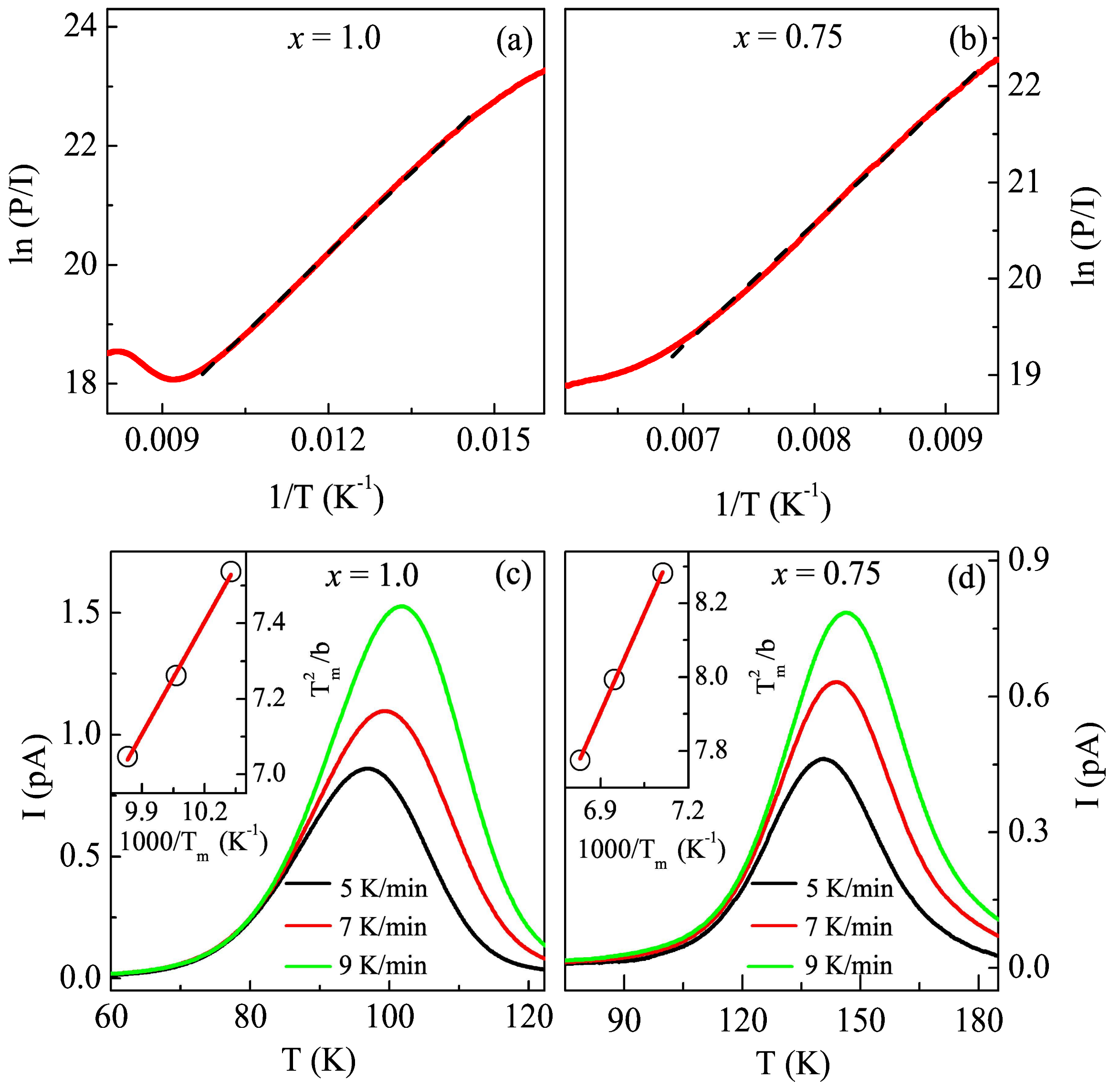

Figure 3.14: Plot of $\ln(P/I)$ vs. inverse of temperature, with dashed line representing the best fit with Eq. 3.8 of $Ga_{2-x}Fe_xO_3$, for $x = 1.0$ (a) and 0.75 (b). Variation of pyroelectric peak with heating rate of $Ga_{2-x}Fe_xO_3$, for $x = 1.0$ (c) and 1.25 (d). Corresponding insets represent fitting with Eq. 3.9, which describes relation between pyroelectric peak temperature (T_m) and heating rate (b).

where no such temperature dependence is expected [135]. Insets of Figure 3.14 (c) and (d) show the fitting of heating rate dependence of T_m with Eq. 3.9. The best fitting gives $E = 0.08 \pm 0.005$ eV and 0.15 ± 0.003 eV for $x = 1.0$ and 0.75 compounds, respectively. The obtained activation energy from TSDC effect is less than that obtained from the dielectric relaxation A, as described above. However, it is of the same order to the activation energy obtained from the dipolar relaxation in single crystal of $GaFeO_3$ [145]. We also observed a weak high frequency bulk relaxation at low temperature dielectric loss data (insets of Figure 3.11 (c) and (d)), which is probably associated with the TSDC effect. Such low activation energy signifies an interplay between lattice and polaronic defects associated with charged oxygen vacancies [145]. The electrons associated with this charged oxygen vacancy are localized and could only hop to neighboring sites and results in reorientation of defect dipoles. With decrease of temperature the freezing of these defect dipoles gives rise to electric polarization. Two bulk relaxations are observed in polycrystalline sample in contrast to single bulk relaxation in single crystal of $GaFeO_3$ [145]. This difference may be possibly due to the presence of Fe divalent (Fe^{2+}) state in polycrystalline $GaFeO_3$ [142], where as there is no Fe^{2+} state in single crystal as confirmed by Mossbauer study [145].

3.2.4 Conclusion

In summary, the detailed dielectric studies show multiple relaxation process. The high frequency relaxations are associated with the Debye type relaxation through the grains/bulk and low frequency relaxation is due to the extrinsic Maxwell-wagner type mechanism at the grain boundaries. Further, pyroelectric study confirmed that emergence of polarization in bulk $Ga_{2-x}Fe_xO_3$ can be understood in terms of TSDC effect rather than the intrinsic ferroelectric behavior. It is seen that TSDC effect is correlated with the dielectric relaxation caused by freezing of defect induced dipoles possibly associated with charged oxygen vacancies.

Chapter 4

Investigating magnetism and origin of ferroelectricity in $GdCrO_3$

This chapter is divided into two parts. In the first part we will discuss detailed mechanism giving rise to ferroelectricity in $GdCrO_3$*. Temperature dependent synchrotron powder x-ray diffraction studies along with first-principles density functional theory calculations revealed preferred symmetry of* $GdCrO_3$ *is non-centrosymmetric* $Pna2_1$ *rather than centrosymmetric Pbnm, supporting polar nature of the system. Polar distortion is driven by Gd off-centering with respect to the oxygen cage. An intimate analogy between* $GdCrO_3$ *and* $YCrO_3$ *systems is also revealed, even though a distinctive difference exists between these that Gd is less displacive compared to Y. It is also found that magnetic coupling between Gd-4f and Cr-3d plays an important role in ferroelectric distortion. EXAFS study also infers the significant role of Gd-O bond polarization for emergence of ferroelectricity in* $GdCrO_3$*. In the second part, we will discuss complex magnetic properties and spin-phonon coupling in the material as it shows a wide spectrum of interesting magnetic features, such as temperature induced magnetization reversal (TMR), spin flipping (SF) and spin reorientation (SR) etc, which arises from symmetric* ($S_i \,.\, S_j$) *and antisymmetric* ($S_i \times S_j$) *exchange interactions within and between Cr and Gd-sublattices.*

4.1 Understanding the origin of ferroelectricity

4.1.1 Introduction

Various mechanisms drive ferroelectricity in different class of materials, as have been discussed in chapter 1. There are diverging opinions about the existence and/or origin of ferroelectricity in rare-earth orthochromites (RCrO$_3$). Most of the members of RCrO$_3$ family have been predicted to be biferroic with a reasonably high ferroelectric (FE) transition temperature (above magnetic transition temperature), caused by polar movement of R-ions associated with phonon instability at zone-centre similar to other perovskite ferroelectrics like PbTiO$_3$ [78, 150–152]. Ramesha *et al.* [153] reported from neutron pair distribution function (PDF) analysis that, YCrO$_3$ possess a locally non-centrosymmetric monoclinic structure ($P2_1$) via Cr off-centering in the ferroelectric state though the average crystal structure is centrosymmetric ($Pnma/Pbnm$) . The non-centrosymmetric structure was also supported from theoretical calculations, however this is associated with the polar Y displacements in a direction opposite to that of the oxygen cage and Cr atoms from ideal cubic structure [78, 150]. It suggests that local non-centrosymmetry could play an important role in understanding the ferroelectric properties in the family of RCrO$_3$ [154].

In addition to the structural distortion ideas where the magnetic coupling plays a minor role, several studies have reported that the multiferroicity in RCrO$_3$ is due to the strong interaction between magnetic R and weakly coupled ferromagnetic (canted) Cr ions below the magnetic-ordering temperature of Cr (T_N) along with a lower symmetry structure than $Pbnm$ [154, 155]. Also, Raman studies show anomalous change of phonon frequency and a decrease in phonon life times across the mutiferroic transition temperature, both in the modes involving CrO$_6$ octahedra and magnetic R-ion [156]. This argument implies that ferroelectricity in RCrO$_3$ is driven by magnetostriction mechanism caused by $3d$-$4f$ coupling, resulting in the displacement of the R-ion and the octahedral distortion via oxygen displacements, hence magnetic R-ion is required in order to stabilize a ferroelectric state in RCrO$_3$. Ghosh *et al.* [157, 158] observed some RCrO$_3$ (R = Sm and Ho) compounds exhibiting structural transformation from centrosymmetric $Pbnm$ to non-centrosymmetric $Pna2_1$ sub-group, resulting in ferroelectric behavior. In these systems magnetic coupling between R-ion and the matrix is not important in stabilizing a ferroelectric phase as it develops in the paramagnetic state. On the contrary, recently it is reported that $GdCrO_3$ can only be ferroelectric at very low temperature *via* magnetostriction effect and it is necessary to have Gd^{3+}-Cr^{3+} interaction along with G-type magnetic structure in both Gd and Cr-sublattices to break the inversion-symmetry which is driven by antipolar X-mode instability [159]. Considering all the contradicting possibilities, it is important to understand the microscopic origin and mechanism of ferroelectricity in $GdCrO_3$ at relatively high temperatures.

In this work, we have done detailed temperature dependent synchrotron powder x-ray diffraction studies along with first-principles density functional theory calculations to find the possible non-centrosymmetric structure of $GdCrO_3$. We have also investigated the possible polar phonon mode instability in the parent cubic structure as it plays a crucial role in understanding classic ferroelectrics. Additionally, we have systematically studied the changes in the local structures around Cr and Gd in $GdCrO_3$ and around Y in $YCrO_3$ by temperature dependent extended x-ray absorption fine structure (EXAFS) studies.

4.1.2 Experimental and theoretical details

Polycrystalline samples of $GdCrO_3$ ($YCrO_3$) were prepared by the solid-state synthesis technique at ambient pressures. Stoichiometric proportions of Gd_2O_3 (Y_2O_3) and Cr_2O_3 were mixed thoroughly and heated at 1300 ^{0}C for 24 h in air with several intermediate heating and grindings. The product was then pressed into pellets and finally sintered at 1400 ^{0}C for 24 h and cooled down to room temperature. Phase purity of the samples were confirmed by powder x-ray diffraction (XRD) measurements as performed in Bruker D8 Advance x-ray diffractometer using Cu K_α radiation. Temperature dependent XRD measurements in $GdCrO_3$ were performed at the XRD1 beamline at ELETTRA synchrotron radiation facility using photons of wavelength 0.85507 $\AA$. Reitveld refinements of the diffraction patterns were performed using the Fullprof package. Temperature dependent EXAFS measurements were done at P-65 beamline at PETRA-III synchrotron source, DESY, Hamburg, Germany. The incident (I_0) and transmitted (I_t) photon intensities were recorded at the Gd-$L3$ (7243 eV) and Cr-K (5989 eV) edges in $GdCrO_3$ and Y-K

(17038 eV) and Cr-K edges in $YCrO_3$. Extraction of structural parameters was carried out using standard procedures such as pre-processing of data, theoretical modeling with basic crystallographic information, and fitting of the R-space experimental data to theoretical EXAFS functions using various applets of the Demeter program [160].

Our theoretical calculations of the structural properties were based on density functional theory, using generalized gradient approximation (GGA) with Perdew Burke Ernzerhof for solids (PBEsol) [97] parameterization for the exchange correlation potential, the projector argumented wave (PAW) method [95], and a plane-wave basis set, as implemented in the Vienna ab-initio simulation package (VASP) [100]. The interaction between ions and electrons was approximated with PAW potentials, treating 3p, 3d and 4s for Cr and 2s and 2p for O as valence electrons. For Gd, 4f state was treated as either a velence state or as a core state. Hubbard U was used for a better treatment of Cr-3d and Gd-4f electrons and chosen to be 3 eV and 4 eV for Cr and Gd, respectively, in line with the earlier report [159]. For Brillouin zone sampling, we chose 12×12×8 and 6×6×6 Monkhorst-Pack k-point mesh [161] for orthorhombic and cubic structures, respectively and the wave-function was expanded in a basis set consisting of plane waves with kinetic energies less than or equal to 770 eV. Using these parameters, an energy convergence of less than 1 meV/formula unit (f.u.) was achieved. Structures were fully relaxed until residual HellmannFeynman (HF) forces were smaller than 0.001 eV/$\AA$ while maintaining the symmetry constraints of the given space group. G-type magnetic structure was considered for both Cr and Gd moments in the calculation [159, 162].In order to impose G-type antiferromagnetic ordering in cubic structure, the unit cell was doubled along the <111> direction, which resulted in 10 atoms unit cell [150]. The phonon frequencies were calculated in high symmetry directions using the 2×2×2 supercell. The real-space force constants of the supercell were calculated using density functional perturbation theory (DFPT) implemented in the VASP package. The unit cell results in 30 phonon branches: 3 acoustic which have a zero frequency at k = (0,0,0) and 27 optical, some of which are triply degenerate. We are mainly interested in optical modes with imaginary phonon frequencies corresponding to instabilities in the structure. Due to the doubling of the unit cell along the <111> direction, we could access zone boundary phonon modes at the R-point along with the zone-center Γ modes [150]. The electric polarization was calculated using the Berry phase method [163], as implemented in VASP. The utility tool phonopy [164] was used to obtain phonon frequencies and phonon dispersions over the entire Brillouin zone.

4.1.3 Results and discussion

4.1.3.1 Structural studies: Global

$GdCrO_3$ crystallizes in to orthorhombic perovskite structure, having Goldschimdts tolerance factor, $t = \frac{(r_{Gd^{3+}} + r_{O^{2-}})}{\sqrt{2}(r_{Cr^{3+}} + r_{O^{2-}})} = 0.862$ [165,166]. Figure 4.1 (a) and (b) depict synchrotron x-ray diffraction patterns acquired at 300 K and 100 K respectively along with the corresponding Rietveld refined data using $Pbnm$ space group superimposed on it. Reasonably small values of reliability parameters (For 300 K: $R_w \sim 0.084$, $R_{exp} \sim 0.041$ and $\chi^2 \sim 4.16$, while for 100 K: $R_w \sim 0.088$, $R_{exp} \sim 0.043$ and $\chi^2 \sim 4.23$) indicate good quality of the fitting and suggest that the centrosymmetric $Pbnm$ space group persists in the entire (studied) temperature range. Additionally, the compound posses a centrosymmetric G-type magnetic structure in Cr-sublattice below $T_N(Cr) = 169$ K [154, 162] (whereas Gd-sublattice remains in paramagnetic state). The globally centrosymmetric magnetic and crystal structures are not compatible with the emergence of ferroelectric polarization. However, a weak electric polarization was also observed below $T_N(Cr)$ suggesting polar nature of the system [154]. This strongly indicates a possibility of local non-centrosymmetric structure in $GdCrO_3$, which might be responsible for its ferroelectric property.

Recent synchrotron x-ray diffraction studies on the other members of rare-earth chromite family ($RCrO_3$, $R =$ Sm, Ho and Nd) over a wide temperature range revealed a structural transition from a high temperature centrosymmetric $Pbnm$ space group to low temperature non-centrosymmetric $Pna2_1$ sub-group close to the onset of polar order [157,158,167]. Also, it has been proposed that local noncentrosymmetry drives ferroelectricity in $YCrO_3$, though, its average crystal structure is centrosymmetric [78, 153]. Keeping this in mind XRD patterns of $GdCrO_3$ were also refined with non-centrosymmetric $Pna2_1$ space group as depicted in insets of Figure 4.1 and the reliability parameters are surprisingly similar to the $Pbnm$ space group for both 300 K and 100 K ($R_w \sim 0.083$, $R_{exp} \sim 0.041$ and $\chi^2 \sim 4.37$ for 300 K and $R_w \sim 0.082$, $R_{exp} \sim 0.041$ and $\chi^2 \sim 3.94$ for 100 K) suggesting

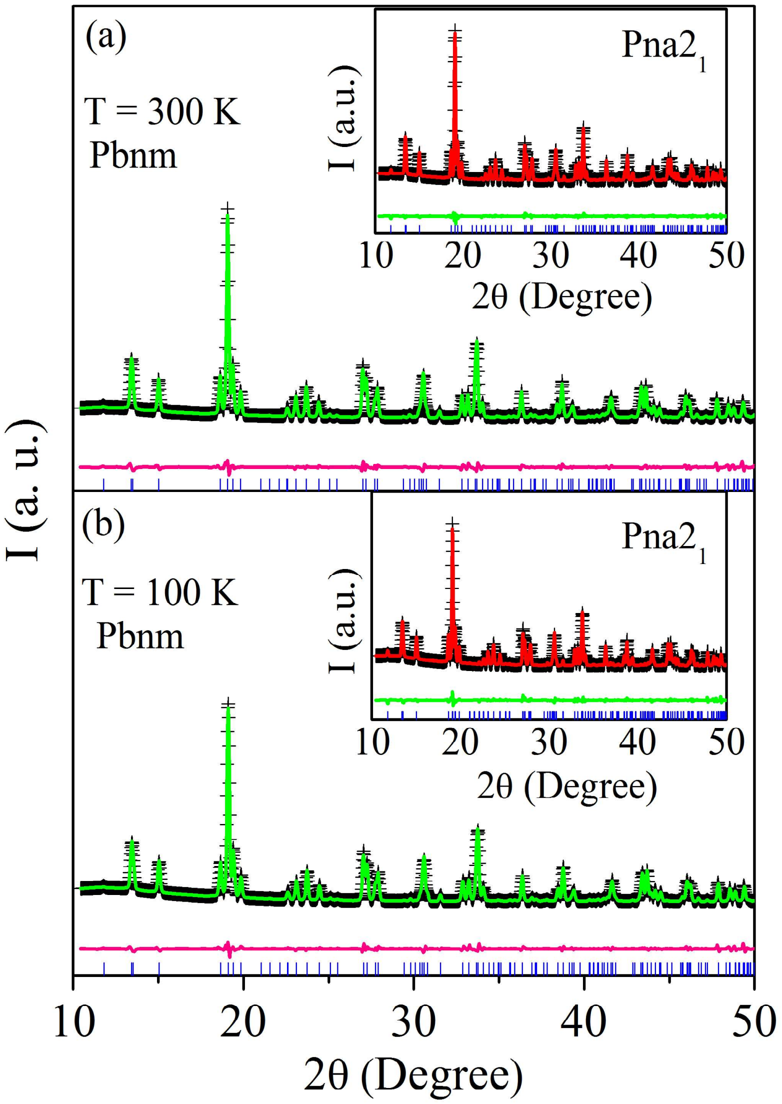

Figure 4.1: X-ray powder diffraction patterns (symbol) obtained at 300 K (a) and 100 K (b) with the refinement patterns (continuous curve) using *Pbnm* space group superimposed on it. Insets represent the same with Reitveld refinement using $Pna2_1$ space group.

that the average long-range ordering obtained by x-ray diffraction can not alone provide an answer to the origin of ferroelectricity in $GdCrO_3$.

We hence performed first-principles density functional calculations with fully optimizing the structure using PBEsol functional [97], as it is shown to be quite accurate in the estimation of lattice parameters and describe the ferroelectric property best [168, 169].

We fully optimized the structure of $GdCrO_3$ using *Pbnm* space group and found that the resulting structure attains non-centrosymmetric $Pna2_1$ symmetry, which was confirmed using FINDSYM software [170, 171]. In order to further confirm the results, we did calculations considering *Pbnm* and $Pna2_1$ structures separately and observed that both the structures converge to structures having same lattice parameters. The optimized lattice parameters for $Pna2_1$ structure are a = 5.530 $\AA$, b = 5.306 $\AA$ and c = 7.601 $\AA$. The energy difference is less than 1 meV (0.3 meV/f.u.), which is within calculation error. We believe that the ground state structure of $GdCrO_3$ is no-ncentrosymmetric $Pna2_1$, as it favors polar ordering. Non-centrosymmetric $Pna2_1$ space group is a sub-group of centrosymmetric *Pbnm* structure and the distortion in the structure is possibly very small, hence it is not distinguished by XRD measurements. Recent theoretical calculations allowing for magnetic interaction for different crystal symmetries by Zhao *et al.* suggested that only $Pna2_1$ crystal symmetry gives a sizable polarization for $GdCrO_3$, which is in agreement with our results [159]. However, according to them $GdCrO_3$ can only be ferroelectric at very low temperature as it is necessary to have G-type magnetic ordering in both Cr and Gd-sublattices to break the inversion symmetry *via* exchange-striction mechanism, which is associated with antipolar X-mode instability in the ideal cubic perovskite. We observed no-ncentrosymmetric $Pna2_1$ symmetry in $GdCrO_3$ both when Gd-4f electrons were treated as valence electrons or as core electrons. This suggests that magnetic coupling between Cr and Gd moments is not necessary for the stability of the polar $Pna2_1$ structure. However, the actual positions of the atoms and the value of the ferroelectric moment does depend on whether Gd-4f electrons are treated as core or valence states.

4.1.3.2 Phonon instability studies

To understand the origin of ferroelectricity in $GdCrO_3$ at relatively high temperature we performed phonon calculations using density functional perturbation theory approach for the ideal cubic perovskite structure of $GdCrO_3$, to access various structural instabilities in the system. Structural instability studies have been used to examine a large variety of ferroelectric perovskite oxides [78, 150–152, 172, 173]. As the structure was fully relaxed using PBEsol functional, the resulting lattice constant was found to be only 0.3% (0.5%) less than that of experimental value considering Gd-4f electrons as valence (core) state.

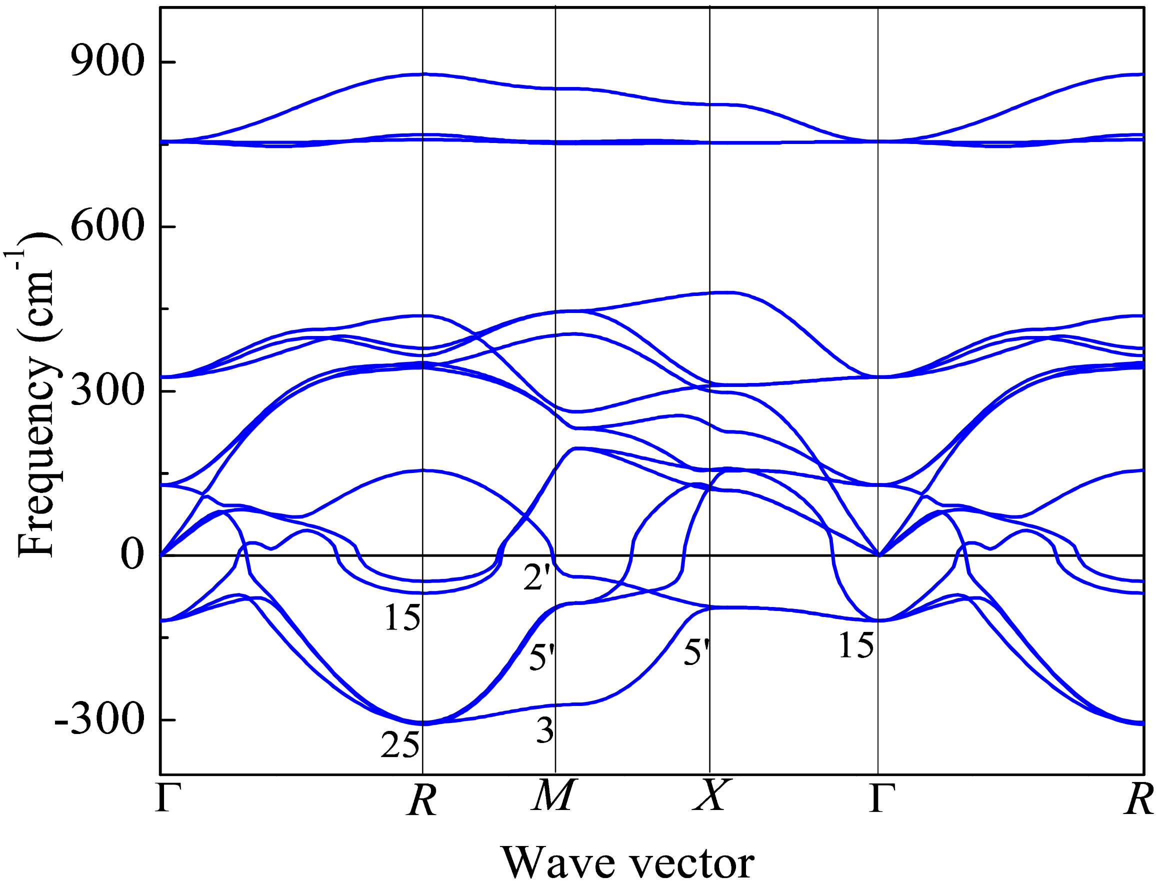

Figure 4.2: Phonon dispersion curves for the cubic phase of $GdCrO_3$ treating Gd-4f as core state. The labels indicate the symmetry of unstable modes.

Calculated phonon dispersion curves treating Gd-4f as core state are shown in Figure 4.2, with imaginary frequencies plotted in the negative axis. Soft modes occur over a wide range of wave vectors, with strong instabilities at R (R_{25}) and M (M_3), symmetry points which are associated with the octahedral rotations. Simultaneous condensation of these soft modes result in cubic-to-orthorhombic phase transition. Polar mode instabilities at R (R_{15}), X ($X_{5'}$) and Γ points, are associated with displacements of Gd and oxygen atoms, case similar to that for $YCrO_3$ [78]. R_{15} and $X_{5'}$ modes correspond to anti-ferroelectric distortions, and can only give rise to non-zero polarization below Gd-ordering temperature via magneto-striction effect with the dominant contribution from X mode as reported by Zhao *et al.* [159]. Γ_{15} mode on the other hand is responsible for the

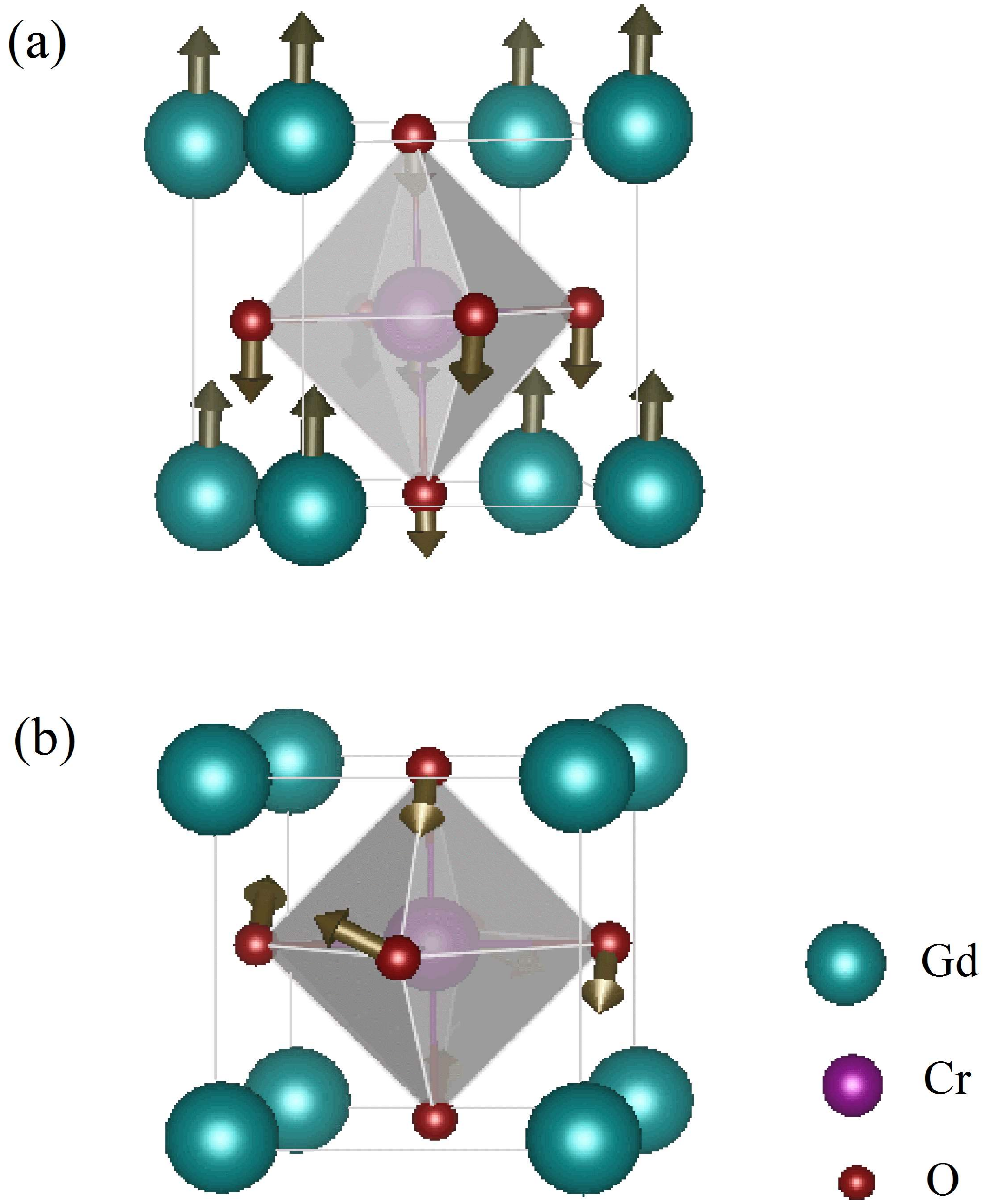

Figure 4.3: Visualization of eigenvectors of unstable (a) polar Γ_{15} and (b) antiferrodistortive R_{25} modes.

polarization at relatively high temperature as described in $YCrO_3$ and other ferroelectric perovskite compounds [78, 150, 152].

To understand more, we determined phonon frequencies only at the Γ point, which gave phonons at Γ and R points of the primitive unit cell due to the doubling of the unit cell along the <111> direction. Treating Gd-4f as core state, we found one triply degenerate zone-center instability at $120i$ cm^{-1} (Γ_{15}) and two triply degenerate zone-boundary instabilities at $60i$ cm^{-1} (R_{15}) and $302i$ cm^{-1} (R_{25}) similar to $YCrO_3$ and other d^3 systems [150]. Considering Gd-4f as valence state in the calculations, we noticed R_{15} is no longer unstable, while the magnitudes of other two modes decreases as $293i$ cm^{-1} (R_{25}) and $92i$ cm^{-1} (Γ_{15}). This clearly indicates a strong influence of Gd-4f electrons on the various instability modes of the cubic structure. The weakest instability mode, R_{15} involves the displacement of the Gd cations along with small oxygen displacements and these are antiparallel in neighboring unit cells. The Γ_{15} mode (Figure 4.3 (a)) involves mainly the Gd ion movement in a direction opposite to that of the oxygen cage and Cr ions where as Cr and O ions move in the same direction, resulting in a ferroelectric polar structural distortion very similar to $YCrO_3$ [78, 150]. The strongest instability R_{25} (Figure 4.3 (b)) is an antiferrodistortive (AFD) mode corresponding to the rotation of the corner connected oxygen octahedra. To probe the strength of ferroelectric instability, we displace the atoms toward the eigenvectors for polar Γ_{15} mode and relaxed it, which resulted in an energy lowering by 0.90 eV/formula unit.

We also calculated the magnitude of ferroelelctric polarization using Berry phase method and found it to be 0.75 μC/cm^2 when the Gd-4f electrons were treated as valence electrons. The strength of the polarization decreased to 0.35 μC/cm^2 when the 4f-electrons were treated as core state. This indicates that magnetic exchange coupling between Gd-4f and Cr-3d electrons does play an important role in ferroelectric distortion. The value of 0.75 μC/cm^2 is in close agreement with the experimental value ($\sim$ 0.7 μC/cm^2) [154]. The XX-component of calculated Born effective charges (BECs) are listed in Table 4.1. The BEC tensor ($Z^*_{i,\alpha\beta}$) is described as the change in polarization component, P_α resulting from a displacement (∂r) of ion i along Cartesian direction β [174, 175],

$$Z^*_{i,\alpha\beta} = \frac{\Omega}{\mid e \mid} \frac{\partial P_\alpha}{\partial r_{i,\beta}} \tag{4.1}$$

Table 4.1: The XX component of Born effective charge tensor for cubic $GdCrO_3$ compared with $YCrO_3$ [150]. Formal charges are given in brackets.

Compound	$Z^{\star}_{Gd/Y}$	$Z^{\star}_{Cr}$	$Z^{\star}_{O_x}$	$Z^{\star}_{O_{y,z}}$
$GdCrO_3$ (With Gd-4f)	4.55(3)	3.33(3)	-3.49(-2)	-2.16(-2)
$GdCrO_3$ (Without Gd-4f)	4.48(3)	3.32(3)	-3.48(-2)	-2.16(-2)
$YCrO_3$	4.45(3)	3.44(3)	-2.62(-2)	-2.66(-2)

where Ω is the unit cell volume and e is the electronic charge. Significantly enhanced BEC of Gd compared to its formal charge indicates large changes in hybridization of Gd with the surrounding ions, which is smoking gun for the emergence of ferroelectricity. It is surprising that polarization value in $GdCrO_3$ is one order of magnitude less than that of $YCrO_3$ [78], even though BEC of Gd is comparable to Y as given in Table 4.1. Also note that BECs are not affected whether one considers Gd-4f as a valence state or inside the core. However, only BEC can not define the tendency of a certain material towards ferroelectricity [175]. Also the ionic radii of Gd^{3+} (1.08 $\mathring{A}$) and Y^{3+} (1.04 $\mathring{A}$) ions are similar, indicating that the reduction in the strength of polarization in the Gd system is not due to the effect of size of R-site like in $LaCrO_3$. The difference in their polarizations arises from smaller displacement of Gd compared to Y and is possibly due to the subtle forces involving Gd orbitals (filled or unfilled) either directly or indirectly. Additionally, the BEC for Cr here is similar to the value found for $YCrO_3$ and other RCrO$_3$ (R = Lu and La) [150]. Anomalous BEC is obtained for O_x, which is slightly less to the value found in $LaCrO_3$ having very high magnetic transition temperature and quite large compared to $YCrO_3$ having low magnetic transition temperature [150, 151]. This suggests that larger BEC in O_x is due to the stronger Cr-O-Cr superexchange interaction, consequently, having relatively higher magnetic transition temperature in $GdCrO_3$ than $YCrO_3$.

The charge density around the O-Gd-O bonds in the [001] plane of the undistorted cubic structure and the distorted structure associated with frozen in ferroelectric phonon mode (Γ_{15}), are shown in Figures 4.4 (a) and (b), respectively. The charge density around the Gd ion for the undistorted cubic structure is quite spherical and the Gd-O hybridization is minimal. The ferroelectric distortion causes the Gd and O ions to displace in opposite direction (Figure 4.3 (a)), which results in one pair of Gd and O ions closer together

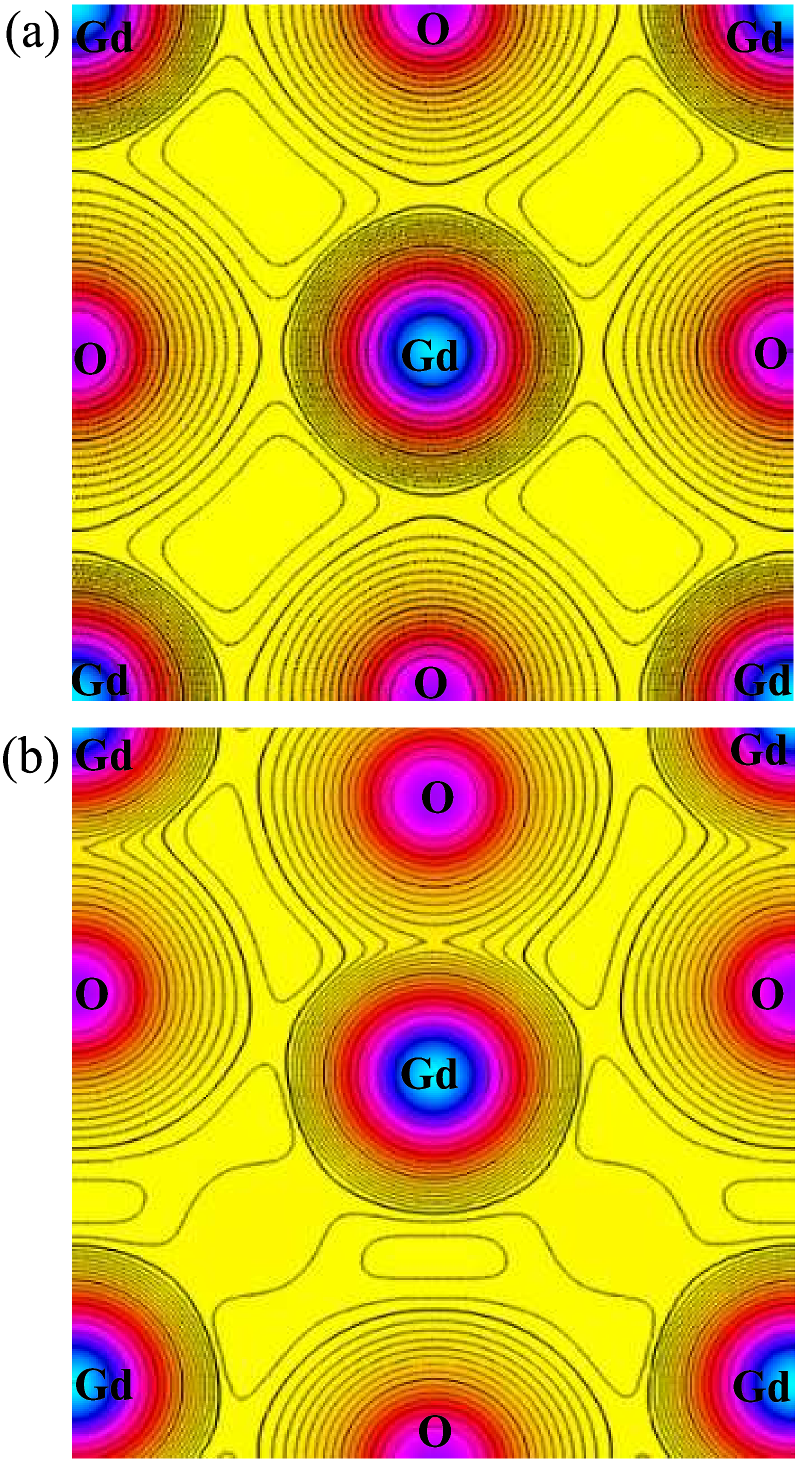

Figure 4.4: Contour plots of charge density around the O-Gd-O bonds in the [001] plane of (a) undistorted cubic $GdCrO_3$ (b) distorted $GdCrO_3$ associated with frozen in ferroelectric phonon mode (Γ_{15}).

and builds up large charge density in the Gd-O bond, indicating an increase in Gd-O hybridization as shown in Figure 4.4 (b). This indicates ferroelectric instability results in asymmetric stretching of the O-Gd-O bond and suggests that Gd-site partial covalency is the driving force for the ferroelectric distortion in the compound.

Further, to see the effect of intra-site Coulomb correlation effects of Cr-3d- and Gd-4f electrons on the structural properties and on phonon modes we also did calculations without U and found same negative modes ($\Gamma_{15} \sim 67i$ cm^{-1} and $R_{25} \sim 266i$ cm^{-1}), however both the modes are affected noticeably. Correlations lead to softening of both the modes by about 25 cm $^{-1}$.

Ferroelectric behavior in GdCrO$_3$ could be explained by the competition between polar (Γ_{15}) mode and AFD rotational (R_{25}) mode [176, 177]. The polar mode favors non-centrosymmetric ferroelectric phase where as AFD mode (octahedral rotation) results in centrosymmetric phase by inducing R-site antipolar displacements and hinders the ferroelectric ordering. The competition among these two modes stabilize various structures as follows. Ferroelectric rhombohedral structure is only associated with polar instability without having AFD instability. Whereas with progressive increase of AFD instability combined with the decrease of polar instability give rise to monoclinic, tetragonal and orthorhombic phases respectively, which in turn suppress the ferroelectric property in the structure gradually [176]. It can be noted that both polar and AFD modes are weaker in GdCrO$_3$ than that of YCrO$_3$ [150]. The dominant contribution of AFD mode together with ferroelectric mode result in $Pna2_1$ phase in GdCrO$_3$ and reduce the ferroelectric property compared to YCrO$_3$, which stabilizes in monoclinic $P2_1$ phase [153]. The intrinsic differences in the bonding in monoclinic YCrO$_3$ and orthorhombic GdCrO$_3$ leads to different magnitude of polarization. Displacements of Gd-atoms *via* polar distortion combined with movements of specific oxygen ions *via* AFD distortion of octahedra lift certain symmetries of centrosymmetric $Pbnm$ structure and stabilize the lower symmetry $Pna2_1$ structure in GdCrO$_3$, which is responsible for the emergence of spontaneous polarization.

4.1.3.3 Structural studies: Local

Based on phonon instability calculations, it is found that Gd-O bond polarization plays a major role in driving ferroelectricity in GdCrO$_3$. To probe it experimentally we performed temperature dependent EXAFS measurements. It is a powerful technique which provides information on the local structure around atoms of a selected type. It provides valuable information about the structural peculiarities and allows one to verify structural model. Figures 4.5 (a) and (b) show k^3-weighted EXAFS data in k space at Cr-K and Gd-L_3 edges, respectively, acquired at room temperature for $GdCrO_3$, along with corresponding fittings superimposed on it. Magnitude of Fourier transform of the corresponding spectra along with fittings are shown in Figs. 2 (c) and (d), respectively. Various contributions in different regions of the spectra are marked in the figures. The scattering contributions for

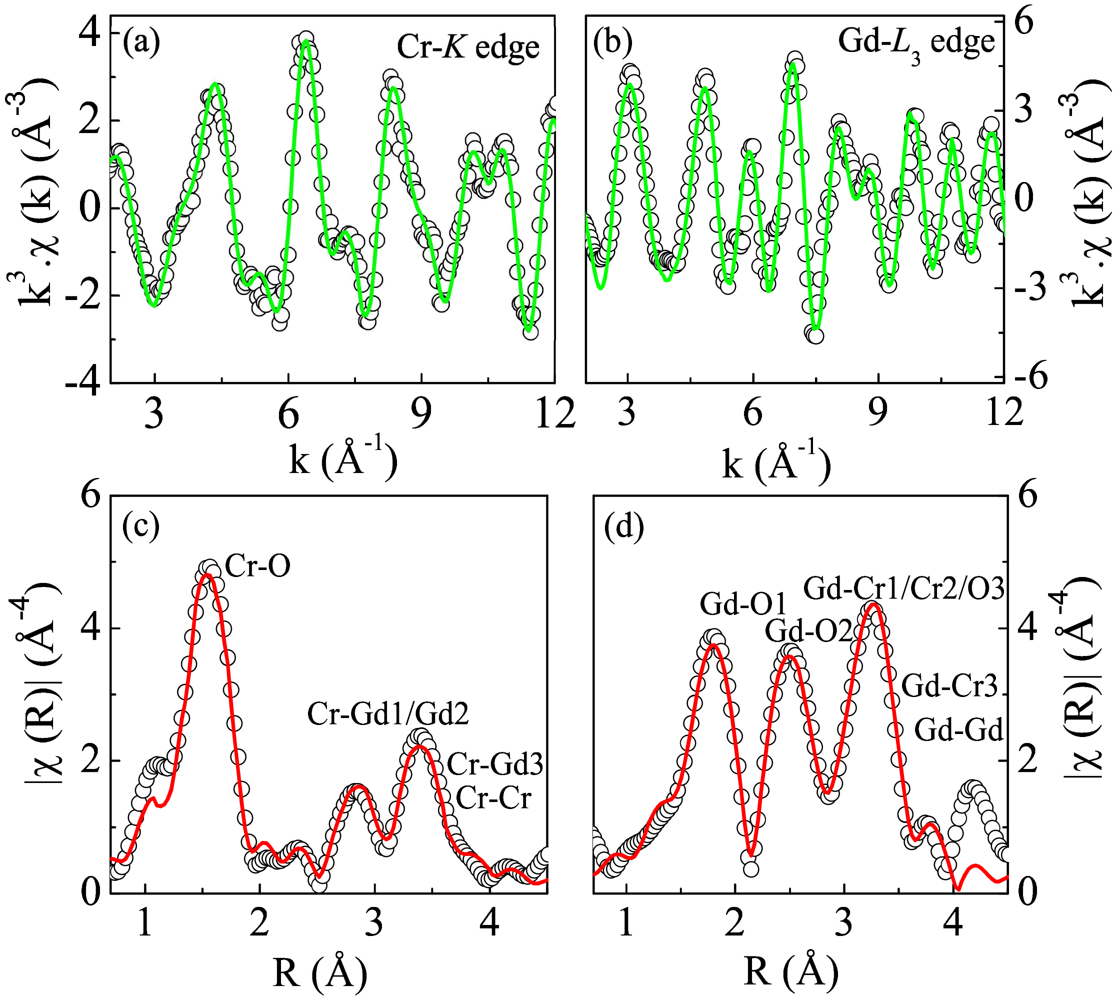

Figure 4.5: k^3-weighted EXAFS data in k space (open circles) at (a) Cr-K edge and (b) Gd-L_3 edge acquired at room temperature for $GdCrO_3$, along with corresponding fittings (solid lines). Magnitude of Fourier transform of corresponding data (open circles) along with fitting (solid lines) are shown in (c) and (d), respectively. Various contributions in different regions are marked in the figures.

atomic shells were derived considering both $Pbnm$ and $Pna2_1$ crystal structures and in either cases the EXAFS data fit well throughout the entire (measured) temperature range having R-factor ~ 0.01 for Cr-K edge and ~ 0.009 for Gd-$L3$ edges. This corroborates that distortion in the structure is very small, is in agreement with the XRD results as discussed above. For Cr-K edge, fits were confined to the k range of $3 < k < 12$ $\mathring{A}^{-1}$ and R-range of $1.2 < R < 4$ $\mathring{A}$. In this region Cr-K edge is originated from the single oxygen shell from the nearest neighbor octahedral oxygens, three Gd subshells with two, four and two Gd atoms, respectively, a single Cr shell with four atoms and other multiple scattering contributions. The fitting of Gd-$L3$ edge was done in the k range of $3 < k < 12.5$ $\mathring{A}^{-1}$ and R-range of $1.1 < R < 4$ $\mathring{A}$, to model Gd-O and Gd-Cr distributions. The Gd-O distribution is more complex having three subshells with four, two and six oxygens, respectively. Cr shell also splits into three subshells with two, four and two Cr atoms.Additionally, a single Gd shell is considered with four atoms. During fitting procedure, co-ordination number was fixed, while bond length and mean square relative displacement (MSRD) or Debye waller factor [σ^2 = <(r - <r>)^2>] were used as free variables. It is seen that Debye waller factor for short (O1) and long (O3) Gd-O bonds are highly correlated, therefore we chose single σ^2 for them and different one for middle bond oxygens (O2). Similarly, there are two σ^2 for Gd-Cr bonds; one for short and long bonds in bc-plane and another for middle bonds. σ^2 are most sensitive to modes contributing to radial motions, basically depending only on the local vibrational structure.

Temperature dependence of σ^2 for all the shells were fitted with Einstein model which consider the bond vibrations as harmonic oscillations with a single effective frequency proportional to Einstein temperature, θ_E, as given by following relation [178],

$$\sigma^2(T) = \sigma_0^2 + \left(\frac{\hbar^2}{2\mu k_B \theta_E}\right) coth\left(\frac{\theta_E}{2T}\right) \tag{4.2}$$

where σ_0^2 is the static contribution, T is in Kelvin and μ is the reduced mass of the bond pair. θ_E provides an approach to characterize the relative stiffness of the bonds. Fitting of temperature dependence of σ^2 using Einstein model for Cr-O bond correlation is shown in Figure 4.6. The best fitting yields $\sigma_0^2 = 0.0012(4)$ and $\theta_E = 818(11)$ K. The large value

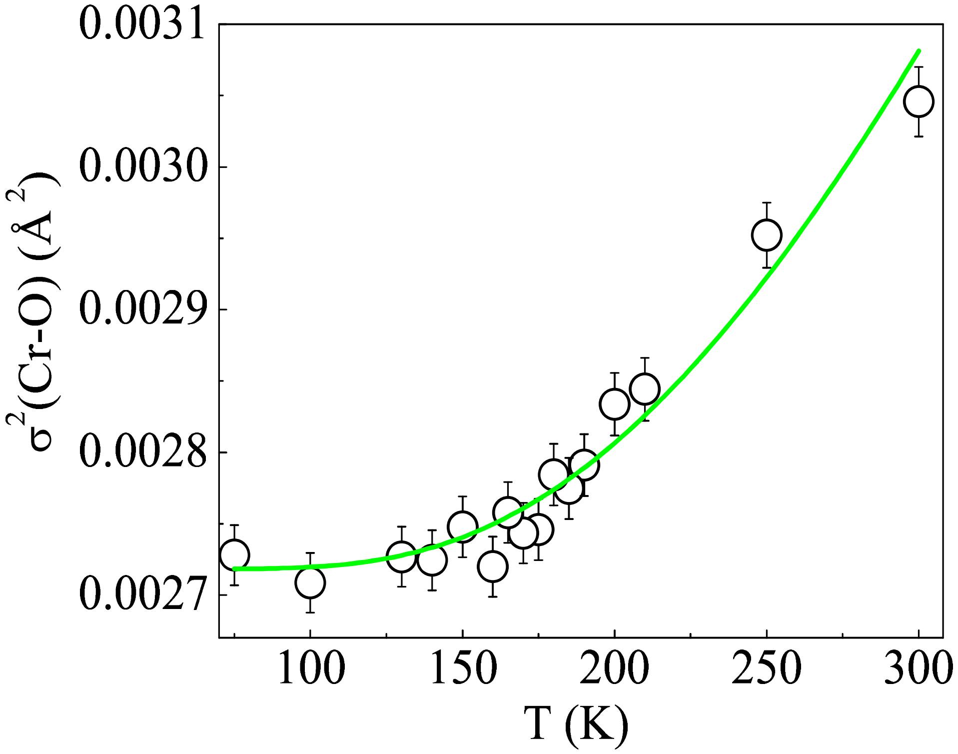

Figure 4.6: Temperature dependence of MSRD (σ^2) of Cr-O bond correlation of $GdCrO_3$. The solid line represents the fitting using Einstein model (Eq. 4.2).

of θ_E indicates the rigidness of CrO_6 octahedra. Furthermore, no anomalous change in the σ^2 is observed around the magnetic/ferroelectric transition temperature ($\sim$ 169 K). The fitting of temperature dependence of σ^2 for Gd-O subshells using Eq. 4.2 are shown in Figure 4.7 (a). From the fitting, it is found σ_0^2 = 0.0015(4) and θ_E = 391(15) K for Gd-O1/O3 bond correlations; and σ_0^2 = 0.0011(4) and θ_E = 458(26) K for Gd-O2 bond correlation.The relatively low values of θ_E of Gd-O subshells compared to Cr-O shell suggest that the Gd-O bonds are weaker than Cr-O bonds i.e. GdO_{12} polyhedra are not as rigid as CrO_6 octahedra. Furthermore, there is clear deviation of σ_0^2 from the expected behavior in the region near the magnetic/ferroelectric transition temperature, suggesting the presence of structural anomalies around the transition. The temperature dependent variation of σ^2 for Gd-Cr bond correlations along with fitting using Eq. 4.2 are shown in Figure 4.7 (b), giving σ_0^2 = 0.0044(1) and θ_E = 293(7) K for Gd-Cr1/Cr3 bonds; and σ_0^2 = 0.0015(3) and θ_E = 428(6) K for Gd-Cr2 bond. The σ^2 for of Gd-Cr1/Cr3 bonds which are in *bc*-plane show anomaly around the transition, where as Gd-Cr2 bond shows no

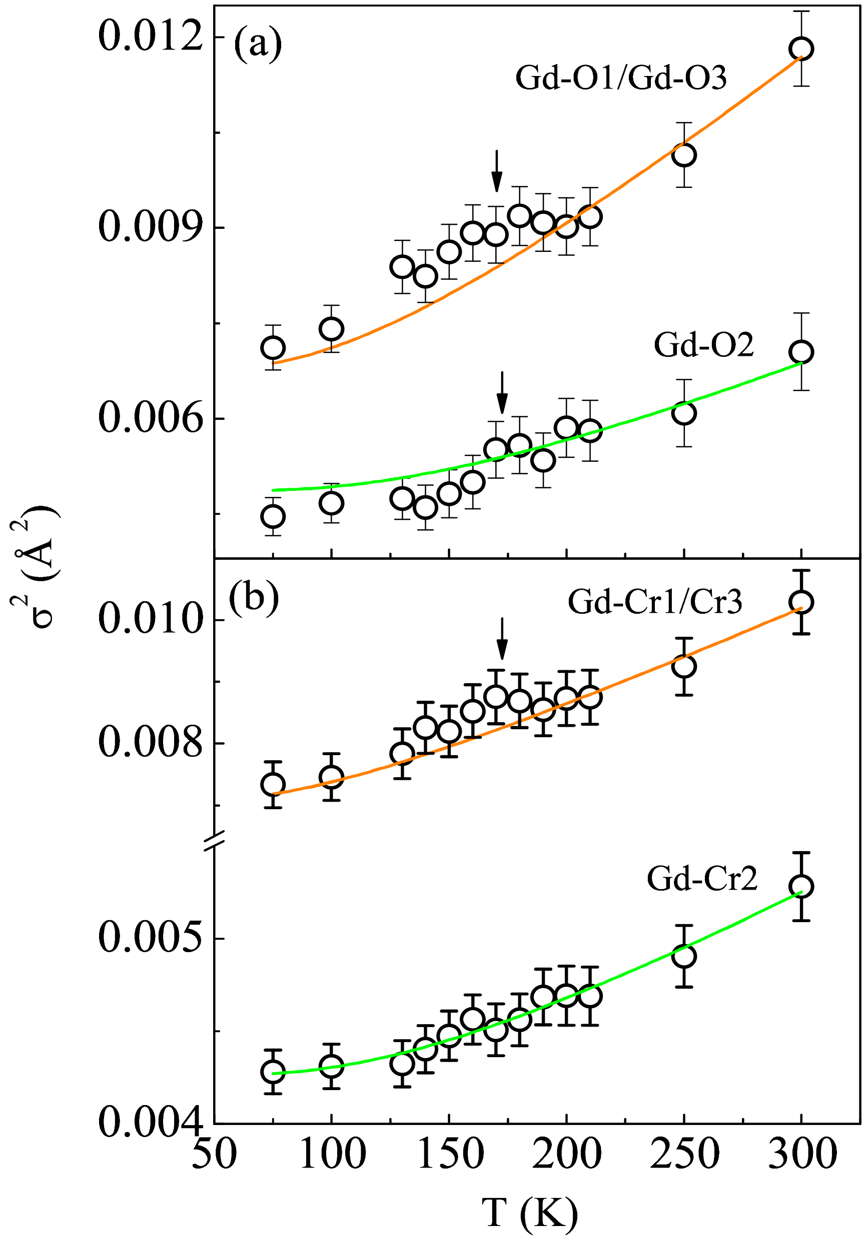

Figure 4.7: (a) Temperature dependence of variation of MSRD (σ^2) of (a) Gd-O bond correlations and (b) Gd-Cr bond correlations of $GdCrO_3$. The solid lines represent the fitting using Einstein model (Eq. 4.2). The arrows indicate the magnetic/ferroelectric ordering temperature.

anomaly. This anomalous behavior is possibly due to the Gd displacements caused by the magnetostriction effect (lattice contribution) and spin-phonon coupling magnetostriction effect associated with the Gd^{3+}-Cr^{3+} interaction [156].

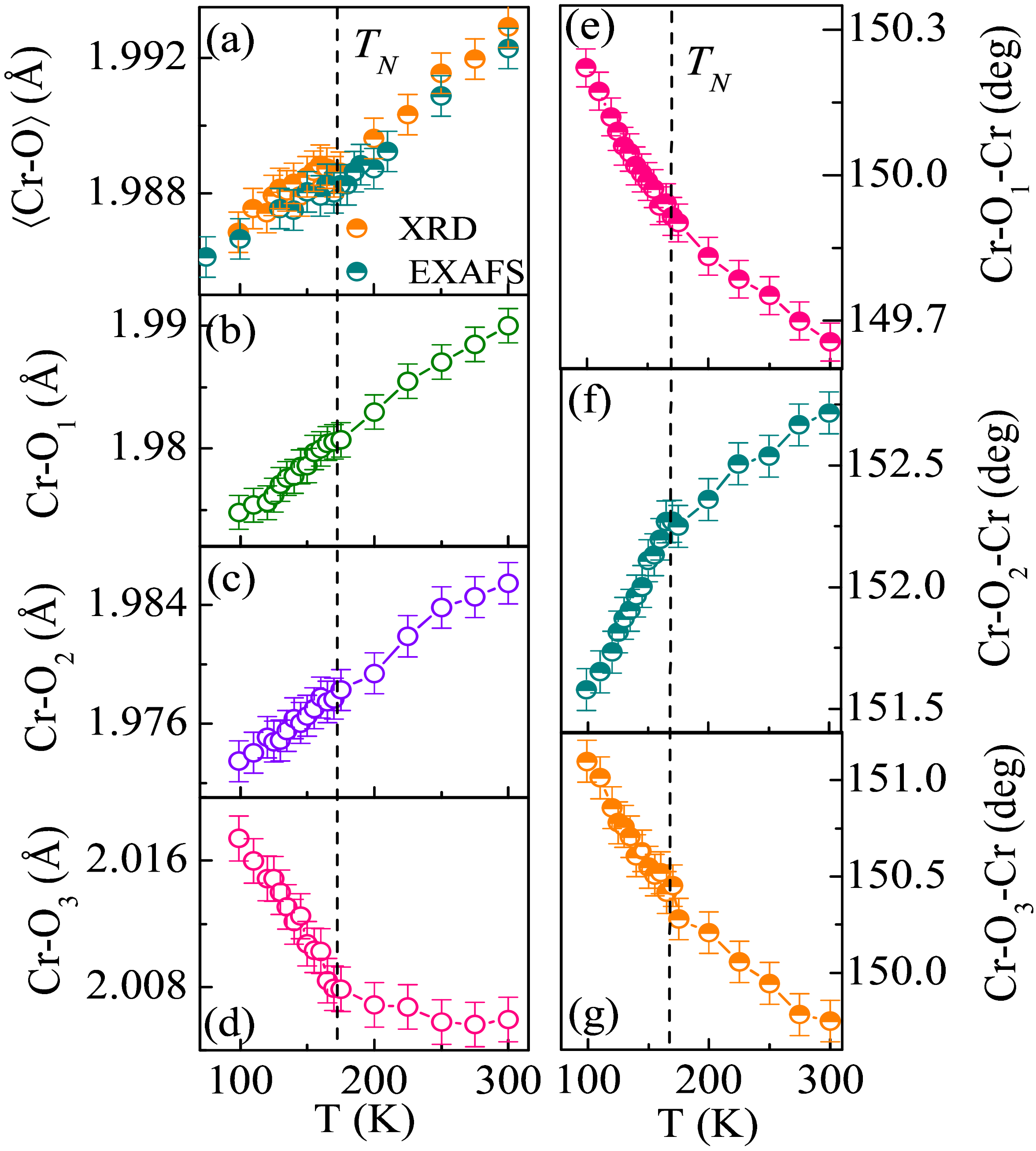

Figure 4.8: (a) Thermal variations of average Cr-O atomic bond of $GdCrO_3$ obtained from both EXAFS and XRD analysis. Thermal variations of bond lengths (Cr-O_1/O_2/O_3) and bond angles (Cr-O_1/O_2/O_3-Cr), obtained from Reitveld refinement of XRD are shown in panels (b)-(g), respectively. Vertical dashed line corresponds to the magnetic/ferroelectric ordering temperature.

For further understanding, we extracted the various bond lengths from EXAFS fiiting and Reitveld refinement of XRD pattern. The thermal variation of average of Cr-O bonds is shown in Figure 4.8 (a). The bond length obtained from both EXAFS and XRD analysis are identical and shows no anomaly around the transition. Figures 4.8 (b-d) represent the individual bond lengths (Cr-O_1/O_2/O_3) extracted fron XRD analysis, in which O_1 occupies the apex and O_2/O_3 occupy the base of CrO_6 octahedra. The bond length Cr-O_1 contracts with decrease of temperature, whereas one bond length in *ab*-plane (Cr-O_2) decreases and other (Cr-O_3) increases with decrease of temperature. The Cr-O_3 bond shows anomalous behavior around the transition indicating the exchange-striction effect and spin-phonon coupling due to the magnetic interactions [156]. The temperature dependent variation of the bond angles with temperature are shown in Figures 4.8 (e)-(g). With decreasing temperature the axial angle (Cr-O_1-Cr) increases and one of the equatorial angles (Cr-O_2-Cr) decreases, whereas other equatorial angle (Cr-O_3-Cr) increases. The bond angles also exhibit anomalous behavior around the transition. This suggests that there exist distortions in the octahedra probably associated with off-center displacements of oxygens via octahedral rotations. The off-center displacement of oxygens, generally in the *ab*-plane is the most important factor for the Dzyaloshinskii-Moriya interaction in the system [179].

The temperature dependent variation of Gd-O and Gd-Cr bonds obtained from EXAFS and XRD analysis are shown in Figures 4.9 (a) and (b), respectively. Except Gd-O3, all the Gd-O and Gd-Cr bonds obtained from EXAFS analysis match reasonably well with that extracted from the Rietveld refinement of XRD. Gd-O3 bond obtained from EXAFS fitting is shorter by $\sim 0.07\mathring{A}$, than that determined from XRD. Discrepancies between EXAFS and diffraction results may arise from either physical or fictitious effects. The systematic errors in the EXAFS data analysis may originate from the correlation between distances and energy scale parameters. On the other hand, discrepancies can be possible due to the differences between local and long-range structure as reported in the literature [180,181]. In the present system the identical length of Gd-O3 and Gd-Cr bonds may lead to the suppression of Gd-O3 contribution. However, the contraction is observed only for one distance (Gd-O3 bond), while all the other bond lengths show a general agreement between XRD and EXAFS results. This points towards the true shorter distance of the Gd-O3, which may possibly be due to the deviations of local structure from the average structure. The change in local structure mainly associated with the Gd-O coor-

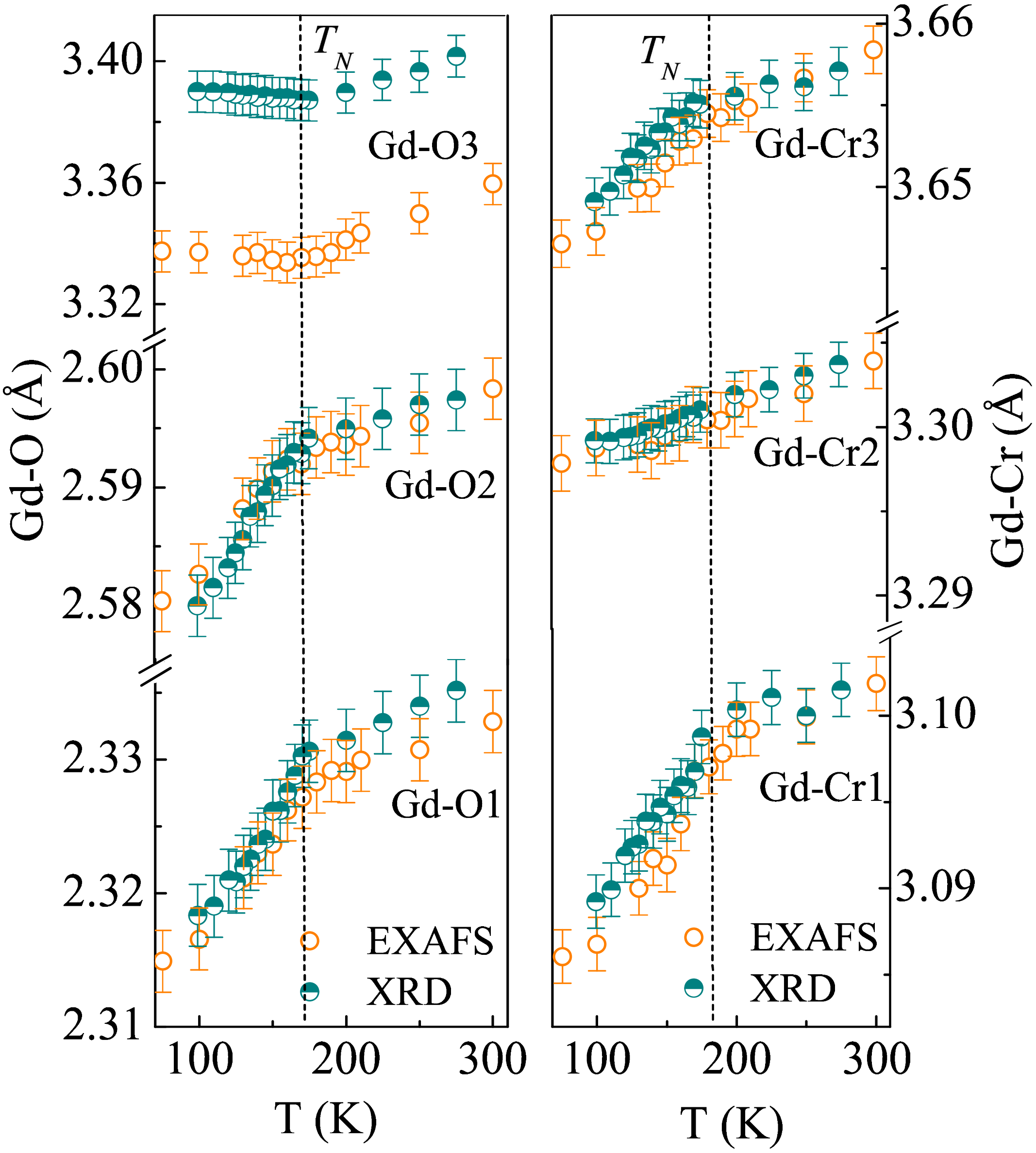

Figure 4.9: Thermal variations of (a) various Gd-O bond distributions and (b) Gd-Cr bond distributions obtained from both EXAFS and XRD analysis. Vertical dashed line corresponds to the magnetic/ferroelectric ordering temperature.

dination sphere, whereas the Cr-O coordination remains less affected, suggesting that the structural distortion is dominated by Gd displacements consistent with phonon instability study. Further, all the Gd-O bonds and Gd-Cr bonds except Gd-Cr2 show slope changes around the transition. Such anomalous behavior can be explained by magnetostriction effect and spin-phonon coupling, which plays a role in ferroelectric modulation [156].

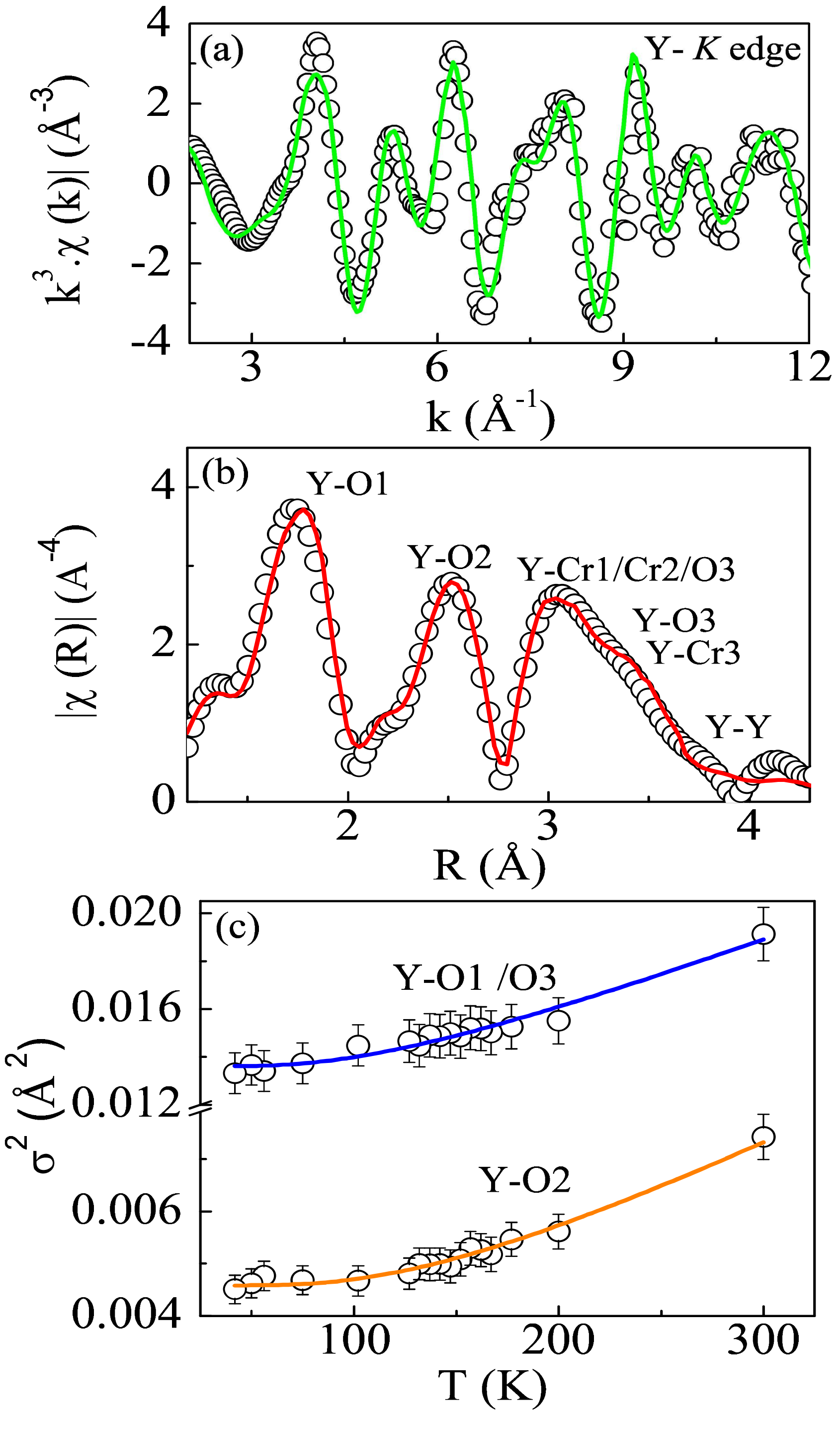

Figure 4.10: (a) k^3-weighted EXAFS data in k space and (b) magnitude of Fourier transform of the data at Y-K edge acquired at room temperature for YCrO$_3$, along with corresponding fittings (solid lines). Various contributions in different regions are marked in the figure. (c) Temperature dependence of MSRD (σ^2) of Y-O bond correlations. The solid lines represent the fitting using Einstein model (Eq. 4.2).

Figures 4.10 (a) and (b) depict the magnitude of Fourier transform of k^3-weighted EXAFS data ($|\chi(R)|$) and back-transformed spectra in k space at Y-K edge acquired at room temperature for $YCrO_3$, respectively, along with corresponding fitting superimposed on these. The scattering contributions for atomic shells were derived considering both $Pbnm$ crystal structure and it fits well throughout entire (measured) temperature range having R-factor ~ 0.01. Fits were confined to the k range of $3 < k < 12.5$ $\AA^{-1}$ and R-range of $1.15 < R < 4$ $\AA$. From the fitting it was found that the oxygen shell is originated from three subshells with four oxygens each. Cr shell splits into three subshells with two, four and two Cr atoms and a single Y shell is considered with four atoms. Total five σ^2 parameters were used. One for both short and long Y-O bonds and other for the middle bonds. Similarly, there are two σ^2 for Gd-Cr bonds; one for both short and long bonds in bc-plane and another for middle bond. Fifth one is for Y-Y correlations. The fitting of temperature dependence σ^2 for Y-O subshells using Eq. 4.2 are shown in Figure 4.10 (c). From the fitting, it is found $\sigma_0^2 = 0.0083(2)$ and $\theta_E = 341(7)$ K for Y-O1/O3 bond distributions; and $\sigma_0^2 = 0.0015(8)$ and $\theta_E = 432(5)$ K for Y-O2 bond distribution. The relatively low values of θ_E for Y-O subshells indicate YO_{12} polyhedra are also not rigid enough like GdO_{12} in $GdCrO_3$. These results suggest an intimate analogy between $GdCrO_3$ and $YCrO_3$ consistent with phonon calculations. However, Gd-O environment (three subshells with four, two and six oxygens, respectively) is different in $GdCrO_3$ from Y-O environment (three subshells with four oxygens each) in $YCrO_3$, which leads to orthorhombic $Pna2_1$ structure in $GdCrO_3$ in contrast to the monoclinic $P2_1$ structure in $YCrO_3$ [78]. The good fitting of EXAFS data using $Pbnm$ structure is possibly due to tiny distortions in these systems, giving rise to very weak polarizations ($GdCrO_3 \sim 0.7$ μ/cm^2, $YCrO_3 \sim 3$ μ/cm^2) [78, 154] .

The above studies indicate the distortion in the structure is associated with the off-centering displacement of Gd-atoms together with octahedral rotations via movements of oxygen ions, which lift certain symmetries of centrosymmetric $Pbnm$ structure [157, 158] and possibly stabilizes a local non-centrosymmeyric $Pna2_1$ structure. Figure 4.11 illustrates a schematic representation of the displacement of oxygens around CrO_6 octahedron (octahedral rotation), as indicated by the arrows and dashed circles represent possible dis-

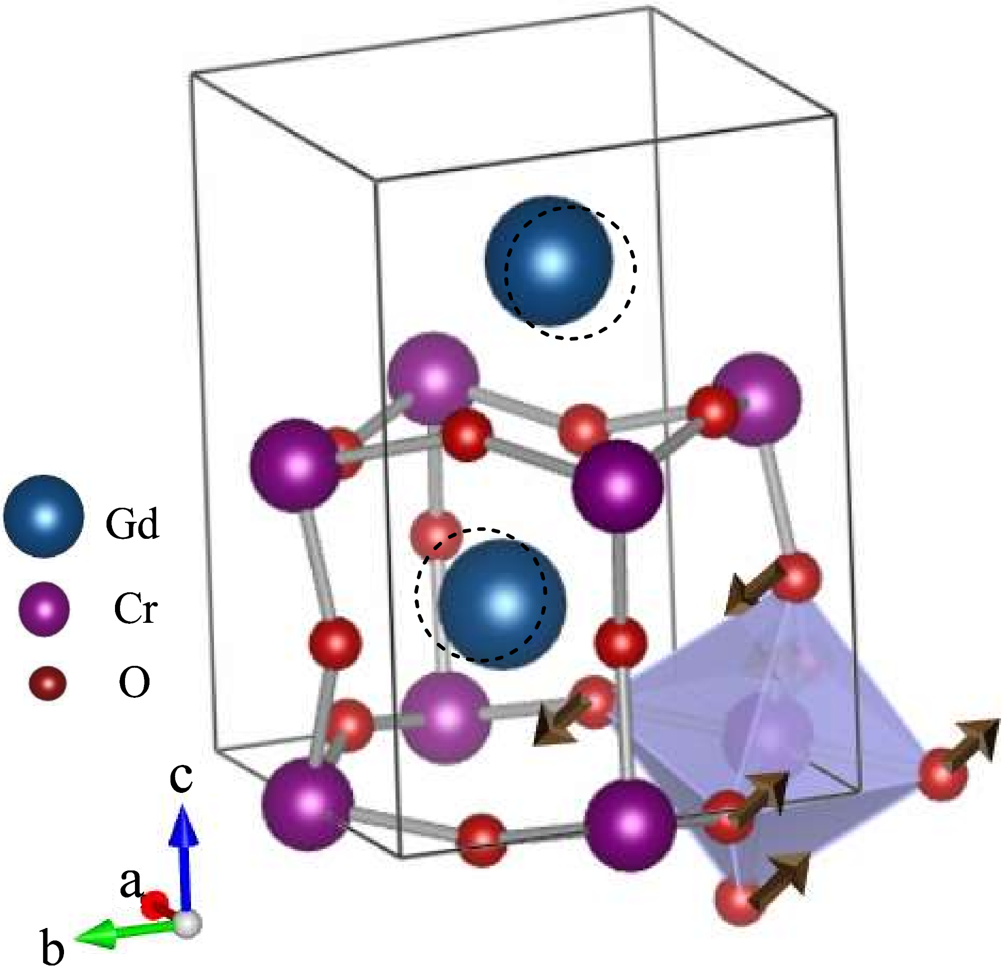

Figure 4.11: Visualization of displacement of oxygens around CrO_6 octahedron (octahedral rotation), as indicated by the arrows and dashed circles represent possible displacement of Gd atoms in $GdCrO_3$.

placement of Gd atoms. The distortion is dominated by mainly Gd displacements, indicating that Gd-O bond polarization plays a major role in driving ferroelectricity. Moreover, density-functional theory calculations showed that $GdCrO_3$ prefers $Pna2_1$ symmetry as reported earlier and XRD also gives better fitting with this space group, suggesting that some sort of long range positional disorder is always present in the system. The magnetic coupling leads to extra distortion in the system via magnetoelectric coupling and plays a complementary tool for the enhancement of ferroelectric polarization [167].

4.1.4 Conclusion

Our results clearly demonstrate that the preferred symmetry of $GdCrO_3$ is found to be non-centrosymmetric $Pna2_1$. There are competing structural instabilities in cubic $GdCrO_3$: the dominating one is of antiferrodistortive type and the weak polarization arises from the small ferroelectric instability resulting in Gd-O bond polarization. The smaller displacement of Gd than that of Y leads to decrease in the strength of ferroelectricity in $GdCrO_3$ compared to $YCrO_3$ in turn stabilizes an orthorhombic $Pna2_1$ structure in $GdCrO_3$ and monoclinic $P2_1$ structure in $YCrO_3$. This indicates a strong influence of Gd orbitals on the suppression of ferroelectric property of the system. It is also found that $3d$-$4f$ magnetic coupling plays an important role in ferroelectric distortion. Further, detailed EXAFS and XRD studies also corroborate the distortion in the structure is associated with the off-centering displacement of Gd-atoms together with octahedral rotations. The magnetic coupling leads to extra distortion in the system via magnetoelectric coupling, indicating its relevance to ferroelectric modulation.

4.2 Complex magnetic behavior and spin-phonon coupling studies

4.2.1 Introduction

In addition to ferroelectric behavior, rare-earth orthochromites ($R\mathrm{CrO}_3$) also exhibit extremely rich magnetic properties like temperature induced magnetization reversal (TMR), spin flipping (SF), spin reorientation (SR), exchange bias etc. [43, 157, 182–184], due to various magnetic interactions such as Cr^{3+}-Cr^{3+} , Cr^{3+}-R^{3+} and R^{3+}-R^{3+} interactions, each of which is generally a combination of symmetric antiferromagnetic (AFM) exchange interaction ($S_i.S_j$) with the antisymmetric Dzyaloshinsky-Moriya (DM) interaction ($S_i \times S_j$) [42,185,186]. The TMR behavior can provide novel opportunities in the fabrication of nonvolatile memory, which facilitates two distinct states of magnetization and magnetic cooling/heating based constant temperature bath, as polarity of magnetization can be switched without changing the direction of external magnetic field [182, 187–189].

$GdCrO_3$ shows TMR behavior below Cr-ordering temperature followed by sharp upturn behavior in field-cooled-cooling (FC(C)) mode. This upturn of magnetization has been attributed to the onset of SR transition [190]. However, similar upturn behavior in polycrystalline $CeCrO_3$ has been explained in terms of SF in Ce and Cr-sublattices [43]. Further, recent report on single crystal of $GdCrO_3$ shows a discontinuous jump from negative magnetization to positive magnetization in FC(C) mode, which has been attributed to SF in Gd and Cr sublattices, though the SF transition temperature (T_{SF}) is quite high [184]. These contradicting results motivated us to reinvestigate the magnetic behavior in polycrystalline $GdCrO_3$. Further, we also studied the magnetoelectric coupling strength in the material from temperature-dependent Raman measurements.

4.2.2 Experimental details

Magnetic measurements were performed using Quantum Design SQUID-VSM magnetometer. Heat capacity ac susceptibility measurements were done in Quantum Design Physical Property Measurement System (QD-PPMS) using relaxation method in external magnetic field up to 9 T. The vibrational properties of the sample were measured using a micro-Raman spectrometer (inVia, Renishaw, UK) with 514.5 nm excitation of an Ar^+ laser. Spectra were collected in the back scattering configuration using a thermoelectrically cooled CCD camera as the detector. A long working distance 50x objective with numerical aperture of 0.45 was used for the spectral acquisition. In order to carry out the temperature dependent Raman spectroscopic measurements, the sample was kept in a Linkam (THMS600) stage, driven by an auto-controlled thermoelectric heating and cooling function within a temperature range of 80 to 300 K.

4.2.3 Results and disscussion

4.2.3.1 Magnetic studies

Temperature dependence of magnetization curves collected in zero-field cooled (ZFC), field-cooled-cooling (FC(C)) and field-cooled-heating (FC(H)) protocols with applied field of 100 Oe are shown in Figure 4.12 (a). Canted-AFM ordering (G_xF_z-type, where AFM coupling along the a-axis (easy axis) and weak ferromagnetism along the c-axis) occurs in Cr-sublattice at around T_N(Cr) $\sim$ 169 K, whilst Gd-sublattice retains its paramagnetic order [162, 190]. The canted antiferromagnetism is due to the antisymmetric Dzyaloshinsky-Moriya (DM) interaction between Cr^{3+} spins, arising from the introduction of spin-orbit coupling as a perturbation on the quenched Cr^{3+} ground state [47, 48, 162, 190]. This perpendicular component of magnetization (weak FM moment perpendicular to magnetic easy axis, $\chi_\perp$) does not follow Curie-Weiss law ($\chi = \frac{C}{T-\theta}$) as it only describes parallel component of magnetization ($\chi_\parallel$). The $\chi_\perp$ can be explained by following modified Curie-Weiss law modeled by Moriya [48, 191],

$$\chi = \frac{C(T - T_0)}{(T - \theta)(T - T_N)} \tag{4.3}$$

Where C is the Curie Constant, T_0 is the fitted parameter, θ is the Weiss temperature and T_N is the Neel temperature. For polycrystals, it is not possible to measure $\chi_\parallel$ and $\chi_\perp$ independently, hence, average susceptibility is expressed as $\chi_{avg} = (\chi_\parallel + 2\chi_\perp)/3$. In $GdCrO_3$, the magnetic structure is G_xF_z-type below T_N(Cr), which leads to negligible contribution of $\chi_\parallel$ to net susceptibility. Total susceptibility near T_N(Cr) can hence be well explained by Eq. 4.3, as evident from excellent fitting (Inset of Figure 4.12 (a)). The best fitted parameters are C = 10.8518 emu.K.Oe^{-1}.mol^{-1}, T_0=168.12 K, T_N = 168.28 K and θ = -87.12 K.

Strength of nearest neighbour symmetric exchange interaction (J_e) and antisymmetric DM exchange interaction (D) between Cr^{3+} ions can further be calculated using following expressions,

$$T_0 = \frac{J_e Z S(S+1)}{3k_B} \tag{4.4}$$

$$T_N = \frac{J_e Z S(S+1)}{3k_B}[1 + (\frac{D}{2J_e})^2]^{\frac{1}{2}} \tag{4.5}$$

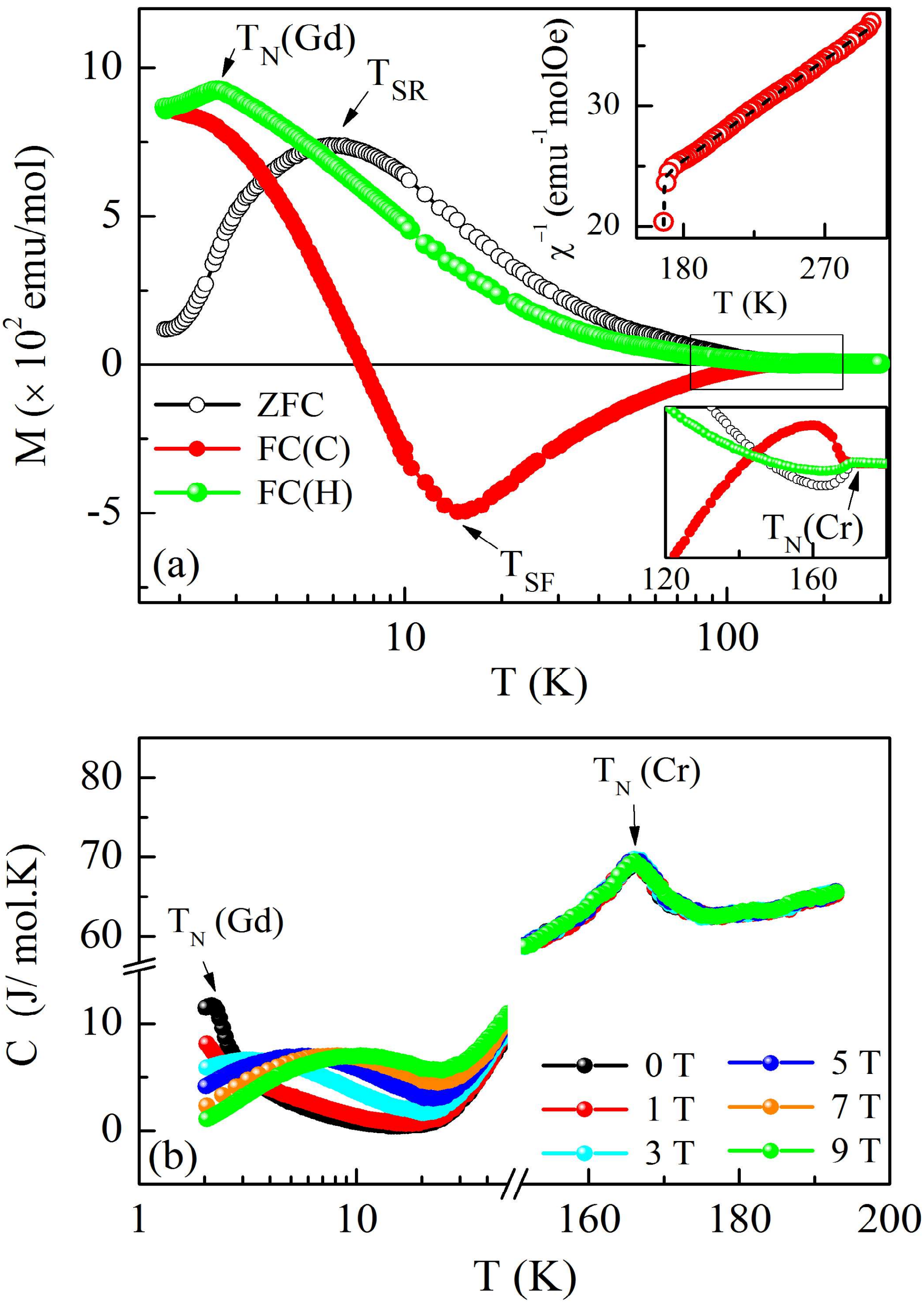

Figure 4.12: ZFC and FC M-T curves for GdCrO$_3$ with an applied field of 100 Oe. Lower Inset: Enlarged view of selected temperature region highlighting Cr-ordering and magnetization reversal in FC(C) mode. Upper Inset: Fitting of inverse susceptibility to the Curie-Weiss law modified by the Dzyaloshinsky-Moriya interaction

Here, $Z = 6$ is the coordination of Cr^{3+}, $S = 3/2$ is the spin quantum number of Cr^{3+}, and k_B is Boltzmann constant. Substituting these values we got $J_e = 11.058$ K and $D = 2.64$ K, Which are quite in agreement with other rare earth chromites [191]. The effective paramagnetic moment (μ_{eff}) is estimated from Curie Constant, using the relationship $\mu_{eff} = \sqrt{\frac{3Ck_B}{N}}$ and it is found to be $9.168\mu_B$, which is slightly higher than theoretical value ($8.846\mu_B$) as estimated from the spin only contribution of Cr^{3+} and Gd^{3+} ions. Temeperature dependence heat capacity data under different magnetic fields is shown in Figure 4.12 (b). A λ-shaped anomaly is found in specific heat around T_N(Cr), suggesting a second-order nature of the transition, and it is observed to be independent of external magnetic fields.

Below 160 K the FC(C) magnetization decreases continuously and finally becomes negative, followed by compensation at around $T_{comp1} \sim 131$ K (Figure 4.12 (a)). Such a behavior can be explained by the polarization of paramagnetic Gd^{3+} spins along the induced field of canted Cr^{3+} spins via isotropic Gd^{3+}-Cr^{3+} interaction [190, 192]. Thus net magnetization is this region can be described by following equation [162, 184, 190]

$$M = M_{Cr} + \frac{C(H_a + H_i)}{T - \theta} \tag{4.6}$$

where first and second terms represent magnetic moments of canted Cr^{3+} spins and magnetic moment of paramagnetic Gd^{3+} ions, respectively. θ, H_a and H_i are the Weiss temperature, the external MF and the induced field at Gd^{3+} sites due to canted Cr^{3+} spins, respectively. C stands for the Curie constant, whose value is taken 7.875, theoretical value for the Gd^{3+} ground state [162].

Thereafter, sharp upturn of magnetization is observed below $T_{min} \sim 18$ K. To understand this behavior we have fitted whole FC(C) curve with Eq. 4.6 as shown in Figure 4.13 (a). It fits well except the region very near below T_{min} and below 5 K. The deviation of fitting below 5 K arises due to the Gd^{3+}-Gd^{3+} interaction. Temperature dependency of M_{Cr} is not considered in Eq. 4.6 due to large Gd^{3+} moment, which can overcome the small canted Cr^{3+} moments. The best fitting for the region above T_{min} provides $M_{Cr} =$

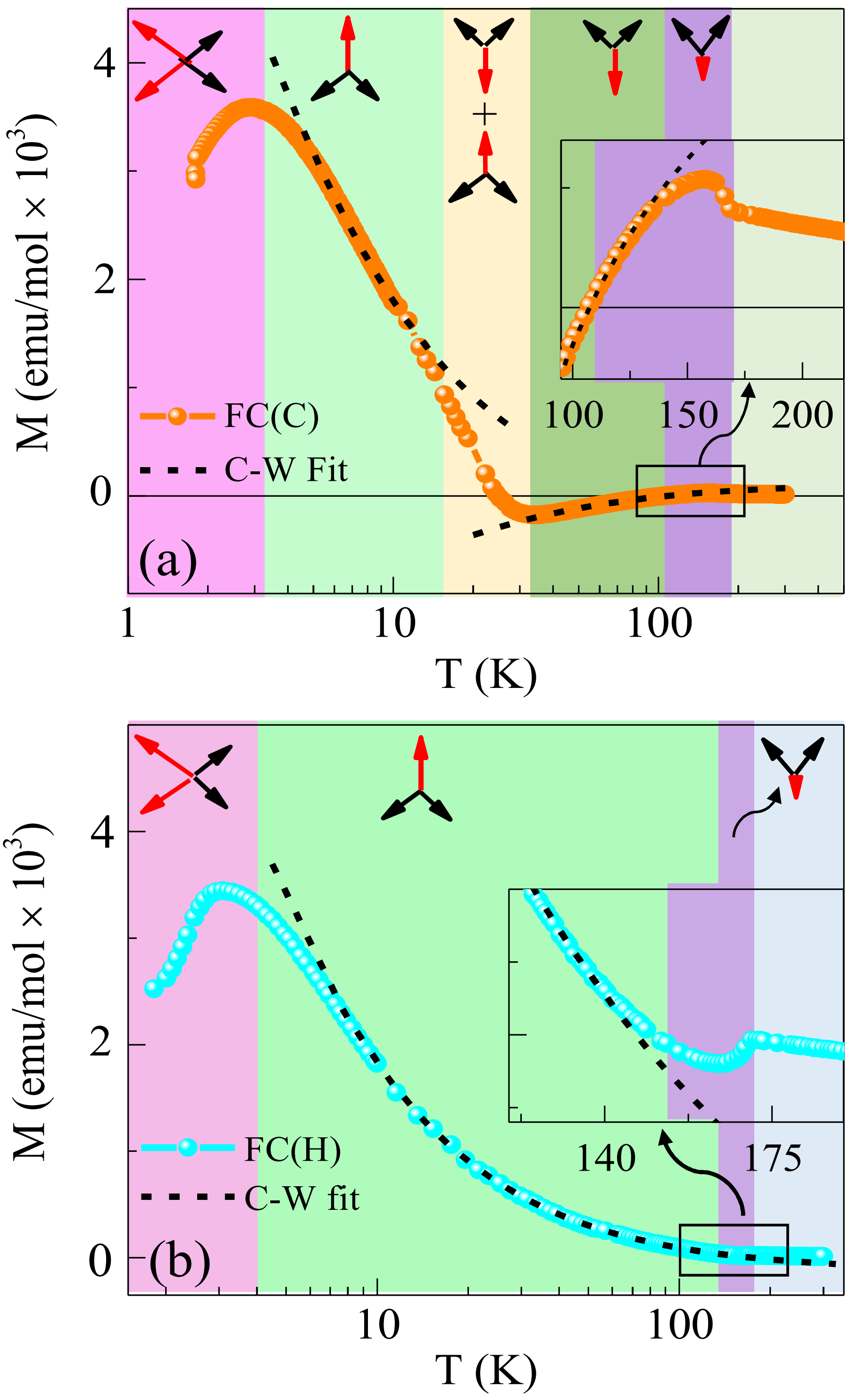

Figure 4.13: Fitting of the FC(C) (a) and FC(H) (b) curves with Eq. 4.6 and a schematic view of temperature evolution of Gd^{3+} and Cr^{3+} spins.

115.93 emu/mol, H_i = -2191.41 Oe and θ = -7.982 K, which are consistent with earlier report [190]. These suggest above T_{min}, canted Cr^{3+} moment is along the direction of applied field and induced field is opposite to the applied field direction, which leads to ferrrimagnetic coupling between Cr and Gd-sublattices [190]. In contrast, for the region below T_{min}, M_{Cr}= -157.77 emu/mol, H_i = 2956 Oe and θ = -2.16 K. Negative value of θ implies Gd and Cr-sublattices retain their ferrimagnetic coupling. However, canted Cr^{3+} moment and H_i have reversed their signs. implying that canted Cr^{3+} moment is opposite to the external field while Gd^{3+} spins are aligned along the external field direction, suggesting spin flipping (SF) below T_{min}. Further, deviation from the fitting very near below T_{min} suggests that flipping of spins occurs continuously. This continuous nature of SF are plausibly due to spatial average of magnetization in the polycrystalline sample, whereas in single crystal the flipping occurs discontinuously [184]. SF is likely caused by Zeeman energy between net moments and the external MF as given by following equation [43],

$$E_{Zeeman} = -\mu_0 M_{Net} H_a Cos\phi \tag{4.7}$$

Here, μ_0, M_{Net}, H_a and ϕ represent the vacuum permeability, net moments of a pair of antiparallel Gd^{3+} and Cr^{3+} in a unit cell, external MF and the angle between net moment and external MF respectively. For $\phi = \pi$, net magnetization is opposite to the external field and it has maximum Zeeman energy. This leads to spontaneous flipping of spins. Again the magnetization becomes zero at 12 K. Yoshii *et. al* [190] reported it as spin-reorientation (SR) transition temperature (T_{SR}), where the Cr^{3+} and Gd^{3+} spins are completely along *a*-axis . Note, in polycrystalline sample magnetization is spatially averaged, so moment can not become zero along c-axis at T_{SR}. So it can be attributed as the second compensation point (T_{comp2}), where antiferromagnetic moment of Gd and Cr sublattices again cancel each other in the SF region. Finally, Gd-ordering (canted-AFM type) sets in around 2.3 K (Figure 4.12 (a)), which results in a broad and cusp like anomaly in heat capacity data as shown in Figure 4.12 (b). Gradually this anomaly smears out and shifts towards high temperature with external field due to the weak magnetic exchange coupling between Gd ions and beyond 1 T the ground state of the system becomes ferromagnetic.

Remarkably, FC(H) curve is vastly different from FC(C) curve (Figure 4.12 (a)). The best fitting to Eq. (4.6) as shown in Figure 4.13 (b) provides M_{Cr} = -112.9 emu/mol, H_i = 2702.5 Oe and θ = -1.22 K, indicating ferrimagnetic coupling between Gd and Cr sublattices with Gd^{3+} moment along external MF direction and canted Cr^{3+} moment is opposite to it. Such a behavior is likely due to strong temperature dependency of different exchange interactions (Gd^{3+}-Gd^{3+}, Gd^{3+}-Cr^{3+} and Cr^{3+}-Cr^{3+}). During cooling

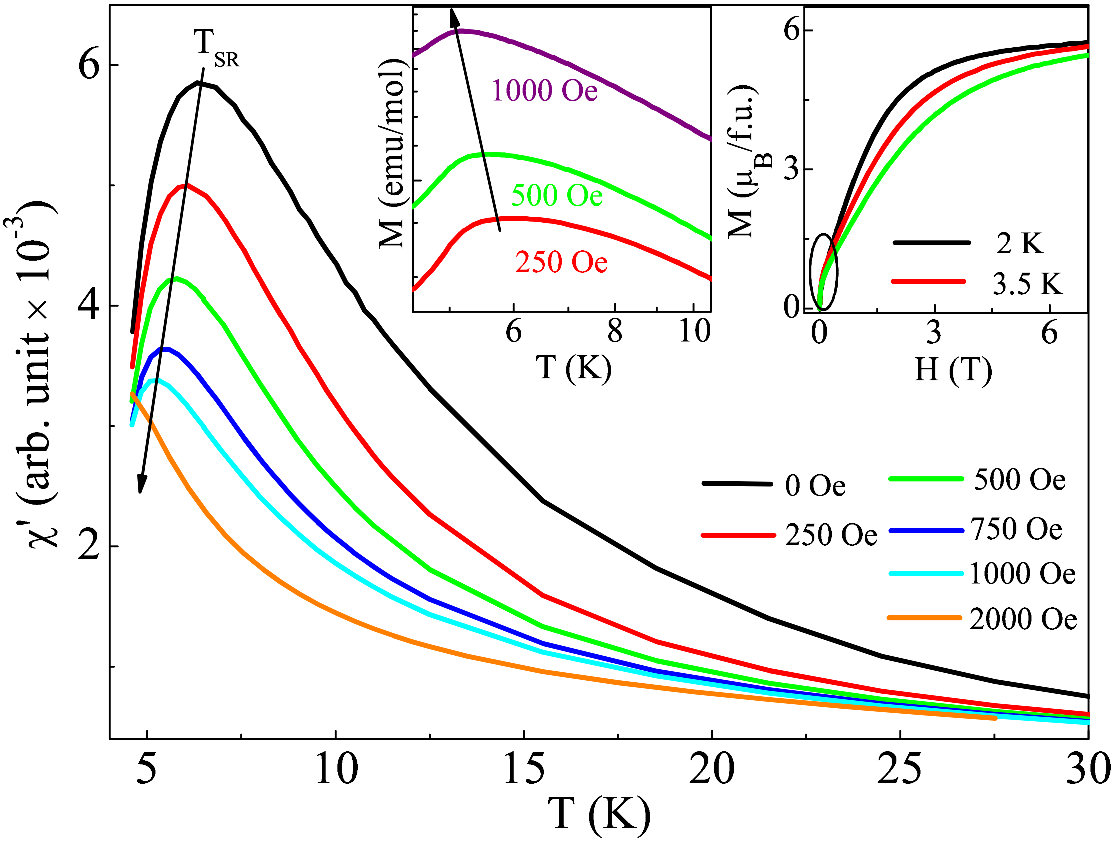

Figure 4.14: Temperature dependence ac susceptibility at different DC fields. Insets shows temperature dependence magnetization under different fields and isothermal $M(H)$ curve at low temperatures displaying spin reorientation behavior.

cycle strong Cr^{3+}-Cr^{3+} interaction at high temperature drives Gd^{3+}-Cr^{3+} interactions resulting alignment of Gd-sublattice opposite to magnetic easy axis,where as in heating cycle dominant Gd^{3+}-Gd^{3+} interactions at low temperature region favors alignment of Gd-sublattice along the external field direction and Cr-sublattice aligns opposite to external field via antiferromagnetic Gd^{3+}-Cr^{3+} interactions. This leads to negative Zeeman energy and kinetically does not favor SF [43].

Additionally, ZFC curve (Figure 4.12 (a)) shows an anomaly at around 7 K, which is attributed as onset of SR transition temperature (T_{SR}) [42, 162, 186, 190], at which continuous rotation of spin configuration occurs in Cr-sublattice from G_zF$_x$-type at low temperature to G_xF$_z$-type at high temperature resulting from the anisotropic Gd^{3+}-Cr^{3+} exchange interaction [42]. Where as, the absence of SR in the FC(C) mode is possibly due to the increment of magnetization caused by SF far exceeds the decrement of magnetization caused by SR.

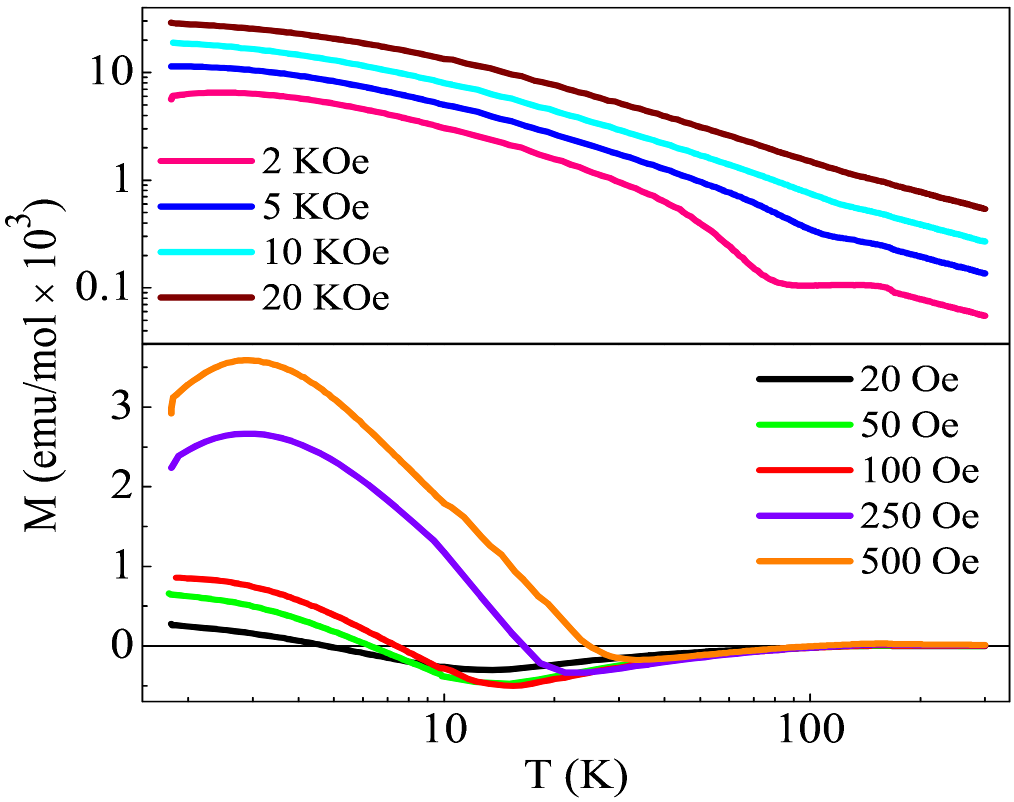

Figure 4.15: Temperature dependence magnetization under different magnetic fields in FC(C) mode.

Further confirmation of SR transition, we performed ac-susceptibility measurements as it is an extremely sensitive technique to detect SR, which depends on the strength of the anisotropies.The real part of ac-susceptibility under different dc magnetic fields are shown in Figure 4.14. SR occurs near 7 K at zero field resembling with ZFC measurement. With increase of applied field, T_{SR} shifts towards low temperature and is suppressed around 2000 Oe resulting G_xF_z phase through out whole temperature region. Sudden change of slope in low temperature M-H curves (Inset) at around 1000 Oe also supports the occurrence of SR in $GdCrO_3$ [162].

Further, M-T measurements in FC(C) protocol under different magnetic fields are shown in Figure 4.15. With increase of external field T_{min} gradually shifts towards high temperature, plausibly because of the increase in the Zeeman energy with the applied field. Finally beyond 2000 Oe, the applied field prevails over the antiferromagnetic Gd^{3+}-Cr^{3+} interaction, resulting in alignment of both sublattices along the field direction, consequently T_{min} disappears and magnetization gradually increases with decrease of temperature. It is observed that the positive and negative magnetization states can be tuned by changing temperature only or by changing the magnetic field at same direction. Such behavior can be utilized in the fabrication of nonvolatile memory, which facilitates two distinct states of magnetization and magnetic cooling/heating based constant temperature bath [193].

Figure 4.16 (a) represents the variation of coercivity (H_c) with temperature. According to Stoner-Wohlfarth (SW) model [194] for a single-domain magnetic particle H_c is directly proportional to the magnetocrystalline anisotropy (K_A), as given by following equation: $H_c = K_A/M_s$, where M_s is the saturation magnetization. In addition, K_A is related to M_s by following relation: $K_A \sim (M_s)^n$, where n is as large as 10 and is often system dependent. Usually, M_s has approximate Brillouin function type temperature dependence behavior (i.e, increase in M_s with decreasing temperature) [194], suggesting that from magneto-crystalline alone, H_c should increase with decrease of temperature. Thus, the observed nonmonotonic behavior of H_c with temperature for the present system can not be explained by magneto-crystalline alone, moreover additional mechanisms are responsible for such variation. It is observed that the initial increasing and then decreasing trend of H_c with decrease in temperature has a good correlation with the decrease of T_{comp1} in magnetization reversal region and increase of T_{comp2} in SF region with increase of applied field, respectively (Figure 4.16 (a)). It corroborates that initial increase in H_c with decreasing temperature is due to the gradual increase of antisymmetric interaction in Cr-sublattice. As below certain temperature Cr^{3+}-Cr^{3+} interaction saturates and contribution from paramagnetic Gd-sublattice via isotropic Gd^{3+}-Cr^{3+} interaction becomes

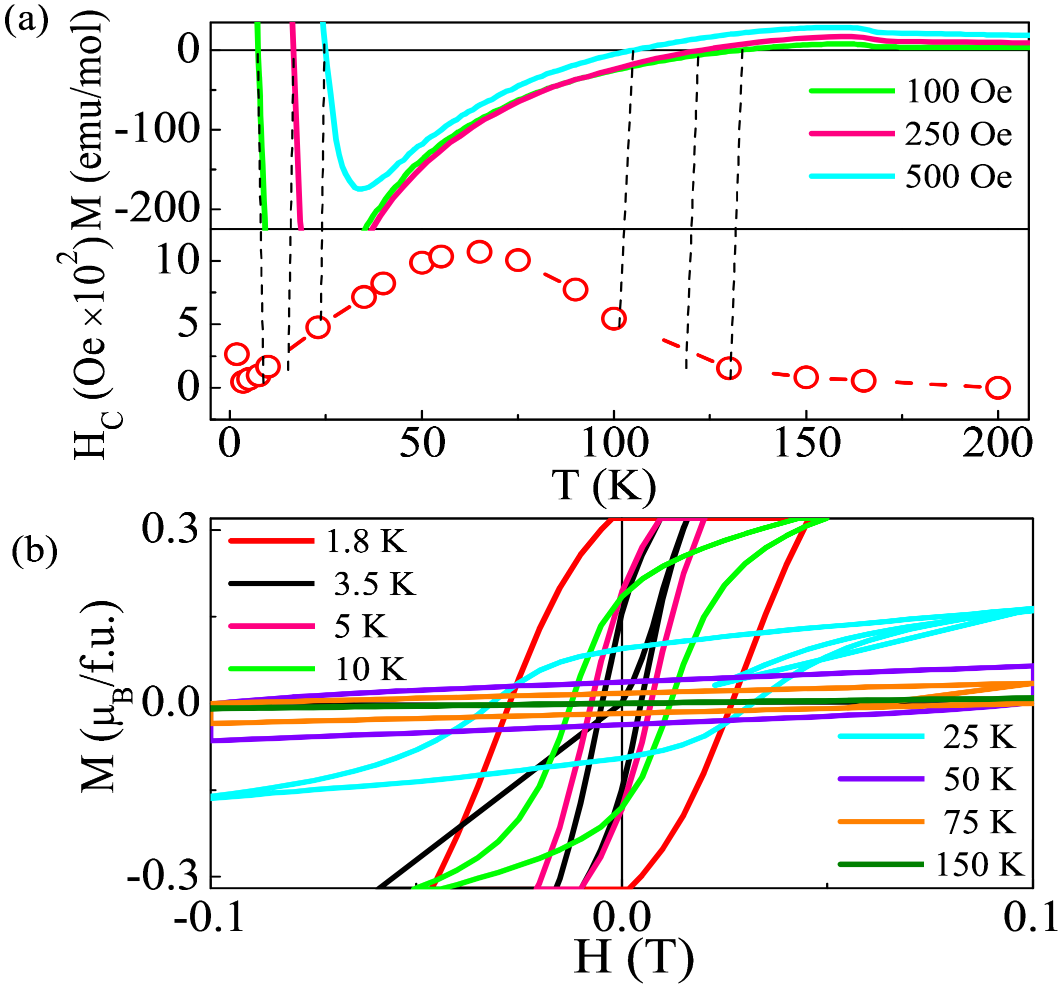

Figure 4.16: (a) Temperature dependence of coercive field (H_c) (bottom) compared with compensation behavior in FC(C) curve at different fields (top). Dotted lines are guide to eye. (b) zoom view of $M(H)$ loops at various temperatures.

increasingly important, resulting in decrease of H_c, as isotropic interaction does not contribute to coercivity [191]. Below T_N(Gd), dominant anisotropic exchange interaction in Gd-sublattice causes again increase of H_c .

4.2.3.2 Raman and spin-phonon coupling studies

We also performed temperature dependent Raman spectroscopy studies. Based on group theoretical analysis of the orthorhombic structure 24 first order Raman active modes are expected for GdCrO$_3$ which are classified as $\Gamma_{Raman} = 7A_g + 7B_{1g} + 5B_{2g} + 5B_{3g}$, involving vibration of Gd and oxygen atoms [195]. Figure 4.17 depicts the temperature dependent Raman spectra at a few selective temperatures both below and above the

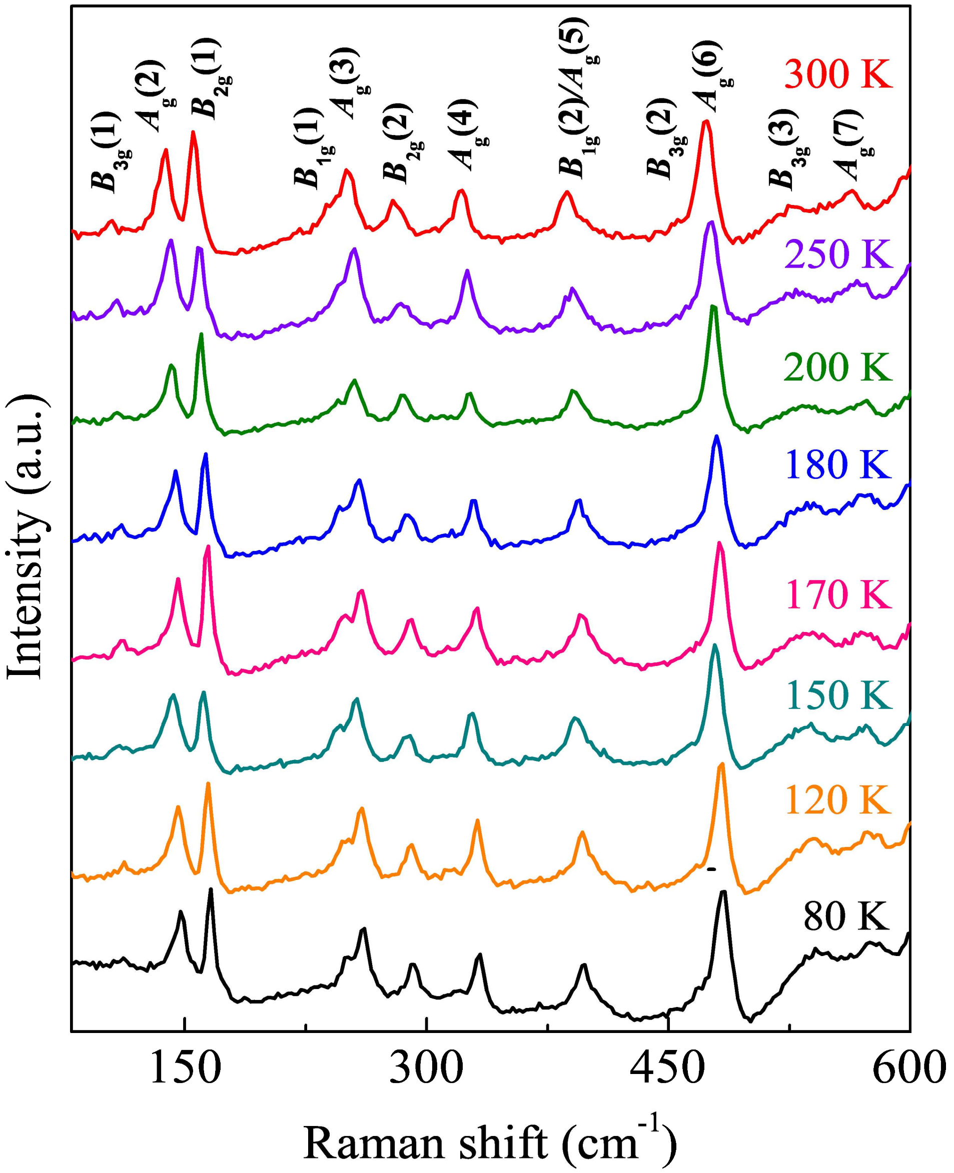

Figure 4.17: Raman spectra of $GdCrO_3$ at few selective temperatures both above and below the magnetic/ferroelectric ordering temperature (169 K).

transition temperature. We see only 14 Raman modes. The absence of other predicted modes are due to very low intensity, which are below the detection limit of the instrument or beyond our experimental range. The phonon modes below 200 cm^{-1} generally arise from the movement of Gd-atoms. $B_{2g}(1)$ and $A_g(3)$ involve out-of-phase and in-phase octahedral z-rotations, respectively. $B_{1g}(2)$ and $A_g(4)$ are related to Gd-O vibrations in GdO_{12} polyhedra. $B_{2g}(2)/A_g(5)$ involve the out-of-phase/in-phase octahedral y-rotations and $B_{3g}(2)$ is associated with out-of- phase bending. $A_g(6)$ involves octahedral bending mode, $B_{1g}(3)$ is associated with in-phase O2 scissor-like vibration and $A_g(7)$ arises from antisymmetric stretching vibration of octahedra [156, 195–197].

At first glance, no new modes emerge down to 80 K from 300 K. Further, to examine the subtle structural changes and the presence of any interactions between lattice and magnetic degrees of freedom, i.e., spin-phonon coupling, the Raman spectra were analyzed by Lorentzian fitting of the peaks. The temperature evolution of the phonon mode frequency comprises various contributions as follows [198],

$$\begin{aligned}\omega(T) &= \omega(0) + (\Delta\omega)_{qh}(T) + (\Delta\omega)_{anh}(T) \\ &\quad + (\Delta\omega)_{el-ph}(T) + (\Delta\omega)_{sp-ph}(T) \end{aligned} \tag{4.8}$$

where $\omega(0)$ is the frequency of the mode at 0 K, $\Delta\omega_{qh}$ (T), $(\Delta\omega)_{anh}$ (T), $(\Delta\omega)_{el-ph}$ (T) and $(\Delta\omega)_{el-ph}$ (T) represent change in phonon frequency due to quasi-harmonic effect (change in lattice parameters of the unit cell), intrinsic anharmonic contribution, electron-phonon coupling and spin-phonon coupling, respectively. The quasi-harmonic effects due to the change in unit cell volume can be approximated by Gruneisen's law relating change in the frquency to the change in lattice volume as given by $(\frac{\Delta\omega}{\omega})_{qh} = \gamma(\frac{\Delta V}{V})$, where γ is the Gruneisen parameter for the given mode and $\frac{\Delta V}{V}$ is the fractional unit cell volume change due to thermal expansion [195, 198]. As $GdCrO_3$ is an insulator, electron-phonon interaction is unlikely to be temperature dependent. Therefore, its contribution to change in phonon modes can be neglected.

The intrinsic anharmonic phonon contribution to the frequency shift can be explained by a simple Klemens model , considering cubic and quartic anharmonic process, i.e., each phonon with frequency ω decays into two (three) phonons of frequency $\omega/2$ ($\omega/3$) for the cubic (quartic) anharmonic process. This process can be described by following relation [199, 200],

$$\begin{aligned}\omega_{anh}(T) &= \omega(0) - A[1 + \frac{2}{e^{\frac{\hbar\omega(0)}{2k_BT}} - 1}] \\ &\quad - B[1 + \frac{3}{e^{\frac{\hbar\omega(0)}{3k_BT}} - 1} + \frac{3}{(e^{\frac{\hbar\omega(0)}{3k_BT}} - 1)^2}], \end{aligned} \tag{4.9}$$

where $\omega(0)$ is the frequency at $T = 0$ K of the mode in harmonic approximation, T is in K, A and B are anharmonicity coefficients for cubic and quartic anharmonic processes, respectively. Figure 4.18 (a) represents the temperature evolution mode associated with

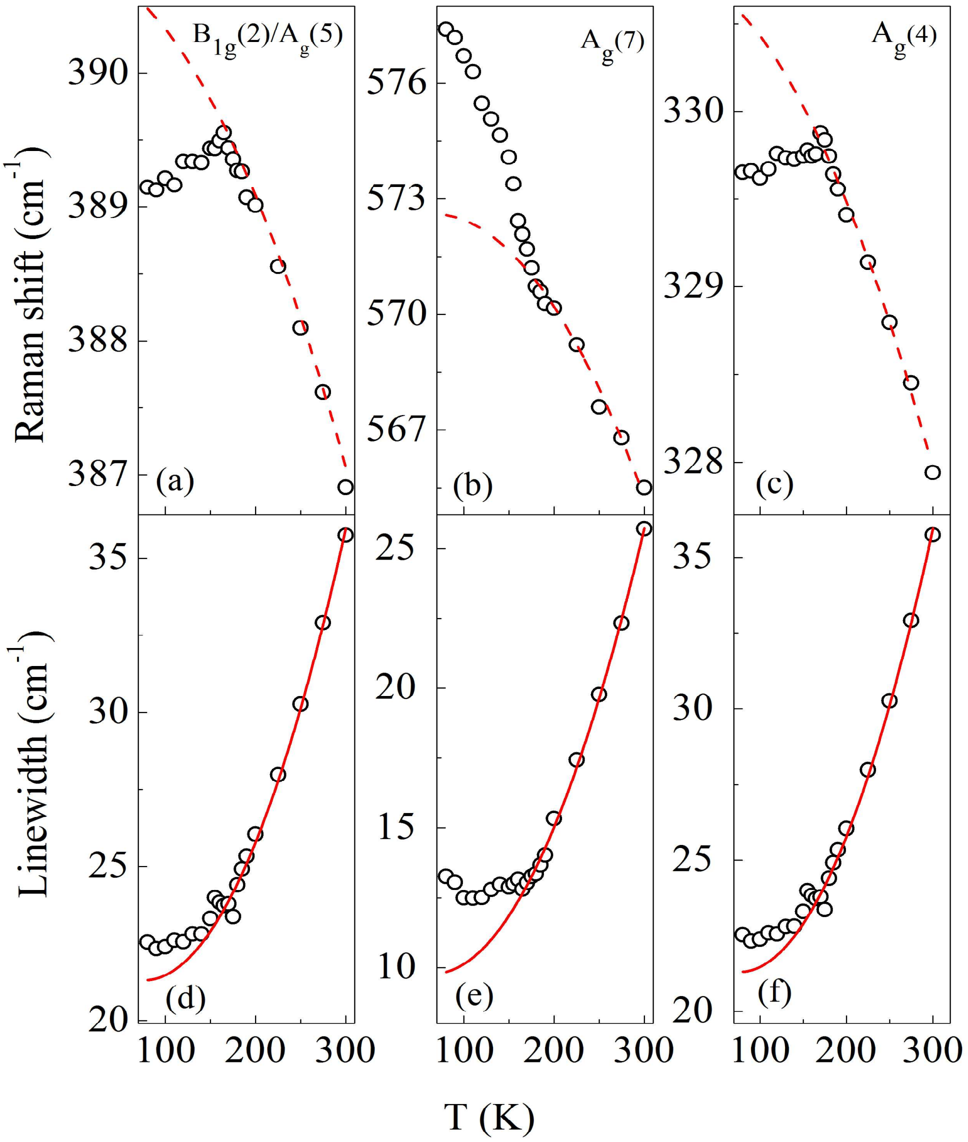

Figure 4.18: (a)-(c) represent temperature dependence of frequencies of few selective modes (octahedral rotation with respect to y-axis ($B_{2g}(2)/(A_g(5))$, antisymmetric stretching ($A_g(7)$) and Gd-O vibration ($A_g(4)$), respectively. The dotted lines represent the fitted curves for anharmonic contributions to these modes according to Eq. 4.9. (d)-(e) represent line widths of corresponding modes and solid lines represent the fitted curves for anharmonic contributions according Eq. 4.9.

the out-of-phase/in-phase octahedral y-rotations ($B_{2g}(2)/A_g(5)$) represented as circles, along with their fitting using Eq. 4.9 marked as dotted line. Below the transition, it shows a pronounced softening from the intrinsic anharmonic contribution. The anomalous behavior of this phonon mode across T_N can be explained by the exchange-striction effect/magnetoelastic coupling. To understand more about the origin of anomalous behavior of various phonon modes such as the presence of spin-phonon coupling, it is necessary to study the temperature dependence of corresponding linewidths as these are related to the phonon lifetime which will not be affected by subtle volume changes due to the exchange-striction effect.

Figure 4.18 (d) shows the temperature evolution of the linewidth of the mode related to octahedral rotations. The anomaly in the linewidth across the transition indicates the presence of spin-phonon coupling in $GdCrO_3$. Such type of spin-phonon coupling was not observed in $R\text{CrO}_3$ having non-magnetic R^{3+} ions such as Y and Lu etc [156]. This suggests the presence of spin-phonon coupling due to the magnetic interaction between Gd^{3+} and Cr^{3+} moments which is mediated by the weak ferromagnetic coupling (canted) of Cr-sublattice. The temperature variations of frequency and corresponding linewidth of antisymmetric stretching mode ($A_g(7)$) are shown in Figure 4.18 (b) and (e), respectively. Such hardening behavior of the antisymmetric stretching mode in $YCrO_3$ has been explained by exchange-striction effect with a major contribution of 30-40% and the remaining contribution coming from magnetic coupling (Cr^{3+}-Cr^{3+} interaction) [195]. Thus spin-phonon coupling can not be ignored in $YCrO_3$ although no significant anomaly in linewidth has been seen by Bhadram *et al.* in this system [156]. Similarly, in $GdCrO_3$ hardening behavior of the antisymmetric stretching mode can be explained by exchange striction effect consistent with the reduction of unit cell volume. In addition, a pronounced anomaly is observed in the linewidth. This indicates a strong spin-phonon coupling, which can be explained by the Gd^{3+}-Cr^{3+} interaction in addition to a contribution from Cr^{3+}-Cr^{3+} interaction. Sharma *et al.* also observed considerable softening of the bending mode along with anomaly in its linewidth in $YCrO_3$ (non-magnetic R-ion) [201], favoring significant contribution of Cr^{3+}-Cr^{3+} magnetic interaction to the spin-phonon coupling below the magnetic transition as discussed here. Moreover, lattice modes related to Gd atoms also show strong softening below the transition along with anomalies in their linewidths as clearly seen in $A_g(4)$ mode (Figure 4.18 (c) and (f)). This suggests a possible displacement of Gd^{3+} ion induced by the spin-phonon coupling caused by Gd^{3+}-Cr^{3+} interaction [156]. As discussed above, the anomalous behavior of various modes is mainly due to exchange-striction effect (lattice contribution) and spin-phonon coupling induced by Cr^{3+}-Cr^{3+} and Gd^{3+}-Cr^{3+} interactions right below the magnetic transition . Granado *et al.* proposed that the spin-phonon coupling strength can be estimated for a given mode by relating the deviation of Raman mode frequency from intrinsic anharmonic contribution to the nearest neighbor spin-spin correlation function $(S_i.S_j)$ as given by [198],

$$\Delta\omega_{sp-ph} = \lambda < S_i.S_j >, \tag{4.10}$$

where λ is the spin-phonon coupling coefficient. In molecular field approximation, the spin-spin correlation function can be described by the square of the sublattice magnetization [202] and also by the normalized order parameter [44]. The temperature dependence of the frequency mode can be written as follows,

$$\Delta\omega_{sp-ph} = \lambda S^2[1-(\frac{T}{T_N})^{\gamma}] \approx \lambda(\frac{M(T)}{M_{max}})^2, \tag{4.11}$$

where T_N is Cr-ordering temperature, $S = 3/2$ is the spin quantum number of Cr^{3+} ion, γ is the critical exponent, $M(T)$ is the magnetization as function of temperature (T). Since different modes involve motions of different atoms, the associated coupling constant (λ) depends on how these motions change the bond lengths and bond angles involving the oxygen atoms which mediate magnetic exchange. As the antisymmetric stretching mode $(A_g(7))$ exhibits the largest deviation from the conventional anharmonic behavior below the transition, this should correspond to possibly the largest value of spin-phonon coupling. Figure 4.19 shows the thermal evolution of $\Delta\omega_{sp-ph}$ below T_N (circle) and its fitting with Eq. 4.10 (dotted line). The good fit obtained by considering only the symmetric Cr^{3+}-Cr^{3+} interaction implies that the antisymmetric interaction (canted ferromagnetism) is very weak. We also found symmetric exchange coupling ($J_e = 11.06$ K) is four times larger than the antisymmetric Dzyaloshinsky-Moriya interaction ($D = 2.64$ K) by fitting the temperature dependence of magnetization with modified Curie-Weiss

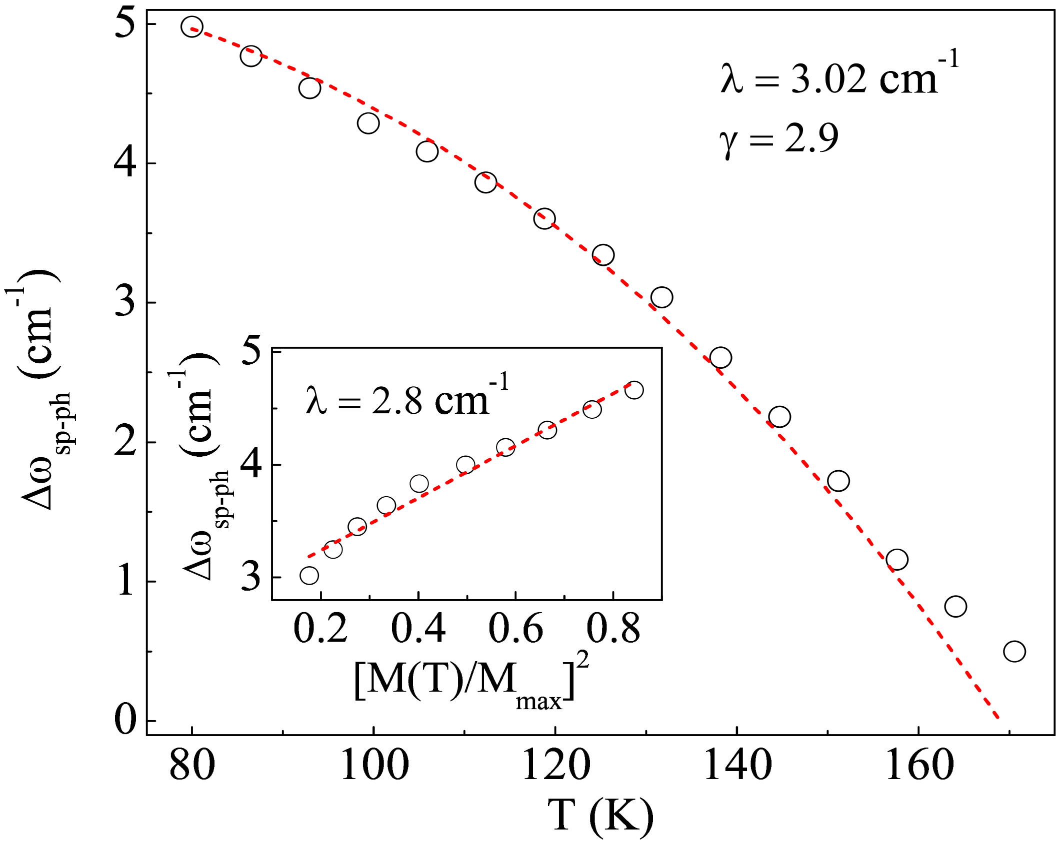

Figure 4.19: Temperature dependence of $\Delta\omega$ of streching mode ($A_g(7)$) below T_N. The dotted line represents the fitting using Eq. 4.10. Inset shows $\Delta\omega$ versus $(M(T)/M_{max})^2$ (circle) and its fitting (dotted line) using Eq. 4.11.

law given by Moriya [48, 191]. From the fitting spin-phonon coupling constant (λ) of 3.02 cm^{-1} and critical exponent (γ) of 2.9 are obtained, while the value calculated for the same from sub-lattice magnetization yields spin-phonon coupling constant (λ) of 2.8 cm^{-1} which is in good agreement with that estimated from the order parameter. The obtained spin-phonon coupling in $GdCrO_3$ is quite comparable to the various systems estimated from Raman modes. For example, in antitiferromagnetic rutile structured MnF_2 and FeF_2 [203] the spin-phonon coupling strength for different modes are in the range from 0.4-1.3 cm^{-1} and for $Sr_4Ru_3O_{10}$ [204], λ is 5.2 cm^{-1}. The above estimated coupling constant considers only the nearest-neighbor Cr^{3+}-Cr^{3+}. In addition, there is an important contribution from Gd^{3+}-Cr^{3+} interaction to spin-phonon coupling as discussed above. These results corroborate the existence of strong magneto-electric coupling in the system as evidenced from dielectric measurement as well as from the enhancement of polarization with magnetic field [154, 156].

4.2.4 Conclusion

In summary, we have studied detailed temperature evolution of magnetic structure in polycrystalline $GdCrO_3$. Strong temperature dependency of various magnetic interactions within and between Gd and Cr-sublatices, leads to emergence of various novel magnetic properties such as TMR, SF and SR. Nearest neighbour symmetric and antisymmetric interaction in Cr-sublattice is found to be $J_e = 11.058$ K and $D = 2.64$ K from modified Curie-Weiss law modeled by Moriya. Occurence of SF in cooling cycle is caused by Zeeman energy between net magnetization and external MF, where as in heating cycle magnetization is along external field direction and does not favor SF. This leads to strong deviation of FC(H) curve from FC(C) curve. In addition, SR occurs in Cr-sublattice at around 7 K and is suppressed at around 2000 Oe. Occurrence of nonlinear behavior of H_c can be successfully explained by competition between antisymmetric Dzyaloshinskii-Moriya interaction in Cr sub-lattice and isotropic Gd^{3+}-Cr^{3+} interaction. Further, we also found a large spin-phonon coupling of 3.02 cm^{-1} from the antisymmetric stretching mode ($A_g(7)$) considering only the symmetric Cr^{3+}-Cr^{3+} interaction, corroborating strong magnetoelectric coupling in this material, which provides a complementary tool for the enhancement of ferroelectric polarization.

Chapter 5

Site-substitution in $GdMnO_3$: effects on structural, electronic and magnetic properties

---

In this chapter, we discuss evolution of structural, electronic and magnetic properties of Cr-doped $GdMnO_3$ *(*$GdMn_{1-x}Cr_xO_3$*,* $0 \leq x \leq 1$*). In the solid solutions, the Jahn-Teller (JT) distortions associated with* Mn^{3+} *ions give rise to major changes in the bc-plane sub-lattice and also the effective orbital ordering in the ab-plane, which persist up to the compositions* $x \sim 0.35$*. These distinct features in the lattice and orbital degrees of freedom are also correlated with bc-plane anisotropy of the local Gd environment. A gradual evolution of electronic states with doping is also clearly seen in O* K*-edge x-ray absorption spectra. Evidence of magnetization reversal in field-cooled-cooling mode for* $x \geq 0.35$ *coinciding with JT-crossover, suggests a close correlation between magnetic interaction and structural distortion. These observations indicate a strong coupling between lattice, spin, electronic and orbital degrees of freedom. Density functional theory calculations using GGA + U type exchange correlation potential showed that the system with intermediate composition (*$GdMn_{0.5}Cr_{0.5}O_3$*) consists of alternate ferromagnetic Mn layers and antiferromagnetic Cr layers, which is distinct from that observed for the end members* $GMnO_3$ *(A-type) and* $GdCrO_3$ *(G-type).*

5.1 Introduction

Functional oxides with perovskite structures (ABO_3) are very active research area due to their potential technological applications and for their fundamental importance in basic scientific research. An unusual aspect of perovskites is their ability to incorporate most of the elements of the periodic table at the A and B sites due to their capacity to accommodate various structural distortions [35]. External parameters like temperature, pressure and chemical compositions can also effect such distortions, which leads to an extraordinary richness of physical properties within the family of perovskites. Structural distortions in perovskites are mainly associated with three main features with respect to their ideal cubic structure: [35–37] (i) rotation (tilt) of BO_6 octahedra, (ii) polar cation displacements, which often lead to ferroelectricity, and (iii) distortions of the octahedra, such as the JT distortion.

Rare-earth manganites (RMnO$_3$) forms an interesting series of materials owing to the JT character of Mn^{3+} ions. A complex interplay among the spin, orbital and lattice degrees of freedom has led to a large number of intriguing physical properties in RMnO$_3$ such as colossal magnetoresistance [205], charge and orbital ordering [206–208], metal-insulator transition [209, 210], complex spin structures [40], multiferroic properties with significant magnetoelectric coupling [4], etc. In contrast, Cr^{3+} is JT inactive ion because of having completely empty e_g orbitals and therefore the oxygen octahedra are more regular. On the other hand, most of the members of RCrO$_3$ family are reported to be multiferroic at considerable high temperature [154]. Additionally, RCrO$_3$ systems are of great interest as these exhibit wide spectrum of magnetic properties as well such as spin-reorientation (SR), spin-flipping (SF) and temperature induced magnetization reversal (TMR), etc [43, 44].

$GdMnO_3$ exhibits incommensurate sinusoidal magnetic structure arising from competing nearest-neighbor ferromagnetic (NN-FM) and next-nearest-neighbor antiferromagnetic (NNN-AFM) interaction followed by canted-A-type ordering in Mn-sublattice [40]. Additionally, a low temperature ferroelectric ordering is established, caused by Gd^{3+}-Mn^{3+} spin interaction and/or lattice distortion associated with magnetic field-induced spin rearrangements [41, 211]. $GdCrO_3$ is one of the G-type antiferromagnetic (AFM) RCrO$_3$ compounds, exhibiting extremely rich magnetic properties like TMR, SF, SR and

others [190]. It has non-centrosymetric $pna2_1$ structure, associated with the ferroelectric transition concurrent to Cr magnetic ordering temperature with significant magnetoelectric coupling [154]. Although the parent compounds, $GdMnO_3$ and $GdCrO_3$ are well investigated, the off-stoichiometry series $GdMn_{1-x}Cr_xO_3$ is largely unexplored [212]. Various interesting properties have been reported in similar type off-stoichiometric compositions such as re-entrant spin reorientation ($\gamma_4 \rightarrow \gamma_1 \rightarrow \gamma_4$) and abundant magnetic phase diagram in $TbMn_{1-x}Fe_xO_3$ [213] and rich magnetic phase diagram in $DyMn_{1-x}Fe_xO_3$ [179], $YbMn_{1-x}Fe_xO_3$ [214] and $TbMn_{1-x}Cr_xO_3$ [215] and many more.
Here, we report on the systematic structural, electronic and magnetic characterizations of the solid solutions of $GdMn_{1-x}Cr_xO_3$ ($0 \leq x \leq 1$). Doping $GdMO_3$ (M = Mn/Cr) gives rise to M-sites dilutions and average lattice distortions in the compound, resulting in a critical crossover from JT active region to JT inactive region in $GdMn_{1-x}Cr_xO_3$.

5.2 Experimental and Theoretical Details

A series of Cr-doped gadolinium manganites, $GdMn_{1-x}Cr_xO_3$ ($0 \leq x \leq 1$) was prepared by the solid-state synthesis technique at ambient pressures. Stoichiometric proportions of Gd_2O_3, Mn_2O_3 and Cr_2O_3 were mixed thoroughly and heated at 1300 ^{0}C for 24 h in air with several intermediate heating and grindings. The product was then pressed into pellets and finally sintered at 1400 ^{0}C for 24 h. The crystalline structure and phase purity of the solid solutions were confirmed by x-ray diffraction (XRD) measurements using Bruker D8 Advance X-ray diffractometer equipped with Cu K_α radiation. Structural investigations were done by Rietveld refinements of the obtained powder XRD patterns using the FULLPROF program. Raman measurements were performed using a micro-Raman spectrometer (inVia, Renishaw, United Kingdom) with 514.5 nm excitation of an Ar^+ laser. Spectra were collected in the backscattering configuration using a thermo-electrically cooled CCD camera as the detector. A long working distance 50× objective with a numerical aperture of 0.45 was used for the spectral acquisition. Magnetization measurements were carried out using SQUID-VSM from Quantum Design US. The O K-edge x-ray absorption spectra were recorded in total electron yield (TEY) mode at the CIRCULARPOLARIZATION beamline at the Elettra synchrotron radiation facility.

Theoretical calculations of the structural, electronic and magnetic properties were based on density functional theory, using generalized gradient approximation (GGA) with Perdew Burke Ernzerhof for solids (PBEsol) [97] parameterization for the exchange correlation potential, the projector argumented wave (PAW) method [95], and a plane-wave basis set, as implemented in the Vienna ab-initio simulation package (VASP) [100]. The interaction between ions and electrons was approximated with PAW potentials, treating $3p$, $3d$ and $4s$ for Cr/Mn and $2s$ and $2p$ for O as valence electrons. For Brillouin zone sampling, we chose 12×12×8 Monkhorst-Pack k-point mesh [161] and the wave-function was expanded in a basis set consisting of plane waves with kinetic energies less than or equal to 770 eV. Using these parameters, an energy convergence of less than 1 meV/formula unit (f.u.) was achieved. Structures were fully relaxed until residual HellmannFeynman (HF) forces were smaller than 0.001 eV/$\AA$ while maintaining the symmetry constraints of the given space group. Gd-$4f$ electrons were treated as valence electrons for parent compounds. We performed calculations using different Hubbard U values up to 4 eV for Mn/Cr and 4 eV for Gd and results for $U = 3$ eV for Mn/Cr and 4 eV for Gd explained satisfactorily the experimental results, which would be explained in later section. In $GdMn_{0.5}Cr_{0.5}O_3$, Gd-$4f$ electrons were assumed as core electrons to reduce the calculations time. Irrespective of this, the $4f$ states lie deep in energy and they are almost completely localized so that they do not affect other valence states [216]. To visualize the orbital ordering in $GdMnO_3$, in addition to the global X, Y, Z orthorhombic frame a local frame specific to each Jahn-Teller-type distorted MnO_6 octahedron was defined choosing x, y, z along the middle, short, and long Mn-O axes, respectively [216].

5.3 Results and discussion

5.3.1 Structural studies

Figure 5.1 (a) depicts room temperature XRD patterns of the solid solutions along with the corresponding refined patterns considering orthorhombic $Pbnm$ space group except for $GdCrO_3$, which posseses $Pna2_1$ space group as discussed in chapter 4. The composition dependent evolution of the lattice parameters (a, b, and $c/\sqrt{2}$) and cell volume (V)

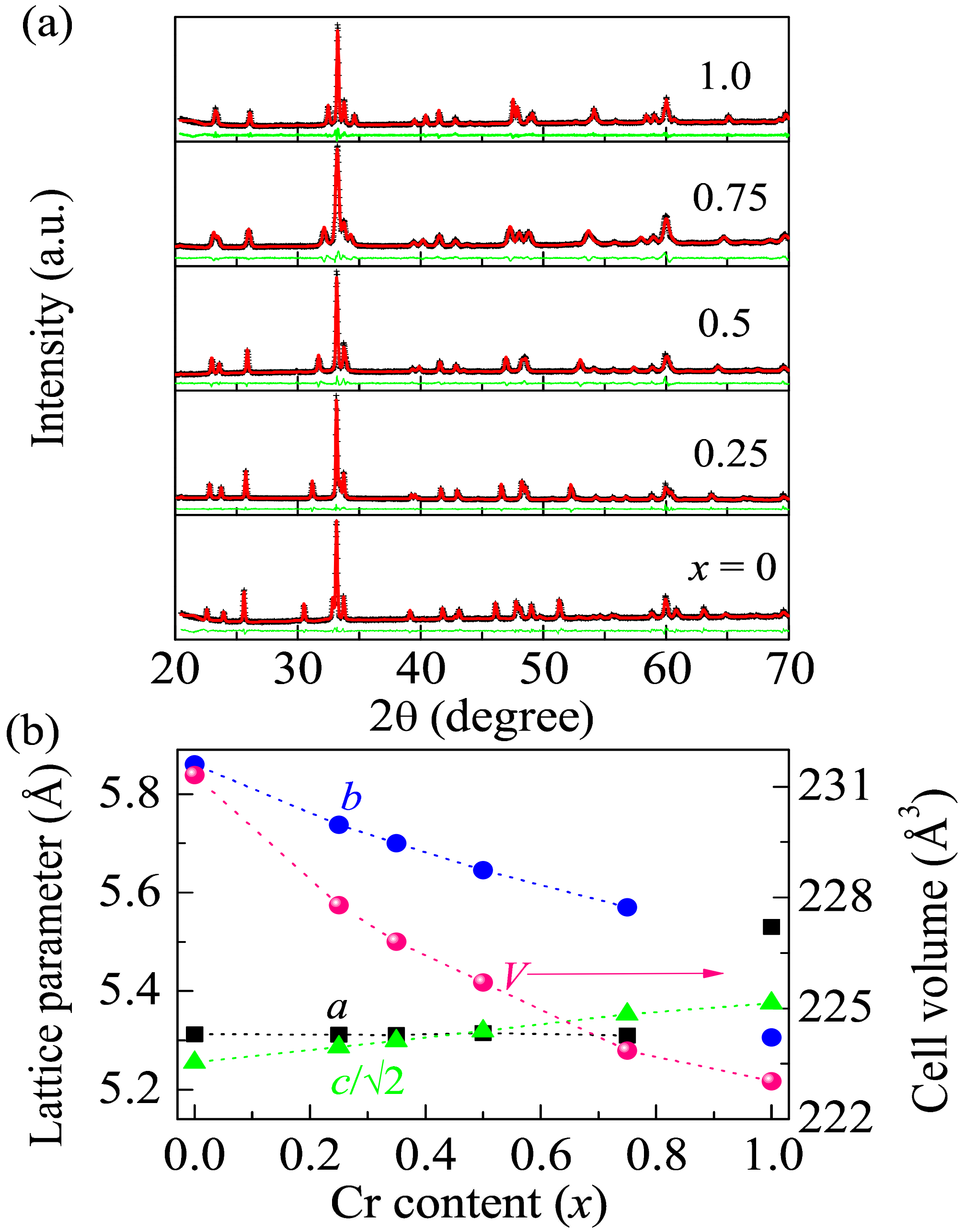

Figure 5.1: (a) The Rietveld-refinement plots of room temperature XRD patterns of $GdMn_{1-x}Cr_xO_3$ ($x = 0$, 0.25, 0.5, 0.75 and 1.0) in the space group of *Pbnm*. Experimental data is presented with symbol while the fitted curves from the Rietveld analysis are represented as red line. Difference spectra (difference between experimental data and fitting) is plotted in blue line. (b) Evolution of the cell parameters (a, b, and, $c/\sqrt{2}$ (left panel) and cell volume (V) (right panel) as a function of compositions (x). As $GdCrO_3$ has $pna2_1$ symmetry, lattice parameters a and b interchanges with respect to other compositions having $Pna2_1$ symmetry.

in $GdMn_{1-x}Cr_xO_3$ are shown in Figure 5.1 (b). There is a remarkable decrease in the b-axis, accompanied with an increase of the c-axis with increase of Cr-content, while the a-axis remains almost constant. This suggests that lattice degrees of freedom confined to the bc-plane are strongly affected by the substitution of Cr. Further, the decrease in the cell volume reveals that the c-axis elongation is dominated by the b-axis reduction. Such structural characteristics can not be explained by only considering the ionic radii of Cr^{3+} ion (0.615 Å) into the site of Mn^{3+} ion (0.645 Å). Therefore, a detailed structural investigation was carried out.

The composition-dependent variations of three M-O bonds (M = Mn/Cr) in the MO_6 octahedra, obtained from Reitveld refinements are shown in Figure 5.2 (a), with l_x, l_y and l_z denoting bond lengths along the respective local axes. The intrinsic octahedral distortion in orthorhombic structure allows the short and long bonds to lie within the ab-plane and the middle-length bond, along the c-axis [179, 217]. The large differences among the three M-O bond-lengths in $GdMnO_3$ are correlated with the cooperative JT distortion of Mn^{3+} ion along with a contribution from intrinsic structural distortion. In contrast, $GdCrO_3$ exhibits a regular structure with the similar bond-lengths for l_x, l_y and l_z, which is consistent with the quenched JT distortion for Cr^{3+} ion. The local modes characterizing the JT distortion are defined as in-(ab) plane orthorhombic distortion, Q_2 [$= l_y$-l_x] and out-of-plane tetragonal-like distortions, Q_3 [$= (2l_z$-l_x-$l_y)/\sqrt{3}$] [179, 218, 219], which are illustrated in Figure 5.2 (b). The large positive value of Q_2 in $GdMnO_3$ is associated with the cooperative JT distortion, which is along the b-axis and Q_3 with negative sign indicates that an out-of-plane distortion along the c- axis is competing with the JT distortion [179, 218]. This implies that the lattice deformation is primarily confined to the bc-plane sub-lattice. In addition, the larger magnitude of Q_2 over Q_3 also indicates that the increase of c-axis is largely overwhelmed by decrease of b-axis. Upon approaching towards $GdCrO_3$ the decrease of both Q_2 and Q_3 reveals gradual decrease of JT and tetragonal distortions. An intriguing slope crossover in both Q_2 and Q_3 around $x \sim 0.35$ (guided by the dotted lines in Q_2) indicates suppression of long range structural distortion associated with local JT distortion at the Mn sites.

Further examination of the average octahedral distortion Δ_d [$= (1/6) \sum_{n=1-6} [(d_n$-$\langle \mathrm{d} \rangle)/\langle \mathrm{d} \rangle]^2$, where d_n ($\langle \mathrm{d} \rangle$) is the individual (average) M-O bond length] is shown in

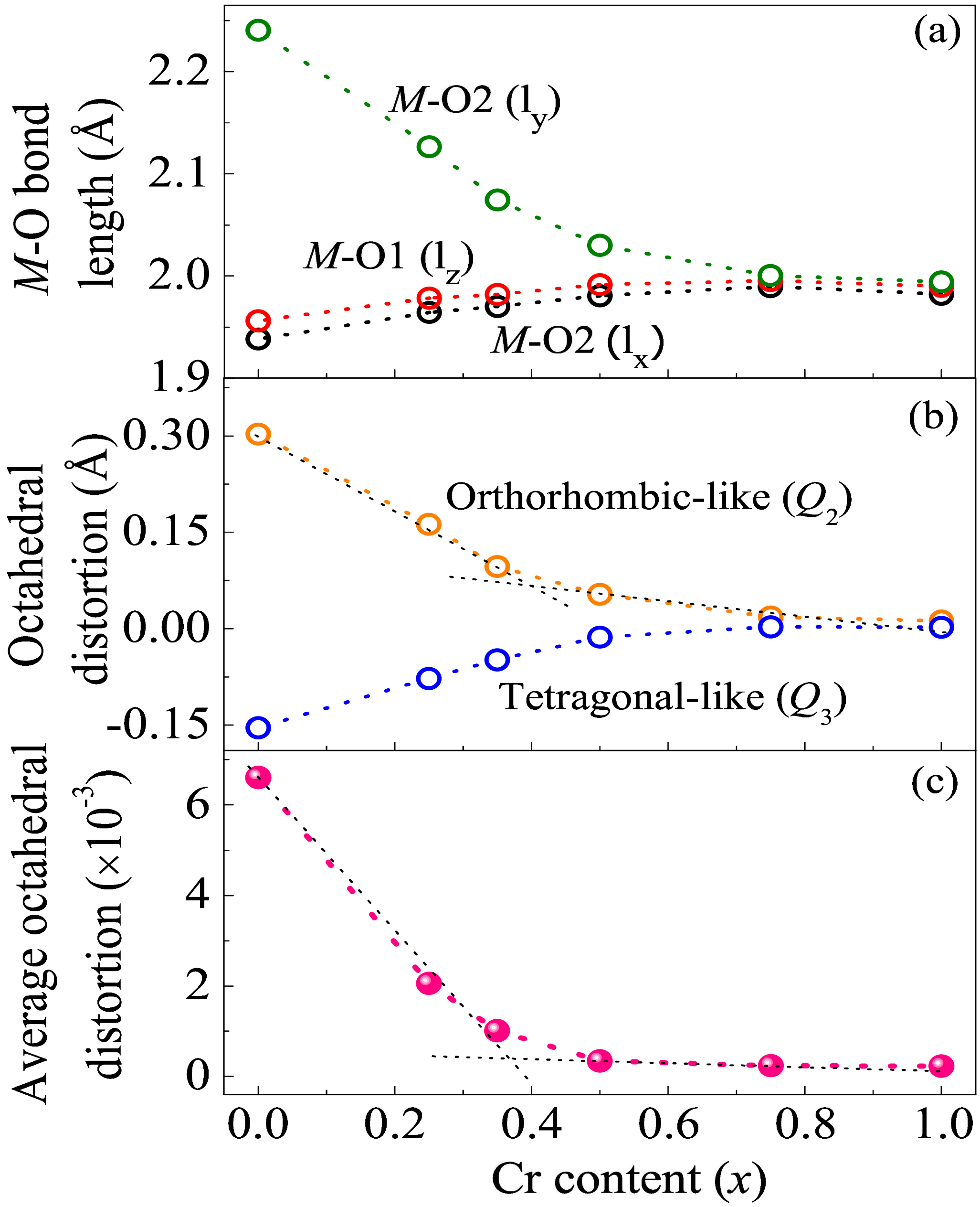

Figure 5.2: (a) The composition-dependent variations of the M-O bonds in the MO_6 octahedra of $GdMn_{1-x}Cr_xO_3$, with the long, short M-O2 bonds and the middle M-O1 bond, respectively. O1 (O2) represents the apical (equatorial) oxygen along the c-axis. (b) The composition-dependent variations of in-(ab)plane orthorhombic-like (Q_2) and out-of-plane tetragonal-like (Q_3) distortions . Dotted line guiding Q_2 point to the slope crossover around $x \sim 0.35$. (c) Variation of average octahedral distortion evaluated by Δ_d . Dotted lines guiding Δ_d to the slope crossover as a result of effective supression of JT orbital ordering around $x \sim 0.35$. All the parameters are derived from the Rietveld refinements of the respective XRD patterns.

Figure 5.2 (c). Δ_d shows an slope changeover around $x \sim 0.35$ (guided by the dotted lines), indicating a critical crossover from JT-active region to JT-inactive region.

JT-effect results in lifting of degeneracy of e_g orbitals of Mn^{3+} ions and builds up *ab*-plane staggered orbital ordering. For more understanding, a polar plot of magnitude of the octahedral-site distortion, ρ_0 $(= Q_2^2 + Q_3^2)$ versus the angle ϕ $(= \tan^{-1}(\frac{Q_3}{Q_2})$ was mapped for the compositions as shown in Figure 5.3 (a), where ϕ opens from the Q_2 axis in anticlockwise direction [220].

The description of the e_g orbital associated with the M atom in an MO$_6$ octahedron can be made by the wave function ψ with a linear combination of orbitals $|x^2 - y^2\rangle$ and $|3z^2 - r^2\rangle$ in the (Q_2, Q_3) space as given by [39, 221]

$$\psi(\theta) = cos(\theta/2)|3z^2 - r^2\rangle + sin(\theta/2)|x^2 - y^2\rangle$$

where the angle θ ($\theta = 90^0 + |\phi|$) represents respective orbital components, which opens anticlockwise from the Q_3 axis. The $\theta = 0$, $2\pi/3$ and $4\pi/3$ correspond to orbitals $|3z^2 - r^2\rangle$, $|3y^2 - r^2\rangle$ and $|3x^2 - r^2\rangle$, respectively and $\theta = \pi/3$, π and $5\pi/3$ represent $|y^2 - z^2\rangle$, $|x^2 - y^2\rangle$ and $|z^2 - x^2\rangle$, respectively. For an octahedral site distortion, which has a θ deviating from these special angles reflects the presence of orbital ordering along with orthorhombic distortion in the material. Figure 5.3 (b) depicts the the schematic representation of orbital ordering in Mn^{3+} ions in GdMnO$_3$. Since for all compositions in GdMn$_{1-x}$Cr$_x$O$_3$, θ falls between the special angle and close to $2\pi/3$ for one of the co-planner Mn-sites (site 1) as defined in Figure 5.3 (b) (it is close to $4\pi/3$ for site 2), we can define a new angle γ = $\pi/6$ - ϕ to simplify the wave functions. Thus, wave functions for occupied (e_g^1) and unoccupied (e_g^2) orbitals for site 1 can be written as follows [39, 221]

$$\psi_{occ}(\gamma) = cos(\gamma/2)|3y^2 - r^2\rangle + sin(\gamma/2)|z^2 - x^2\rangle$$
$$\psi_{unocc}(\gamma) = -sin(\gamma/2)|3y^2 - r^2\rangle + cos(\gamma/2)|z^2 - x^2\rangle$$

The total site distortion as measured by, ρ_0 remains above 0.3 up to $x \sim 0.1$ composi-

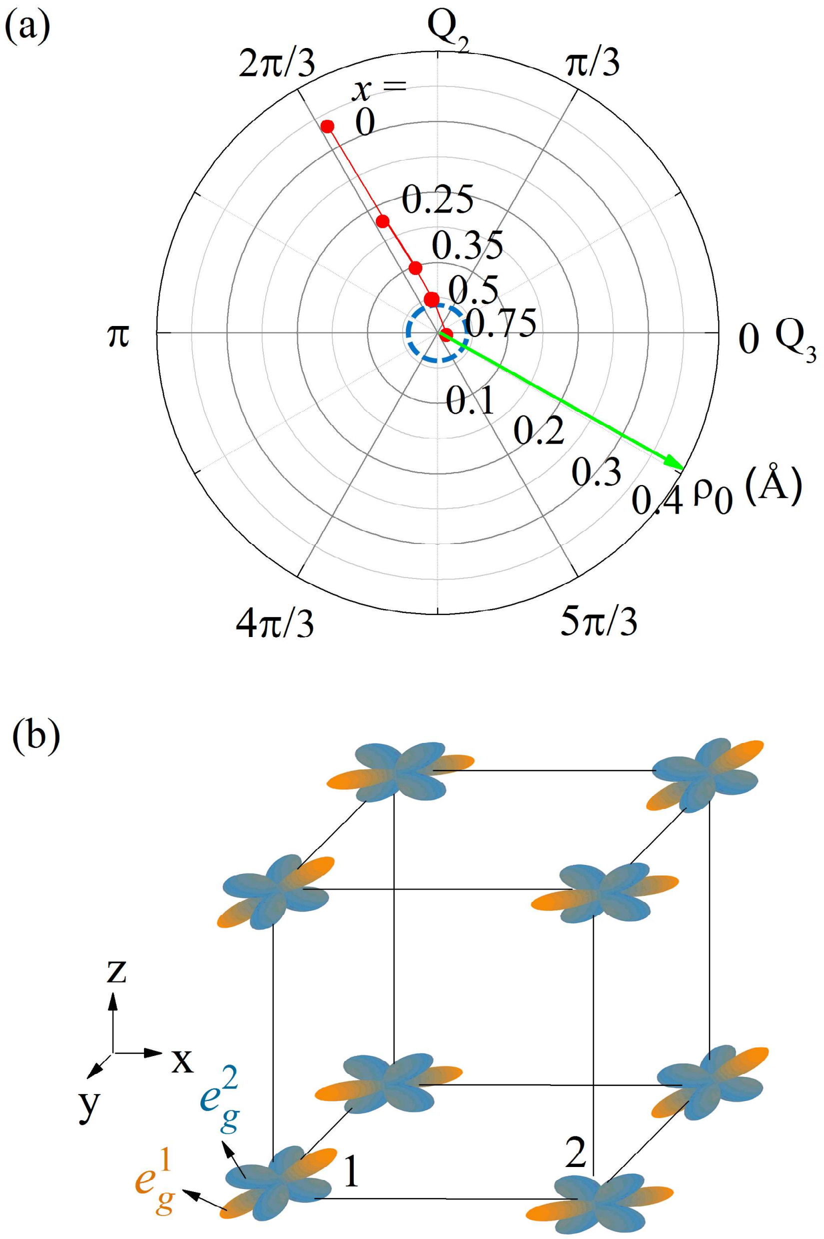

Figure 5.3: (a) The polar plot of ρ_0 $(= Q_2^2 + Q_3^2)$ and ϕ $(= \tan^{-1}(\frac{Q_3}{Q_2}))$, which are used to describe the orbital mixing in $GdMn_{1-x}Cr_xO_3$. (b) Schematic diagram of e_g orbitals of Mn^{3+} due to the JT orbital ordering.

tions, reflecting a dominant contribution from a static JT orbital mixing along with the octahedral distortion [39, 221]. Whereas for $x = 0.5$ and higher compositions, ρ_0 is about one order of magnitude smaller than that of JT-active $GdMnO_3$ and other manganites ($RMnO_3$) and compared to the value found in JT-inactive rare-earth ferrites ($RFeO_3$) and

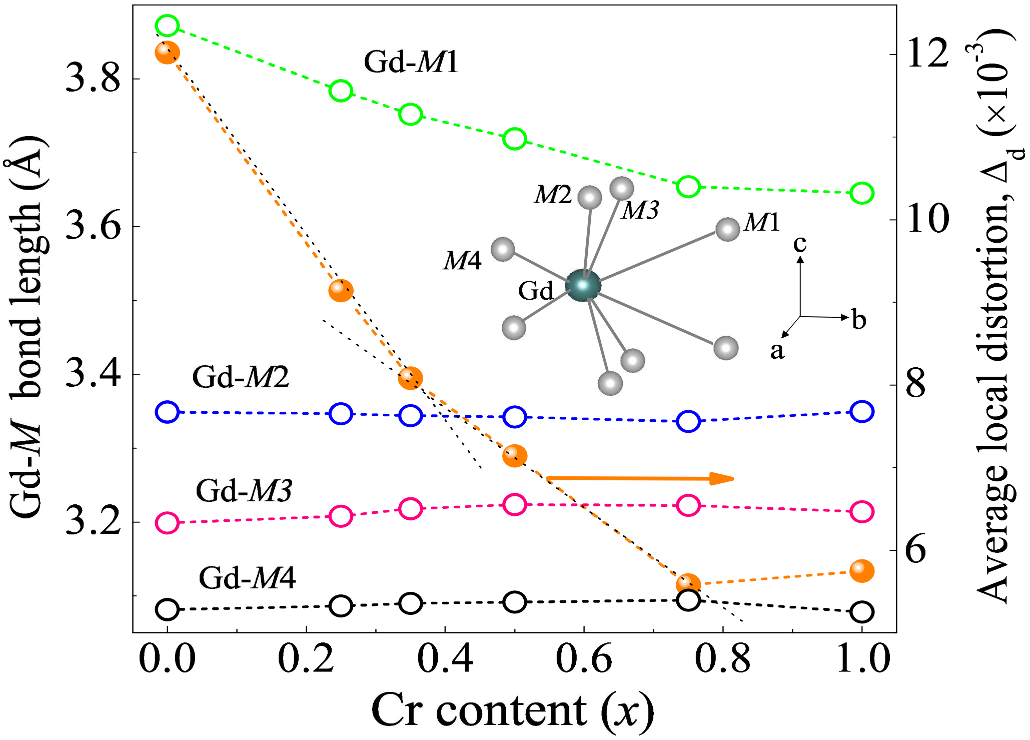

Figure 5.4: The evolution of the lattice anisotropy specific to the local Gd environment through variations in the nearest neighbor Gd-M bond lengths. Right panel represents corresponding average distortion (Δ_d) in the local Gd-M environment. Dotted lines guiding Δ_d signify the slope crossover around x ∼ 0.35. Inset represents nearest neighbor Gd-M bond lengths with blue atom,Gd and gray atoms, M. All the parameters are derived from the Rietveld refinements of the respective XRD patterns.

vanadites (RVO$_3$) indicating the disappearance of orbital ordering [39, 218, 221].

To examine lattice anisotropy specific to the local Gd environment, NN Gd-M bond lengths are plotted, as shown in Figure 5.4. There are eight NN-coordinated M which are doubly paired as M1-M4, as viewed schematically in the inset of Figure 5.4. Each pair of Gd-M lengths are equivalent for all compositions except GdCrO$_3$, in which they are unequal (slightly) due to the $Pna2_1$ symmetry. The longest Gd-M1(shortest Gd-M4) lying in the bc-plane, shows visible reduction (slight increase) towards $x = 1$, which is due to the suppression of JT distortion predominantly along the b-axis. The corresponding average local distortion, Δ_d [$= (1/8) \sum_{n=1-8} [(d_n\text{-}\langle \mathrm{d} \rangle)/\langle \mathrm{d} \rangle]^2$, where d_n ($\langle \mathrm{d} \rangle$) is the individual (average) Gd-M bond length] also shows a decrease of local anisotropy with increase of Cr-content and further slight increase in GdCrO$_3$ owing to having $Pna2_1$ symmetry. A slop change occurs (guided by dotted line) around the critical concentration, $x \sim 0.35$ of

JT-crossover, consistent with earlier discussions. This suggests that the evolution of lattice and orbital degrees freedom in the solid solutions is also correlated with the *bc*-plane anisotropy in the local Gd-environment [179].

5.3.2 Raman studies

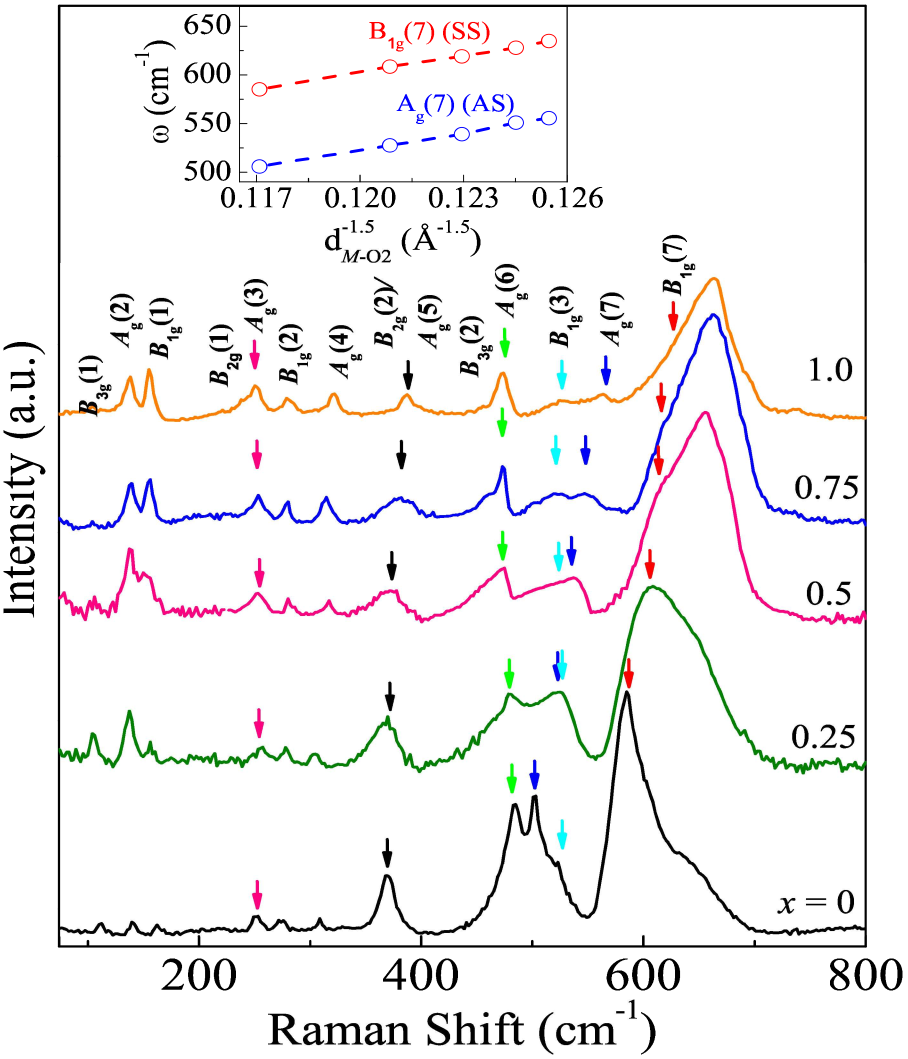

Figure 5.5: (a) Evolution of room temperature Raman spectra with compositions (x) in $GdMn_{1-x}Cr_xO_3$ (x = 0, 0.25, 0.5, 0.75 and 1.0). The inset shows the linear dependence of the JT symmetric stretching [$B_{1g}(7)$] and antisymmetric stretching [$A_g(7)$] modes frequency with the $d_{M-O2}^{-1.5}$, where d_{M-O2} is the average of short and long M-O2 bond lengths.

The knowledge of the lattice/atomic vibrations and their correlations to the structural distortion is of crucial importance. In order to throw some light on this issue, room temperature Raman measurements were performed in $GdMn_{1-x}Cr_xO_3$, as depicted in Figure 5.5. For isostructural orthorhombic structure, the group theory predicts 24 Raman active modes $(7A_g + 7B_{1g} + 5B_{2g} + 5B_{3g})$ at the Γ point of the Brillouin zone [222, 223]. However, we see only 14 Raman active modes. The other predicted modes are either of too low intensity to be observed or are beyond our experimental range. The details about the observed modes up to 600 cm^{-1} are described in chapter 4. We believe the modes around 670 cm^{-1} may be the disorder-induced phonon density of states of oxygen vibrations [224,225]. Besides, Kovaleva *et al.* argued that there is an additional component to the multi-order scattering, which may arise from coupling between the low-energy electronic motion and the vibrational modes [226].

The most common distortion in orthorhombic *Pbnm* stucture is the tilting of BO_6 octahedra, which can be described either by orthogonal tilt angles (denoted by $a^-a^-c^+$ Glazers notation) or by octahedral tilts θ, ϕ and Φ around the pseudocubic $[110]_{pc}$ and $[001]_{pc}$ and $[111]_{pc}$ axis [37, 196, 227, 228]. The Raman modes, $A_g(3)$ and $A_g(5)$ are correlated with the tilt angles ϕ and θ, respectively [196, 222]. The position of $A_g(3)$ remains unchanged throughout the series i.e. ϕ remains constant. In contrast, $A_g(5)$ shows hardly any shift up to $x \sim 0.5$ compositions, whereas it shifts around 15 cm^{-1} towards high frequency for $x = 0.75$ and 1.0 compositions. This, in turn, suggests that θ remains more or less constant up to $x \sim 0.5$ compositions and slightly increase (negligibly small) for $x = 0.75$ and 1.0 compositions. Furthermore, Φ is correlated with θ and ϕ via the relation, $\cos\Phi = \cos\theta \cos\phi$ [196, 227]. This implies Φ remains constant up to $x = 0.5$, thereafter it slightly increases for $x = 0.75$ and 1.0 compositions. The in-plane antisymmetric stretching $[A_g(7)]$ and symmetric stretching $[B_{1g}\ (7)]$ modes are the JT modes, which are associated with the M-O2 bond lengths in ab-plane. The variation of frequency of these modes are correlated with M-O2 bond lengths by the relation as given by, $\omega \propto d_{M-O2}^{-1.5}$ [222, 229] and this holds good here, as shown in the inset of Figure 5.5. With Cr-doping there is a rapid decrease of M-O2 bond length up to $x \sim 0.5$ (Figure 5.2) leading to clear shift of these two modes after that shift is less. Furthermore, the spectral weight also decreases dramatically with increase of Cr-content (x) due to the reduction of JT distortion and becomes weak for 0.75 and 1.0 compositions, which are the JT-inactive compounds.

5.3.3 Electronic structure studies

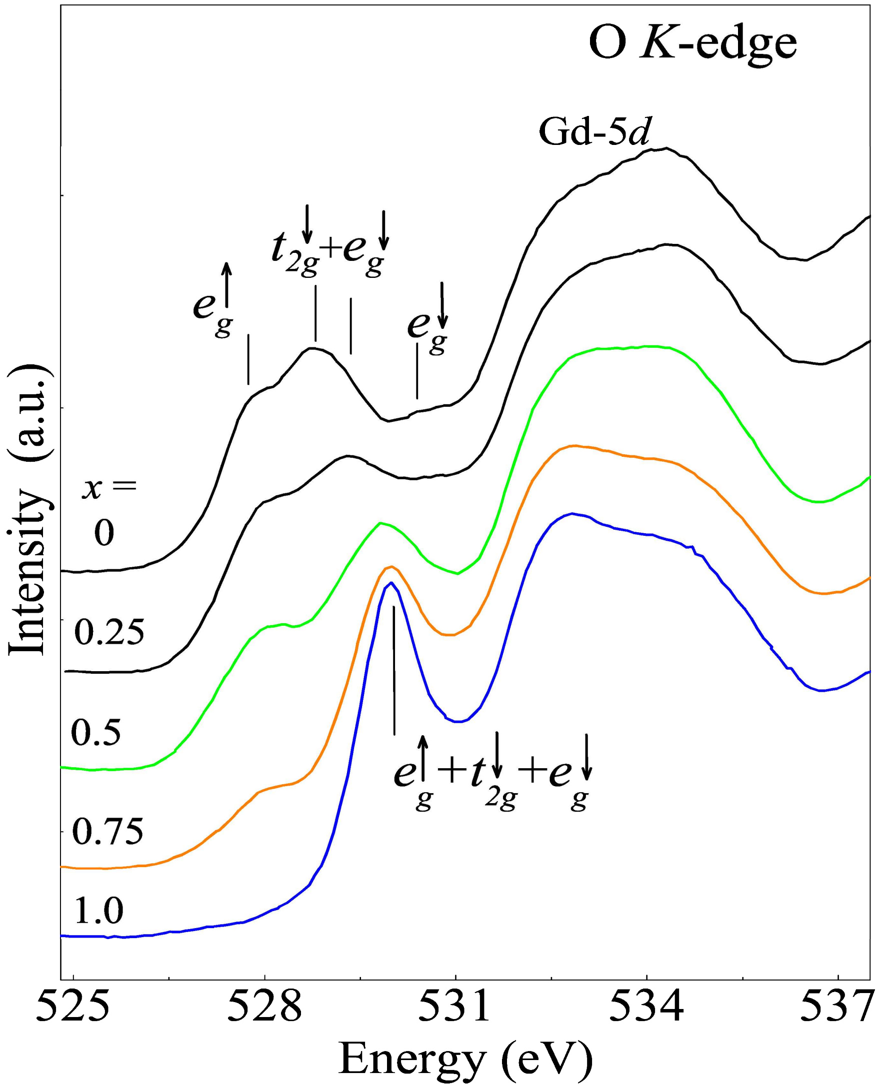

Figure 5.6: Evolution of O K-edge XAS spectra with compositions (x) in $\mathrm{GdMn_{1-x}Cr_xO_3}$ ($x = 0$, 0.25, 0.5, 0.75 and 1.0).

X-ray absorption spectroscopy (XAS) is a widely used technique for determining the electronic structure of material. We performed XAS measurements at O K-edge in $\mathrm{GdMn_{1-x}Cr_xO_3}$ ($x = 0$, 0.25, 0.5, 0.75 and 1), as shown in Figure 5.6, which provides

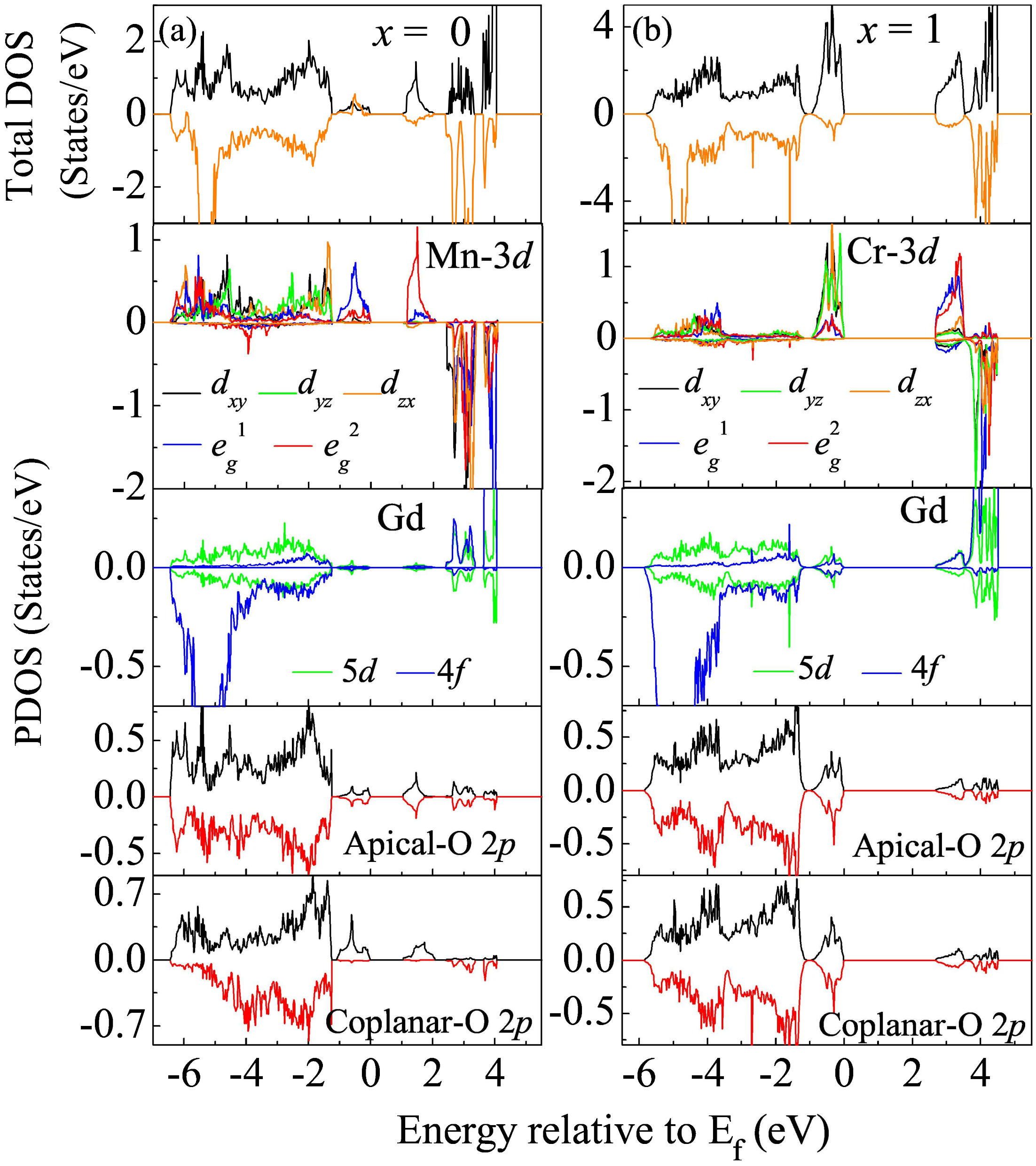

Figure 5.7: The total and site-decomposed DOS of GdMnO$_3$ (a) and GdCrO$_3$ (b)

information about the unoccupied M-3d, Gd-5d and deep Gd/M states via the hybridization with the O-2p states [179, 230]. To provide a proper assignment to XAS features, we also performed density of state (DOS) calculations for parent compounds ($x = 0$ and 1.0). The total and site decomposed DOS of GdMnO$_3$ and GdCrO$_3$ are shown in Figure 5.7 (a) and (b), respectively. Due to JT orbital ordering, the $e_g\uparrow$ band splits into two sub-bands: occupied $e_g^1\uparrow$ mainly dominated by $|3y^2 - r^2\rangle$ with a small contribution from

$|z^2-x^2\rangle$ and unoccupied $e_g^2\uparrow$, mainly contributed by $|z^2-x^2\rangle$ mixing with $|3y^2-r^2\rangle$ for one co-planer Mn sites (for other co-planer Mn sites, these two e_g orbits are mixture of $|3x^2-r^2\rangle$ and $|y^2-z^2\rangle$), as discussed earlier. Based on the DOS calculations, the features between 526.5-531 eV in O K-edge of $GdMnO_3$ are contributed by unoccupied $e_g\uparrow$ ($e_g^2\uparrow$), $t_{2g}\downarrow$+$e_g\downarrow$ and $e_g\downarrow$ [179, 230, 231], as labeled in Figure 5.6. The first peak around 527.8 eV arises from unoccupied $e_g^2\uparrow$ states. From the PDOS of $GdMnO_3$ (Figure 5.7 (a)), a band gap of 1.2 eV is obtained between these JT-split Mn $e_g\uparrow$ bands. This is in agreement with the indirect band gap obtained from absorption study of polycrystalline $GdMnO_3$ [232]. The second peak of XAS spectrum around 529 eV is associated with $t_{2g}\downarrow$ and $e_g\downarrow$ states, with a small contribution from $e_g\downarrow$ around 530.5 eV. Further there is a splitting of 1.4 eV between $e_g^2\uparrow$, $t_{2g}\downarrow$+$e_g\downarrow$ states, which agrees satisfactorily with the calculations.

In contrast to $GdMnO_3$, the O K-edge for JT-inactive $GdCrO_3$ (Figure 5.6) is very simple, having one single peak between 529-531 eV contributed by all unoccupied states of Cr^{3+} i.e. $e_g\uparrow$, $t_{2g}\downarrow$ and $e_g\downarrow$ states and is in good agreement with the calculated PDOS as shown in Figure 5.7 (b). The energy gap of 2.7 eV obtained from the calculation agrees well with the reported experimentally obtained band gap values in chromite family [233, 234]. Above studies suggest that the first hump (527.8 eV) in XAS spectra for all compositions generally arise from contribution of $e_g^2\uparrow$ state of Mn-atoms and second broad hump contributes from $e_g\uparrow$ state of Cr and $t_{2g}\downarrow$ and $e_g\downarrow$ state of both Mn and Cr ions. This results in a gradual decrease of spectral weight of first peak with increase of Cr composition.

The broad feature between 531-537 eV (Figure 5.6) corresponds to Gd-5d states, indicating hybridization of Gd-5d and M-3d ($e_g\uparrow$) states through the mediation of oxygen, this in turn evidences Gd(4f)-M(3d) electronic interactions in these compounds [235, 236]. The 4f states are highly localized, therefore the direct 3d(M)-4f(Gd) coupling is not likely. The interaction occurs via 5d states as they are partially polarized by the 4f electrons via intra-atomic 4f-5d exchange interactions and finally couples with the M-3d states mediated by the O-2p states [235, 236]. The 3d-4f interactions via hybridized 5d and O-2p states is also evidenced from the calculated DOS of $GdMnO_3$ and $GdCrO_3$ (Figure 5.7 (a) and (b)).

5.3.4 Magnetic studies

Temperature dependent magnetization for GdMnO$_3$ under ZFC and FC protocols are shown in Figure 5.8 (a). The co-operative JT-distortions in GdMnO$_3$ result in to inequivalent Mn-O bond lengths as described earlier. As a result one pair of opposite Mn atoms (Mn2-Mn4) in *ab*-plane come closer, as shown schematically in Figure 5.9. This bond shortening facilitates the magnetic interactions between Mn2 and Mn4 (next-nearest-neighbor) *via* two oxygen atoms, O2 and O4. Thus in addition to nearest-neighbor (NN) interaction, next-nearest-neighbor (NNN) interaction plays a significant role in GdMnO$_3$ [40]. The NN interaction is ferromagnetic (FM) in nature as it occurs between one occupied and other unoccupied e_g orbitals. Whereas, NNN interaction takes place between two filled e_g orbitals, resulting in antiferromagnetic (AFM) coupling between them. The competition between these two interactions (NN-FM and NNN-AFM) leads to various complex magnetic structure in this compound. In addition, along the c-axis there is antiferromagnetic coupling between these layers. Bifurcation of ZFC and FC curves is observed around T_N(Mn) $\sim$ 40 K (Figure 5.8 (a)). However, no noticeable change in magnetization is observed in the ZFC curve immediate below T_N(Mn), suggesting onset of an incommensurate sinusoidal spin structure in Mn-sublattice, which gives no macroscopic magnetic moment. This implies NN-FM interaction and the NNN-AFM interactions are comparable in strength [40]. The $M(H)$ curve at $T = 35$ K ($< T_N$(Mn)) shows PM type behavior (Figure 5.8 (c)), corroborating occurrence of the sinusoidal spin structure in Mn-sublattice. Further lowering of temperature results in a sharp rise of magnetization around $T_{CA} = 25$ K in M vs. T (Figure 5.8 (a)), which is likely associated with the onset of canted A-type antiferromagnetic ordering (A_yF_z-type, in Bertaut's notation) in Mn-sublattice. A clear opening of $M(H)$ loop at $T = 25$ K also favors the occurrence of canted A-type antiferromagnetic ordering (Figure 5.8 (c)). This is possibly due to the relative predominance of the NN-FM exchange interaction against the NNN-AFM one, with decrease of temperature. The spin canting can be explained by the antisymmetric Dzyaloshinsky-Moriya interaction ($D.\ (S_i \times S_j)$) between Mn-spins, originating from the interplay between the spin-orbit interaction and the lattice distortions [40, 237]. A dip is observed around 10 K in the ZFC curve, which is possibly resulting from the onset

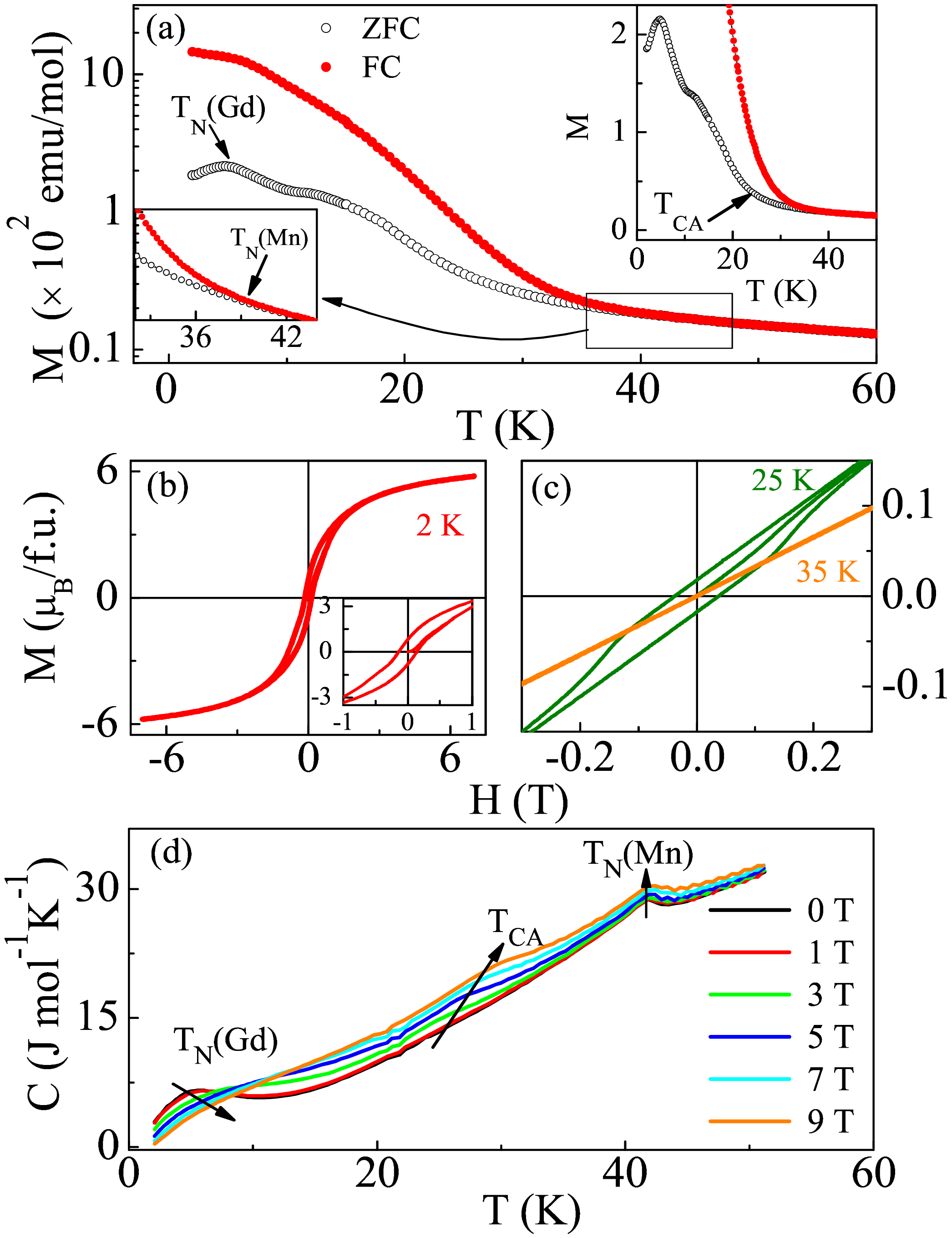

Figure 5.8: (a) Temperature dependent magnetization under zero-field-cooled and field-cooled protocols of $GdMnO_3$. Upper inset shows an enlarged view to highlight the canted-antiferromagnetic transition (T_{CA}). Lower inset shows an enlarged view of the selected region clearly depicting the bifurcation of zero-field-cooled and field-cooled curves. (b) $M(H)$ loop acquired at 2 K and inset represent the enlarged view of the loop. (c) Enlarged view of $M(H)$ loops above and below the (T_{CA}). (d) Temperature dependent heat capacity at various magnetic fields ranging from 0 T to 9 T of $GdMnO_3$.

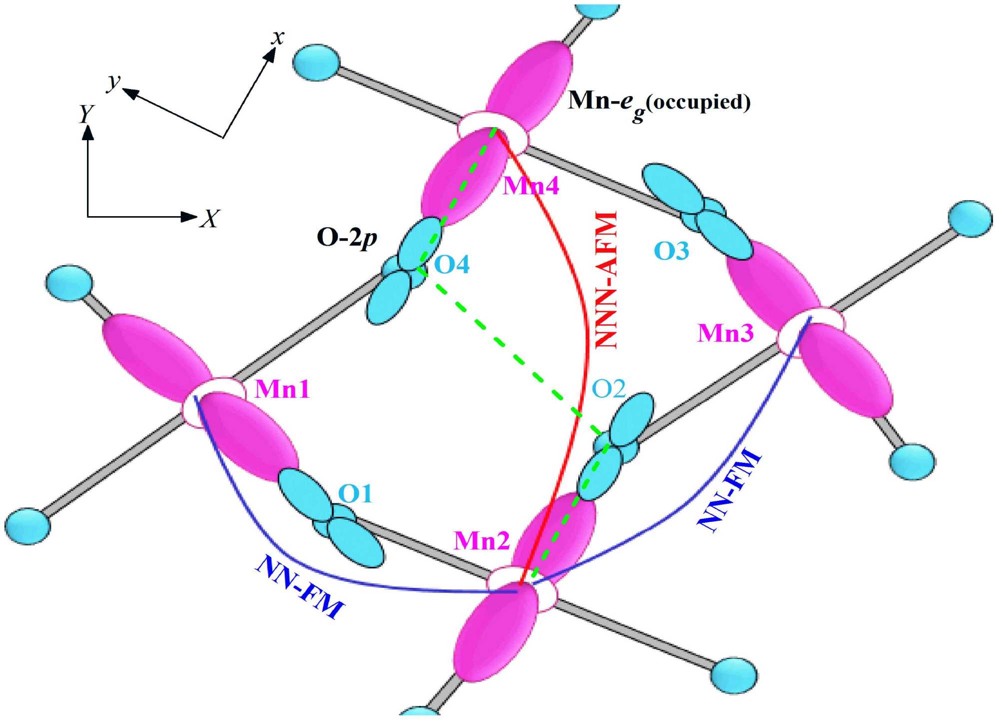

Figure 5.9: Schematic representation of the occupied Mn-e_g orbitals and NN-FM and NNN-AFM superexchange interactions (solid curves) in the ab-plane. Exchange path for the NNN-AFM interaction via two O-2p orbitals is indicated by a dashed line. In addition to global X and Y axes, local x and y axes are shown with respect to Jahn-Teller Mn-sites.

of ferroelectric transition [41, 211]. Finally, canted-antiferromagnetic Gd-ordering occurs around 4.5 K. The presence of small hysteresis in the $M(H)$ loop at $T = 2$ K (Figure 5.8 (b)), also favors this canting nature of Gd-spins. The temperature dependent heat capacity acquired at various magnetic fields ranging from 0 T to 9 T of $GdMnO_3$ are shown in Figure 5.8 (d). A λ-shaped anomaly is found around $T_N(\mathrm{Mn}) \sim 40$ K, suggesting a second-order nature of the sinusoidal magnetic transition, and it is observed to be independent of external magnetic fields, whereas the canted-antiferromagnetic ordering (T_{CA}) stabilizes slightly at higher temperatures in the presence of external magnetic fields. Further, a broad and cusp like anomaly is observed at $T_N(\mathrm{Gd})$, which shifts towards higher temperatures in the presence of external magnetic field and smears out eventually, resulting in a FM ground state [238]. The details magnetic interactions of $GdCrO_3$ is described in chapter 4. In $GdCrO_3$, Cr^{3+} ions have t^3e^0 cubic-field d-electron configurations, which leads to an isotropic t^3-O-t^3 AFM interactions. The isotropic AFM superexchange interactions along with the antisymmetric Dzyaloshinsky-Moriya interactions result in canted G-type ordering (G_xF_z, in Bertaut's notation) in Cr-sublattice in GdCrO$_3$.

In order to understand the magnetic evolution in the solid solutions, we carried out

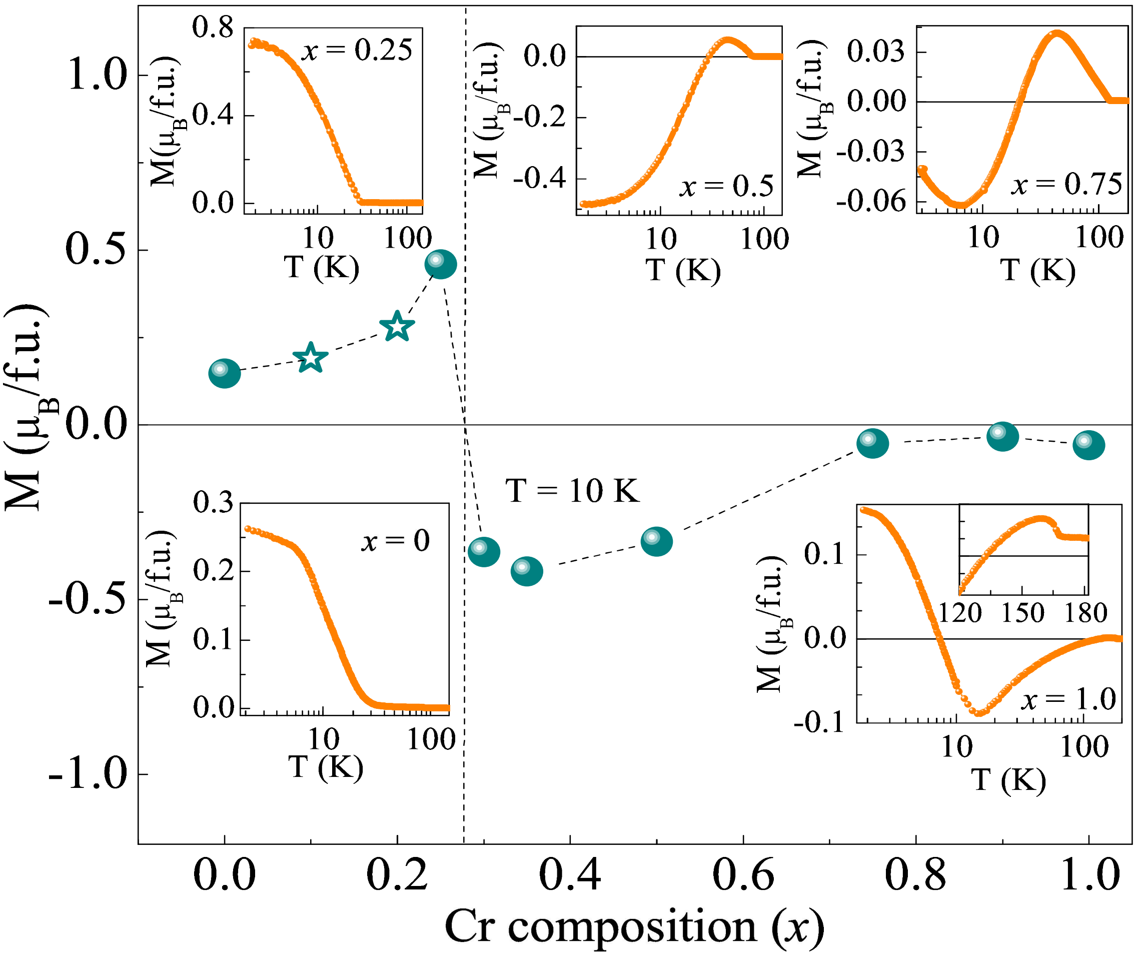

Figure 5.10: Variation in magnetic moment at 10 K with compositions (x) in GdMn$_{1-x}$Cr$_x$O$_3$. Stars ($*$) represent the results extracted from Ref. [212]. Insets represent temperature dependent magnetization measured in field-cooled-cooling protocol of the solid solutions for $x = 0$, 0.25, 0.5, 0.75 and 1.

temperature and field dependent a magnetization measurements throughout the series. Figure 5.10 depicts variation in magnetic moment at 10 K with doping concentration and insets represent temperature dependent magnetization measured in FCC mode of the solid solutions. Remarkably, magnetization at low temperature (10 K) increases gradually upon Cr-doping up to $x \sim 0.25$ in spite of the fact that Cr^{3+} moment is smaller than the Mn^{3+} moment. This indicates strengthening of FM interactions in the system.

This is probably due to the increase in the strength of NN-FM coupling as compared to NNN-AFM coupling in Mn-sublattice caused by progressive decrease of JT distortion. Furthermore, there is possibility of having magnetic interactions between the Mn^{3+} and Cr^{3+} ions, which is probably FM in nature. Such Mn^{3+}-Cr^{3+} FM coupling was also reported in $TbMn_{1-x}Cr_xO_3$ [215], $LaMn_{1-x}Cr_xO_3$ [239] and $YMn_{1-x}Cr_xO_3$ [240] systems. The interaction between two Cr^{3+} moments at the lower Cr concentration may not be important. However, for Cr-rich compositions Cr^{3+}-Cr^{3+} interaction dominates, thus having similar behavior to that of $GdCrO_3$ i.e. G-type magnetic structure. Notably, FCC magnetization curve for $x = 0$ and 0.25 compositions show positive magnetization in the entire temperature region. However, one sees a magnetization reversal effect for all other compositions suggesting the strengthening of AFM coupling between Gd and M-sublattices with increase of Cr-content. The observation of magnetization reversal as a function of temperature above a critical Cr concentration suggests that there is a strong correlation between the structural distortion and magnetic coupling.

5.3.5 DFT Calculations and Spin Hamiltonian for $GdMn_{0.5}Cr_{0.5}O_3$

Further, we performed DFT calculations to determine the possible low temperature magnetic ground state in $GdMn_{0.5}Cr_{0.5}O_3$. It has been reported that magnetic interaction in $RMn_{0.5}Cr_{0.5}O_3$ composition strongly depends on the R-sites. $TbMn_{0.5}Cr_{0.5}O_3$ exhibits G-type magnetic structure with the alternate arrangements of Mn and Cr atoms as confirmed from neutron diffraction study and DFT calculations [241]. $DyMn_{0.5}Cr_{0.5}O_3$ has a random distributions of Mn and Cr ions, which leads to two distinct magnetic orderings associated with Cr^{3+}-Cr^{3+} and Cr^{3+}-Mn^{3+} interactions as clearly seen in temperature dependent magnetization data [242]. From DFT calculations, $LaMn_{0.5}Cr_{0.5}O_3$ was found to have stable structure with the layer-by-layer doping type (Mn and Cr are alternatively arranged along the c-axis). The DFT calculations also showed FM interactions between Mn ions and AFM interactions between Cr ions in ab-plane and satisfactorily explained its magnetization [243]. All the compounds discussed above possess $Pbnm$ symmetry. On the contrary, $YMn_{0.5}Cr_{0.5}O_3$ has monoclinic structure with a layer-by-layer arrangements of Mn and Cr along the *c*-axis and exhibits ferrimagnetic behavior [244, 245]. For $GdMn_{0.5}Cr_{0.5}O_3$, Reitveld refinement of XRD pattern using orthorhombic *Pbnm* structure fitted better than that of the monoclinic structure. Temperature dependence magnetization measurement did not show two magnetic transitions like in $DyMn_{0.5}Cr_{0.5}O_3$ implying Mn and Cr are well ordered. To understand the magnetic coupling in $GdMn_{0.5}Cr_{0.5}O_3$, the total energy was calculated within the framework of GGA including Hubbard U, for various possible arrangements of Mn and Cr ions and various possible spin configurations, as listed in Table 5.1. The results of GGA+U are consistent with GGA+U+SOC results as reported in $TbMn_{0.5}Cr_{0.5}O_3$ [241]. It is found that structure with the layer-by-layer doping type with a FM interaction between Mn^{3+} spins and AFM interaction between Cr^{3+} spins is the most stable configuration similar to $LaMn_{0.5}Cr_{0.5}O_3$ [243].

In constructing an effective Hamiltonian (H) to understand the spin dependent energetics

Table 5.1: Calculated relative energies (E, in meV/unit cell) of various magnetic structures of $GdMn_{0.5}Cr_{0.5}O_3$. The unit cell contains two Mn and two Cr spins. The energies of the FM phase with layer-by-layer arrangements is used as the reference energy. Subscripts m and c represent Mn and Cr ions, respectively.

Magnetic structure	c↑ c↑ m↑ m↑	c↓ c↑ m↑ m↑	c↓ c↓ m↑ m↑	c↑ c↓ m↓ m↑	c↑ c↓ m↑ m↓
E	0	-16.15	12.25	131.02	125.33
Magnetic structure	m↑ c↑ m↑ c↑	m↑ c↓ m↑ c↑	m↓ c↑ m↑ c↑	m↓ c↓ m↑ c↑	
E	354.87	332.98	420.76	421.31	
Magnetic structure	c↑ m↑ m↑ c↑	c↓ m↓ m↑ c↑	c↑ m↓ m↑ c↑	c↓ m↑ m↑ c↓	
E	321.31	306.16	343.92	372.3	

of $GdMn_{0.5}Cr_{0.5}O_3$ we have considered only Mn^{3+} and Cr^{3+} spins, since in our total energy calculations the Gd^{3+} spins were not included. The unit cell used in the calculation of the energies for different Mn and Cr arrangements and different spin orientations consists of 20 atoms, $Gd_4Mn_2Cr_2O_{12}$, consisting of two Mn and two Cr ions. The unit cell then consists of 4 magnetic atoms I-IV; I, II are in one basal plane representing the Mn atoms and III, IV are in the other basal plane representing the Cr atoms as shown schematically in Figure 5.11. The structure in the figure is denoted as (Mn↑,Mn↑)(Cr↑,Cr↓), which is

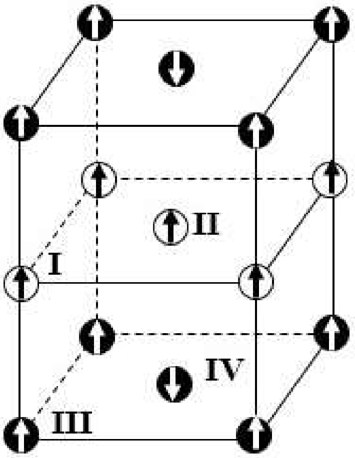

Figure 5.11: The calculated most stable magnetic structures in one unit cell for $GdMn_{0.5}Cr_{0.5}O_3$. Only the transition-metal ions Mn and Cr are shown (Filled circles: Mn; Empty circles: Cr). The ions labeled as I, II, III and IV are the non-equivalent atoms in the unit cell.

the lowest energy atomic structure obtained from the calculations.

The Hamiltonian for the system is given by

$$\begin{aligned} H = -J_1 \sum_{<ij>l} \vec{S}^{Mn}_{il}.\vec{S}^{Mn}_{jl} - J_2 \sum_{<ij>l} \vec{S}^{Cr}_{il}.\vec{S}^{Cr}_{jl} \\ -J_3 \sum_{<ll'>l} \vec{S}^{Mn}_{il}.\vec{S}^{Cr}_{il'} + \Delta \end{aligned} \tag{5.1}$$

where i, j indicate lattice sites in the basal (ab) plane and l indicates different layers along the c axis. In the Figure 5.11, the number of Mn-Mn bonds/unit cell is 4, the number of Cr-Cr bonds/unit cell is 4 and the number of Mn-Cr bonds/uc is also 4. There are 4 parameters in the Hamiltonian which we estimate using calculated DFT energies for different spin configurations with a layer-by-layer arrangements of Mn and Cr along the c-axis (see Table 5.1 first row). Here S^{Mn}=2; S^{Cr}=3/2. In the mean-field approximation, energy/unit-cell for 4 different spin configurations are given below. Energy for a fifth configuration can be predicted using parameters obtained from the first four spin configurations and compared with calculated DFT energy. All the energies are in meV/unit cell.

$$E_I = -16J_1 - 9J_2 - 12J_3 + \Delta = 0 \tag{5.2}$$

$$E_{II} = -16J_1 + 9J_2 + \Delta = -16.15 \tag{5.3}$$

$$E_{III} = -16J_1 - 9J_2 + 12J_3 + \Delta = +12.25 \tag{5.4}$$

$$E_{IV} = +16J_1 + 9J_2 + 12J_3 + \Delta = +131.02 \tag{5.5}$$

$$E_V = +16J_1 + 9J_2 - 12J_3 + \Delta \tag{5.6}$$

Solving Eqs. 5.2-5.5, it is obtained: J_1=J^{Mn-Mn} = 4.39 meV (Ferro), $J_2 = J^{Cr-Cr}$ = -1.26 meV (Antiferro), $J_3 = J^{Mn-Cr}$ = 0.55 meV (Ferro) and Δ = 65.48 meV. Using these parameters we predict E$_v$ = 117.78 meV, whereas the calculated DFT energy is 125.33 meV. Looking at the calculated exchange parameters, the coupling between Mn spins is ferromagnetic and strong, similar to the parent manganite, i.e. GdMnO$_3$. The coupling between Cr spins is antiferromagnetic, again similar to the parent compound GdCrO$_3$. The cross coupling between Mn and Cr spin is ferromagnetic and weak. In an earlier study of transport in LaMn$_{1-x}$Cr$_x$O$_3$; 0$\leq x \leq$ 0.15. Morales *et al.* [**?**] argued that the experimental findings could be understood through a simple model of the electronic structure of the alloy, which included FM double exchange interaction between Mn and Cr spins and a CPA type approximation to handle disorder. It is possible that the small magnitude of J^{Mn-Cr} results from a near cancellation between two competing contributions, one the usual AFM super-exchange and the other FM double exchange.

Variation of the remnant magnetization (M_r) at 10 K with compositions and corresponding M-H loops are shown in Figure 5.12 (a) and (b), respectively. M_r shows a

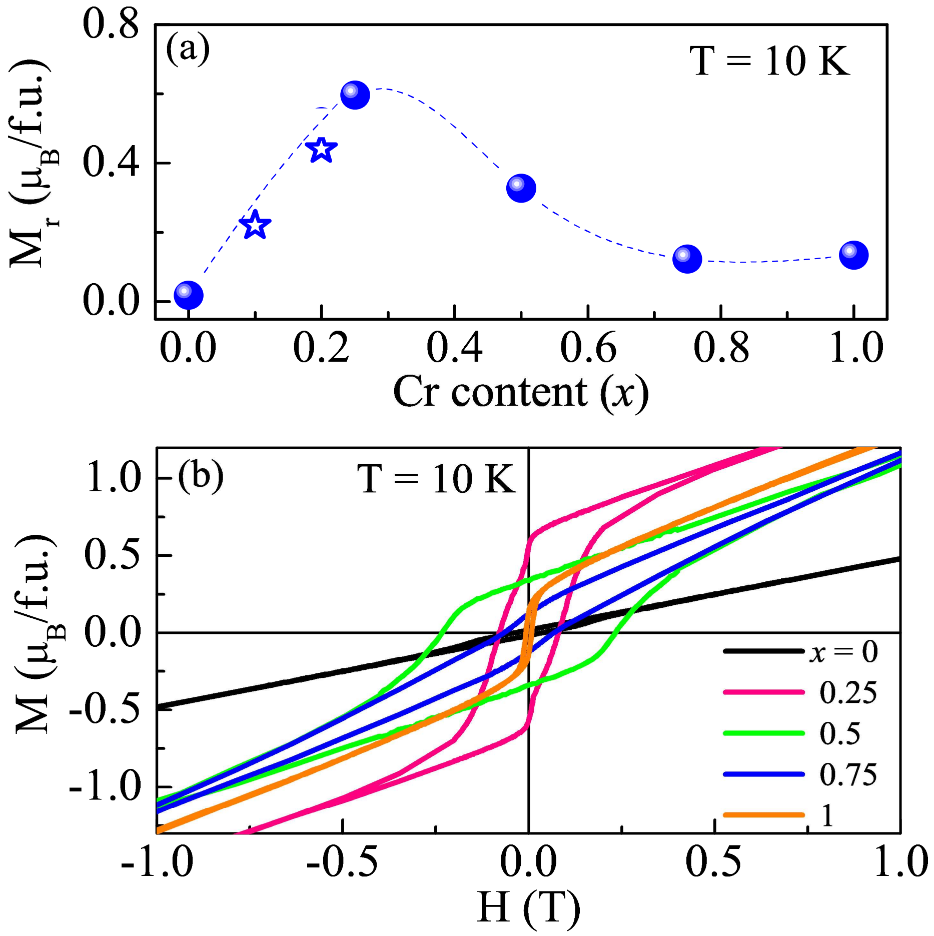

Figure 5.12: (a) Variation of remnant magnetization (M_r) at 10 K with compositions (x). Stars ($*$) represent the results extracted from Ref. [212] (b) Enlarged view of M-H loops measured at 10 K of the solid solutions for x = 0, 0.25, 0.5, 0.75 and 1.

non-monotonic variation with compositions: initially it increases with increasing Cr concentration (x) and reaches a maximum value for $x \sim 0.3$ and then starts to decrease with further increase in x followed by no distinct variation beyond $x \sim 0.7$. As discussed above, magnetic behavior in the solid solutions are contributed by variety of magnetic interactions such as symmetric exchange interactions (FM and AFM type) and antisymmetric DM interaction coupled to octahedral tilting. The DM interaction is directly proportional to the perpendicular displacement of oxygen in the M-O-M chain, which, in turn, depends on the tilt angles [246, 247]. It is evident from Raman data that there is hardly any change of tilt angles throughout the series. This suggests contributions from canted ferromagnetism (DM interaction) remains almost constant throughout the series. Thus, the increase of M_r up to $x \sim 0.3$ suggests an increase of NN-FM coupling as compared to NNN-AFM coupling caused by the progressive decrease of JT-orbital ordering and incorporation of Mn^{3+}-Cr^{3+} FM interactions as discussed earlier. Beyond that ferrimagnetic type structure arises due to the incorporation of AFM Cr^{3+}-Cr^{3+} interactions, thus resulting in decrease of M_r. In Cr-rich compositions ($x \geq 0.7$) AFM Cr^{3+}-Cr^{3+} interactions are more dominating resulting in no further change in M_r.

5.4 conclusion

The structural, electronic and magnetic properties of $GdMn_{1-x}Cr_xO_3$ were studied. In the structural investigations, it was found that the JT distortion characteristic to Mn^{3+} results in bond anisotropy and effective orbital ordering for $x \leq 0.35$. A gradual variation of electronic states with doping is also clearly seen in O-K edge x-ray absorption spectra. The temperature dependence of magnetization under the FCC mode shows sign reversal effect for $x \geq 0.35$, whereas magnetization does not change sign in the JT-active region. The change in magnetic polarity at the critical concentration coinciding with JT-crossover, infers a complex interplay of magnetic interaction and structural distortion. The nonmonotonic variation of remnant magnetization can be explained in terms of doping induced modification of symmetric magnetic interactions (FM/AFM type). DFT calculations using GGA+U type exchange correlation potential find that the system with $x = 0.5$ consists of alternate ferromagnetic Mn layers and antiferromagnetic Cr layers. The strength of the ferromagnetic exchange interaction between nearest neighbor Mn spins is stronger than the NN Cr antiferromagnetic exchange. The exchange interaction between NN Mn and Cr is quite small but ferromagnetic. This is distinctly different from that observed for both end members $GMnO_3$ and $GdCrO_3$.

Chapter 6

Magnetocaloric studies in GdMO$_3$ (M = Al, Mn and Cr)

In this chapter, we will discuss magnetocaloric effect (MCE) of polycrystalline GdMO$_3$ (M = Al, Mn and Cr) near Gd-spin ordering temperature. We found GdAlO$_3$ has a giant magnetic entropy change (-ΔS_M) under moderate magnetic field change, while GdMnO$_3$ exhibits comparably less -ΔS_M due to the Gd-Mn negative exchange interaction. Even though GdMnO$_3$ has quite low magnetic entropy change compared to GdAlO$_3$, both the compounds have comparable cooling power and adiabatic temperature change (ΔT_{ad}) . Absence of magnetic and thermal hysteresis in GdAlO$_3$ make it more efficient and reversible magnetic refrigerant than that of GdMnO$_3$. It is observed that GdCrO$_3$ exhibits exceptionally large value of -ΔS_M, ΔT_{ad} and relative cooling power (RCP) at moderate magnetic field change. Such exceptionally large MCE arises from suppression of the spin entropy associated with the suppression of spin reorientation transition in addition to the Gd-ordering, which makes it one of best candidate for magnetic refrigeration among all the potential low temperature magnetic refrigerants discovered so far.

6.1 Introduction

The vapor-compression refrigerators have become ubiquitous in a large number of cooling applications. However, the use of volatile refrigerants such as chlorofluorocarbons (CFCs) and hydrochlorofluorocarbons (HCFCs) have raised serious environmental concerns, primarily for the destruction of ozone layer and the global warming [53, 248]. Replacement by liquid hydrofluorocarbons (HFCs), which contain no chlorine and therefore have no ozone depletion potential, is not without problems because HFCs are greenhouse gases with higher global warming potential than CO_2 [53, 248]. Therefore, scientist and engineers have begun to explore alternative environmental-friendly technologies to replace the conventional gas refrigeration. Magnetic refrigeration can provide such an opportunity as it does not use any hazardous chemicals. In addition to environmental concerns, the magnetic refrigeration technology is more efficient compared to gas refrigeration technology. Cooling efficiency of magnetic refrigerant working with Gd has been reached 60% of the theoretical limit, where as best gas-compression refrigerator has reached a limit only 40% [53]. Besides, it offers considerable operating cost savings by eliminating the most inefficient part of the gas refrigerator: the compressor. Depending upon the magnetic transition of various materials, magnetic refrigerants work in wide range of temperatures from room temperature to the temperatures of hydrogen and helium liquefaction ($\sim$ 20 - 4.2 K). Materials having a room temperature cooling capacity can be used for domestic and industrial refrigeration purposes. It has been reported that utilization of magnetic hydrogen liquefier (20 K) is more cost effective than a conventional liquefier, which could make hydrogen the best alternative fuel [249]. Magnetic refrigeration near the liquid helium temperature ($\sim$ 4 K) also has application in space science [53]. Recently, an active magnetic regenerative refrigeration (AMRR) has been developed for space application [250]. To achieve cooling below 1 K, the adiabatic demagnetization refrigeration is an attractive process compared to ^{3}He/^{4}He dilution refrigeration because of the growing cost of helium and scarcely available ^{3}He isotope. In addition, magnetic refrigeration also has significant applications in the medical field, such as magnetic hyperthermia and drug delivery [251].

For effective refrigeration capacity, it is paramount important to have following properties of the materials [252] :

(i) large effective quantum number to have large magnetization i.e. large magnetic entropy

(ii) high electrical resistivity to avoid eddy current loss

(iii) small specific heat and large thermal conductivity for remarkable temperature change and rapid heat exchange

(iv) weak magnetic exchange interaction, so that spins can easily align along the field direction

(v) small or zero magnetic and thermal hysteresis for multistage operation as to avoid magnetic-work losses due to the rotation of domains in a magnetic-refrigeration cycle

A large number of compounds based on rare-earths [253, 254], manganites [252], Heusler alloys [255], etc have since been discovered to show large magnetocaloric effect (MCE). Of these, compounds based on rare-earth alloys and oxides are the candidates with the most potential, especially for low temperature applications, due to the low AFM ordering temperature in rare-earth sublattice. Also, since the AFM coupling is not so strong, moderate field strengths can induce a metamagnetic transition and suppress the antiferromagnetic ordering. Another advantage of rare-earth oxides is the presence of minimal thermal and field hysteresis. Moreover, Gd and Gd based alloys [256–258], have continued to receive large attention because large magnetic moment of Gd. In this chapter, we will discuss magnetocaloric effect (MCE) of various Gd-based oxides ($GdMO_3$, M = Al, Mn and Cr) near the Gd-ordering temperature to assess their potential usage as magnetic refrigerants at cryogenic temperatures.

6.2 Experimental details

Polycrystalline samples of $GdMO_3$ (M = Al, Mn and Cr) were prepared by the solid-state synthesis technique at ambient pressures. Stoichiometric proportions of Gd_2O_3 and Al_2O_3 were used to synthesize $GdAlO_3$. The precursors were thoroughly mixed and heated at 1400 ^{0}C for 24 h in air with several intermediate heating and grindings. Detailed synthesis procedure for $GdMnO_3$ and $GdCrO_3$ are described in chapter 4 and

5. Powder x-ray diffraction measurements were performed in Bruker D8 Advance x-ray diffractometer using Cu K_α radiation to confirm the phase purity of the samples. Magnetization measurements were performed on a SQUID-VSM, Quantum Design Inc. with external magnetic fields up to 7 T. Heat capacity measurements were carried out using a relaxation method in the Physical Property Measurement System (PPMS) from Quantum Design Inc., with external magnetic fields up to 9 T.

6.3 Results and discussion

6.3.1 Structural studies

Figure 6.1 (a-c) represent x-ray powder diffraction pattern acquired from $GdAlO_3$, $GdMnO_3$ and $GdCrO_3$ samples, respectively. The obtained XRD of $GdAlO_3$ matches well with the one reported in the JCPDS (Joint Committee on Powder Diffraction Standards) database (46-0395). The system shows an orthorhombic distorted perovskite structure with *Pbnm* symmetry [259]. Rietveld refinement (using FULLPROF software) of the XRD pattern confirms that there are no detectable impurities in these compounds. Lattice parameters, obtained from refinements are: a = 5.249 Å, b = 5.297 Å and c = 7.441 Å, are in good agreement with the literature. $GdMnO_3$ and $GdCrO_3$ also crystallize in to orthorhombic distorted perovskite structure having *Pbnm* and $Pna2_1$ space group, respectively. The detailed structural characterization of $GdMnO_3$ and $GdCrO_3$ are described in chapter 4 and 5.

6.3.2 Magnetic studies

$GdAlO_3$

Temperature dependent magnetization for $GdAlO_3$ acquired at 100 Oe applied field is shown in Figure 6.2, where open and closed circles show the zero-field-coled (ZFC) and field-cooled (FC) data, respectively. Transition from PM to AFM ordering is clearly seen at $T_N(\mathrm{Gd}) = 3.9$ K, resulting from indirect exchange interaction between Gd^{3+} ions [260]. Variation of inverse susceptibility, $1/\chi$ with temperature is represented by open squares and the graph in the PM region is fitted using Curie-Weiss law, $\chi = \frac{C}{T-\theta}$, where $C =$

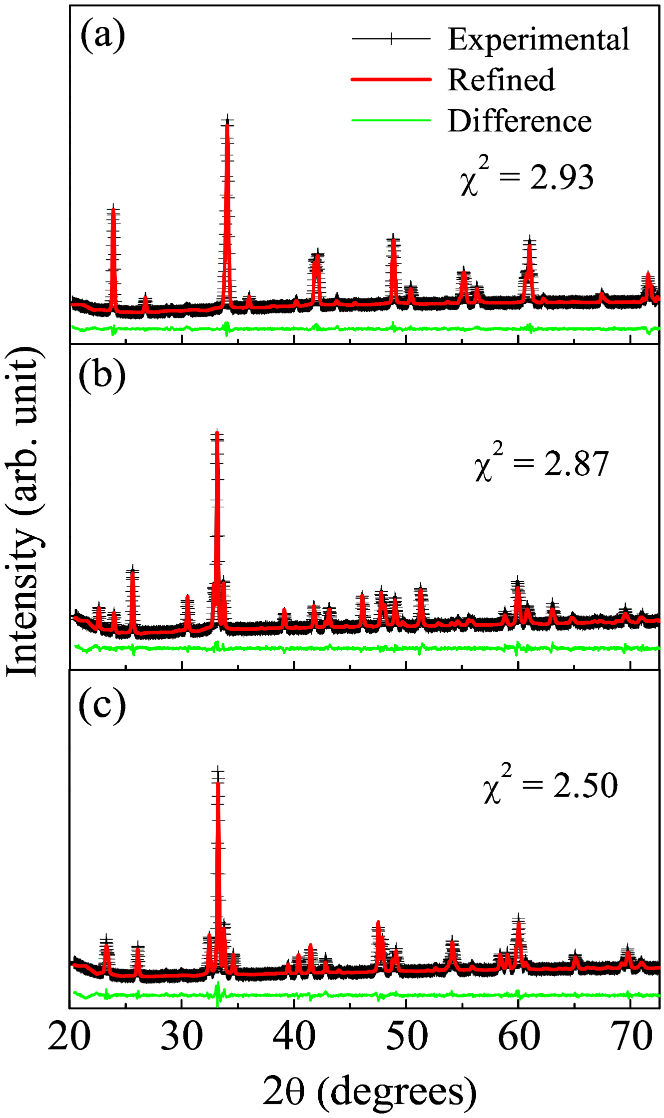

Figure 6.1: X-ray powder diffraction patterns of $GdAlO_3$ (a), $GdMnO_3$ (b) and $GdCrO_3$ (c) along with the corresponding Reitveld refinement pattern and difference spectra, χ^2 represents the quality of the fit.

Curie constant and θ = Weiss constant (shown as dashed lines). Estimated values of parameters are C = 6.178 emu.K/mol.Oe and θ = -4.95 K. The effective paramagnetic moment (μ_{eff}) of Gd^{3+} ion was calculated using the expression, $\mu_{eff} = \sqrt{\frac{3Ck_B}{N}}$, where C = Curie constant, k_B = Boltzmann Constant and N = Avogadro's constant, giving μ_{eff} = 7.028μ_B, which is close to the theoretical spin only moment of Gd^{3+} ion (7.937μ_B). Nearest neighbor exchange interaction J_{ex} between Gd^{3+} ions was calculated using the

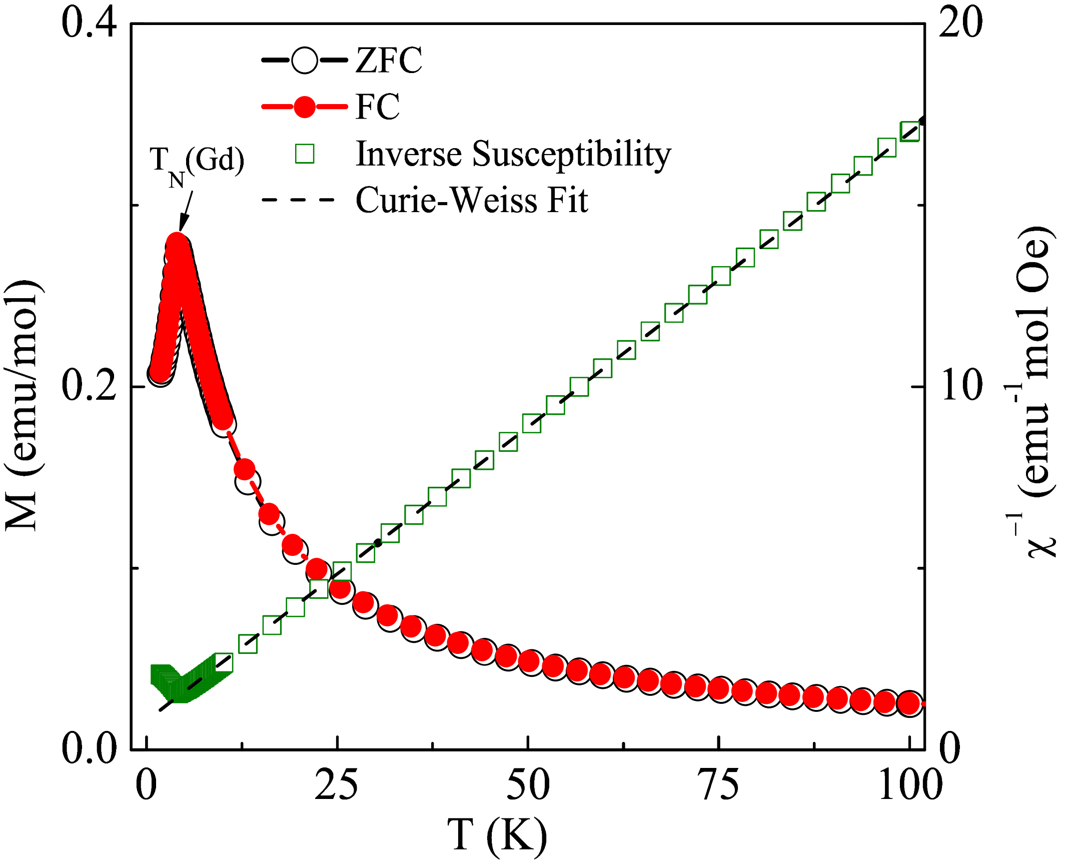

Figure 6.2: Temperature dependent magnetization of GdAlO$_3$. Open and closed circles show the zero-field-cooled and field-cooled data, respectively. Open squares show the inverse susceptibility where as the Curie-Weiss fit for the same is represented as dashed line.

following relation, [261]

$$\sum n_i.J_{ex} = \frac{3k_B\theta}{2S(S+1)} \tag{6.1}$$

where S is the spin quantum number = $\frac{7}{2}$, n_i is the number of nearest neighbours of each Gd^{3+} ion = 6. Substituting these values, it was obtained J_{ex} = - 0.054(6) cm^{-1} = -0.078 K, which is quite in agreement with other reports [262, 263], suggesting that the low temperature magnetic ordering is predominantly due to antiferromagnetic exchange coupling between nearest-neighbour Gd^{3+} ions. Hence, well below T_N, GdAlO$_3$ is a uniaxial two-sublattice antiferrromagnet, in which each Gd^{3+} ion in one sublattice is surrounded by

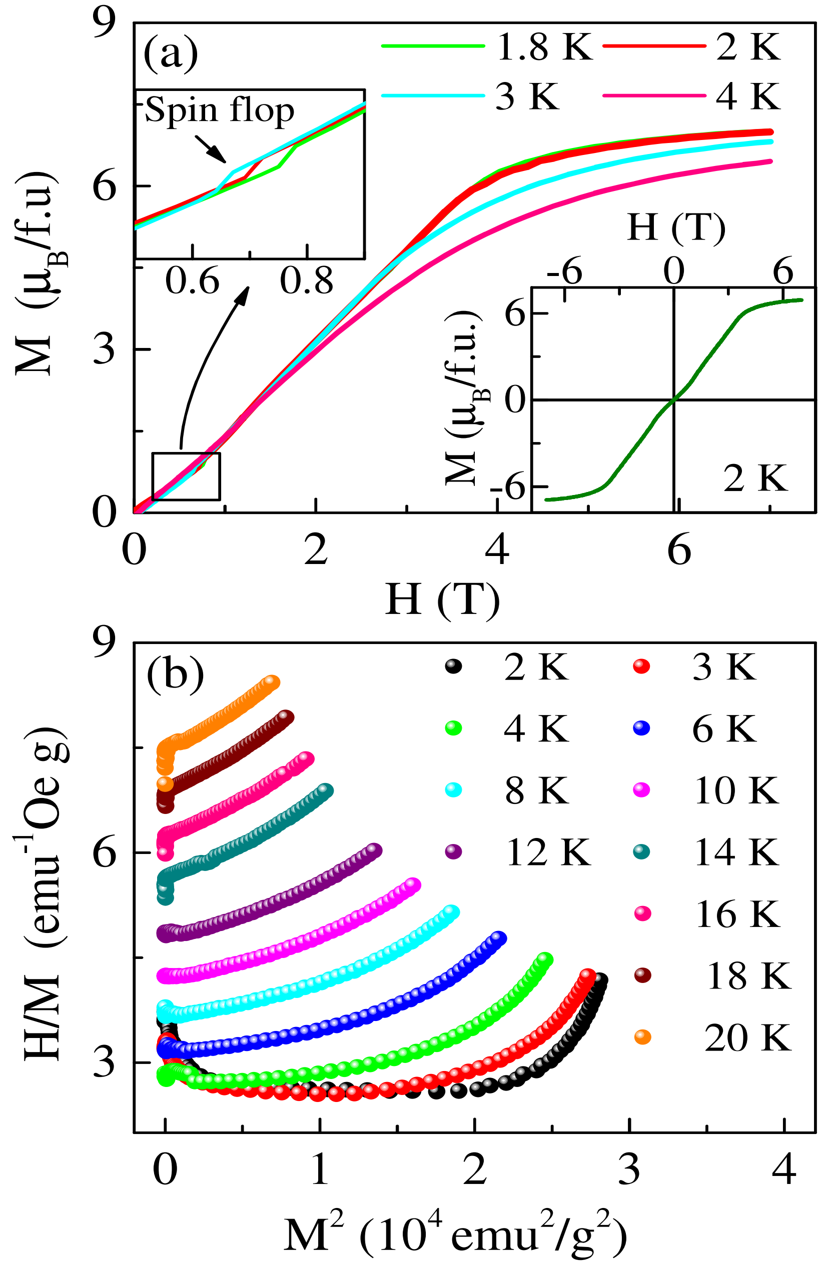

Figure 6.3: (a) Isothermal Magnetization Vs *H* curve for $GdAlO_3$ acquired at various temperatures. Upper inset shows an enlarged view of selected region clearly depicting a spin flop transition. Lower inset shows complete *M(H)* loop acquired at 2 K. (b) Arrott plots at various temperatures ranging from 2 K to 20 K.

six nearest neighbours Gd^{3+} ions belonging to the opposite sublattice [264, 265].

Isothermal magnetizations as a function of applied field *H* ranging from 1.8 to 4 K for $GdAlO_3$ are shown in Figure 6.3 (a). An enlarged view of selected region of *M(H)* curves and *M(H)* loop acquired at 2 K are shown in upper and lower insets, respectively. All the magnetization curves at temperatures below T_N(Gd) showed a sharp jump at about a small critical field (H_{SF}) of 0.76 T as clearly seen in the upper inset of Figure 6.3 (a). This suggests the occurrence of a spin flop (SF) type transition, as reported in single crystal samples by Blazey *et al.* [264], where the direction of two sublattice magnetizations suddenly turn (flop) perpendicular to the easy axis direction, consequently perpendicular to the applied magnetic field direction. The discontinuity jump in *M(H)* indicates that the field-induced spin flop transition is first-order in nature. With further increase of magnetic field, the sublattice magnetization rotates gradually, until at a certain critical field their mean direction is parallel to the applied field and the ferromagnetic phase sets in, beyond that magnetization is almost independent of applied field. With increase of temperature, critical field of spin flop transition (H_{SF}) decreases slightly [264,265]. Absence of hysteresis in *M(H)* loop acquired at 2 K also indicates that $GdAlO_3$ is a uniaxial two-sublattice antiferrromagnet. Belov-Arrott plots (M^2 Vs H/M) at various temperatures ranging

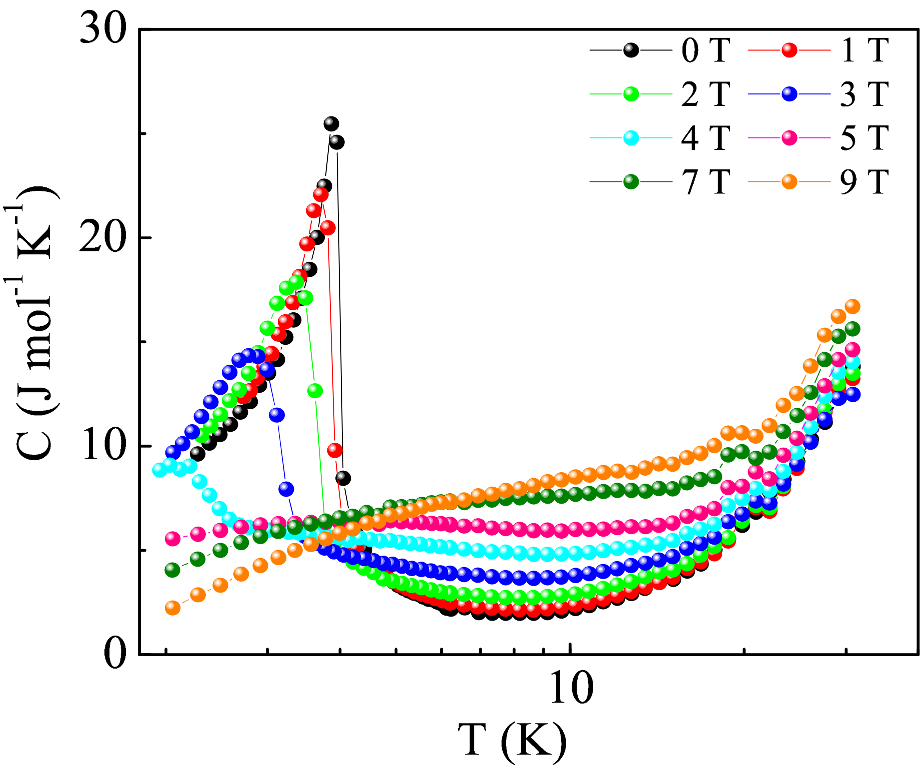

Figure 6.4: Temperature dependence of specific heat at various magnetic fields ranging from 0 T to 9 T of $GdAlO_3$.

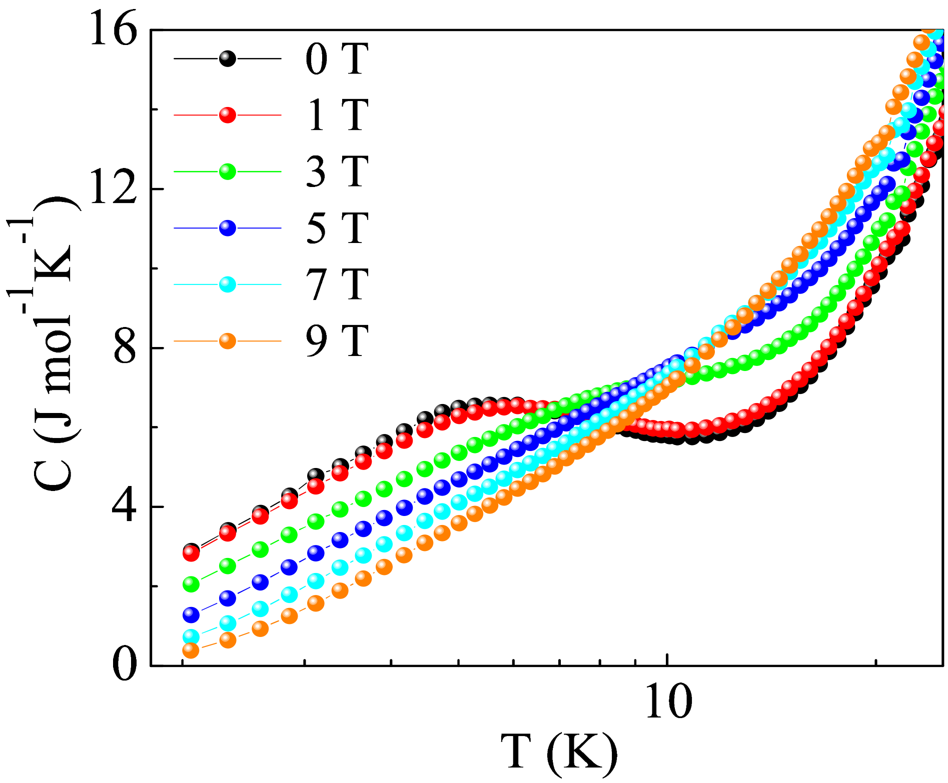

Figure 6.5: Temperature dependence of specific heat at various magnetic fields ranging from 0 T to 9 T of GdMnO$_3$ near the Gd-ordering temperature.

from 2 K to 20 K are shown in Figure 6.3 (b). According to Banerjee criterion, for a first-order magnetic transition, the slope of the Arrott plot will be negative, whereas it will be positive when the transition is second-order in nature [266, 267]. Negative slope of the plots at temperatures below T_N(Gd) for field $H \leq 0.76$ T confirms that the field induced antiferomagnetic to spin flop transition is first order in nature, while positive slope of high field data indicates that spin flop to paramagnetic transition is second order in nature.

Temperature dependent specific heat variation at various magnetic fields ranging from 0 T to 9 T are shown in Figure 6.4. Zero field specific heat result shows a sharp λ-shaped anomaly at T_N(Gd), which is characteristic of second order phase transition coinciding with magnetization results as discussed above. Gradually, with increasing field this anomaly is observed to be shifting towards low temperature in spin flop region and beyond 4 T applied field, the peak is nearly suppressed resulting in a paramagnetic ground state [264].

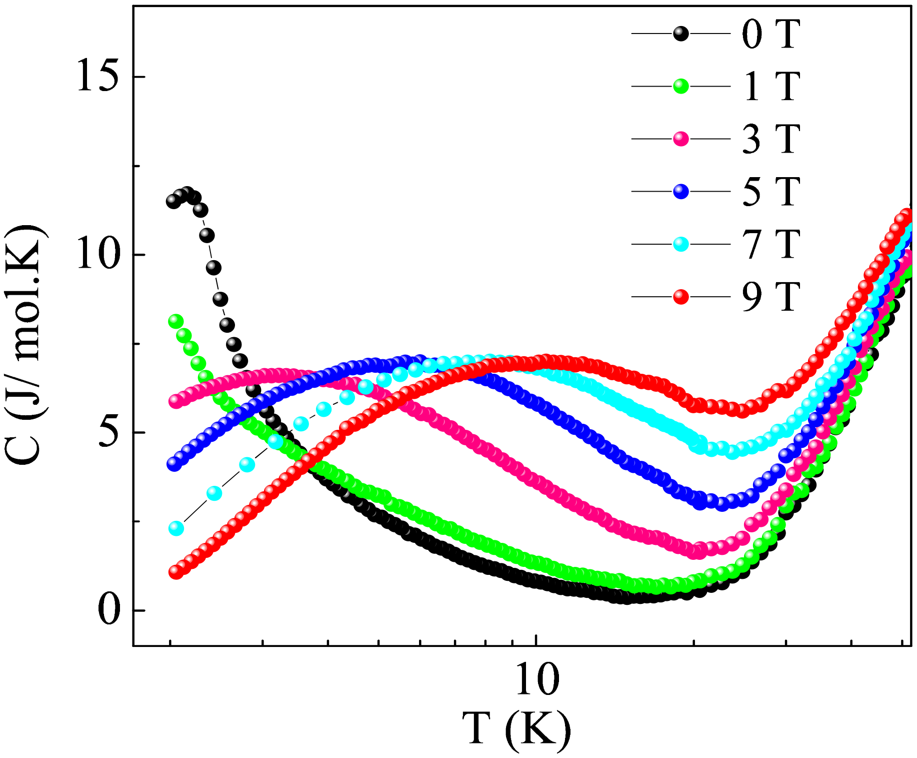

Figure 6.6: Temperature dependence of specific heat at various magnetic fields ranging from 0 T to 9 T of $GdCrO_3$ near the Gd-ordering temperature.

$GdMnO_3$

As in $GdMnO_3$, both Gd and Mn are magnetic species leads to complex magnetic behavior in the the system. The detailed magnetic behavior of $GdMnO_3$ is described in chapter 5. Canted antiferromagnetic Gd-ordering occurs at around 4.5 K, which leads to broad and cusp like anomaly in heat capacity data as shown in Figure 6.5, which shifts towards higher temperatures in the presence of external magnetic field and smears out eventually, resulting in a FM ground state.

$GdCrO_3$

$GdCrO_3$ exhibits extremely rich magnetic properties driven by symmetric ($S_i.S_j$) and antisymmetric ($S_i{\times}S_j$) exchange interactions within and between Cr and Gd-sublattices. The detailed magnetic behavior is described in chapter 4 and 5. At low temperature a broad anomaly appears in heat capacity data (Figure 6.6) at around 2.5 K resembling canted-antiferromagnetic Gd-ordering [162]. Gradually this anomaly smears out and shifts towards high temperature with external field due to the weak anti-ferromagnetic exchange coupling between Gd ions and beyond 1 T the ground state of the system becomes ferromagnetic.

6.3.3 Magnetocaloric studies

In order to understand if the present systems under investigation are suitable for magnetic refrigeration applications, we have performed detailed investigations of ΔS_M, ΔT_{ad} and RCP at various change in magnetic field (H) as all these parameters are the measure of effective refrigeration capacity of the material.

Total entropy (S) has been calculated from specific heat data by using following equation,

$$S(T,H) = \int_0^T \frac{C(T,H)}{T} dT \tag{6.2}$$

ΔS_M at different field variations have been calculated from specific heat data acquired at various magnetic fields, using the following relations [53],

$$\Delta S_m(T,H) = \Big(S(T,H) - S(T,0)\Big)_T = \int_0^T \frac{C(T,H)}{T} dT - \int_0^T \frac{C(T,0)}{T} dT \tag{6.3}$$

For comparison, we have also calculated the same from field dependence magnetization data at different temperatures using the following thermodynamic Maxwell relation [53],

$$\Delta S_m(T,\Delta H) = \int_0^H \left(\frac{\partial M(T,H)}{\partial T}\right)_H dH \tag{6.4}$$

Adiabatic temperature change (ΔT_{ad}), which is the isentropic temperature difference between $S(H,T,)$ and $S(0,T)$ has been calculated by using the following equation [268],

$$\Delta T_{ad}(T,\Delta H) = -\int_0^H \left(\frac{T}{C(T,H)}\right)_H \left(\frac{\partial M(T,H)}{\partial T}\right)_H dH \tag{6.5}$$

For GdCrO$_3$, it is extracted from the isentropic line connecting $S(H,\, T_i)$ and $S(0,T_f)$ for a magnetic field change from zero to a final value H [269] Relative cooling power (RCP) is a measure of heat energy that is extracted for each refrigeration cycle and defined as [257]

$$RCP = \int_{T_1}^{T_2} \mid \Delta S_m \mid dT \tag{6.6}$$

where T_1 and T_2 are the temperatures corresponding to both sides of the half maximum value of the isothermal magnetic entropy change ($\Delta S_M(T)$) peak. Maximum of RCP value (RCP^{max}) is typically reported as the product of ΔS_M^{max} and the full width half maximum (FWHM) of the ΔS_M peak,

$$RCP^{max} = \Delta S_m^{max} \times \delta T_{FWHM} \tag{6.7}$$

6.3.3.1 Magnetocaloric effect in GdAlO$_3$ and a comparative study with GdMnO$_3$

Theoretically, it was predicted that rare earth orthoaluminates (RAlO$_3$) are also efficient magnetic refrigerants in low temperature range and experimentally, it was confirmed for R= Dy, Ho and Er [270–272]. But so far such investigations are not yet reported on GdAlO$_3$. Also MCE was studied in various single crystal of rare-earth manganites (RMnO$_3$, R = Dy, Tb, Ho, Yb, Tm.Gd) having giant -$\Delta S_M \sim$ 10-32 JKg^{-1}K^{-1} at liquid helium temperature [257, 273–275]. However, hardly any detailed investigations have been performed on polycrystalline samples, which are relatively simple to synthesize and are cost effective compared to their single crystal counterparts. This motivated us to investigate the magnetocaloric effect in polycrystalline GdAlO$_3$ and GdMnO$_3$.

Total entropy (S) as a function of temperature for GdAlO$_3$ and GdMnO$_3$ at zero field and 9 T applied field, calculated from heat capacity measurements are presented in Figure 6.7 (a) and (b), respectively and closed Carnot cycles (ABCDA), are shown schematically. Note that both $\triangle S_M$ and $\triangle T_{ad}$ are crucial for the achievement of magnetic refrigeration. Therefore, we have done detailed calculations of these parameters from specific heat data acquired at various magnetic fields as well as from isothermal magnetization curve at various temperatures.

Temperature dependence of -$\triangle S_M$ and $\triangle T_{ad}$ for GdAlO$_3$, with varying magnetic field

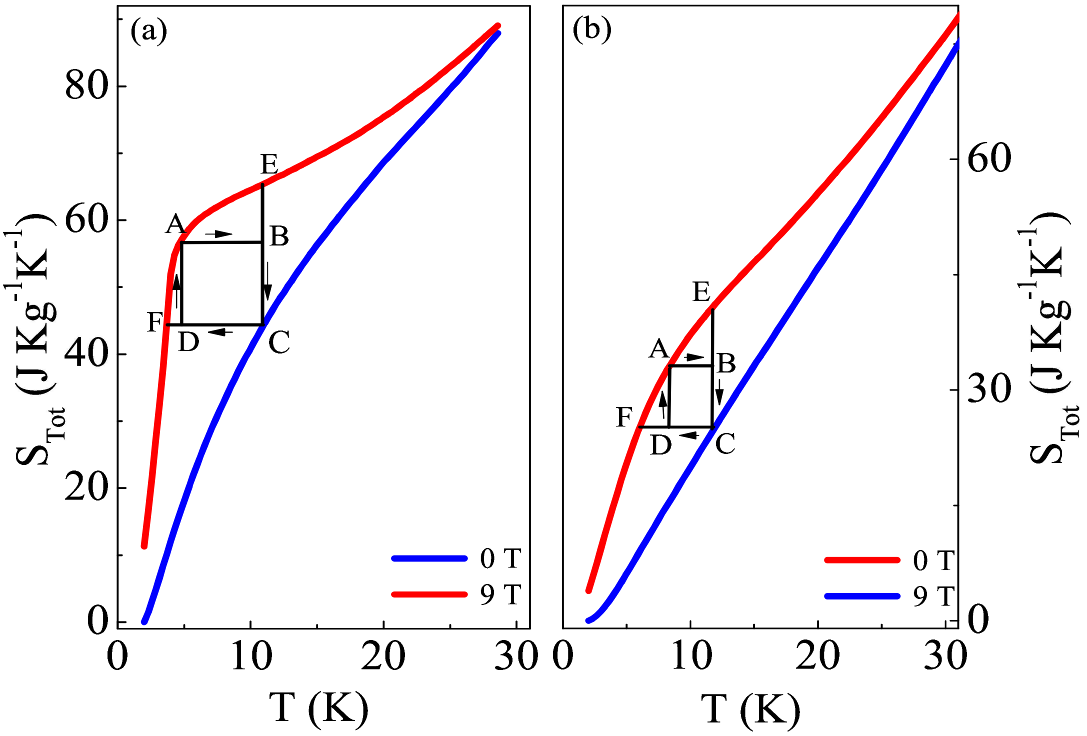

Figure 6.7: Total entropy (S) as a function of temperature for zero field and 9 T applied field for $GdAlO_3$ (a) and $GdMnO_3$ (b). A schematic of the Carnot cycle (ABCD) is shown for both the cases.

from 1 T to 9 T calculated from heat capacity are shown in Figure 6.8 (a) and (b), respectively. Below T_N(Gd), -$\triangle S_M$ is negative up to 4 T. Hence, $GdAlO_3$ exhibits an inverse magnetocaloric effect in the antiferromagnetic as well as in the spin flop region. -$\triangle S_M$ is observed to be more and more negative with increasing magnetic fields up to 3 T. This is caused by the field-induced spin disordering since an initial increase of magnetic field enhances the magnetic moment fluctuation in one of the two antiferromagnetic sublattices which is antiparallel to the magnetic field. With further increase of magnetic field beyond 4 T as the system becomes ferromagnetic, the majority of spins in antiparallel sublattice orient along the field direction resulting in an ordered state, which in turn, results in positive -$\triangle S_M$ that means conventional magnetocaloric effect. Similarly, $\triangle T_{ad}$ also shows negative hump in antiferromagnetic/spin flop region and becomes positive in the ferromagnetic region.

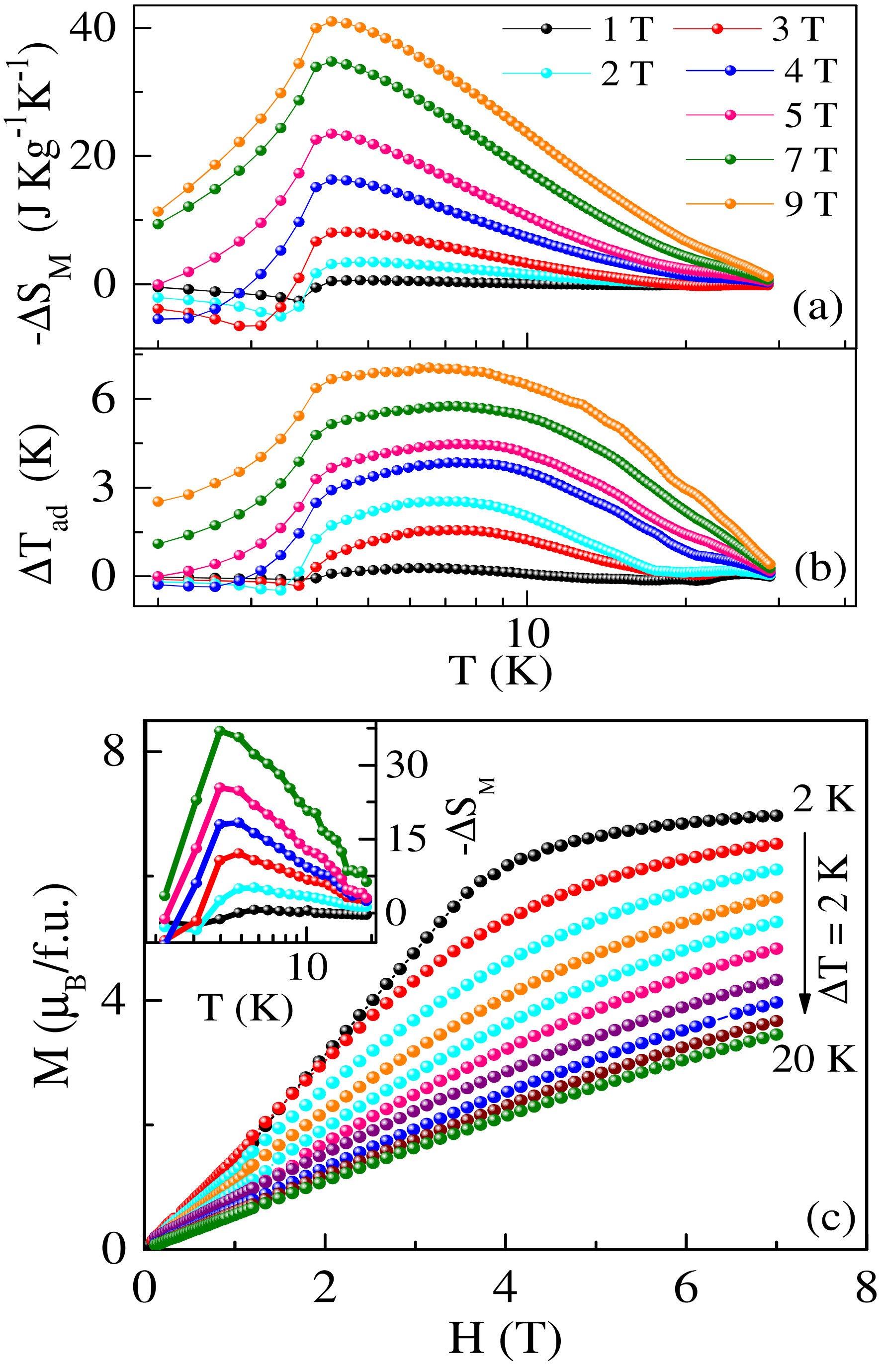

Figure 6.8: Temperature dependence of (a) isothermal entropy change (-$\triangle S_M$) and (b) adiabatic temperature change ($\triangle T_{ad}$) of GdAlO$_3$, with varying magnetic field from 1 T to 9 T with x-axis in log-scale. Inset shows temperature dependence of -$\triangle S_M$ calculated from isothermal magnetization curves.

Temperature dependence of -$\triangle S_M$ and $\triangle T_{ad}$ for GdMnO$_3$, with varying magnetic field

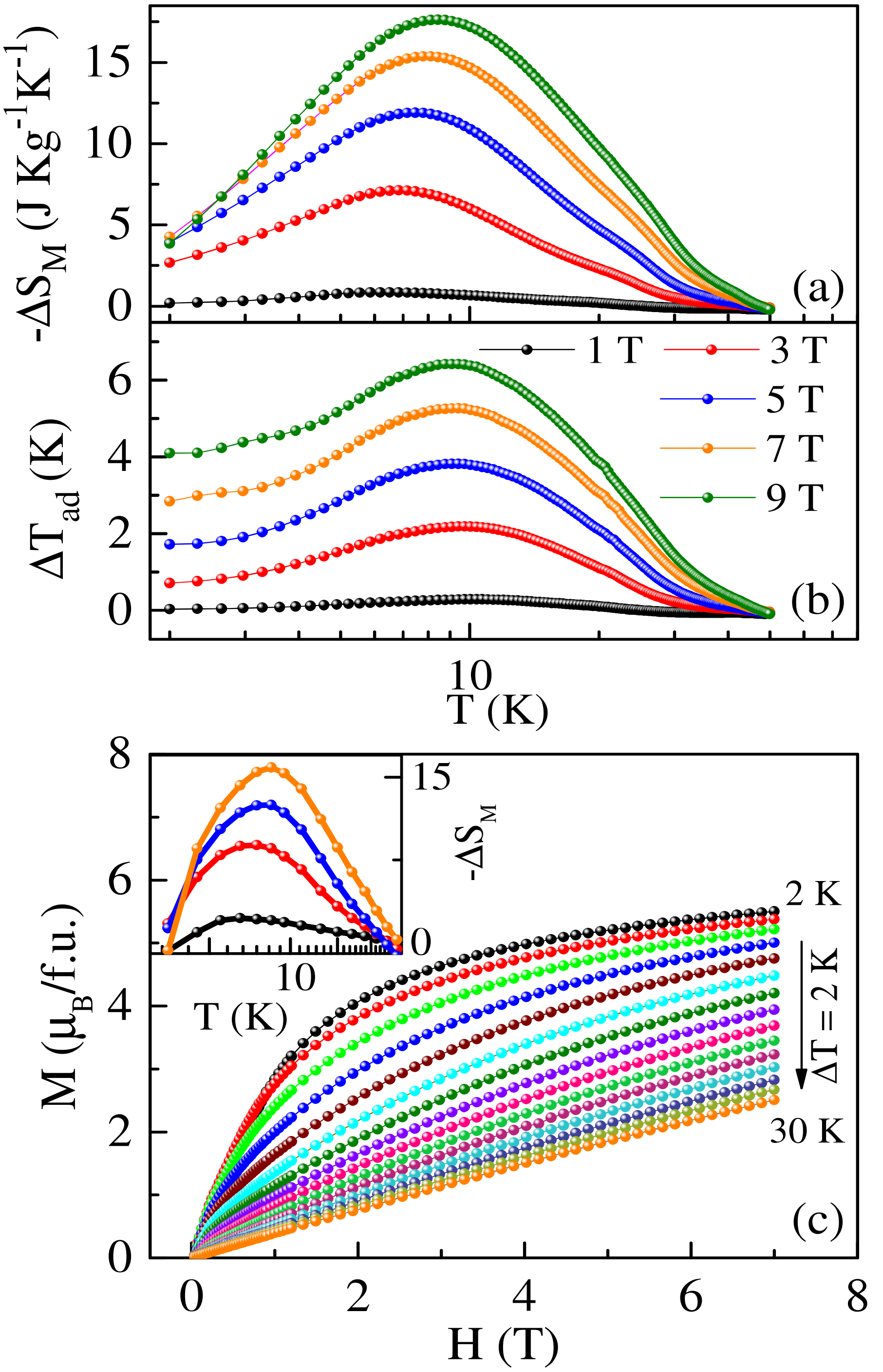

Figure 6.9: Temperature dependence of (a) isothermal entropy change (-$\triangle S_M$) and (b) adiabatic temperature change ($\triangle T_{ad}$) of GdMnO$_3$, with varying magnetic field from 1 T to 9 T with x-axis in log-scale. Inset shows temperature dependence of -$\triangle S_M$ calculated from isothermal magnetization curves.

from 1 T to 9 T are shown in Figure 6.9 (a) and (b), respectively. Unlike $GdAlO_3$, here -$\triangle S_M$ is positive down to the lowest measured temperature under all magnetic field changes (1-9 T). This suggests antiferromagnetic ground state in $GdMnO_3$ is less stable against the applied field and metamagnetic transition from antiferromagnetic to ferromagnetic state occurs at a small value of magnetic field. Similarly, $\triangle T_{ad}(T)$ is also positive in the whole temperature range under all magnetic field changes.

A comparison of the variation of maximum of isothermal entropy change (-$\triangle S_M^{max}$), maximum of adiabatic temperature change ($\triangle T_{ad}^{max}$) for $GdMnO_3$ and $GdAlO_3$ as a function of external magnetic field are depicted in Figure 6.10(a) and (b), respectively . At lower field changes (1-3 T), the -$\triangle S_M^{max}$ is almost same in both the compounds. But a rapid increase of -$\triangle S_M^{max}$ occurs in $GdAlO_3$ afterwords. Beyond 5 T, rate of increasing of -$\triangle S_M^{max}$ reduces as the moment is approaching towards saturation. For $GdMnO_3$ ferromagnetic state is established below 1 T resulting in a smooth variation of -$\triangle S_M^{max}$. It is found, -$\triangle S_M^{max}$ is as high as 40.9 J/Kg.K for $GdAlO_3$ while for $GdMnO_3$, it is 18 J/Kg.K at $\triangle H = 9$ T. So the value of $\triangle T_{ad}^{max}$ for $GdAlO_3$ is slightly higher compared to that of $GdMnO_3$. Also for $GdAlO_3$, the rate of increase of $\triangle T_{ad}^{max}$ reduces slightly above 4 T, whereas that of $GdMnO_3$ it varies smoothly throughout the whole magnetic field changes. The low value of magnetic entropy change in $GdMnO_3$ is possibly due to the $3d$-$4f$ negative exchange interaction.

In order to assures the potentiality as good magnetic refrigerant materials, along with -$\triangle S_M^{max}$ and $\triangle T_{ad}^{max}$ the relative cooling power (RCP) of materials also needs to be taken into account. The maximum of RCP (RCP^{max}) at different applied fields for both the materials has been calculated using Eq. 6.7, which is depicted in Figure 6.10 (c). It is observed that in spite of having larger magnetic entropy change for $GdAlO_3$ than that of $GdMnO_3$, both the systems show almost same RCP for an external field greater than 4 T . This is because RCP not only depends on -$\triangle S_M^{max}$, but also on FWHM of -$\triangle S_M$ peak. For $GdAlO_3$, -$\triangle S_M$ shows a rapid fall on both sides of the maximum value, where as for $GdMnO_3$ it decreases smoothly on both sides of the -$\triangle S_M$ peak, resulting in a higher FWHM in $GdMnO_3$ than that of $GdAlO_3$, as shown in inset of Figure 6.10 (c). RCP of $GdAlO_3$ at $\triangle H = 7$ T and 9 T is estimated to be 203 and 271 J/Kg for ,

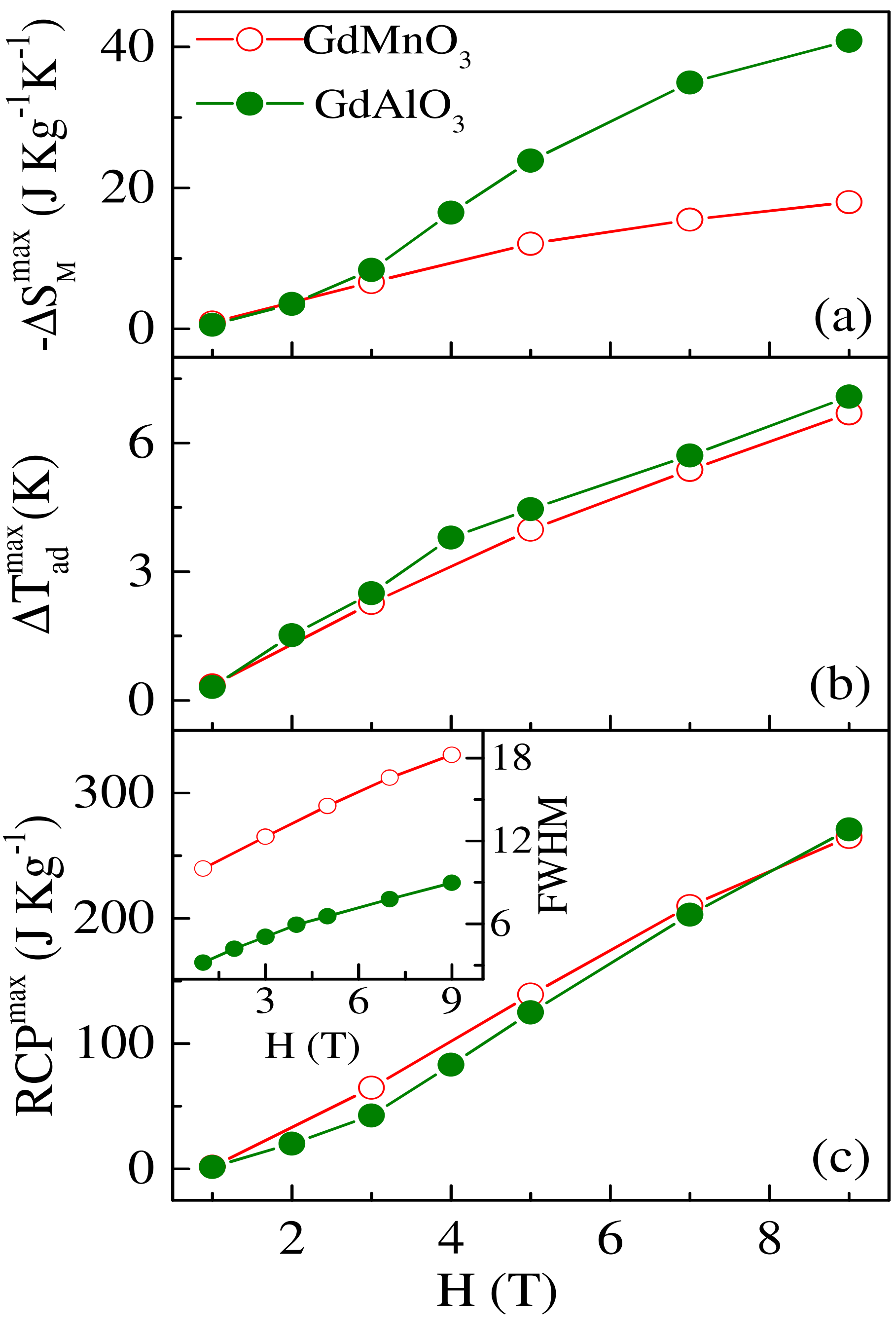

Figure 6.10: Variation of maximum of isothermal entropy change (-$\triangle S_M^{max}$), maximum of adiabatic temperature change $\triangle T_{ad}^{max}$) and relative cooling power (RCP) for $GdMnO_3$ and $GdAlO_3$ as a function external magnetic fields are shown in panels (a), (b) and (c), respectively. Inset shows variation of full-width-half maximum (FWHM) of -$\triangle S_M$ peak for $GdMnO_3$ and $GdAlO_3$ as a function external magnetic fields.

respectively, whereas that for GdMnO$_3$ is 211 and 265 J/Kg, respectively. The obtained values of -$\triangle S_M^{max}$, $\triangle T_{ad}^{max}$ and relative cooling power for these systems are comparable to several other systems in the same temperature range as well as for same magnetic field changes [256,258,276,277]. So these systems can be used as efficient magnetic refrigerants in low temperature region. Since GdAlO$_3$ does not show any thermal and magnetic hysteresis, whereas GdMnO$_3$ do exhibit a small magnetic hysteresis at low temperature, hence one may conclude that GdAlO$_3$ is a more efficient candidate for cryogenic magnetic refrigeration than GdMnO$_3$ at moderate magnetic field changes [252].

6.3.3.2 GdCrO$_3$: Potential candidate for low temperature magnetic refrigeration

Some of the rare-earth chromites (RCrO$_3$) have also been studied from the prospective of magnetocaloric effect and are found promising systems for low-temperature magnetic refrigeration [184, 278, 279]. Single crystal of GdCrO$_3$ exhibits a giant -ΔS_M at moderate magnetic field, indicating that it is a potential candidate for effective magnetic refrigeration [184]. Yin *et al.* [280] also observed exceptionally high -ΔS_M and RCP in polycrystalline GdCrO$_3$. However, a good magnetic refrigerant should also possess large values for ΔT_{ad}). Besides, they have evaluated -ΔS_M from magnetic measurements only. MCE at low temperature calculated from magnetization data sometimes gives high error ($\sim$ 20-30%), whereas calculated from heat capacity data shows a better accuracy [252]. Therefore, we reinvestigated the magnetocaloric effect of polycrystalline GdCrO$_3$ from heat capacity measurements.

Figure 6.11 (a) represents total entropy (S) as a function of temperature for zero field and 9 T applied field, as calculated from heat capacity data and temperature dependent -ΔS_M for different field variations are shown Figure 6.11 (b). The maximum of -ΔS_M reaches as high as 41.24 J.Kg^{-1}.K^{-1} at around 3.8 K for $\Delta H = 9$ T. This is exceptionally large in comparison with the similar rare-earth perovskites, such as RMnO$_3$ [257,273,281, 282], RFeO$_3$ [283–285] and other RCrO$_3$, R = Ho and Dy [278,279]. Generally, the above said compounds containing magnetic 3d-elements (Mn, Cr and Fe) exhibit less -ΔS_M in comparison to than that of RAlO$_3$ [271,272,286], where R is the only magnetic sublattice,

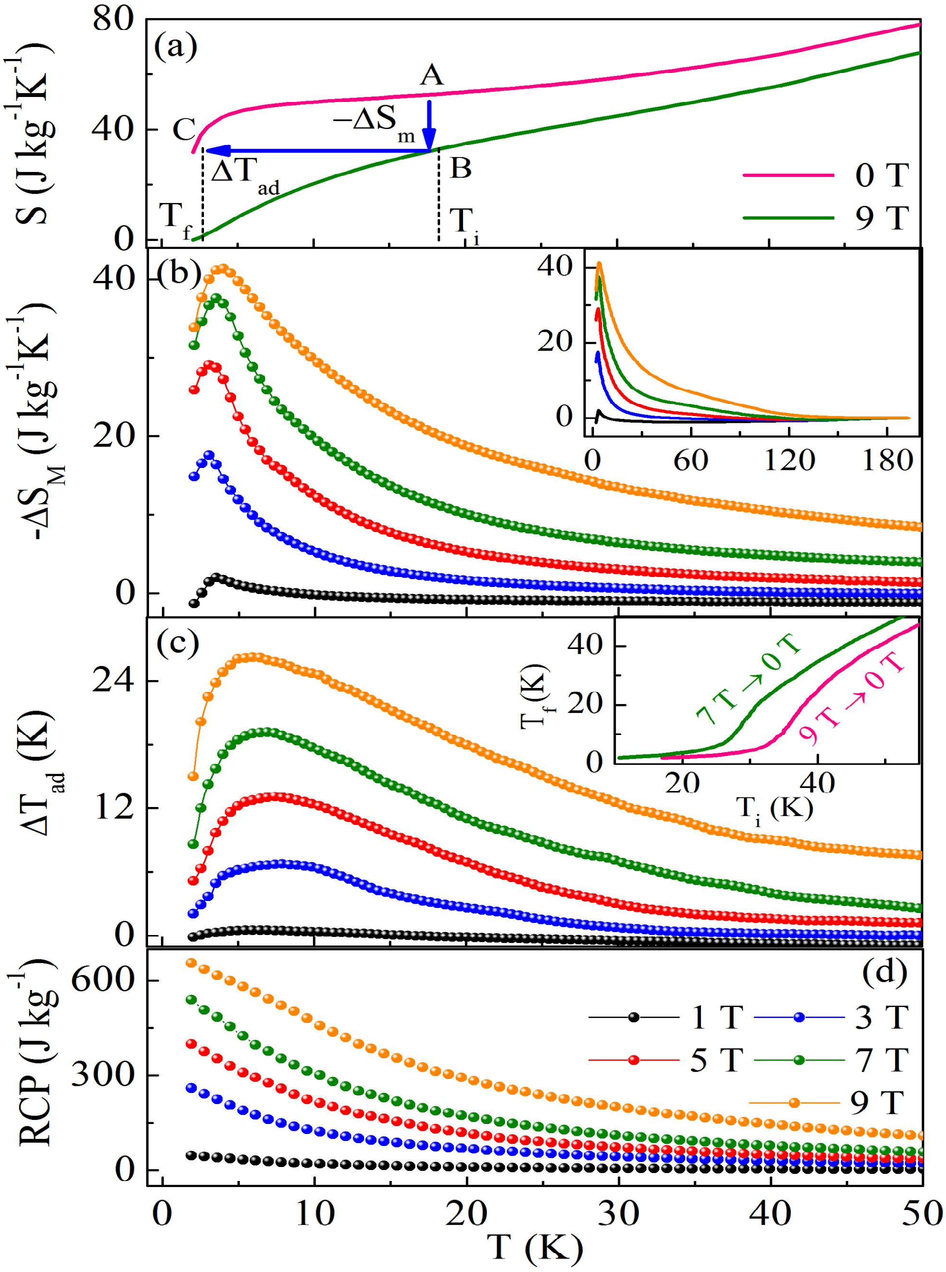

Figure 6.11: (a) Total entropy (S) as a function of temperature for zero field and 9 T applied field for GdCrO$_3$, calculated from the heat capacity data. Arrows (AB) and (BC) represent isothermal entropy change and isentropic temperature change, respectively. Temperature dependence of (b) isothermal entropy change (-ΔS_M) and (c) adiabatic temperature change (ΔT_{ad}) and (d) relative cooling power (RCP) at various magnetic field changes up to 9 T. Inset of (b) represent -ΔS_M up to the temperature well above magnetic ordering temperature (190 K) and inset of (c) represent final temperature (T_f) as a function of initial temperature (T_i) in the adiabatic demagnetization process for 9 T and 7 T magnetic fields.

due to the presence of negative 3d-4f exchange interactions. In contrast, $GdCrO_3$ shows larger -ΔS_M as compared to RAlO_3 [271, 272, 286], indicating that change in magnetic entropy is not simply induced by the ordering of R-sublattice or the interactions between R-4f and Mn-3d, moreover some new mechanism is expected to be responsible for this giant magnetic entropy change. It is clearly seen that the magnetic entropy changes rapidly below 10 K (Figure 6.11 (b)). Further, M vs. T measurement decreases rapidly below the spin reorientation transition ($\sim$ 7 K) i.e, dM/dT is large and change in magnetic entropy is proportional to the dM/dT . All these observations corroborates that the extra contribution from suppression of spin reorientation under the applied field along with the suppression of Gd-ordering is responsible for giant magnetic entopy change in $GdCrO_3$ [184, 280].

In order to have a better understanding on the application potential of $GdCrO_3$, we calculated MCE in terms ΔT_{ad}. It is extracted from the isentropic line connecting $S(H, T_i)$ and $S(0,T_f)$ for a magnetic field change from zero to a final value H [269], as shown in Figure 6.11 (a). The temperature dependence of ΔT_{ad} with varying magnetic fields from 1 T to 9 T are shown in Figure 6.11 (c) and inset represent final temperature (T_f) as a function of initial temperature (T_i) in the adiabatic demagnetization process for 9 T and 7 T magnetic fields. The maximum value of ΔT_{ad} reaches as high as 26.2 K for a field change of 9 T. If the sample is initially at 32 K and magnetized by 9 T, decreasing the magnetic field adiabatically to zero causes the sample temperature drop to 6.5 K. Values of -ΔS_M^{max} and ΔT_{ad}^{max} for the present compound are quite large as comparable to that of most of the potential magnetic refrigerant materials with low magnetic transition temperatures.

RCP is another important paramter, that we calculated. The maximum value of RCP is typically reported as the product of ΔS_M^{max} and the full width half maximum of the ΔS_M peak (Eq. 6.7). In the the present system the full peak is not observed since it occurs at very low temperature . Therefore, the temperature depent RCP was evaluated from high temperature (T_2 = 190 K) to low temperature (T_1 = 2 K), using Eq. 6.6 [279]. RCP as a function of temperature for different magnetic field changes (1-9 T) is shown in Figure 6.13 (d). It is observed that $GdCrO_3$ exhibit a giant RCP of 648 J Kg^{-1} at 2 K for 9 T field change. For comparison of the magnetocaloric properties, the values

Table 6.1: -ΔS_M^{max}, ΔT_{ad}^{max} and RCP^{max} of various potential magnetic refrigerant materials having operating temperature below 20 K along with $GdCrO_3$.

Compound	-ΔS_M^{max} (J.Kg^{-1}.K^{-1})	ΔT_{ad}^{max} (K)	RCP^{max} (J.Kg^{-1})	H (T)
$GdCrO_3$[This work]	36.97	19.12	542	7
$Ho_{0.67}Gd_{0.33}CrO_3$ [279]	14	5	490	7
$GdAlO_3$	34.27	6	209	7
$EuTiO_3$ [269]	42.4	16.6	353	5
$Gd(HCOO)_3$ [287]	55	22	503	7
$Eu_{0.99}La_{0.01}TiO_3$ [288]	41.5	17.2	445	5
$EuTi_{0.85}Nb_{0.15}O_3$ [289]	36.3	15.5	410	5
$EuHo_2O_4$ [290]	37	10.4	275	5
EuS [291]	37	10.4	782	5
EuSe [292]	37.5	...	580	5
Gd_2NiMnO_6 [256]	36	11.5	...	7

of -ΔS_M^{max}, ΔT_{ad}^{max} and RCP^{max} of various promising magnetocaloric materials having operating temperature below 20 K along with $GdCrO_3$ are listed in Table 6.1. $EuTiO_3$ and $Gd(HCOO)_3$ exhibit quite large -ΔS_M^{max} and comparable ΔT_{ad}^{max}, however their RCP is still lower than that obtained for $GdCrO_3$. Even though EuS has largest RCP^{max} and comparable -ΔS_M^{max}, ΔT_{ad}^{max} is quite less in comparison to $GdCrO_3$. Comparison of all the parameters shows that, polycrystalline $GdCrO_3$ indeed possesses large MCE. The giant MCE parameters in polycrystalline $GdCrO_3$ along with high insulating nature of the sample, weak magnetic hysteresis and easy synthesis procedures make it a promising candidate for low temperature magnetocaloric applications.

6.4 Conclusion

For $GdAlO_3$ antiferromagnetic interaction in Gd-sublattice is strong, thus it exhibits both inverse and conventional magnetocaloric effect below and above 4 T, respectively. Where as, $GdMnO_3$ shows only conventional magnetocaloric effect as antiferromagnetic state is suppressed at very small extenal magnetic field. At moderate magnetic field $GdAlO_3$ shows a giant magnetic entropy change of 40.9 J kg^{-1} K^{-1} compared to $GdMnO_3$ 18 J kg^{-1} K^{-1} for a field change of 9 T. However, relative cooling power and ΔT_{ad} are comparable for both the systems. All the magnetocaloric parameters obtained for these systems are comparable to several potential magnetic refrigeration materials and can be used as potential magnetic refrigerant at cryogenic temperature. Moreover, the absence of magnetic and thermal hysteresis in GdAlO$_3$ make it more efficient magnetic refrigerant than GdMnO$_3$. We have also studied the detailed magnetocaloric properties of polycrystalline GdCrO$_3$ sample from heat capacity measurements. It exhibits giant isothermal entropy change of 36.97 J kg^{-1} K^{-1}, adiabatic temperature change of 19.12 K, and a refrigeration capacity of 542 J kg^{-1} for a field change of 7 T at low temperature. Thus, polycrystalline GdCrO$_3$ is one of the best candidate for cryogenic magnetic refrigeration. In addition to giant MCE parameters, high insulating nature of materials and negligible magnetic hysteresis make it a potential low temperature magnetic refrigerant.

Chapter 7

Summary and outlook

In this thesis we present detailed investigation of magnetic and feroelectric properties and related phenomena on two kinds of functional oxides: one gallium ferrites with various stoichiometric compositions ($Ga_{2-x}Fe_xO_3$) and other perovskite oxides of the type $GdM_xM'_{1-x}O_3$, where M, M' = Cr, Mn and Al. Our findings of complex spin glass behavior and TSDC phenomena in polycrystalline $Ga_{2-x}Fe_xO_3$ are presented in chapter 3. Investigations on origin ferroelectricity and complex magnetic behavior of $GdCrO_3$ are discussed in chapter 4. Studies on structural, electronic and magnetic evolutions in $GdCr_{1-x}Mn_xO_3$ are presented in chapter 5 and investigations on magnetocaloric effect of polycrystalline $GdMO_3$ (M = Al, Mn and Cr) are presented in chapter 6. In the following sections we summarize our main results and outlook of the of the present work.

7.1 $Ga_{2-x}Fe_xO_3$

These are unique systems, where the properties are heavily influenced by disorder at the atomic level and hence can be tuned either by varying compositions or by various synthesizing techniques. In particular, the spin glass behavior and ferroelectric behavior in polycrystalline sample had long been under dispute. We prepared a series of polycrystalline compounds of the type $Ga_{2-x}Fe_xO_3$ ($x = 0.75$, 1, 1.25) . Magnetic behavior in this series of compounds could broadly be explained by the molecular-field-approximation of three-sublattice ferrimagnetic model. Detailed analysis revealed a transition from cluster-glass-like phase to spin-glass-like phase with decreasing temperature for $x = 0.75$ composition. Mentioned glassy behavior is found to gradually evolve with the composition (x) from the Ising type character to Heisenberg type behavior to unconventional glassy behavior for the $x = 1.25$ composition. This system hence can serve as an ideal system for modeling complex spin glasses.The complex spin glass behavior in these systems is due to the inherent site disorder driven magnetic inhomogeneity, competing FM and AFM interactions along with spin frustration and their modifications with compositions (x). Detailed dielectric and pyroelectric studies confirmed that the emergence of polarization in these systems is a thermally stimulated process caused by the freezing of defect dipoles possibly associated with charged oxygen vacancies rather than being the intrinsic ferroelectric behavior.

7.2 Gd$M_xM'_{1-x}$O$_3$, M, M' = Cr, Mn, Al

Conflict between the observations of the ferroelectric behavior and the centrosymmetric lattice and magnetic structure in $GdCrO_3$ is a puzzling issue. As a key to solve the problem, we found that the preferred lattice symmetry in $GdCrO_3$ is non-centrosymmetric orthorhombic $Pna2_1$, supporting polar nature of the system. The distortion in the structure is associated with the off-centering displacement of Gd-atoms together with octahedral rotations via movements of oxygen ions. The weak polarization arises from the small ferroelectric instability resulting in Gd-O bond polarization. Furthermore, magnetic coupling between Gd-4f and Cr-3d also plays an important role in ferroelectric distortion. Additionally, it exhibits various complex magnetic phenomena like temperature induced magnetization reversal, spin flipping, spin reorientation and many more, which can be successfully explained by symmetric ($S_i\ .\ S_j$) and antisymmetric ($S_i \times S_j$) exchange interactions within and between Cr and Gd-sublattices.

Investigating structural evolution from Jahn-Teller active region to Jahn-Teller inactive region with increasing Cr content in $GdMn_{1-x}Cr_xO_3$, we found there is close correlation between lattice, spin, electronic and orbital degrees of freedom. Jahn-Teller distortion associated with Mn^{3+} ions gives rise to major changes in the bc-plane sublattice and also the effective orbital ordering in the ab-plane, which persists up to the compositions $x \sim 0.35$. These distinct features in the lattice and orbital degrees of freedom are also correlated with the bc-plane anisotropy in the local Gd environment Progressive modification of magnetic coupling with the compositions results into complex and distinct magnetic behavior throughout the series. DFT calculations using GGA + U type exchange correlation potential find that the system with intermediate composition ($GdMn_{0.5}Cr_{0.5}O_3$) consists of alternate ferromagnetic Mn layers and antiferromagnetic Cr layers, which is distinct from that observed for the end members $GMnO_3$ (A-type) and and $GdCrO_3$ (G-type).

We have also investigated magnetocaloric effect in polycrystalline GdMO$_3$ (M = Al, Mn and Cr) to assess their potential usage as magnetic refrigerants at cryogenic temperatures. $GdAlO_3$ exhibits a giant magnetic entropy change under moderate magnetic field change, where as $GdMnO_3$ exhibits comparably less magnetic entropy at same magnetic field changes, possibly due to the Gd-Mn negative exchange interaction. All the magnetocaloric parameters (magnetic entropy, adiabatic temperature, relative cooling power) are found to be exceptionally high for $GdCrO_3$, which makes it one of the best material for magnetic refrigeration among all the potential low temperature magnetic refrigerants discovered so far. Such extraordinarily large MCE in $GdCrO_3$ possibly arises from the suppression of the spin entropy associated with the suppression of spin reorientation transition, in addition to the Gd-ordering.

References

[1] P. Coleman, “*Handbook of Magnetism and Advanced Magnetic Materials*”, 2007. 1

[2] R. E. Cohen, “*Origin of ferroelectricity in perovskite oxides*”, Nature **358** (1992) 136–138. 1, 18

[3] M. M. Kumar, V. Palkar, K. Srinivas and S. Suryanarayana, “*Ferroelectricity in a pure* $BiFeO_3$ *ceramic*”, Applied Physics Letters **76** (2000) 2764–2766. 1

[4] S.-W. Cheong and M. Mostovoy, “*Multiferroics: a magnetic twist for ferroelectricity*”, Nature materials **6** (2007) 13–20. 1, 19, 20, 126

[5] S. Shao, J. Zhang, Z. Zhang, P. Zheng, M. Zhao, J. Li and C. Wang, “*High piezoelectric properties and domain configuration in* $BaTiO_3$ *ceramics obtained through the solid-state reaction route*”, Journal of Physics D: Applied Physics **41** (2008) 125408. 1

[6] R. Kajimoto, K. Ishizaka, H. Yoshizawa and Y. Tokura, “*Spontaneous rearrangement of the checkerboard charge order to stripe order in* $La_{1.5}Sr_{0.5}NiO_4$”, Physical Review B **67** (2003) 014511. 1

[7] M. Imada, A. Fujimori and Y. Tokura, “*Metal-insulator transitions*”, Reviews of modern physics **70** (1998) 1039. 1

[8] R. von Helmolt, J. Wecker, B. Holzapfel, L. Schultz and K. Samwer, “*Giant negative magnetoresistance in perovskitelike* $La_{2/3}Ba_{1/3}MnO_x$ *ferromagnetic films*”, Physical Review Letters **71** (1993) 2331. 1

[9] Y. Tokura and N. Nagaosa, “*Orbital physics in transition-metal oxides*”, science **288** (2000) 462–468. 1

[10] H. Gretarsson, S. Saha, T. Drye, J. Paglione, J. Kim, D. Casa, T. Gog, W. Wu, S. Julian and Y.-J. Kim, “*Spin-state transition in the Fe pnictides*”, Physical review letters **110** (2013) 047003. 1

[11] A. Schilling, M. Cantoni, J. Guo and H. Ott, “*Superconductivity above 130 K in the Hg–Ba–Ca–Cu–O system*”, Nature **363** (1993) 56–58. 1

[12] C. Wang, L. Li, S. Chi, Z. Zhu, Z. Ren, Y. Li, Y. Wang, X. Lin, Y. Luo, S. Jiang et al., “*Thorium-doping–induced superconductivity up to 56 K in* $Gd_{1-x}Th_xFeAsO$”, EPL (Europhysics Letters) **83** (2008) 67006. 1

[13] S. Cao, H. Zhao, B. Kang, J. Zhang and W. Ren, "*Temperature induced spin switching in* $SmFeO_3$ *single crystal*", Scientific reports **4** (2014) . 1

[14] V. Pardo and W. E. Pickett, "*Pressure-induced metal-insulator and spin-state transition in low-valence layered nickelates*", Physical Review B **85** (2012) 045111. 1

[15] N. Sakiyama, I. Zaliznyak, S.-H. Lee, Y. Mitsui and H. Yoshizawa, "*Doping-dependent charge and spin superstructures in layered cobalt perovskites*", Physical Review B **78** (2008) 180406. 1

[16] Y. Tokura, "*COMOP today*", Physics Today (2003) 50–55. 1

[17] S. Dhar, R. Kulkarni, P. Manfrinetti, M. Pani, Y. Yonezawa and Y. Aoki, "*Synthesis, crystal structure, and physical properties of YbTZn (T= Pd, Pt, and Au) and LuPtZn*", Physical Review B **76** (2007) 054411. 1

[18] L. Jiao, S. Rößler, D. Kim, L. Tjeng, Z. Fisk, F. Steglich and S. Wirth, "*Additional energy scale in* SmB_6 *at low-temperature*", Nature communications **7** (2016) . 1

[19] J. Merino and R. H. McKenzie, "*Phonon anomalies due to strong electronic correlations in layered organic metals*", Physical Review B **62** (2000) 16442. 1

[20] M. Filibian, P. Carretta, M. Mozzati, P. Ghigna, G. Zoppellaro and M. Ruben, "*Strong electronic correlations in* Li_xZnPc *organic metals*", Physical review letters **100** (2008) 117601. 1

[21] K. Khamoushi, "*Characterization and dielectric properties of microwave rare earth ceramics materials for telecommunications*", arXiv preprint arXiv:1509.04445 (2015) . 1

[22] K. Yokoyama, Y. Fujine, S. Fujinuma, K. Noto and M. Yamaguchi, "*Homogenous magnetic field generation by high-*T_c *oxide superconductors*", IEEE transactions on applied superconductivity **12** (2002) 1171–1175. 1

[23] J.-G. J. Zhu, "*New heights for hard disk drives*", Materials Today **6** (2003) 22–31. 2

[24] D. Scott, P. Coveney, J. Kilner, J. Rossiny and N. M. N. Alford, "*Prediction of the functional properties of ceramic materials from composition using artificial neural networks*", Journal of the European Ceramic Society **27** (2007) 4425–4435. 2

[25] Z. L. Wang and Z. C. Kang, "*FUNCTIONAL AND SMART MATERIALS: Structural evolution and structure analysis*", 2002. 2

[26] T. Arima, D. Higashiyama, Y. Kaneko, J. He, T. Goto, S. Miyasaka, T. Kimura, K. Oikawa, T. Kamiyama, R. Kumai et al., "*Structural and magnetoelectric properties of* $Ga_{2-x}Fe_xO_3$ *single crystals grown by a floating-zone method*", Phys. Rev. B **70** (2004) 064426. 2, 3, 4, 56, 57, 59, 62, 68

[27] N. Wang, F. Wen, L. Li, Y. Lü, S. Liu, Y. Lu, Z. Liu, B. Xu, J. He, D. Yu and Y. Tian, "*Magnetic frustration effect in polycrystalline* $Ga_{2-x}Fe_xO_3$", J. Magn. Magn. Mater. **322** (2010) 3595–3600. 2, 4, 56, 62, 67, 68

[28] S. Mukherjee, A. Roy, S. Auluck, R. Prasad, R. Gupta and A. Garg, "*Room temperature nanoscale ferroelectricity in magnetoelectric* $GaFeO_3$ *epitaxial thin films*", Phys. Rev. Lett. **111** (2013) 087601. 2, 4, 73

[29] S. H. Oh, J. H. Lee, R. H. Shin, Y. Shin, C. Meny and W. Jo, "*Room-temperature polarization switching and antiferromagnetic coupling in epitaxial* $(Ga,Fe)_2O_3/SrRuO_3$ *heterostructures*", Appl. Phys. Lett. **106** (2015) 142902. 2, 4, 73

[30] S. Song, H. M. Jang, N.-S. Lee, J. Y. Son, R. Gupta, A. Garg, J. Ratanapreechachai and J. F. Scott, "*Ferroelectric polarization switching with a remarkably high activation energy in orthorhombic* $GaFeO_3$ *thin films*", NPG Asia Materials **8** (2016) e242. 2, 4, 73

[31] J. Remeika, "$GaFeO_3$*: A ferromagnetic-piezoelectric compound*", J. Appl. Phys. **31** (1960) 263. 2, 56

[32] M. J. Han, T. Ozaki and J. Yu, "*Magnetic ordering and exchange interactions in multiferroic* $GaFeO_3$", Phys. Rev. B **75** (2007) 060404. 3

[33] K. U. Kang, S. B. Kim, S. Y. An, S.-W. Cheong and C. S. Kim, "*Magnetic properties of* $GaFeO_3$ *prepared by slow cooling and quenched heat treatment method*", Journal of Magnetism and Magnetic Materials **304** (2006) e769–e771. 4

[34] D. Stoeffler, "*First principles study of the electric polarization and of its switching in the multiferroic* $GaFeO_3$ *system*", J. Phys. Condens. Matter **24** (2012) 185502. 4, 73

[35] R. H. Mitchell, " *Perovskites: Modern and Ancient* ", (Almaz Press, Ontario, 2002) p. 318. 4, 5, 126

[36] A. Glazer, "*The classification of tilted octahedra in perovskites*", Acta Crystallographica Section B: Structural Crystallography and Crystal Chemistry **28** (1972) 3384–3392. 5, 126

[37] A. Glazer, "*Simple ways of determining perovskite structures*", Acta Crystallographica Section A: Crystal Physics, Diffraction, Theoretical and General Crystallography **31** (1975) 756–762. 5, 126, 136

[38] C. J. Howard and H. T. Stokes, "*Group-theoretical analysis of octahedral tilting in perovskites*", Acta Crystallographica Section B: Structural Science **54** (1998) 782–789. 6

[39] J.-S. Zhou and J. Goodenough, "*Unusual evolution of the magnetic interactions versus structural distortions in* $RMnO_3$ *perovskites*", Physical review letters **96** (2006) 247202. 6, 132, 133, 134

[40] M. Mochizuki and N. Furukawa, "*Microscopic model and phase diagrams of the multiferroic perovskite manganites*", Physical Review B **80** (2009) 134416. 7, 126, 140

[41] T. Kimura, G. Lawes, T. Goto, Y. Tokura and A. Ramirez, "*Magnetoelectric phase diagrams of orthorhombic RMnO*$_3$ *(R= Gd, Tb, and Dy)*", Physical Review B **71** (2005) 224425. 7, 20, 126, 142

[42] T. Yamaguchi, "*Theory of spin reorientation in rare-earth orthochromites and orthoferrites*", Journal of Physics and Chemistry of Solids **35** (1974) 479–500. 7, 106, 114

[43] Y. Cao, S. Cao, W. Ren, Z. Feng, S. Yuan, B. Kang, B. Lu and J. Zhang, "*Magnetization switching of rare earth orthochromite CeCrO*$_3$", Applied Physics Letters **104** (2014) 232405. 7, 106, 107, 112, 114, 126

[44] M. El Amrani, M. Zaghrioui, V. T. Phuoc, F. Gervais and N. E. Massa, "*Local symmetry breaking and spin–phonon coupling in SmCrO*$_3$ *orthochromite*", Journal of Magnetism and Magnetic Materials **361** (2014) 1–6. 7, 121, 126

[45] J. B. GoodenoughMagnetism and the Chemical Bond, Interscience (Wiley), New York (1963) . 9

[46] M. A. Ruderman and C. Kittel, "*Indirect exchange coupling of nuclear magnetic moments by conduction electrons*", Physical Review **96** (1954) 99. 10

[47] I. Dzyaloshinsky, "*A thermodynamic theory of weak ferromagnetism of antiferromagnetics*", Journal of Physics and Chemistry of Solids **4** (1958) 241–255. 11, 108

[48] T. Moriya, "*Anisotropic superexchange interaction and weak ferromagnetism*", Physical Review **120** (1960) 91. 11, 108, 122

[49] F. Keffer, "*Moriya interaction and the problem of the spin arrangements in* β *mns*", Physical Review **126** (1962) 896. 11

[50] J. A. Mydosh, *Spin Glasses: An Experimental Introduction.* Taylor & Francis, 1993. 11, 12, 56, 62, 64

[51] S. Bedanta and W. Kleemann, "*Supermagnetism*", Journal of Physics D: Applied Physics **42** (2008) 013001. 13

[52] A. Bray and M. Moore, "*Chaotic nature of the spin-glass phase*", Physical review letters **58** (1987) 57. 13

[53] K. A. GschneidnerJr, V. Pecharsky and A. Tsokol, "*Recent developments in magnetocaloric materials*", Reports on progress in physics **68** (2005) 1479. 13, 152, 161

[54] E. Warburg, "*Magnetische untersuchungen*", Annalen der Physik **249** (1881) 141–164. 13

[55] A. Smith, "*Who discovered the magnetocaloric effect*", Eur. Phys. J. H **38** (2013) 507–17. 13

[56] P. Debye, "*Einige bemerkungen zur magnetisierung bei tiefer temperatur*", Annalen der Physik **386** (1926) 1154–1160. 13

[57] W. Giauque, "*A thermodynamic treatment of certain magnetic effects. A proposed method of producing temperatures considerably below 1° absolute*", Journal of the American Chemical Society **49** (1927) 1864–1870. 13

[58] W. Giauque and D. MacDougall, "*Attainment of temperatures below 1° absolute by demagnetization of* $Gd_2(SO_4)_3{\cdot}8H_2O$", Physical Review **43** (1933) 768. 13

[59] G. Brown, "*Magnetic heat pumping near room temperature*", Journal of Applied Physics **47** (1976) 3673–3680. 13

[60] N. A. Hill, "*Why are there so few magnetic ferroelectrics?*", The Journal of Physical Chemistry B **104** (2000) 6694–6709. 18

[61] G. Kwei, A. Lawson, S. Billinge and S. Cheong, "*Structures of the ferroelectric phases of barium titanate*", The Journal of Physical Chemistry **97** (1993) 2368–2377. 18

[62] J. Wang, J. Neaton, H. Zheng, V. Nagarajan, S. Ogale, B. Liu, D. Viehland, V. Vaithyanathan, D. Schlom, U. Waghmare et al., "*Epitaxial* $BiFeO_3$ *multiferroic thin film heterostructures*", science **299** (2003) 1719–1722. 18

[63] R. Seshadri and N. A. Hill, "*Visualizing the role of Bi 6s lone pairs in the off-center distortion in ferromagnetic* $BiMnO_3$", Chemistry of materials **13** (2001) 2892–2899. 18

[64] B. B. Van Aken, T. T. Palstra, A. Filippetti and N. A. Spaldin, "*The origin of ferroelectricity in magnetoelectric* $YMnO_3$", Nature materials **3** (2004) 164–170. 19

[65] J. Van Den Brink and D. I. Khomskii, "*Multiferroicity due to charge ordering*", Journal of Physics: Condensed Matter **20** (2008) 434217. 19, 20

[66] N. Ikeda, H. Ohsumi, K. Ohwada, K. Ishii et al., "*Ferroelectricity from iron valence ordering in the charge-frustrated system* $LuFe_2O_4$", Nature **436** (2005) 1136. 20, 77

[67] G. Giovannetti, S. Kumar, D. Khomskii, S. Picozzi and J. van den Brink, "*Multiferroicity in Rare-Earth Nickelates* $RNiO_3$", Physical review letters **103** 156401. 20

[68] D. V. Efremov, J. Van Den Brink and D. I. Khomskii, "*Bond-versus site-centred ordering and possible ferroelectricity in manganites*", Nature materials **3** (2004) 853–856. 20

[69] M. Kenzelmann, A. B. Harris, S. Jonas, C. Broholm, J. Schefer, S. Kim, C. Zhang, S.-W. Cheong, O. P. Vajk and J. W. Lynn, "*Magnetic inversion symmetry breaking and ferroelectricity in* $TbMnO_3$", Physical Review Letters **95** (2005) 087206. 20

[70] A. Arkenbout, T. Palstra, T. Siegrist and T. Kimura, "*Ferroelectricity in the cycloidal spiral magnetic phase of* $MnWO_4$", Physical Review B **74** (2006) 184431. 20

[71] H. Katsura, N. Nagaosa and A. V. Balatsky, "*Spin current and magnetoelectric effect in noncollinear magnets*", Physical review letters **95** (2005) 057205. 20, 21

[72] Y. Choi, H. Yi, S. Lee, Q. Huang, V. Kiryukhin and S.-W. Cheong, "*Ferroelectricity in an ising chain magnet*", Phys. Rev. Lett. **100** (2008) 047601. 21, 62, 68

[73] C. Jia, S. Onoda, N. Nagaosa and J. H. Han, "*Microscopic theory of spin-polarization coupling in multiferroic transition metal oxides*", Physical Review B **76** (2007) 144424. 22

[74] T.-h. Arima, "*Ferroelectricity induced by proper-screw type magnetic order*", Journal of the Physical Society of Japan **76** (2007) 073702–073702. 22

[75] H. Murakawa, Y. Onose, S. Miyahara, N. Furukawa and Y. Tokura, "*Ferroelectricity induced by spin-dependent metal-ligand hybridization in* $Ba_2CoGe_2O_7$", Physical review letters **105** (2010) 137202. 22

[76] Y. J. Shan, H. Mori, K. Tezuka, H. Imoto and M. Itoh, "*Ferroelectric Phase Transition in* $CdTiO_3$ *Single Crystal*", Ferroelectrics **284** (2003) 107–112. 22

[77] H. Moriwake, A. Kuwabara, C. A. Fisher, H. Taniguchi, M. Itoh and I. Tanaka, "*First-principles calculations of lattice dynamics in* $CdTiO_3$ *and* $CaTiO_3$*: Phase stability and ferroelectricity*", Physical Review B **84** (2011) 104114. 22

[78] C. R. Serrao, A. K. Kundu, S. Krupanidhi, U. V. Waghmare and C. Rao, "*Biferroic* $YCrO_3$", Physical Review B **72** (2005) 220101. 22, 84, 87, 89, 90, 92, 93, 104

[79] N. A. Benedek and C. J. Fennie, "*Hybrid improper ferroelectricity: a mechanism for controllable polarization-magnetization coupling*", Physical review letters **106** (2011) 107204. 22

[80] N. A. Benedek, A. T. Mulder and C. J. Fennie, "*Polar octahedral rotations: a path to new multifunctional materials*", Journal of Solid State Chemistry **195** (2012) 11–20. 22

[81] J. Young, A. Stroppa, S. Picozzi and J. M. Rondinelli, "*Anharmonic lattice interactions in improper ferroelectrics for multiferroic design*", Journal of Physics: Condensed Matter **27** (2015) 283202. 22

[82] T. Choi, S. Lee, Y. Choi, V. Kiryukhin and S.-W. Cheong, "*Switchable ferroelectric diode and photovoltaic effect in* $BiFeO_3$", Science **324** (2009) 63–66. 23

[83] Z. Zhang, P. Wu, L. Chen and J. Wang, “*Density functional theory plus U study of vacancy formations in bismuth ferrite*”, Applied Physics Letters **96** (2010) 232906. 23

[84] H. Ke, W. Wang, Y. Wang, H. Zhang, D. Jia, Y. Zhou, X. Lu and P. Withers, “*Dependence of dielectric behavior in* $BiFeO_3$ *ceramics on intrinsic defects*”, Journal of Alloys and Compounds **541** (2012) 94–98. 23

[85] B. M. Maoz, E. Tirosh, M. B. Sadan and G. Markovich, “*Defect-induced magnetism in chemically synthesized nanoscale sheets of MgO*”, Physical Review B **83** (2011) 161201. 23

[86] Y. Kohara, Y. Yamasaki, Y. Onose and Y. Tokura, “*Excess-electron induced polarization and magnetoelectric effect in yttrium iron garnet*”, Phys. Rev. B **82** (2010) 104419. 23, 74, 77, 79, 80

[87] C. Bucci, R. Fieschi and G. Guidi, “*Ionic thermocurrents in dielectrics*”, Phys. Rev. **148** (1966) 816. 23

[88] M. Eckert, “*Max von laue and the discovery of x-ray diffraction in 1912*”, Annalen der Physik **524** (2012) . 31

[89] W. Bragg, “*The diffraction of short electromagnetic waves by a crystal*”, Proceedings of the Cambridge Philosophical Society **17** (1913) . 31

[90] C. V. Raman, “*A new radiation*”, Indian J. Phys **2** (1928) 387–398. 43

[91] M. Born and R. Oppenheimer, “*Zur quantentheorie der molekeln*”, Annalen der Physik **389** (1927) 457–484. 50

[92] P. Hohenberg and W. Kohn, “*Inhomogeneous electron gas*”, Physical review **136** (1964) B864. 51

[93] W. Kohn and L. J. Sham, “*Self-consistent equations including exchange and correlation effects*”, Physical review **140** (1965) A1133. 51

[94] D. Vanderbilt, “*Soft self-consistent pseudopotentials in a generalized eigenvalue formalism*”, Physical Review B **41** (1990) 7892. 52

[95] G. Kresse and D. Joubert, “*From ultrasoft pseudopotentials to the projector augmented-wave method*”, Physical Review B **59** (1999) 1758. 52, 86, 128

[96] J. P. Perdew, K. Burke and M. Ernzerhof, “*Generalized gradient approximation made simple*”, Physical review letters **77** (1996) 3865. 52

[97] J. P. Perdew, A. Ruzsinszky, G. I. Csonka, O. A. Vydrov, G. E. Scuseria, L. A. Constantin, X. Zhou and K. Burke, “*Restoring the density-gradient expansion for exchange in solids and surfaces*”, Physical Review Letters **100** (2008) 136406. 52, 86, 88, 128

[98] X. Gonze, “*Adiabatic density-functional perturbation theory*”, Physical Review A **52** (1995) 1096. 52

[99] X. Gonze, “*Perturbation expansion of variational principles at arbitrary order*”, Physical Review A **52** (1995) 1086. 52

[100] G. Kresse and J. Furthmüller, “*Efficient iterative schemes for ab initio total-energy calculations using a plane-wave basis set*”, Physical review B **54** (1996) 11169. 53, 86, 128

[101] D. Stein, “*A model of protein conformational substates*”, Proc. Natl. Acad. Sci. **82** (1985) 3670–3672. 56

[102] A. G. Hudetz, C. J. Humphries and J. R. Binder, “*Spin-glass model predicts metastable brain states that diminish in anesthesia*”, Front. Syst. Neurosci. **8** (2014) 234. 56

[103] L. Personnaz, I. Guyon and G. Dreyfus, “*Information storage and retrieval in spin-glass like neural networks*”, J. Phys. Lett. **46** (1985) 359–365. 56

[104] R. Ang, Y. Sun, X. Luo, C. Hao, X. Zhu and W. Song, “*The evidence of the glassy behavior in the layered cobaltites*”, App. Phys. Lett. **92** (2008) 162508. 56, 62, 65

[105] A. Gubkin, E. Sherstobitova, P. Terentyev, A. Hoser and N. Baranov, “*A cluster-glass magnetic state in* R_5Pd_2 *(R= Ho, Tb) compounds evidenced by AC-susceptibility and neutron scattering measurements*”, J. Phys.: Condens. Matter **25** (2013) 236003. 56, 62, 64, 65

[106] D. Li, S. Nimori, T. Yamamura and Y. Shiokawa, “*Ac susceptibility studies of the spin freezing behavior in* U_2CuSi_3”, J. Appl. Phys. **103** (2008) 7B715. 56, 62, 64

[107] S. Mukherjee, A. Garg and R. Gupta, “*Spin glass-like phase below* $\sim$ *210 K in magnetoelectric gallium ferrite*”, App. Phys. Lett. **100** (2012) 112904. 56, 64, 67, 68

[108] V. Singh, S. Mukherjee, C. Mitra, A. Garg and R. Gupta, “*Aging and memory effect in magnetoelectric gallium ferrite single crystals*”, J. Magn. Magn. Mater. **375** (2015) 49–53. 56

[109] K. Sharma, V. R. Reddy, A. Gupta, A. Banerjee and A. Awasthi, “*Magnetic and* ^{57}*Fe Mössbauer study of magneto-electric* $GaFeO_3$ *prepared by the sol–gel route*”, J. Phys.: Condens. Matter **25** (2013) 076002. 56

[110] S. Mukherjee, V. Ranjan, R. Gupta and A. Garg, “*Compositional dependence of structural parameters, polyhedral distortion and magnetic properties of gallium ferrite*”, Solid State Communications **152** (2012) 1181. 57

[111] G. Gruener, F. Vitucci, P. Calvani and J.-C. Soret, “*Evidence of large nonlinear magnetic effects in the paramagnetic phase of* $GaFeO_3$”, Phys. Rev. B **84** (2011) 224427. 60

[112] K. Sharma, V. R. Reddy, A. Gupta, R. Choudhary, D. Phase and V. Ganesan, "*Study of site-disorder in epitaxial magneto-electric $GaFeO_3$ thin films*", Appl. Phys. Lett. **102** (2013) 212401. 62, 73

[113] S. Karmakar, B. Chaudhuri, C. Chan and H. Yang, "*Origin of low temperature memory and aging effects in spin glass like $La_{0.7}Ca_{0.3}MnO_3$ nanomanganite*", J. Appl. Phys. **108** (2010) 113916. 62, 64, 70, 71, 72

[114] D. Nam, R. Mathieu, P. Nordblad, N. Khiem and N. Phuc, "*Spin-glass dynamics of $La_{0.95}Sr_{0.05}CoO_3$*", Phys. Rev. B **62** (2000) 8989. 64

[115] A. Kumar, R. Tandon and V. Awana, "*Study of spin glass and cluster ferromagnetism in $RuSr_2Eu_{1.4}Ce_{0.6}Cu_2O_{10}$-$\delta$ magneto superconductor*", J. Appl. Phys. **110** (2011) 043926. 64

[116] C. Mulder, A. Van Duyneveldt and J. Mydosh, "*Susceptibility of the CuMn spin-glass: Frequency and field dependences*", Phys. Rev. B **23** (1981) 1384. 64

[117] J. K. Murthy and A. Venimadhav, "*Reentrant cluster glass behavior in La_2CoMnO_6 nanoparticles*", J. Appl. Phys. **113** (2013) 163906. 64

[118] W. Chen, F. Zhang, J. Miao, B. Xu, X. Dong, L. Cao, X. Qiu, B. Zhaoa and P. Dai, "*Re-entrant spin glass behavior in Mn-rich $YMnO_3$*", change **4** (2005) 6. 64

[119] I. Deac, J. Mitchell and P. Schiffer, "*Phase separation and low-field bulk magnetic properties of $Pr_{0.7}Ca_{0.3}MnO_3$*", Phys. Rev. B **63** (2001) 172408. 68

[120] W. Kim, J. H. We, S. J. Kim and C. S. Kim, "*Effects of cation distribution for $AFeO_3$ (A= Ga, Al)*", J. Appl. Phys. **101** (2007) 09M515. 68

[121] M. Svedberg, S. Majumdar, H. Huhtinen, P. Paturi and S. Granroth, "*Optimization of $Pr_{0.9}Ca_{0.1}MnO_3$ thin films and observation of coexisting spin-glass and ferromagnetic phases at low temperature*", J. Phys.: Condens. Matter **23** (2011) 386005. 68

[122] C. Sow, D. Samal, P. A. Kumar, A. Bera and S. Yusuf, "*Structural-modulation-driven low-temperature glassy behavior in $SrRuO_3$*", Phys. Rev. B **85** (2012) 224426. 68

[123] P. Baker, T. Lancaster, S. Blundell, M. Brooks, W. Hayes, D. Prabhakaran and F. Pratt, "*Thermodynamic and magnetic properties of the layered triangular magnet $NaNiO_2$*", Phys. Rev. B **72** (2005) 104414. 68

[124] M. Sasaki, V. Dupuis, J.-P. Bouchaud and E. Vincent, "*Deviations from perfect memory in spin glass temperature cycling experiments*", Eur. Phys. J. B **29** (2002) 469–479. 70

[125] K. Jonason, E. Vincent, J. Hammann, J. Bouchaud and P. Nordblad, "*Memory and chaos effects in spin glasses*", Phys. Rev. Lett. **81** (1998) 3243. 71

[126] M. Ulrich, J. García-Otero, J. Rivas and A. Bunde, "*Slow relaxation in ferromagnetic nanoparticles: Indication of spin-glass behavior*", Phys. Rev. B **67** (2003) 024416. 72

[127] F. Rivadulla, M. López-Quintela and J. Rivas, "*Origin of the glassy magnetic behavior of the phase segregated state of the perovskites*", Phys. Rev. Lett. **93** 167206. 72

[128] W. Eerenstein, N. Mathur and J. F. Scott, "*Multiferroic and magnetoelectric materials*", nature **442** (2006) 759–765. 73

[129] S. Mishra, R. Mittal, R. Singh, M. Zbiri, T. Hansen and H. Schober, "*Phase stability of multiferroic* $GaFeO_3$ *up to 1368 K from in situ neutron diffraction*", J. Appl. Phys. **113** (2013) 174102. 73

[130] D. Stoeffler, "*First principles study of the spontaneous electric polarization in* $Ga_{2-x}Fe_xO_3$", Thin Solid Films **533** (2013) 93–96. 73

[131] M. Trassin, N. Viart, G. Versini, J.-L. Loison, J.-P. Vola, G. Schmerber, O. Cregut, S. Barre, G. Pourroy, J. Lee et al., "*Epitaxial thin films of multiferroic* $GaFeO_3$ *on conducting indium tin oxide (001) buffered yttrium-stabilized zirconia (001) by pulsed laser deposition*", Appl. Phys. Lett. **91** (2007) 202504. 73

[132] V. Naik and R. Mahendiran, "*Electrical, magnetic, magnetodielectric, and magnetoabsorption studies in multiferroic* $GaFeO_3$", J. Appl. Phys. **106** (2009) 123910. 73

[133] R. Saha, A. Shireen, S. N. Shirodkar, U. V. Waghmare, A. Sundaresan and C. Rao, "*Multiferroic and magnetoelectric nature of* $GaFeO_3$, $AlFeO_3$ *and related oxides*", Solid State Comm. **152** (2012) 1964–1968. 73, 78, 79

[134] K. Cho, S. Hur and S. Park, "*The absence of ferroelectricity and the origin of depolarization currents in* $YFe_{0.8}Mn_{0.2}O_3$", Appl. Phys. Lett. **110** (2017) 162905. 74, 76

[135] X. Zhang, Y. Zhao, Y. Cui, L. Ye, D. Zhao, P. Li, J. Wang, M. Zhu, H. Zhang and G. Rao, "*Investigation on the pyroelectric property of polycrystalline* $GdMnO_3$", Appl. Phys. Lett. **104** (2014) 062903. 74, 81

[136] T. Zou, Z. Dun, H. Cao, M. Zhu, D. Coulter, H. Zhou and X. Ke, "*Excess-hole induced high temperature polarized state and its correlation with the multiferroicity in single crystalline* $DyMnO_3$", Appl. Phys. Lett. **105** (2014) 052906. 74

[137] T. Zou, Z. Dun, H. Cao, M. Zhu, H. Zhou and X. Ke, "*Tuning the ferroelectric state in multiferroic* $TbMnO_3$ *single crystal by a trapped-charge-induced internal electric field*", J. Appl. Phys. **116** (2014) 104101. 74

[138] D. Choudhury, P. Mandal, R. Mathieu, A. Hazarika, S. Rajan, A. Sundaresan, U. Waghmare, R. Knut, O. Karis, P. Nordblad et al., "*Near-room-temperature colossal magnetodielectricity and multiglass properties in partially disordered* La_2NiMnO_6", Phys. Rev. Lett. **108** (2012) 127201. 76

[139] S. Hunpratub, P. Thongbai, T. Yamwong, R. Yimnirun and S. Maensiri, "*Dielectric relaxations and dielectric response in multiferroic* $BiFeO_3$ *ceramics*", Appl. Phys. Lett. **94** (2009) 062904. 76, 77, 78

[140] R. Schmidt, J. Wu, C. Leighton and I. Terry, "*Dielectric response to the low-temperature magnetic defect structure and spin state transition in polycrystalline* $LaCoO_3$", Phys. Rev. B **79** (2009) 125105. 76, 78

[141] S. Chattopadhyay, S. Giri and S. Majumdar, "*Phase coexistence and multiple dielectric relaxations in the single layered manganite* $Nd_{0.22}Sr_{1.78}MnO_4$", J. Appl. Phys. **107** (2010) 014108. 76, 78

[142] V. Singh, A. Daryapurkar, S. S. Rajput, S. Mukherjee, A. Garg and R. Gupta, "*Effect of annealing atmosphere on leakage and dielectric characteristics of multiferroic gallium ferrite*", J. Am. Ceram. Soc. (2017) . 76, 77, 82

[143] J. Yang, J. He, J. Zhu, W. Bai, L. Sun, X. Meng, X. Tang, C.-G. Duan, D. Remiens, J. Qiu et al., "*Small polaron migration associated multiple dielectric responses of multiferroic* $DyMnO_3$ *polycrystal in low temperature region*", Applied Physics Letters **101** (2012) 222904. 77

[144] Y. Liu, X. Chen, X. Liu and L. Li, "*Giant dielectric response and relaxor behaviors induced by charge and defect ordering in* $Sr(Fe_{1/2}Nb_{1/2})O_3$ *ceramics*", Appl. Phys. Lett. **90** (2007) 192905. 77

[145] S. Mukherjee, R. Gupta and A. Garg, "*Dielectric response and magnetoelectric coupling in single crystal gallium ferrite*", AIP Advances **3** (2013) 052115. 78, 82

[146] Q. Ke, X. Lou, Y. Wang and J. Wang, "*Oxygen-vacancy-related relaxation and scaling behaviors of* $Bi_{0.9}La_{0.1}Fe_{0.98}Mg_{0.02}O_3$ *ferroelectric thin films*", Phys. Rev. B **82** (2010) 024102. 78

[147] F. Kröger and H. Vink, "*Relations between the concentrations of imperfections in crystalline solids*", Solid state phys. **3** (1956) 307–435. 78

[148] K. D. Chandrasekhar, S. Mallesh, J. K. Murthy, A. Das and A. Venimadhav, "*Role of defects and oxygen vacancies on dielectric and magnetic properties of* Pb^{2+} *ion doped* $LaFeO_3$ *polycrystalline ceramics*", Physica B: Condensed Matter **448** (2014) 304–311. 78

[149] G. G. Raju, *Dielectrics in electric fields.* CRC press, 2016. 79

[150] N. Ray and U. V. Waghmare, "*Coupling between magnetic ordering and structural instabilities in perovskite biferroics: A first-principles study*", Physical Review B **77** (2008) 134112. 84, 86, 89, 92, 93, 95

[151] J. R. Sahu, C. R. Serrao, N. Ray, U. V. Waghmare and C. Rao, "*Rare earth chromites: A new family of multiferroics*", Journal of Materials Chemistry **17** (2007) 42–44. 84, 89, 93

[152] U. Waghmare and K. Rabe, "*Ab initio statistical mechanics of the ferroelectric phase transition in* $PbTiO_3$", Physical Review B **55** (1997) 6161. 84, 89, 92

[153] K. Ramesha, A. Llobet, T. Proffen, C. Serrao and C. Rao, "*Observation of local non-centrosymmetry in weakly biferroic* $YCrO_3$", Journal of Physics: Condensed Matter **19** (2007) 102202. 84, 87, 95

[154] B. Rajeswaran, D. Khomskii, A. Zvezdin, C. Rao and A. Sundaresan, "*Field-induced polar order at the Néel temperature of chromium in rare-earth orthochromites: Interplay of rare-earth and Cr magnetism*", Physical Review B **86** (2012) 214409. 84, 87, 92, 104, 123, 126, 127

[155] A. Apostolov, I. Apostolova and J. Wesselinowa, "*Microscopic approach to the magnetoelectric coupling in* $RCrO_3$", Modern Physics Letters B **29** (2015) 1550251. 84

[156] V. S. Bhadram, B. Rajeswaran, A. Sundaresan and C. Narayana, "*Spin-phonon coupling in multiferroic* $RCrO_3$ *(RY, Lu, Gd, Eu, Sm): A Raman study*", EPL (Europhysics Letters) **101** (2013) 17008. 84, 99, 101, 102, 118, 120, 121, 123

[157] A. Ghosh, K. Dey, M. Chakraborty, S. Majumdar and S. Giri, "*Polar octahedral rotations, cation displacement and ferroelectricity in multiferroic* $SmCrO_3$", EPL (Europhysics Letters) **107** (2014) 47012. 84, 87, 104, 106

[158] A. Ghosh, A. Pal, K. Dey, S. Majumdar and S. Giri, "*Atypical multiferroicity of* $HoCrO_3$ *in bulk and film geometry*", Journal of Materials Chemistry C **3** (2015) 4162–4167. 84, 87, 104

[159] H. J. Zhao, L. Bellaiche, X. M. Chen and J. Íñiguez, "*Improper electric polarization in simple perovskite oxides with two magnetic sublattices*", Nature Communications **8** (2017) . 85, 86, 89, 90

[160] B. Ravel and M. Newville, "*ATHENA, ARTEMIS, HEPHAESTUS: data analysis for X-ray absorption spectroscopy using IFEFFIT*", Journal of synchrotron radiation **12** (2005) 537–541. 86

[161] H. J. Monkhorst and J. D. Pack, "*Special points for brillouin-zone integrations*", Physical review B **13** (1976) 5188. 86, 128

[162] A. Cooke, D. Martin and M. Wells, "*Magnetic interactions in gadolinium orthochromite,* $GdCrO_3$", Journal of Physics C: Solid State Physics **7** (1974) 3133. 86, 87, 108, 110, 114, 115, 161

[163] R. King-Smith and D. Vanderbilt, "*Theory of polarization of crystalline solids*", Physical Review B **47** (1993) 1651. 87

[164] A. Togo, F. Oba and I. Tanaka, "*First-principles calculations of the ferroelastic transition between rutile-type and* $CaCl_2$*-type* SiO_2 *at high pressures*", Physical Review B **78** (2008) 134106. 87

[165] J. Coey, M. Viret and S. Von Molnar, "*Mixed-valence manganites*", Advances in physics **58** (2009) 571–697. 87

[166] R. I. Hines, *Atomistic simulation and ab initio studies of polar solids.* PhD thesis, University of Bristol, 1997. 87

[167] A. Indra, K. Dey, A. Midya, P. Mandal, O. Gutowski, U. Rütt, S. Majumdar and S. Giri, "*Erratum: Magnetoelectric coupling and exchange bias effects in multiferroic $NdCrO_3$*", J. Phys.: Condens. Matter **28** (2016) 279601. 87, 105

[168] S. F. Yuk, K. C. Pitike, S. M. Nakhmanson, M. Eisenbach, Y. W. Li and V. R. Cooper, "*Towards an accurate description of perovskite ferroelectrics: exchange and correlation effects*", Sci. Rep. **7** (2017) 43482. 88

[169] R. Wahl, D. Vogtenhuber and G. Kresse, "*$SrTiO_3$ and $BaTiO_3$ revisited using the projector augmented wave method: Performance of hybrid and semilocal functionals*", Physical Review B **78** (2008) 104116. 88

[170] H. T. Stokes and D. M. Hatch, "*FINDSYM: program for identifying the space-group symmetry of a crystal*", J. Appl. Cryst. **38** (2005) 237–238. 89

[171] H. T. Stokes, D. M. Hatch and B. J. Campbell, "*FINDSYM: program for identifying the space-group symmetry of a crystal*", ISOTROPY Software Suite, iso.byu.edu . 89

[172] P. Ghosez, E. Cockayne, U. Waghmare and K. Rabe, "*Lattice dynamics of $BaTiO_3$, $PbTiO_3$, and $PbZrO_3$: A comparative first-principles study*", Physical Review B **60** (1999) 836. 89

[173] S. Bhattacharjee, E. Bousquet and P. Ghosez, "*Engineering multiferroism in $CaMnO_3$*", Physical review letters **102** (2009) 117602. 89

[174] W. Zhong, R. King-Smith and D. Vanderbilt, "*Giant LO-TO splittings in perovskite ferroelectrics*", Phys. Rev. Lett. **72** (1994) 3618. 92

[175] C. Ederer, T. Harris and R. Kováčik, "*Mechanism of ferroelectric instabilities in non-d^0 perovskites: $LaCrO_3$ versus $CaMnO_3$*", Physical Review B **83** (2011) 054110. 92, 93

[176] W. Zhong and D. Vanderbilt, "*Competing structural instabilities in cubic perovskites*", Physical review letters **74** (1995) 2587. 95

[177] U. Aschauer and N. A. Spaldin, "*Competition and cooperation between antiferrodistortive and ferroelectric instabilities in the model perovskite $SrTiO_3$*", Journal of Physics: Condensed Matter **26** (2014) 122203. 95

[178] J. Mustre de Leon, S. D. Conradson, I. Batistić, A. R. Bishop, I. D. Raistrick, M. C. Aronson and F. H. Garzon, "*Axial oxygen-centered lattice instabilities in $YBa_2Cu_3O_7$: An application of the analysis of extended x-ray-absorption fine structure in anharmonic systems*", Phys. Rev. B **45** (Feb, 1992) 2447–2457. 97

[179] F.-K. Chiang, M.-W. Chu, F. Chou, H. Jeng, H. Sheu, F. Chen and C. Chen, "*Effect of Jahn-Teller distortion on magnetic ordering in Dy(Fe,Mn)O_3 perovskites*", Physical Review B **83** (2011) 245105. 101, 127, 130, 135, 138, 139

[180] B. N. Rao, L. Olivi, V. Sathe and R. Ranjan, "*Electric field and temperature dependence of the local structural disorder in the lead-free ferroelectric $Na_{0.5}Bi_{0.5}TiO_3$: An EXAFS study*", Physical Review B **93** (2016) 024106. 101

[181] C. Monesi, C. Meneghini, F. Bardelli, M. Benfatto, S. Mobilio, U. Manju and D. Sarma, "*Local structure in $LaMnO_3$ and $CaMnO_3$ perovskites: a quantitative structural refinement of Mn K-edge XANES data*", Physical Review B **72** (2005) 174104. 101

[182] K. Yoshii, "*Magnetization reversal in $TmCrO_3$*", Materials Research Bulletin **47** (2012) 3243–3248. 106

[183] A. Indra, K. Dey, A. Midya, P. Mandal, O. Gutowski, U. Rütt, S. Majumdar and S. Giri, "*Magnetoelectric coupling and exchange bias effects in multiferroic $NdCrO_3$*", Journal of Physics: Condensed Matter **28** (2016) 166005. 106

[184] L. Yin, J. Yang, X. Kan, W. Song, J. Dai and Y. Sun, "*Giant magnetocaloric effect and temperature induced magnetization jump in $GdCrO_3$ single crystal*", Journal of Applied Physics **117** (2015) 133901. 106, 107, 110, 112, 168, 170

[185] R. Hornreich, "*Magnetic interactions and weak ferromagnetism in the rare-earth orthochromites*", Journal of Magnetism and Magnetic Materials **7** (1978) 280–285. 106

[186] S. Washimiya and C. Satoko, "*Molecular Field Theory of Magnetization in Rare Earth Orthochromites and Orthoferrites–Application to $GdCrO_3$*", Journal of the Physical Society of Japan **45** (1978) 1204–1212. 106, 114

[187] P. Mandal, A. Sundaresan, C. Rao, A. Iyo, P. Shirage, Y. Tanaka, C. Simon, V. Pralong, O. Lebedev, V. Caignaert et al., "*Temperature-induced magnetization reversal in $BiFe_{0.5}Mn_{0.5}O_3$ synthesized at high pressure*", Physical Review B **82** (2010) 100416. 106

[188] H. Adachi and H. Ino, "*A ferromagnet having no net magnetic moment*", Nature **401** (1999) 148–150. 106

[189] S. Yusuf, A. Kumar and J. Yakhmi, "*Temperature-and magnetic-field-controlled magnetic pole reversal in a molecular magnetic compound*", Applied Physics Letters **95** (2009) 182506. 106

[190] K. Yoshii, "*Magnetic properties of perovskite $GdCrO_3$*", Journal of Solid State Chemistry **159** (2001) 204–208. 107, 108, 110, 112, 114, 127

[191] A. McDannald, L. Kuna, M. Seehra and M. Jain, "*Magnetic exchange interactions of rare-earth-substituted $DyCrO_3$ bulk powders*", Physical Review B **91** (2015) 224415. 108, 110, 116, 122

[192] A. Jaiswal, R. Das, K. Vivekanand, T. Maity, P. M. Abraham, S. Adyanthaya and P. Poddar, "*Magnetic and dielectric properties and Raman spectroscopy of $GdCrO_3$ nanoparticles*", Journal of Applied Physics **107** (2010) 013912. 110

[193] J. Mao, Y. Sui, X. Zhang, Y. Su, X. Wang, Z. Liu, Y. Wang, R. Zhu, Y. Wang, W. Liu et al., "*Temperature-and magnetic-field-induced magnetization reversal in perovskite $YFe_{0.5}Cr_{0.5}O_3$*", Applied Physics Letters **98** (2011) 192510. 115

[194] A. H. Morrish, "*The physical principles of magnetism*", The Physical Principles of Magnetism (IEEE Press, New York, 2001) **344** pp. 310–320. 115

[195] M. Udagawa, K. Kohn, N. Koshizuka, T. Tsushima and K. Tsushima, "*Influence of magnetic ordering on the phonon Raman spectra in $YCrO_3$ and $GdCrO_3$*", Solid State Communications **16** (1975) 779–783. 116, 118, 120

[196] M. C. Weber, J. Kreisel, P. A. Thomas, M. Newton, K. Sardar and R. I. Walton, "*Phonon Raman scattering of $RCrO_3$ perovskites (R= Y, La, Pr, Sm, Gd, Dy, Ho, Yb, Lu)*", Physical Review B **85** 054303. 118, 136

[197] V. S. Bhadram, D. Swain, R. Dhanya, M. Polentarutti, A. Sundaresan and C. Narayana, "*Effect of pressure on octahedral distortions in $RCrO_3$ (R= Lu, Tb, Gd, Eu, Sm): the role of R-ion size and its implications*", Materials Research Express **1** 026111. 118

[198] E. Granado, A. Garcia, J. Sanjurjo, C. Rettori, I. Torriani, F. Prado, R. Sanchez, A. Caneiro and S. Oseroff, "*Magnetic ordering effects in the Raman spectra of $La_{1-x}Mn_{1-x}O_3$*", Physical Review B **60** (1999) 11879. 118, 121

[199] M. Balkanski, R. Wallis and E. Haro, "*Anharmonic effects in light scattering due to optical phonons in silicon*", Physical Review B **28** (1983) 1928. 118

[200] P. Klemens, "*Anharmonic decay of optical phonons*", Physical Review **148** (1966) 845. 118

[201] Y. Sharma, S. Sahoo, W. Perez, S. Mukherjee, R. Gupta, A. Garg, R. Chatterjee and R. S. Katiyar, "*Phonons and magnetic excitation correlations in weak ferromagnetic $YCrO_3$*", Journal of Applied Physics **115** (2014) 183907. 120

[202] M. Iliev, H. Guo and A. Gupta, "*Raman spectroscopy evidence of strong spin-phonon coupling in epitaxial thin films of the double perovskite La_2NiMnO_6*", Applied physics letters **90** (2007) 151914. 121

[203] D. Lockwood and M. Cottam, "*The spin-phonon interaction in FeF_2 and MnF_2 studied by Raman spectroscopy*", Journal of Applied Physics **64** (1988) 5876–5878. 122

[204] R. Gupta, M. Kim, H. Barath, S. Cooper and G. Cao, "*Field-and pressure-induced phases in $Sr_4Ru_3O_{10}$: A spectroscopic investigation*", Physical review letters **96** (2006) 067004. 122

[205] C. N. R. Rao and B. Raveau, *Colossal magnetoresistance, charge ordering and related properties of manganese oxides.* World Scientific, 1998. 126

[206] S. Mori, T. Katsufuji, N. Yamamoto, C. Chen and S. Cheong, "*Microstructure related to charge and orbital ordering in* $Pr_{0.5}Ca_{0.5}MnO_3$", Physical Review B **59** (1999) 13573. 126

[207] J. van den Brink, G. Khaliullin and D. Khomskii, "*Charge and orbital order in half-doped manganites*", Physical Review Letters **83** (1999) 5118. 126

[208] T. Asaka, S. Yamada, S. Tsutsumi, C. Tsuruta, K. Kimoto, T. Arima and Y. Matsui, "*Charge/Orbital Ordering Structure of* $Pr_{1-x}Ca_xMnO_3$ *(x= 3/8) Examined by Low-Temperature Transmission Electron Microscopy*", Physical review letters **88** (2002) 097201. 126

[209] H. Kawano, R. Kajimoto, H. Yoshizawa, Y. Tomioka, H. Kuwahara and Y. Tokura, "*Magnetic ordering and relation to the metal-insulator transition in* $Pr_{1-x}Sr_xMnO_3$ *and* $Nd_{1-x}Sr_xMnO_3$ *with* $x \sim 1/2$", Physical Review Letters **78** (1997) 4253. 126

[210] N. Fukumoto, S. Mori, N. Yamamoto, Y. Moritomo, T. Katsufuji, C. Chen and S. Cheong, "*Microscopic electronic phase separation and metal-insulator transition in* $Nd_{0.5}Sr_{0.5}MnO_3$", Physical Review B **60** (1999) 12963. 126

[211] J. A. Moreira, A. Almeida, M. Chaves, J. Kreisel, J. Oliveira, F. Carpinteiro and P. Tavares, "*Magnetically-induced lattice distortions and ferroelectricity in magnetoelectric* $GdMnO_3$", Journal of Physics: Condensed Matter **24** (2012) 436002. 126, 142

[212] A. Modi and N. Gaur, "*Structural, electrical and magnetic phase evolution of Cr substituted* $GdMn_{1-x}Cr_xO_3$ $(0 \leq x \leq 0.2)$ *manganites*", Journal of Alloys and Compounds **644** (2015) 575–581. 127, 143, 148

[213] Y. Fang, Y. Yang, X. Liu, J. Kang, L. Hao, X. Chen, L. Xie, G. Sun, V. Chandragiri, C.-W. Wang et al., "*Observation of re-entrant spin reorientation in* $TbFe_{1-x}Mn_xO_3$", Scientific reports **6** (2016) 33448. 127

[214] Y.-H. Huang, M. Karppinen, N. Imamura, H. Yamauchi and J. B. Goodenough, "*Structural transformation and magnetic competition in* $Yb(Mn_{1-x}Fe_x)O_3$", Physical Review B **76** (2007) 174405. 127

[215] M. Staruch and M. Jain, "*Evidence of antiferromagnetic and ferromagnetic superexchange interactions in bulk* $TbMn_{1-x}Cr_xO_3$", Journal of Physics: Condensed Matter **26** (2014) 046005. 127, 144

[216] K. Yamauchi, F. Freimuth, S. Blügel and S. Picozzi, "*Magnetically induced ferroelectricity in orthorhombic manganites: Microscopic origin and chemical trends*", Physical Review B **78** (2008) 014403. 128

[217] J.-S. Zhou, J. Alonso, V. Pomjakushin, J. Goodenough, Y. Ren, J.-Q. Yan and J.-G. Cheng, "*Intrinsic structural distortion and superexchange interaction in the orthorhombic rare-earth perovskites $RCrO_3$*", Physical Review B **81** (2010) 214115. 130

[218] J.-S. Zhou and J. Goodenough, "*Intrinsic structural distortion in orthorhombic perovskite oxides*", Physical Review B **77** (2008) 132104. 130, 134

[219] M. Tachibana, T. Shimoyama, H. Kawaji, T. Atake and E. Takayama-Muromachi, "*Jahn-Teller distortion and magnetic transitions in perovskite $RMnO_3$ (R= Ho, Er, Tm, Yb, and Lu)*", Physical Review B **75** (2007) 144425. 130

[220] J. Kanamori, "*Crystal distortion in magnetic compounds*", Journal of Applied Physics **31** (1960) S14–S23. 132

[221] J.-S. Zhou and J. Goodenough, "*Orbital mixing and ferromagnetism in $LaMn_{1-x}Ga_xO_3$*", Physical Review B **77** (2008) 172409. 132, 133, 134

[222] M. Iliev, M. Abrashev, J. Laverdiere, S. Jandl, M. Gospodinov, Y.-Q. Wang and Y.-Y. Sun, "*Distortion-dependent Raman spectra and mode mixing in $RMnO_3$ perovskites (R= La, Pr, Nd, Sm, Eu, Gd, Tb, Dy, Ho, Y)*", Physical Review B **73** (2006) 064302. 136

[223] N. Todorov, M. Abrashev, V. Ivanov, G. Tsutsumanova, V. Marinova, Y.-Q. Wang and M. Iliev, "*Comparative Raman study of isostructural $YCrO_3$ and $YMnO_3$: Effects of structural distortions and twinning*", Physical Review B **83** (2011) 224303. 136

[224] M. Iliev, V. Hadjiev, A. Litvinchuk, F. Yen, Y.-Q. Wang, Y. Sun, S. Jandl, J. Laverdiere, V. Popov and M. Gospodinov, "*Multiple-order Raman scattering from rare-earth manganites: Oxygen isotope and rare-earth substitution effects*", Physical Review B **75** (2007) 064303. 136

[225] M. Iliev, M. Abrashev, V. Popov and V. Hadjiev, "*Role of Jahn-Teller disorder in Raman scattering of mixed-valence manganites*", Physical Review B **67** (2003) 212301. 136

[226] N. N. Kovaleva, O. E. Kusmartseva, K. Kugel, A. Maksimov, D. Nuzhnyy, A. Balbashov, E. Demikhov, A. Dejneka, V. Trepakov, F. Kusmartsev et al., "*Anomalous multi-order Raman scattering in LaMnO3: a signature of quantum lattice effects in a Jahn–Teller crystal*", Journal of Physics: Condensed Matter **25** (2013) 155602. 136

[227] Y. Zhao, D. J. Weidner, J. B. Parise and D. E. Cox, "*Critical phenomena and phase transition of perovskiteData for $NaMgF_3$ perovskite. Part II*", Physics of the Earth and Planetary Interiors **76** (1993) 17–34. 136

[228] L. M. Daniels, M. C. Weber, M. R. Lees, M. Guennou, R. J. Kashtiban, J. Sloan, J. Kreisel and R. I. Walton, "*Structures and Magnetism of the Rare-Earth*

Orthochromite Perovskite Solid Solution $La_xSm_{1-x}CrO_3$", Inorganic chemistry **52** (2013) 12161–12169. 136

[229] L. Martín-Carrón, A. De Andres, M. Martínez-Lope, M. Casais and J. Alonso, "*Raman phonons as a probe of disorder, fluctuations, and local structure in doped and undoped orthorhombic and rhombohedral manganites*", Physical Review B **66** (2002) 174303. 136

[230] J. Chen, J. Lee, C. Chen, T. Chou, K. Lu, S. Haw, K. Liang, C. Chen, H. Jeng, S. Huang et al., "*Bonding anisotropy in multiferroic* $TbMnO_3$ *probed by polarization dependent x-ray absorption spectroscopy*", Applied Physics Letters **94** (2009) 044105. 138, 139

[231] J. Chen, Z. Hu, H. Jeng, Y. Chin, J. Lee, S. Huang, K. Lu, C. Chen, S. Haw, T. Chou et al., "*Strong orbital polarization in orthorhombic* $DyMnO_3$*: A combined x-ray linear dichroism and ab initio electronic structure study*", Physical Review B **81** (2010) 201102. 139

[232] S. Bukhari and J. Ahmad, "*Infrared Active Phonons and Optical Band Gap in Multiferroic* $GdMnO_3$ *Studied by Infrared and UV-Visible Spectroscopy*", Acta Phys. Pol. A **129** (2016) 43. 139

[233] G. Kotnana and S. N. Jammalamadaka, "*Band gap tuning and orbital mediated electron–phonon coupling in* $HoFe_{1-x}Cr_xO_3$ $(0\leq x\leq 1)$", Journal of Applied Physics **118** (2015) 124101. 139

[234] P. Gupta and P. Poddar, "*Study of magnetic and thermal properties of* $SmCrO_3$ *polycrystallites*", RSC Advances **6** (2016) 82014–82023. 139

[235] M. Richter, "*Band structure theory of magnetism in 3d-4f compounds*", Journal of Physics D: Applied Physics **31** (1998) 1017. 139

[236] A. Stroppa, M. Marsman, G. Kresse and S. Picozzi, "*The multiferroic phase of* $DyFeO_3$*: an ab initio study*", New Journal of Physics **12** (2010) 093026. 139

[237] I. Solovyev, N. Hamada and K. Terakura, "*Crucial Role of the Lattice Distortion in the Magnetism of* $LaMnO_3$", Phys. Rev. Lett. **76** (Jun, 1996) 4825–4828. 140

[238] J. Hemberger, S. Lobina, H.-A. K. Von Nidda, N. Tristan, V. Y. Ivanov, A. Mukhin, A. Balbashov and A. Loidl, "*Complex interplay of 3d and 4f magnetism in* $La_{1-x}Gd_xMnO_3$", Physical Review B **70** (2004) 024414. 142

[239] U. Bents, "*Neutron Diffraction Study of the Magnetic Structures for the Perovskite-Type Mixed Oxides* $La(Mn,Cr)O_3$", Physical Review **106** (1957) 225. 144

[240] S. Li, T. Wang, H. Han, X. Wang, H. Li, J. Liu and J. Liu, "*Modulated multiferroicity of Cr-doped orthorhombic polycrystalline* $YMnO_3$", Journal of Physics D: Applied Physics **45** (2012) 055003. 144

[241] M. Staruch, V. Sharma, C. dela Cruz, R. Ramprasad and M. Jain, "*Magnetic ordering in* $TbMn_{0.5}Cr_{0.5}O_3$ *studied by neutron diffraction and first-principles calculations*", Journal of Applied Physics **116** (2014) 033919. 144, 145

[242] B. Yuan, J. Yang, X. Zuo, X. Kan, L. Zu, X. Zhu, J. Dai, W. Song and Y. Sun, "*Dielectric relaxation and magnetodielectric response in* $DyMn_{0.5}Cr_{0.5}O_3$", Journal of Applied Physics **118** (2015) 124103. 144

[243] Z. Yang, L. Ye and X. Xie, "*Density-functional studies of magnetic and electronic structures for the perovskite oxides* $LaMn_{1-x}Cr_xO_3$", Journal of Physics: Condensed Matter **12** (2000) 2737. 144, 145

[244] L. Yang, Q. Duanmu, L. Hao, Z. Zhang, X. Wang, Y. Wei and H. Zhu, "*Ferrimagnetism and possible double perovskite structure in half Cr-doped* $YMn_{0.5}Cr_{0.5}O_3$", Journal of Alloys and Compounds **570** (2013) 41–45. 145

[245] L. Hao, L. Yang, M.-H. Lee, T.-H. Lin, Z. Zhang, X. Xie and H. Zhu, "*Layered B-site cation ordering: A key factor in ferrimagnetism of* Y_2MnCrO_6", Journal of Alloys and Compounds **601** (2014) 14–18. 145

[246] L. Bellaiche, Z. Gui and I. A. Kornev, "*A simple law governing coupled magnetic orders in perovskites*", Journal of Physics: Condensed Matter **24** (2012) 312201. 148

[247] A. Singh, A. Senyshyn, H. Fuess, S. J. Kennedy and D. Pandey, "*Magnetic transitions and site-disordered induced weak ferromagnetism in* $(1\text{-}x)BiFeO_3\text{-}xBaTiO_3$", Physical Review B **89** (2014) 024108. 148

[248] B. Yu, Q. Gao, B. Zhang, X. Meng and Z. Chen, "*Review on research of room temperature magnetic refrigeration*", International Journal of Refrigeration **26** (2003) 622–636. 152

[249] L. Zhang, S. Sherif, A. DeGregoria, C. Zimm and T. Veziroglu, "*Design optimization of a 0.1-ton/day active magnetic regenerative hydrogen liquefier*", Cryogenics **40** 269–278. 152

[250] W. Chen, "*Development of an active magnetic regenerator for space applications*", Cryogenics **62** (2014) 206–212. 152

[251] J. Li, Y. Qu, J. Ren, W. Yuan and D. Shi, "*Magnetocaloric effect in magnetothermally-responsive nanocarriers for hyperthermia-triggered drug release*", Nanotechnology **23** (2012) 505706. 152

[252] M.-H. Phan and S.-C. Yu, "*Review of the magnetocaloric effect in manganite materials*", Journal of Magnetism and Magnetic Materials **308** (2007) 325–340. 153, 168

[253] L. Li, T. Namiki, D. Huo, Z. Qian and K. Nishimura, "*Two successive magnetic transitions induced large refrigerant capacity in HoPdIn compound*", Applied Physics Letters **103** (2013) 222405. 153

[254] L. Li, M. Kadonaga, D. Huo, Z. Qian, T. Namiki and K. Nishimura, "*Low field giant magnetocaloric effect in RNiBC (R= Er and Gd) and enhanced refrigerant capacity in its composite materials*", Applied Physics Letters **101** (2012) 122401. 153

[255] J. Liu, T. Gottschall, K. P. Skokov, J. D. Moore and O. Gutfleisch, "*Giant magnetocaloric effect driven by structural transitions*", Nature materials **11** (2012) 620–626. 153

[256] J. K. Murthy, K. D. Chandrasekhar, S. Mahana, D. Topwal and A. Venimadhav, "*Giant magnetocaloric effect in* Gd_2NiMnO_6 *and* Gd_2CoMnO_6 *ferromagnetic insulators*", Journal of Physics D: Applied Physics **48** (2015) 355001. 153, 168, 171

[257] A. Midya, S. Das, P. Mandal, S. Pandya and V. Ganesan, "*Anisotropic magnetic properties and giant magnetocaloric effect in antiferromagnetic* $RMnO_3$ *crystals (R= Dy, Tb, Ho, and Yb)*", Physical Review B **84** (2011) 235127. 153, 161, 162, 168

[258] S. Gupta, R. Rawat and K. Suresh, "*Large field-induced magnetocaloric effect and magnetoresistance in ErNiSi*", Applied Physics Letters **105** (2014) 012403. 153, 168

[259] S. Geller and V. Bala, "*Crystallographic studies of perovskite-like compounds. ii. rare earth alluminates*", Acta Crystallographica **9** (1956) 1019–1025. 154

[260] D. Petrov and B. Angelov, "*Indirect exchange interactions in orthorhombic lanthanide aluminates*", Acta Physica Polonica-Series A General Physics **122** (2012) 737. 154

[261] S. Hatscher, H. Schilder, H. Lueken and W. Urland, "*Practical guide to measurement and interpretation of magnetic properties (IUPAC Technical Report)*", Pure and applied chemistry **77** (2005) 497–511. 156

[262] D. Cook and J. Cashion, "*Mossbauer measurements in canted antiferromagnetic* $GdAlO_3$", Journal of Physics C: Solid State Physics **13** (1980) 4199. 156

[263] D. Petrov, "*Nanocrystalline* $GdAlO_3$*: XPS, EPR and magnetic susceptibility studies*", Applied Physics A: Materials Science & Processing **104** (2011) 1237–1242. 156

[264] K. Blazey and H. Rohrer, "*Antiferromagnetism and the Magnetic Phase Diagram of* $GdAlO_3$", Physical Review **173** (1968) 574. 157, 158, 159

[265] J. Cashion, A. Cooke, J. Hawkes, M. Leask, T. Thorp and M. R. Wells, "*Magnetic Properties of Antiferromagnetic* $GdAlO_3$", Journal of Applied Physics **39** (1968) 1360–1361. 157, 158

[266] A. Arrott and J. E. Noakes, "*Approximate equation of state for nickel near its critical temperature*", Physical Review Letters **19** (1967) 786. 159

[267] B. Banerjee, "*On a generalised approach to first and second order magnetic transitions*", Physics Letters **12** (1964) 16–17. 159

[268] A. Rostamnejadi, M. Venkatesan, P. Kameli, H. Salamati and J. Coey, "*Magnetocaloric effect in* $La_{0.67}Sr_{0.33}MnO_3$ *manganite above room temperature*", Journal of Magnetism and Magnetic Materials **323** (2011) 2214–2218. 161

[269] A. Midya, P. Mandal, K. Rubi, R. Chen, J.-S. Wang, R. Mahendiran, G. Lorusso and M. Evangelisti, "*Large adiabatic temperature and magnetic entropy changes in* $EuTiO_3$", Physical Review B **93** (2016) 094422. 161, 170, 171

[270] M. Kuz'min and A. Tishin, "*Magnetic refrigerants for the 4.2-20 K region: garnets or perovskites*", Journal of Physics D: Applied Physics **24** (1991) 2039. 162

[271] M. D. Kuzmin and A. M. Tishin, "$DyAlO_3$*: A more promising refrigerant than* $Dy_3Al_5O_{12}$", Journal of applied physics **73** (1993) 4083–4085. 162, 168, 170

[272] H. Kimura, T. Numazawa, M. Sato, T. Ikeya, T. Fukuda and K. Fujioka, "*Single crystals of* $RAlO_3$ *(R: Dy, Ho and Er) for use in magnetic refrigeration between 4.2 and 20 K*", Journal of materials science **32** (1997) 5743–5747. 162, 168, 170

[273] A. Midya, P. Mandal, S. Das, S. Banerjee, L. S. Chandra, V. Ganesan and S. R. Barman, "*Magnetocaloric effect in* $HoMnO_3$ *crystal*", Applied Physics Letters **96** (2010) 142514. 162, 168

[274] J.-L. Jin, X.-Q. Zhang, H. Ge and Z.-H. Cheng, "*Rotating field entropy change in hexagonal* $TmMnO_3$ *single crystal with anisotropic paramagnetic response*", Physical Review B **85** (2012) 214426. 162

[275] A. A. Wagh, K. Suresh, P. A. Kumar and S. Elizabeth, "*Low temperature giant magnetocaloric effect in multiferroic* $GdMnO_3$ *single crystals*", Journal of Physics D: Applied Physics **48** (2015) 135001. 162

[276] T. Samanta, I. Das and S. Banerjee, "*Giant magnetocaloric effect in antiferromagnetic* $ErRu_2Si_2$ *compound*", Applied Physics Letters **91** (2007) 152506. 168

[277] G. Heng, Z. Xiang-Qun, K. Ya-Jiao, J. Jin-Ling, L. Zhi-Xin and C. Zhao-Hua, "*Large reversible magnetocaloric effect in* $HoMn_2O_5$", Chinese Physics B **22** (2013) 057502. 168

[278] A. McDannald and M. Jain, "*Magnetocaloric properties of rare-earth substituted* $DyCrO_3$", Journal of Applied Physics **118** (2015) 043904. 168

[279] S. Yin, M. S. Seehra, C. J. Guild, S. L. Suib, N. Poudel, B. Lorenz and M. Jain, "*Magnetic and magnetocaloric properties of* $HoCrO_3$ *tuned by selective rare-earth doping*", Physical Review B **95** (2017) 184421. 168, 170, 171

[280] S. Yin and M. Jain, "*Enhancement in magnetocaloric properties of holmium chromite by gadolinium substitution*", Journal of Applied Physics **120** (2016) 043906. 168, 170

[281] J.-L. Jin, X.-Q. Zhang, G.-K. Li, Z.-H. Cheng, L. Zheng and Y. Lu, "*Giant anisotropy of magnetocaloric effect in $TbMnO_3$ single crystals*", Physical Review B **83** (2011) 184431. 168

[282] M. Shao, S. Cao, S. Yuan, J. Shang, B. Kang, B. Lu and J. Zhang, "*Large magnetocaloric effect induced by intrinsic structural transition in $Dy_{1-x}Ho_xMnO_3$*", Applied Physics Letters **100** (2012) 222404. 168

[283] Y.-J. Ke, X.-Q. Zhang, Y. Ma and Z.-H. Cheng, "*Anisotropic magnetic entropy change in $RFeO_3$ single crystals (R= Tb, Tm, or Y)*", Scientific reports **6** (2016) 19775. 168

[284] R. Huang, S. Cao, W. Ren, S. Zhan, B. Kang and J. Zhang, "*Large rotating field entropy change in $ErFeO_3$ single crystal with angular distribution contribution*", Applied Physics Letters **103** (2013) 162412. 168

[285] Y. Cao, M. Xiang, W. Zhao, G. Wang, Z. Feng, B. Kang, A. Stroppa, J. Zhang, W. Ren and S. Cao, "*Magnetic phase transition and giant anisotropic magnetic entropy change in $TbFeO_3$ single crystal*", Journal of Applied Physics **119** (2016) 063904. 168

[286] X. Zhang, Y. Wu, Y. Ma, Q. Dong, Y. Ke and Z. Cheng, "*Large rotating magnetocaloric effect in $ErAlO_3$ single crystal*", AIP Advances **7** (2017) 056418. 168, 170

[287] G. Lorusso, J. W. Sharples, E. Palacios, O. Roubeau, E. K. Brechin, R. Sessoli, A. Rossin, F. Tuna, E. J. McInnes, D. Collison et al., "*A dense metal–organic framework for enhanced magnetic refrigeration*", Advanced Materials **25** 4653–4656. 171

[288] K. Rubi, A. Midya, R. Mahendiran, D. Maheswar Repaka and R. Ramanujan, "*Magnetocaloric properties of Eu_{1-x} La_xTiO_3 ($0.01 \leq x \leq 0.2$) for cryogenic magnetic cooling*", Journal of Applied Physics **119** (2016) 243901. 171

[289] S. Roy, N. Khan and P. Mandal, "*Giant low-field magnetocaloric effect in single-crystalline $EuTi_{0.85}Nb_{0.15}O_3$*", APL Materials **4** (2016) 026102. 171

[290] A. Midya, N. Khan, D. Bhoi and P. Mandal, "*Giant magnetocaloric effect in magnetically frustrated $EuHo_2O_4$ and $EuDy_2O_4$ compounds*", Applied Physics Letters **101** (2012) 132415. 171

[291] D. Li, T. Yamamura, S. Nimori, Y. Homma, F. Honda, Y. Haga and D. Aoki, "*Large reversible magnetocaloric effect in ferromagnetic semiconductor EuS*", Solid State Communications **193** (2014) 6–10. 171

[292] D. Li, T. Yamamura, S. Nimori, Y. Homma, F. Honda and D. Aoki, "*Giant and isotropic low temperature magnetocaloric effect in magnetic semiconductor EuSe*", Applied Physics Letters **102** (2013) 152409. 171